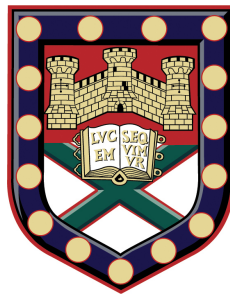


Modelling the Microwave Transmission of Metal Arrays using Modal-Matching



Melita Clare Taylor

School of Physics

University of Exeter

A thesis submitted for the degree of
Doctor of Philosophy by Research in Physics

February 2012

Modelling the Microwave Transmission of Metal Arrays using Modal-Matching

Submitted by

MELITA CLARE TAYLOR

to the University of Exeter as a thesis for the degree of

Doctor of Philosophy by Research in Physics

February 2012

This thesis is available for Library use on the understanding that it is copyright material and that no quotation from the thesis may be published without proper acknowledgement.

I certify that all material in this thesis which is not my own work has been identified and that no material has previously been submitted and approved for the award of a degree by this or any other University.

Melita Clare Taylor

February 2012

“Confusion is a word we have invented for an order which is not understood.”

Henry Miller, Interlude, Tropic of Capricorn

Abstract

This work explores the interaction of electromagnetic radiation with periodic metal-dielectric composite materials. In particular, the majority of the studies explore the role of evanescent diffraction in the regime where the wavelength of the incident radiation is of the order of the period of the array just below the onset of diffraction. The underlying aim of the thesis is to build on the current knowledge and gain deeper understanding into the causal mechanism of the electromagnetic response of these periodic materials.

Developments in metamaterial research have led to a resurgence of interest in the use of periodic metallic surface to control the transmission of electromagnetic radiation. The response of these surfaces can be ‘tuned’ to provide the required response simply by altering the geometric parameters of the material. Numerical modelling techniques are often used to predict the response of such structures. However, the aim of this work is to gain a deeper understanding of the reasons for the response and therefore an analytical modal matching method has been used. The modal matching method provides the opportunity to extract greater understanding of the resonant phenomena by linking them to specific mathematical terms in the analytical formulation.

The modal matching technique is initially used to study the response from a single layer bigrating comprising a square array of square holes in a PEC sheet and its complementary system of a square array of square PEC patches. The importance of evanescent diffraction in both resonant phenomena and tunneling responses is discussed and it is shown that complete transmission (reflection) is supported by these structures even for very high (low) metal occupancy. This technique is extended and adapted to describe a variety of structures in chapters 5 and 6, exploring how resonant excitation of surface waves via evanescent diffraction leads to highly interesting

electromagnetic responses. In chapter 7, alternating multilayer stacks of two different subwavelength meshes provide an observable one-dimensional topological mode in a physical system for particular mesh configurations.

Acknowledgements

Throughout this journey I have received constant help and support from a variety of sources. It is certainly true to state that I couldn't have done it on my own. However, there are a number of people whose contributions have been so significant that they deserve specific mention. Therefore, before anything else, I wish to take the opportunity to thank (in no particular order) the following people.

As the man who started the whole process off, I would like to thank Prof Roy Sambles. Roy had the dubious pleasure of being my tutor as a first year undergraduate. During this year he encouraged me, bullied me, pushed me, praised me and eventually made me realise that I had not lost all my brain cells during the birth of my children. It was during this first year that he challenged my pre-conceived master plan and suggested that I consider taking a Ph.D after graduating. After a bit (a lot) of bullying on my part and eventual bribery with chocolate cake, Roy was pushed into being my tutor in my final year as well. Despite looking at other Ph.D opportunities, there was only ever one person whom I wanted to be supervised by. As has no doubt been said countless times, Roy is an inspiring physicist and educator. He has an intuitive grasp of physics that is often intimidating and is still incredibly enthusiastic and this is contagious. His particular brand of straight talking has served me well, allowing me to believe his praise when given and take notice of his criticism and advice when required. Over the years we have squabbled, argued, laughed, hammered out ideas and generally had a lot of fun. I am proud to be able to say that I am one of 'Roy's Students'.

However that is not the full story as far as supervisors go; I was lucky enough to have two supervisors (although I times I questioned the 'lucky' part - as no doubt did he!). Dr Alastair Hibbins has been the cheese to Roy's chalk and I am honoured to have worked with him. My first encounter with Al

was as a summer student at the end of my second year as an undergraduate, although I had little to do with him as I was working in a different regime. However, he approached me with the PhD grant proposal and we went from there. Al has a very different supervisory approach from Roy and this duality has worked well. He has provided calm and clarity at moments of confusion and has listened to my rants and moans at various times without laughing (too much).

As we all know, we cannot survive on air alone and money is essential to survive. I am eternally grateful for the financial support that I have received. Without this support I would not have been able to take up this opportunity, and so in that respect, my industrial sponsors have provided my most critical support. Therefore I wholeheartedly thank BAE Systems for sponsoring me through my PhD. In particular, I would like to thank Dr Sajad Haq for his personal support and for allowing me to pursue my research goals. My thanks also go to the School of Physics for supplementing my stipend and allowing me to pay my bills and buy food. This was invaluable and I could not have survived without it.

As in any work environment there is a whole supporting cast of people who have been an integral part of my life for the past three (plus) years. These people have fulfilled different needs and in different ways, but have all been necessary to me. Dr Ian Hooper, what can I say? Without you as our 'toy', Helen and I would have been bored on Thursday afternoons. Thank you for tolerating all the interruptions to your own work and stupid questions that you answered. Dr Euan Hendry, thank you for all your help with Mathematica and theoretical queries and for never giving in to that urge to hide behind your door when you heard me approaching. Dr Matt Lockyear, thank you for adding interest to my life; the constant abuse and occasional (disturbing) kiss have kept me going. As for allowing me to organise you, there aren't words to express my gratitude. Nick, thank you for the smiles and for being willing to fix anything I'd been near.

Peer support is also essential in these undertakings and I was fortunate enough to have many special people around me. Biggy, I will miss your cuddles and hair and thank you for all the times you listened to me panic and then picked me up, comforted me and put me back on track. James,

rest assured that it is not only dogs that like you and as far as psychopaths go, you're doing fine! Helen, I can't think of anyone else I would rather play with Ian with. I will never forget the fun we have had stealing shoes and making paper clothes, not to mention 'preeties'. Thank you for all the help you have given me on HFSS and the patience you have shown when I've broken it - again. Celia, you have been my greatest support and friend since you arrived - it was worth doing the Ph.D just to have met you. Thank you for the hours spent explaining how to model things on HFSS and listening to my bizarre explanations of EM phenomena. I will miss our early morning chats. Ed, without your help with LaTeX and anything technical, this thesis would have never emerged. Thank you for fixing all my problems with only the minimum amount of sarcasm! Lizzy, despite being an insane American you have regularly brightened my day - I will miss your ears. To Tim, my own personal bug boy, thank you for the breakfasts, hugs, kisses, essential cups of tea and for brightening up the office - you kept me sane and I will miss you loads.

When I returned to university as a mature student following my divorce I was unsure how I would handle being a single parent and a student, let alone if I had the ability to cope with the work intellectually. Despite the upheaval, my family have supported me through it. I'd like to thank my parents for their unshakeable belief in me and my ability, not to mention their pride in my achievements. I'm not sure I can find the right words to express my gratitude to my children. My boys have supported my decision, coped and accepted the demands on my time that my studies have made and encouraged me. I hope they have seen the benefits to me as a person and, as I have watched them grow and develop, they have also had the opportunity to see me develop and grow into a happier, more rounded person. I am glad I shared this journey with you, thank you Sam, Alex and Jack.

Last, but by no means least I want to thank Nick. You have encouraged me when I couldn't remember why I was doing this. You have picked me up when I didn't want to go on. You have listened to so many technical explanations of my work. You have accepted the long hours I have worked and the time I have not spent with you. You have coped with being woken up at night by me shouting equations. You have shared in my triumphs and managed to stay awake whilst I burred at you. Thank you my love for

believing in me always.

Contents

Contents	ix
List of Figures	xiv
Nomenclature	xxiii
1 Introduction	1
1.1 Motivations for the Thesis	1
1.2 Outline of Thesis Structure	2
2 Background	7
2.1 Introduction	7
2.1.1 Definition of a metamaterial	8
2.1.2 Applications of metamaterials	9
2.1.3 Diffraction	11
2.2 Scattering in periodic media	11
2.2.1 Wavelength much greater than the period	12
2.2.1.1 Clausius-Mossotti relation and Lorentz-Lorenz EMA	13
2.2.1.2 Maxwell-Garnett Approximation (MGA)	16
2.2.1.3 Bruggeman's Effective Medium Theory (EMT)	16
2.2.1.4 Extensions to basic effective medium theories	16
2.2.2 Wavelength of the same order as the period	19
2.2.3 Surface plasmons and spoof surface plasmons	20
2.2.3.1 The surface plasmon polariton dispersion relation	21
2.2.3.2 Spoof Surface Plasmons	25
2.3 Waveguide Modes	28
2.3.1 Waveguide Modes	29
2.3.1.1 TE Waves	31

2.3.1.2	TM Waves	31
2.3.1.3	Rectangular Waveguide Modes	32
2.4	Summary	35
3	Analytical and Numerical Modelling Techniques	37
3.1	Introduction	37
3.2	Analytical Methods	38
3.2.1	Equivalent Circuit Modelling	38
3.2.2	Modal matching	41
3.2.2.1	Method	42
3.2.2.2	Approximations and Simplifications	46
3.2.2.3	Advantages and Limitations	48
3.3	Numerical Methods	49
3.3.1	Finite Element Method	50
3.3.1.1	Introduction to HFSS TM	51
3.3.1.2	Using HFSS TM	52
3.3.1.3	Advantages and Limitations	54
3.4	Conclusion	56
4	The Microwave Response of Square Arrays of Square Elements	57
4.1	Introduction	57
4.2	Background	59
4.2.1	Bigrating dispersion	60
4.2.2	Babinet's Principle	61
4.2.3	Derivation of Babinet's Principle	62
4.3	Method	64
4.4	Results	66
4.4.1	Geometric Parameter Variations	68
4.4.1.1	Variations in Pitch and Element Size	68
4.4.1.2	Variations in Mesh Thickness	71
4.4.2	Dispersion Plots	72
4.5	Discussion	75
4.5.1	Mathematical Analysis	75
4.5.2	Physical meaning	76
4.6	Rotated holes and patches	78
4.6.1	Method	78

4.6.2	Results and Discussion	80
4.7	Summary	82
5	The Aspect Ratio Dependence of the Microwave Response of Hole Arrays	84
5.1	Introduction	84
5.2	Method	85
5.2.1	Square Array of Rectangular Holes	85
5.2.2	Rectangular Array of Square Holes	87
5.2.3	Rectangular Array of Rectangular Holes	88
5.3	Results and Discussion	91
5.3.1	Square Array of Rectangular Holes	91
5.3.1.1	Analysis of results	93
5.3.2	Rectangular Array of Square Holes	95
5.3.2.1	Analysis of results	96
5.3.3	Rectangular Array of Rectangular Holes	99
5.3.3.1	Analysis of results	103
5.4	Conclusion	104
6	The Microwave Response of Closely Spaced Metal Meshes	105
6.1	Introduction	105
6.2	Background	106
6.2.1	Fabry-Pérot Modes	106
6.3	Method	107
6.4	Results and Discussion	111
6.4.1	Lateral displacement parallel to the incident polarisation	111
6.4.2	Lateral displacement perpendicular to the incident polarisation	121
6.5	Summary	125
7	The Microwave Response of Finite Multilayer Stacks of Alternating Metal Meshes	128
7.1	Introduction	128
7.2	Background	129
7.2.1	Fresnel Equations	129
7.2.1.1	Single Interface Fresnel Equations	130
7.2.1.2	Recursive Fresnel Equations	134

7.2.2	Bragg Stacks and Metal-Dielectric Stacks	137
7.2.3	Topology	137
7.3	Methods	138
7.3.1	Adaptation of the Modal Matching Method for a Double Mesh Structure with Different Mesh Layers	138
7.3.2	Description of a Metal Mesh using an Effective Medium Approach	140
7.3.3	Application of the Effective Medium Approach to Multilayer Sys- tems	141
7.4	Results and Discussion	142
7.4.1	Double Mesh Structure with Different Mesh Layers	142
7.4.1.1	Comparison of Effective Medium Approach with Modal Matching Method	142
7.4.2	Multilayer Structures	146
7.4.2.1	Varying Multilayer System Parameters	147
7.4.2.2	Topological Modes	150
7.4.2.3	Tunnel Barrier Analogy	153
7.5	Conclusion	156
8	Conclusions and Future Work	157
8.1	Introduction	157
8.2	Summary of Thesis	158
8.3	Future Work	162
8.3.1	Extension of the Modal Matching Model for Real Metals	162
8.3.2	Bilateral Displacement in Double Mesh Structures	163
8.3.3	Experimental Determination of a One Dimensional Topological Mode in a Real System	163
8.3.4	Random and Quasi-Random Systems	164
8.4	Publications and Conference Presentations	166
8.4.1	Publications	166
8.4.2	Conference Presentations	166
A	Full Modal Matching Calculation	168
A.1	Introduction	168
A.2	Wolfram Mathematica File	168
A.2.1	Manipulation of Equations and Workings	168
A.2.2	Mathematica Solution	173

References

175

List of Figures

2.1	<i>Photograph of a double negative metamaterial.</i>	9
2.2	<i>Schematic of an effective medium.</i>	13
2.3	<i>Schematic of homogeneous material with cubic lattice structure for (a) single material surrounded by vacuum, (b) points of polarisability surrounded by vacuum and (c) points of polarisability surrounded by a host material</i>	14
2.4	<i>Schematic representation of the difference in interpretation of the composite structure for the Maxwell-Garnett Approximation and Bruggeman's Effective Medium Theory.</i>	17
2.5	<i>Screening of small metal sphere in a dielectric medium under an applied field</i>	18
2.6	<i>Theoretical reflectivity data illustrating both Rayleigh and Wood's anomalies.</i>	19
2.7	<i>The incident, reflected and transmitted fields associated with a p-polarised wave incident on a planar interface between a metal and a dielectric.</i>	22
2.8	<i>Schematic representation of the polarisation of the surface charge density and associated electric field for the SPP mode.</i>	24
2.9	<i>Schematic representation of the SPP dispersion curve.</i>	25
2.10	<i>Dispersion curve for grating-coupled SPP's reflected at the Brillouin zone boundaries.</i>	27
2.11	<i>Schematic illustrating the coordinate system used to describe the grating orientation.</i>	27
2.12	<i>A reciprocal space representation in two dimensions of the SPP modes and light circles produced by a grating.</i>	28
2.13	<i>Schematic illustrating the field alignments and plane of incidence for (a) TE polarisation, (b) TM polarisation and (c) TEM polarisation.</i>	29

2.14	<i>Schematic showing the geometry and coordinate system for the rectangular waveguide.</i>	32
2.15	<i>Electric field profiles in the xy-plane corresponding to the eigensolutions of the first four TE modes supported by an air filled perfectly conducting metal waveguide.</i>	34
2.16	<i>Electric field profiles in the xy-plane corresponding to the eigensolutions of the first four TM modes supported by an air filled perfectly conducting metal waveguide.</i>	36
3.1	<i>Schematic of metal mesh with square holes and its equivalent circuit diagram.</i>	39
3.2	<i>Equivalent circuit for a single metal mesh layer detailing the single components required to accurately represent the mesh.</i>	39
3.3	<i>Schematic showing a pair of parallel inductive meshes with square apertures.</i>	40
3.4	<i>Equivalent circuit diagram for a pair of parallel inductive meshes with square apertures.</i>	40
3.5	<i>Schematic of the investigated system and the defined regions used by the modal matching method.</i>	42
3.6	<i>Schematic showing master-slave boundaries of an infinite periodic structure.</i>	53
3.7	<i>Screen shots from HFSSTM illustrating (a) master-slave boundaries and (b) Floquet Port excitation.</i>	54
3.8	<i>A sample mesh produced by HFSSTM on the top face of the unit cell of a hole array.</i>	55
4.1	<i>Schematic of a bigrating with two orthogonal grating periods</i>	59
4.2	<i>Schematic illustrating the parabolic diffracted light line formed from the intersection of light cones.</i>	60
4.3	<i>A reciprocal space representation of a bigrating for a fixed frequency. . .</i>	61
4.4	<i>Schematic diagram illustrating the scattered light lines and SPP modes for a square bigrating.</i>	62
4.5	<i>Schematic showing the coordinate system, incident and scattered fields for (a) a rectangular hole in a PEC sheet, and (b) a rectangular PEC patch.</i>	63
4.6	<i>Graphical illustration of Babinet's Principle.</i>	65

4.7	<i>Schematic showing the investigated structure A and its complementary structure A^*.</i>	65
4.8	<i>Comparison between the modal matching model with up to and including the third family of evanescent orders in the calculation, and the HFSSTM solution for a square array of square holes in a PEC sheet.</i>	67
4.9	<i>Comparison between the modal matching model data after application of Babinet's Principle and the HFSSTM solution for a square array of square PEC patches.</i>	68
4.10	<i>The varying transmission response for a square array of square holes in a PEC sheet at normal incidence as a result of increasing the number of evanescent diffracted orders included in the calculation</i>	69
4.11	<i>Normal incidence transmission for a 2D hole array (structure A) with: (a) fixed pitch and varying hole sizes, including Bethe's predicted transmission; (b) square holes with fixed side length with varying array pitch; (c) pitch to hole side length ratio of 5:3.</i>	70
4.12	<i>The transmission response for a hole array at normal incidence for increasing values of mesh thickness.</i>	72
4.13	<i>Comparison for normal incidence transmission between the modal matching transmission data for the finite depth hole arrays after application of Babinet's Principle with the HFSSTM solution for finite depth patch arrays.</i>	73
4.14	<i>Dispersion plots using the modal matching model for the transmission for p- and s-polarisations for structures A and A^*</i>	74
4.15	<i>(a) Schematic of dipole array description showing the regions of enhanced \vec{E} field for a square array of square PEC patches; \vec{E} field plots produced from the modal matching model for a patch array showing the \vec{E} field enhancement for (b) 0.5 mm below the structure and (c) 4 mm below the structure.</i>	77
4.16	<i>(a) Schematic of surface current description showing the regions of enhanced \vec{H} field for a square array of square holes in a PEC sheet; \vec{H} field plots produced from the modal matching model for a hole array showing the \vec{H} field enhancement for (b) 0.5 mm below the structure and (c) 4 mm below the structure.</i>	79
4.17	<i>Schematic of the modified structure of a square array of square holes rotated by 45° with respect to the coordinate system in a PEC sheet and its complementary system of a square array of rotated square PEC patches.</i>	80

LIST OF FIGURES

4.18	<i>Transmission through a square array of rotated square holes in a PEC sheet at normal incidence as a function of metal filling fraction.</i>	81
5.1	<i>Schematic of a regular square array of rectangular holes in a PEC sheet.</i>	86
5.2	<i>Schematic of a regular rectangular array of square holes in a PEC sheet.</i>	87
5.3	<i>Schematic of a regular rectangular array of rectangular holes in a PEC sheet.</i>	89
5.4	<i>Comparison between the modal matching model and the solution derived using a finite element method model for a square array of rectangular holes in a PEC sheet.</i>	91
5.5	<i>Transmission response for a square array of rectangular holes in a PEC sheet</i>	92
5.6	<i>Schematic of a square array of rectangular holes showing the capacitive and inductive components.</i>	95
5.7	<i>Comparison between the modal matching model and the solution derived using a FEM model for a rectangular array of square holes in a PEC sheet.</i>	96
5.8	<i>Transmission response for a rectangular array of square holes in a PEC sheet with side length 8 mm for (a) $d_y = 10$ mm, (b) $d_x = 10$ mm, at normal incidence with the incident radiation polarised parallel to the x-axis, and (c) a scale schematic of the change in unit cell for each graph. The onset of diffraction is indicated by the dashed lines.</i>	97
5.9	<i>Comparison between the modal matching model and the solution derived using a FEM model for a rectangular array of rectangular holes in a PEC sheet.</i>	99
5.10	<i>Transmission response for a rectangular array of rectangular holes in a PEC sheet for varying hole sizes.</i>	100
5.11	<i>Transmission response for a rectangular array of rectangular holes in a PEC sheet for varying pitches.</i>	102
6.1	<i>Schematic of a Fabry-Pérot etalon comprising a pair of highly reflecting parallel surfaces filled with a dielectric spacer.</i>	107
6.2	<i>\vec{E} Field profiles corresponding to the eigensolutions of the first four Fabry-Pérot modes supported by a pair of perfectly conducting square metal meshes, with holes much smaller than the wavelength, separated by an air gap.</i>	108

6.3	<i>Schematic of the investigated geometry showing a double layer of a square array of square holes in a PEC sheet separated by a dielectric layer. . .</i>	109
6.4	<i>Schematic showing the defined regions for the double mesh layer structure.</i>	109
6.5	<i>Schematic defining the unit cell and the origin for the double mesh layers as used in the analytical formulation.</i>	111
6.6	<i>Transmission plots for the double mesh arrangement for three different separation distances, g, between the meshes. Each graph shows the transmission profile for both the aligned system and when the meshes are laterally displaced by half a pitch with respect to each other along the polarisation axis.</i>	114
6.7	<i>Schematic showing (a) cosh-like symmetric \vec{E} field and (b) sinh-like antisymmetric \vec{E} field. The mesh layers are indicated by the thick black vertical lines.</i>	115
6.8	<i>Greyscale plot of the normal incidence transmission as a function of frequency and mesh separation for (a) $b_x = 0$ mm, $b_y = 0$ mm and (b) $b_x = 5$ mm, $b_y = 0$ mm.</i>	117
6.9	<i>Colour-scale plot of the normal incidence transmission as a function of frequency and lateral misalignment parallel to the incident polarisation for (a) mesh separation $g = 14$ mm and (b) mesh separation $g = 0.1$ mm.</i>	118
6.10	<i>Complex magnitude \vec{E} field plots in the xz-plane for a double mesh layer system with pitch $d = 10$ mm, square holes of side length $a = 4.5$ mm and mesh separation $g = 0.1$ mm at: (a) $f \approx 27.7$ GHz with misalignment $b_x = 0$ mm, $b_y = 0$ mm; (b) $f \approx 20.4$ GHz with misalignment $b_x = 5$ mm, $b_y = 0$ mm; (c) $f \approx 25.5$ GHz with misalignment $b_x = 0$ mm, $b_y = 0$ mm; (d) $f \approx 29.9$ GHz with misalignment $b_x = 5$ mm, $b_y = 0$ mm.</i>	120
6.11	<i>Schematic of possible charge distributions for a double layer of identical metal slit arrays (i.e., one dimensional grids).</i>	121
6.12	<i>Directional \vec{E} field plots in the xz-plane in the region between the two meshes for a double mesh layer system of pitch $d = 10$ mm, square holes of side length $a = 4.5$ mm and mesh separation $g = 1$ mm for misalignment parallel to the incident radiation.</i>	122

6.13	<i>Transmission reponse for two meshes laterally misaligned relative to each other both parallel (black line) and perpendicular to (red line) the incident polarisation at normal incidence. Both meshes have a pitch of $d = 10$ mm and square hole of side length $a = 4.5$ mm. The red line represents relative misalignment of $b_x = 0$ mm, $b_y = 5$ mm and the black line represents relative misalignment of $b_x = 5$ mm, $b_y = 0$ mm. The incident radiation is polarised parallel to the x-axis.</i>	123
6.14	<i>Greyscale plot of the normal incidence transmission as a function of frequency and mesh separation for (a) $b_x = 5$ mm, $b_y = 0$ and (b) $b_x = 0$ mm, $b_y = 5$ mm.</i>	124
6.15	<i>Schematic of possible charge distributions for double layer metal grids at maximum misalignment with respect to each other where the misalignment is perpendicular to the incident radiation.</i>	125
6.16	<i>\vec{E} field plots in the region between the two meshes for a double mesh layer system of pitch $d = 10$ mm, square holes of side length $a = 4.5$ mm and mesh separation $g = 1$ mm for misalignment perpendicular to the incident radiation.</i>	126
7.1	<i>Schematic of light propagating through a planar multilayer structure with $(N-1)$ layers.</i>	130
7.2	<i>Schematic showing the reflection (R) and transmission (T) of incident light (I) at a single interface between two different media.</i>	131
7.3	<i>The incident, reflected and transmitted fields associated with a p-polarised wave incident on a planar interface between two different media.</i>	132
7.4	<i>The incident, reflected and transmitted fields associated with a s-polarised wave incident on a planar interface between two different media.</i>	134
7.5	<i>Schematic of EM waves propagating in a three media system.</i>	135
7.6	<i>Transmission through a multilayer Bragg stack of 16 layers of alternating dielectric with relative permittivity of 2 and 4. Each dielectric layer is 6.35 mm thick.</i>	138
7.7	<i>Schematic illustrating a mathematical joke regarding the identical topology of a coffee mug and a doughnut.</i>	139
7.8	<i>A Hilbert Cube [1].</i>	139
7.9	<i>Schematic of the unit cell in the z-direction of an ‘ACBC’ multilayer arrangement.</i>	142

7.10	<i>Transmission response at normal incidence for a double mesh structure comparing the modelled response from an effective medium approximation with that from a modal matching model.</i>	143
7.11	<i>Transmission response at normal incidence for a double mesh structure comparing the modelled response from an effective medium approximation with that from a modal matching model for different mesh separations.</i>	144
7.12	<i>Decay length of the fields for a mesh with period $d = 5$ mm for the frequency range 5 - 40 GHz.</i>	145
7.13	<i>(a) Transmission response for a 4 unit cell geometry where each cell is comprised of an ACBC structure. Layers A and B are identical PEC mesh layers of thickness $h = 18$ μm with pitch $d = 5$ mm and hole side of $a = 4.5$ mm. Layer C is a dielectric spacer of thickness $g = 6$ mm with a permittivity of 1 (i.e. air), (b) schematic of the structure.</i>	147
7.14	<i>Transmission response at normal incidence for a 4 unit cell geometry where each cell is comprised of an ACBC structure where A and B are PEC mesh layers and C is a dielectric spacer layer of thickness $g = 6$ mm. (a) the parameters of mesh A are fixed whilst those of mesh B are varied, (b) the parameters of mesh A are varied whilst those of mesh B are fixed and (c) a schematic of the structure.</i>	148
7.15	<i>Transmission response at normal incidence for a 3+ unit cell geometry where each cell is comprised of an ACBC structure where A and B are PEC mesh layers and C is a dielectric spacer layer of thickness $g = 6$ mm. (a) the parameters of mesh A are fixed whilst those of mesh B are varied, (b) the parameters of mesh A are varied whilst those of mesh B are fixed and (c) a schematic of the structure.</i>	149
7.16	<i>Greyscale plot of normal incidence transmission as a function of frequency and mesh B hole side length (a_B) for mesh A hole side length of: (a) $a_A = 4.5$ mm and 4 unit cells; (b) $a_A = 3.5$ mm and 4 unit cells; (c) $a_A = 4.5$ mm and 3+ unit cells; (d) $a_A = 3.5$ mm and 3+ unit cells.</i>	151
7.17	<i>Field plots showing time averaged \vec{E}_z fields through the structure normalised to an incident field of unity. The structure has 3+ unit cells and mesh A has a hole side length of $a_A = 4.5$ mm. The illustrated modes are: (a) the 3rd mode for $a_B = 4.5$ mm; (b) the 4th mode for $a_B = 4.5$ mm; (c) the 3rd mode for $a_B = 3.7$ mm; (d) the 3rd mode for $a_B = 4.8$ mm; (e) the 4th mode for $a_B = 4.8$ mm.</i>	152

7.18	<i>Schematic illustrating quantum mechanical analogy for the 4 unit ACBC structure, where $A = B$, in terms of 8 potential barriers.</i>	154
7.19	<i>Schematic illustrating quantum mechanical analogy for; (a) the 4 unit ACBC structure, where $a_A > a_B$, (b) the 4 unit ACBC structure, where $a_A < a_B$, (c) the 3+ unit ACBC structure, where $a_A > a_B$ and (d) the 3+ unit ACBC structure, where $a_A < a_B$, in terms of potential barriers.</i>	155
8.1	<i>Schematic defining the unit cell and the origin for a double mesh structure illustrating lateral displacement in one and two directions.</i>	163
8.2	<i>Greyscale plot of normal incidence transmission as a function of frequency and mesh B hole side length (a_B) for an ACBC structure where A and B are PEC mesh layers of thickness $h = 18 \mu\text{m}$ and C is a dielectric spacer layer of thickness $g = 6 \text{ mm}$. Mesh A has a hole side length of $a_A = 4.5 \text{ mm}$ and the structure consists of 4 unit cells in the z-direction.</i>	164
8.3	<i>Schematic illustrating three possible randomisations of a square lattice.</i>	165
8.4	<i>Schematic illustrating the effect of perturbing the orientation in a square ‘checkerboard’ lattice.</i>	165

Nomenclature

Roman Symbols

α	Polarisability
ϵ	Permittivity
ϵ_0	Permittivity of free space
λ	Wavelength
μ	Permeability
ω	Angular frequency
ω_P	Bulk plasma frequency
ω_{SP}	Surface plasma frequency
σ	Conductivity
\vec{B}	Magnetic field intensity
\vec{D}	Electric displacement
\vec{E}	Electric field strength
\vec{H}	Magnetic induction
c	The speed of light
d	Period
k	Wavevector
k_g	Grating vector

t	Time
X	Reactance
Y	Admittance
Z	Impedance
CAD	Computer Aided Design
DNG	Double negative media
DPS	Double positive media
EM	Electromagnetic
EOT	Extraordinary optical transmission
FDTD	Finite Difference Time Domain
FEM	Finite Element Method
FSS	Frequency Selective Surfaces
PEC	Perfect electrical conductor
SNG	Single negative media
SPP	Surface plasmon polariton
SRR	Split ring resonator
TE	Transverse electric
TEM	Transverse electromagnetic
TM	Transverse magnetic

Chapter 1

Introduction

1.1 Motivations for the Thesis

The overarching aim of the thesis is to gain a greater level of understanding on how periodic metal-dielectric composite materials interact with electromagnetic radiation. There has been a resurgence of recent studies considering periodic arrays of subwavelength elements, initiated perhaps by the work of Ebbesen *et al* in 1998 [2]. Numerical modelling has often been used to predict the response of these structures and to explore their electromagnetic field solutions. However, this thesis is specifically concerned with the use of analytical modal matching methods to explore the response of novel structures and to gain the deeper understanding implicit in the analytical basis on which the model is constructed. The study of the interaction of light with matter is a wide reaching and complex field with a rich history of research which dates back as early as 1665. Whilst commercial numerical modelling methods (for example, Finite Element Methods or Finite Difference Time Domain models) can predict the response of complex structures to radiation, they provide little information on the reasons for the response or the physics governing its behaviour, whereas analytical modelling does. In this thesis, the motivation is therefore to employ analytical methods that offer a mathematical breakdown of the origin of the electromagnetic response leading to enhanced understanding of the phenomena.

The response of these composite materials is determined by a range of factors, including the fractional occupancy and material properties of the individual constituents, their geometry and their spatial arrangement. Interdependence of these parameters on the structure's electromagnetic response is complex and the response can be difficult to predict. By improving the understanding of how these materials interact with electro-

magnetic radiation, we are better able to optimise their response for a given application. Composite materials have uses in many differing fields, for example as electromagnetic shields as well as in imaging and lithography applications.

The scope of the thesis is limited to metal-dielectric materials comprising regular arrays of regular geometric elements with both metal and dielectric constituents. In addition, it is only concerned with non-magnetic materials and therefore it is assumed that all materials have a permeability equal to unity. The other main assumption is that the conductivity of the metal is infinite, otherwise known as a perfect electrical conductor (PEC). Therefore, as most metals behave as almost perfect metals at microwave frequencies, the modelling throughout the thesis has focused on the microwave regime of the spectrum. This and other assumptions are explained fully in the following chapter.

1.2 Outline of Thesis Structure

The thesis comprises three broad parts. The initial part contains chapters 2 and 3 and covers the background and theory relating to the original studies that follow. The second (main) part covers chapters 4 to 7 and concerns the modelling of the electromagnetic response of various metal-dielectric structures using the methods detailed in chapter 3. The final part comprises chapter 8 and concludes the thesis. A brief outline of the contents of each chapter is detailed below.

Chapter 2 provides a general background to the thesis. In order to investigate the electromagnetic behaviour of composite media, it is important to explain what is meant by this description. Therefore, the term ‘metamaterial’ (or composite material) is introduced and its definition discussed, along with a few applications of these special materials. The present work focuses on how radiation interacts with periodic structures and it is important to place this work in the context of established knowledge. Therefore, the definition of a metamaterial is followed by a discussion on electromagnetic scattering in periodic media. It is well known that light interacts with matter and that it is the ratio between the wavelength of the incident radiation and the period of the media that dictates how that particular material responds to electromagnetic radiation. For clarity, the discussion has been divided into subsections relating to this ratio. Each subsection begins with an historical review of the literature and a brief description of the main theories and their development. The discussion focuses on two regimes in particular. For the regime where the wavelength of the incident radiation is much greater than the

period of the media, effective medium approximations are applicable. The main basic theories are presented along with a brief review of some of the extension theories that have been developed. This has particular relevance to the work presented in chapter 7 relating to multilayer metal-dielectric stacks involving subwavelength PEC meshes. Most of the investigated structures involve the coupling of surface waves supported on periodic PEC meshes. It is therefore necessary to present a brief background of the nature of such surface waves. The next subsection of this introductory chapter provides a brief summary of the history of surface waves. Although surface plasmons only exist at visible frequencies, some aspects of the theory are still relevant to aid understanding of this current work. The concept of surface plasmons and how this led to structurally dictated surface waves is briefly introduced in the regime where the incident wavelength is the same order as the period of the medium. The final section in this chapter presents the derivation of waveguide modes for both transverse electric and transverse magnetic polarisations with a focus on the form of rectangular waveguides. The main section of the thesis comprises four chapters, each investigating a different structure. Whilst none of the structures explored within the thesis support standing wave resonances (waveguide modes) in the frequency regime of interest as they are too thin, the majority of the work involves ‘hole arrays’ (regular geometric arrays of regular shaped ‘holes’ in a sheet of PEC). The fields inside these ‘holes’ take the same form as waveguide modes and therefore an understanding of these modes and their mathematical formulation is necessary to understand the response of the structures.

Different modelling techniques are discussed in chapter 3. The chapter is divided into analytical and numerical methods. In each section, the most common methods are described briefly along with their general advantages and disadvantages. This is followed by a more detailed description of the methods chosen for use in this thesis. In the case of the analytical modal matching method used in the majority of the investigations, a derivation is given along with the reason behind the use of this method and an evaluation of the strengths and limitations of it. The numerical method used is a commercially available software package, and an overview of its main features is given including an evaluation of the technique. This chapter concludes the initial part of the thesis.

Chapter 4 is the first investigative chapter in the main part of the thesis and examines the electromagnetic response of a single layer PEC-dielectric bigrating and its complementary structure. A bigrating is a two dimensional array of elements and this chapter looks at the response of both a ‘hole array’ and a ‘patch array’. The application of Babinet’s Principle allows the response of one structure to be used to predict the

response from its complement. This chapter begins with the derivation of Babinet's Principle and a discussion of its importance. We review the remarkable result that at frequencies just below the onset of diffraction a square array of square holes supports a 100% transmission resonance, even for high metal occupancy. Conversely for the complementary patch array structure, a 100% reflection resonance is supported. This phenomenon is associated with evanescent diffraction. An evanescent wave decays exponentially with distance from the point at which it was formed and therefore does not propagate. It is characterised by an imaginary wavevector. A complete analytical solution for the transmission through the structure is presented using the modal matching technique and the importance of the role of evanescent diffraction for these resonance phenomena is illustrated and discussed. The chapter concludes with an exploration of the transmission response with regards to electrical connectivity.

Chapter 5 also concerns single layer bigrating systems. However, this chapter focuses on the effect breaking the four-fold symmetry inherent in the previous system has on the predicted electromagnetic response. The simple structure investigated in chapter 4 is extended to three different structures. The investigated structures are a square array of rectangular holes in a PEC sheet, a rectangular array of square holes in a sheet of PEC and a rectangular array of rectangular holes in a PEC sheet. The aspect ratio of both the hole and the periodicity have been investigated in other studies. However these are primarily at optical frequencies and the majority of modelling is numerical. This chapter uses the same basic methodology as the previous chapter altered to reflect the geometrical changes of the unit cell. An analytical solution for the transmission is produced and the significance of the parameters is explored both mathematically, and more importantly from a physical perspective.

The previous two chapters have investigated single layer meshes. In this chapter the understanding gained from the work presented in previous chapters is applied to more complex structures. Chapter 6 introduces a system involving a double mesh layer. The modelling method is extended to account for the complex near field interactions between the PEC mesh layers. Earlier chapters have established that a single mesh layer supports a strong transmission resonance due to a resonantly excited surface wave. Evanescent diffraction has been shown to be of paramount importance to this phenomenon. This chapter focuses particularly on the effect on the transmission of lateral translation of one mesh relative to the other and the role that evanescent diffraction plays in this. A Fabry-Pérot etalon is the name given to highly reflecting partial mirrors a distance apart. The two PEC meshes in this structure are highly reflecting partial mirrors

and can therefore support resonant Fabry-Pérot modes. The chapter begins with a brief overview of Fabry-Pérot etalons followed by a description of the adaptations and extensions made to the modelling method to accurately represent the double layer geometry. The effect on the transmission profile of parameter variations is shown and the electromagnetic response analysed mathematically to gain further understanding. It is shown that the structure supports families of standing wave modes together with surface modes and that close to the onset of diffraction these modes interact with each other. The analysis shows that the separation of the meshes is the critical parameter in determining the response of the structure.

Chapter 7 explores the response of multiple layer stacks consisting of alternating PEC mesh and dielectric layers. The exploration of multilayer structures has been established for many years, however, what makes this study original is that two different meshes are used within the structure. The mesh parameters of each mesh are varied, from identical parameters, through slight parametrical differences (perturbations) to large differences between the parameters of each mesh. The chapter begins with the introduction and derivation of both simple and recursive Fresnel coefficients used in describing the response of multilayer planar homogeneous media to electromagnetic radiation. The discussion continues with the response of conventional dielectric-dielectric stacks (Bragg stacks). A different modelling approach is taken in this chapter in comparison to previous chapters; using the modal-matching model for a single mesh layer an effective medium approximation is obtained for each mesh layer. This is then applied to a multilayer approach to provide the transmission through the finite stack. This approach has been utilised to reduce the computational requirements involved in a full modal matching approach involving multiple layers. The results part of this chapter is separated into two distinct parts. The first compares the validity of the effective medium approach with the modal matching model for a double mesh system where each mesh has differing parameters. The second part is concerned with the electromagnetic response of the alternating mesh multilayer stack configuration for larger numbers of layers. The existence of a topological mode is presented for specific conditions. Topological properties are defined as properties that are invariant under particular transformations and topology forms an extensive branch of mathematics concerned with studying continuity and connectivity. These concepts are introduced in this chapter and analogies drawn with the multilayer system explored therein.

The final chapter, chapter 8, summarises the salient points of the investigative work presented in this thesis and discusses some of the possible directions for future work

suggested by the conclusions within it. It is concluded by a list of publications and conferences attended (including submitted and planned future publications).

Chapter 2

Background

2.1 Introduction

The response of matter to electromagnetic (EM) radiation has been of interest to the scientific community for almost two hundred years. Both homogeneous and composite materials have been investigated, along with bulk matter, periodic and aperiodic media. In this chapter a review of the basic underlying principles, along with a brief historical overview is presented.

Metamaterials are generally artificial materials; ‘meta’ from the greek $\mu\epsilon\tau\alpha$ meaning after, or beyond. In other words, materials enhanced in relation to those found naturally. Metamaterials are of great interest to a wide range of business sectors, including defence, medical and IT industries, due to their individual electromagnetic properties. Consequently much research is being done to design materials for specific applications. The ability to predict the electromagnetic properties of composites prior to manufacture has a crucial role in the design, manufacture and application of these important materials.

This section sets out what is meant by the term ‘metamaterial’ in the context of this thesis, followed by a brief look at some of the applications of metamaterials and the unusual properties that make them so important. Section 2.2 introduces the basic theories and historical developments in the field of scattering in periodic media. Lastly, section 2.3 discusses waveguide modes and the physics behind them followed by a summary of the salient points in section 2.4.

2.1.1 Definition of a metamaterial

Whilst composite materials (by which we mean materials with more than one constituent) have been investigated for many years, the term ‘metamaterial’ was first used in 2001 by Walser [3] in reference to engineered composites that “achieve material performance beyond the limitations of conventional composites” [3]. Since then there have been numerous attempts to categorise (and re-categorise) these fascinating materials. As such, there is no definitive definition, as stated by Sihvola [4]. However, the two common themes in all definitions are that the material exhibits properties that are very different from those of the constituent materials and that these properties are not observed in nature. For the purposes of this thesis, the following broad definition, as given by Metamorphose, the Virtual Institute for Artificial Electromagnetic Materials and Metamaterials [5], is most appropriate:

“(A) metamaterial is an arrangement of artificial structural elements, designed to achieve advantageous and unusual electromagnetic properties.”

The properties of metamaterials are due to their subwavelength structure as opposed to their chemical composition. It is this that allows them to be specifically designed as the properties can be changed simply by altering the structure of the material. The electric and magnetic properties of materials are characterised by the complex parameters permittivity, ϵ and permeability, μ . The permittivity of a material describes how a material changes to absorb electrical energy when subjected to an electric field. It is defined as the ratio between the electric displacement \vec{D} and the electric field strength \vec{E} (equation 2.1). Similarly, permeability is the ratio between magnetic induction, \vec{H} and magnetic field intensity, \vec{B} . By creating the right structure, even properties that do not exist in nature can be achieved, for example materials with a negative index of refraction [6, 7]. In nature the majority of materials have positive permittivity and permeability and are often referred to as double positive media (DPS). Materials with one parameter negative are referred to as single negative media (SNG) and some natural materials do exhibit these characteristics at specific frequencies. For example many metals have negative permittivities at optical frequencies, and some ferromagnetic materials have negative permeability at frequencies close to resonance. Materials with negative values of both permittivity and permeability are referred to as double negative media (DNG) and these properties are never experienced in natural materials. Many metamaterials are created using machined structures and the geometry of the structure is often the key element in determining the electromagnetic behaviour of the composite.

2.1.2 Applications of metamaterials

There are many varied applications of metamaterials and their properties, and many more being currently investigated, across a wide range of sectors. Summarised below are a few of these properties along with their applications.

The term ‘negative index material’ is also used to define DNG media as described in section 2.1.1. This is of considerable interest as there is no naturally occurring material with these characteristics. There has been much work done on creating such metamaterials as well as investigation of the effect and application of these parameters [8–10]. For example, Shelby *et al.* [7] have used split-ring resonators (SRR’s) embedded in a dielectric to create a material with simultaneously negative permittivity and permeability (figure 2.1). A time varying magnetic field applied parallel to the axis of the SRR’s produces a magnetic resonance. The periodic array results in strong magnetic coupling and the material can be described by an effective permeability due to the inclusions being significantly subwavelength.

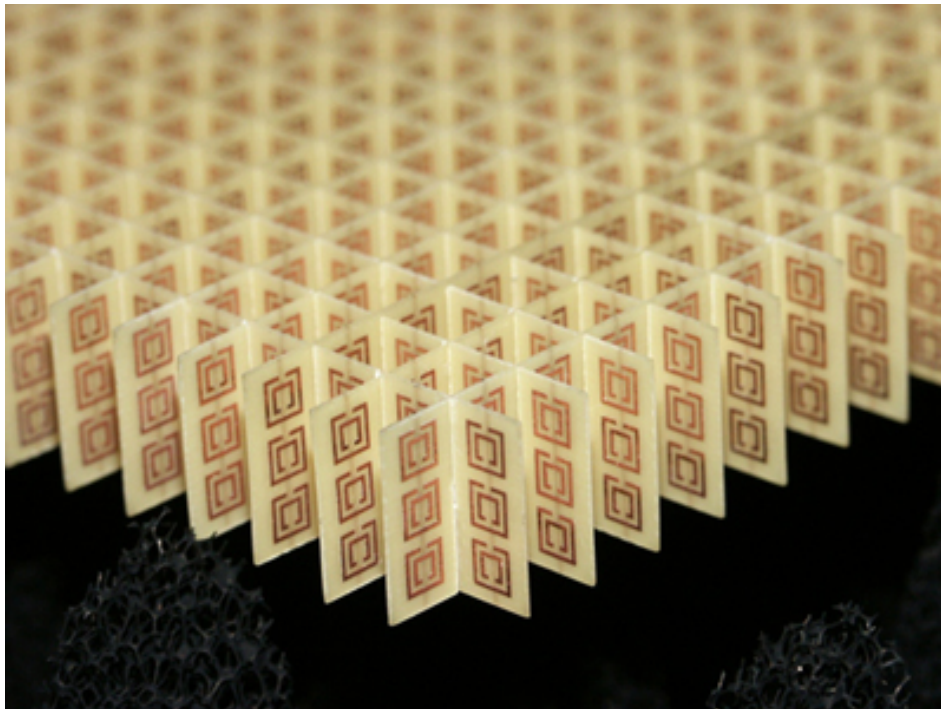


Figure 2.1: *Photograph of a DNG metamaterial. The sample consists of square copper split ring resonators and copper wire strips on fiber glass circuit board material. The rings and wires are on opposite sides of the boards and the boards have been cut and assembled into an interlocking lattice [7].*

This is a rapidly growing area and there are countless examples; some other appli-

cations and structures are reviewed in [11] and [12]. Arbitrarily high refractive index also has some useful applications. It is used in imaging and lithography applications to achieve increased resolution as well as slow light applications. Shin *et al* [13] describe how metamaterials with a high refractive index over a broad bandwidth can be created using cubic arrays of inclusions that produce a large electric dipole response whilst still retaining small area current loops. This results in a large permittivity enhancement without suppression of the permeability, therefore leading to a high refractive index.

Materials have been used to control electromagnetic fields for many years. This is generally done using homogeneous materials and altering the interface; for example in glass lenses or metal cages. However, in recent years there has been much interest in using inhomogeneous materials, such as metamaterials, as they have far more design flexibility. In particular, the use of metamaterials to produce ‘cloaking’ media has created a lot of interest. Pendry *et al* [14] discuss designing materials that redirect conserved EM fields to create a ‘cloaking’ medium utilising a conformal mapping technique that uses a co-ordinate change to calculate the required permittivity and permeability of the metamaterials. Leonhardt [15, 16] developed similar conformal mapping techniques at the same time. At present, the main limitation to this approach are that it only works for a small frequency range due to the requirement of permittivity and permeability with absolute values less than one [17].

Another cloaking method has been presented by Alú and Engheta [18, 19], and uses the scattering cancellation method. The cloak and the object are treated as a single composite material in order to reduce the scattering. However, this method requires knowledge of the shape and the material properties of the object to be cloaked. Although it is a broad-band solution, each cloak is individual to the object it is concealing and this approach can only be used with objects much smaller than the wavelength of the incident radiation. Lai *et al* have also proposed an alternative cloak for prespecified objects [20] that utilises the scattering cancellation method.

Metamaterials have been used as electromagnetic shields in a variety of sectors for many years. The communications industry is one of the largest users of this application, in particular shielding microwave radiation from areas that are using fibre optic technology. Matumura *et al* [21] explain how metal fibres embedded into an optically transparent polymer and then stacked can shield microwave radiation whilst allowing optical frequencies through. Antenna design has also benefited from metamaterial developments allowing highly directional antennas to be created that rely on the metamaterial resonance, as well as enhancing the performance of small antennas. At present,

one of the major disadvantages of metamaterials is their characteristic high loss and limited operational bandwidths [22].

2.1.3 Diffraction

The term diffraction is used to describe the effects that occur when waves encounter an obstacle. It comes from the Latin ‘diffringere’, meaning ‘to break into pieces’ and the term was first introduced by Francesco Grimaldi [23] in 1665 and it is believed that he was the first person to record diffraction observations. The first documented study into diffraction gratings was performed by Gregory [24] when he investigated the diffraction patterns observed through a bird’s feather. In 1803, Thomas Young devised his seminal double slit experiment [25], in which he described the patterns produced when light passed through two closely spaced narrow slits. By explaining his observations as interference between waves passing through each of the slits, he concluded that light propagates as a wave. His work was extended by Fresnel [26] and provided evidence for Huygens’ theory that light was a wave [27].

A diffraction grating is an example of a periodic medium which can be described as a collection of identical elements arranged in a one, two or three dimensional regular infinite array. As a final comment on the term diffraction, it is worth noting that interference and diffraction are often used to describe the same process.

2.2 Scattering in periodic media

How waves scatter when they encounter periodic media is of interest in a wide variety of fields, from x-ray scattering [28] to photonic crystals [29]. For the scope of this thesis, the term scattering will refer to the scattering of electromagnetic waves when they encounter matter. The process of linear scattering of electromagnetic waves is the same across all length scales due to distances being defined in terms of the wavelength and Maxwell’s equations being in the form of first-order spatial derivatives. The response of periodic media is governed by the ratio between the wavelength, λ , and the period of the material, d . These can be grouped into three distinct regions: $\lambda \gg d$, $\lambda \sim d$ and $\lambda \ll d$. The classical ray picture is sufficient to explain the response of periodic media when the wavelength is much less than the period. This regime is not investigated in this thesis and therefore no further explanation will be given.

2.2.1 Wavelength much greater than the period

As the wavelength is much greater than the period of the structure, the radiation is not affected by the details of the structure and the material can often be described as a homogeneous medium. However, even with subwavelength periodicity, there are structures which cannot be described as a homogeneous medium due to evanescent interaction. This is explored in more depth in chapter 7. Effective medium theories are a way of describing the macroscopic material properties of microscopically inhomogeneous media. Effective medium approximations are used in a variety of fields but for the purpose of this discussion it is assumed the term refers to the electromagnetic properties of composite media.

This field has its beginnings in the mid 19th century when heterogeneous materials were first being investigated. These older papers are notoriously hard to get hold of and most of the information in this history has been collected from various secondary sources [30, 31].

When looked at on an atomic level, all materials are inhomogeneous. In 1837, Faraday described a dielectric as polarisable spheres surrounded by insulating material that ensured they never touched. Mossotti [32] extended this work by applying his work on the polarisation of a single molecule (1836) to this model. This work, in connection to Clausius's [33] work published in 1879 led to the Clausius-Mossotti model for polarisability, which will be explored in more detail later.

Around a similar time period, Lorenz [34] and Lorentz [35] were also working (separately) on the problem of describing material responses to electromagnetic radiation, and effective electric field expressions. A combination of their work led to the first effective medium expression in 1880.

In 1904, J.C. Maxwell Garnett [36] produced a paper on the colours produced by glass when small metal spheres were mixed with the glass and heated during the manufacturing process. In this paper he derived a relationship between the effective material parameters of the composite medium and the material parameters of the individual constituents using the Clausius-Mossotti relation and applying Maxwell's Equations. This formula became known as the Maxwell Garnett Approximation (MGA). Although the MGA is based on the Clausius-Mossotti (or the Lorentz-Lorentz) relation, he extended it from static behaviour to the behaviour of propagating waves.

The next significant approximation to deal with inhomogeneous media was provided by Bruggeman [37–39] in 1935. Over the period from 1935 to 1937 he produced a series of papers detailing his effective media theory, which will be addressed in more detail in

section 2.2.1.3. There have been many other theories developed but they are all based to some extent on either the Maxwell-Garnett Approximation or Bruggeman's Effective Medium Theory (EMT). A comprehensive list and evaluation of the major theories has been produced by Ian Youngs in his Thesis [40].

Firstly, it is important to note that these approximations may apply to permittivity (ϵ), permeability (μ) and conductivity (σ) due to the relationship between permittivity, permeability and conductivity with Maxwell's Equations. Effective medium theories describe the material properties of a composite medium in terms of its constituents' parameters and applications are common for all three parameters [41–43]. Figure 2.2 gives a schematic illustration of an effective medium.

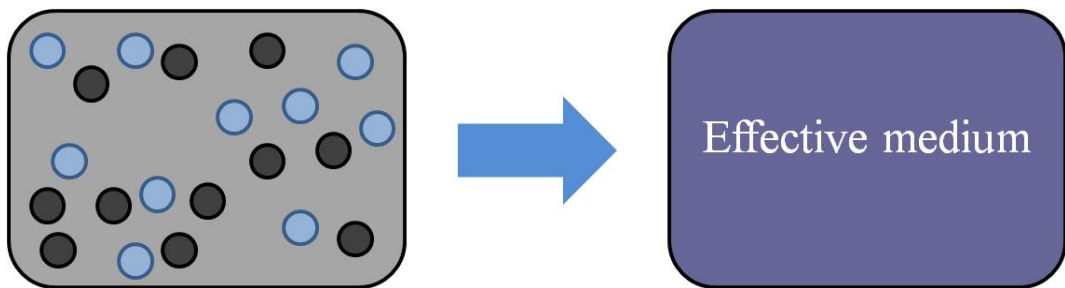


Figure 2.2: *Schematic of an effective medium. A substance composed of filler particles embedded in a surrounding medium can be represented as an homogenous effective medium.*

The dielectric response of a homogeneous medium is described in terms of the total electric field (\vec{E}) and the polarisation (\vec{P}). For a given material, the response is calculated by first determining the exact local solution per unit volume for the local electric field and the dipole moment ($\vec{E}_{loc}(\vec{r})$ and $\vec{p}(\vec{r})$ respectively). These are microscopic solutions however, and therefore need to be averaged to obtain their respective macroscopic parameters. The dielectric function is then determined using the relation:

$$\vec{D} = \epsilon \vec{E} = \vec{E} + 4\pi \vec{P} \quad (2.1)$$

In most cases, however, even for homogeneous media, the exact internal structure is not known and therefore the microscopic exact solution cannot be obtained.

2.2.1.1 Clausius-Mossotti relation and Lorentz-Lorenz EMA

Figure 2.3(a) shows a model of a homogeneous material as a mix of polarisable points and 'space'. When a uniform electric field is applied, these points will polarise according

2. Background

to equation (2.2), where \vec{p} is the dipole moment, α is the polarisability and \vec{E}_{loc} is the local field at that particular lattice site.

$$\vec{p} = \alpha \vec{E}_{loc}. \quad (2.2)$$

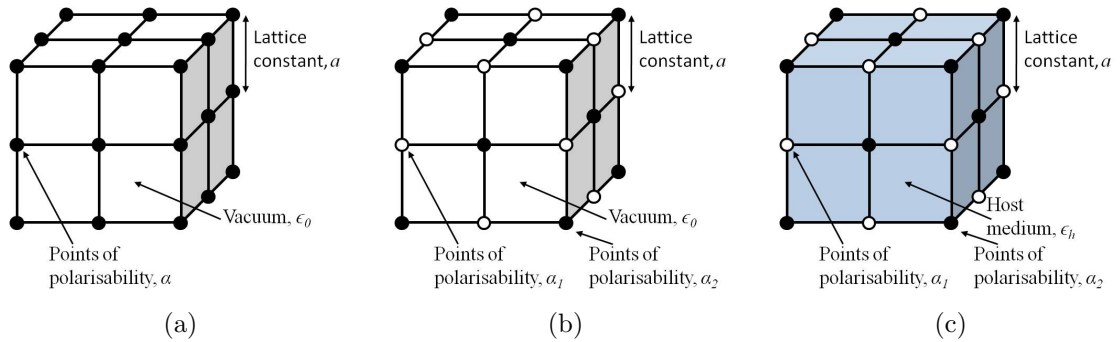


Figure 2.3: *Schematic of homogeneous material with cubic lattice structure and lattice constant a for (a) single material with points of polarisability α surrounded by vacuum, (b) points of polarisability α_1 or α_2 surrounded by vacuum and (c) points of polarisability α_1 or α_2 surrounded by a host material.*

The local field at each lattice site is given by the superposition of the incident field and the fields arising from \vec{p} due to all other lattice points. Summing over all lattice points and averaging will give us the macroscopic solution:

$$\vec{P} = n\alpha \vec{E}_{loc}, \quad (2.3)$$

where n is the volume density of lattice points with polarisability α . The Lorentz relation (equation 2.4) defines the local field (\vec{E}_{loc}) at a particular lattice site as

$$\vec{E}_{loc} = \vec{E} + \frac{1}{3\epsilon_0} \vec{P}, \quad (2.4)$$

where \vec{E} is the macroscopic average field and \vec{P} is the polarisation from other lattice points, and the factor of $1/3$ arises from the integrating sphere at the lattice point. Rearranging equation 2.4 and substituting in equation 2.3 gives an average field of

$$\vec{E} = \vec{E}_{loc} \left(1 - \frac{4\pi}{3} n\alpha \right). \quad (2.5)$$

Substitution of this relation into equation (2.1) and simplifying the resultant expression

produces the Clausius-Mossotti relation, where ϵ is the permittivity of the points

$$\frac{\epsilon - 1}{\epsilon + 2} = \frac{4\pi}{3} n\alpha. \quad (2.6)$$

To extend this result, we can apply the same model to a composite material with two constituents (figure 2.3(b)). We assume that the lattice points are one or other of the two materials and that the points are assigned randomly. The polarisability of these points is different for each material (α_1, α_2). Applying the same derivation gives us a relation of

$$\frac{\epsilon - 1}{\epsilon + 2} = \frac{4\pi}{3} (n_1\alpha_1 + n_2\alpha_2). \quad (2.7)$$

In equation (2.7), ϵ is now the effective permittivity of the points formed from the composite of the two constituents. This result can obviously be extended to any number of constituents. We can calculate the constituent permittivities using the Clausius-Mossotti relation. The Lorentz-Lorenz effective medium expression can be obtained by substitution of these constituent permittivities into equation (2.7), where f_i is the volume fraction of each constituent

$$\frac{\epsilon - 1}{\epsilon + 2} = f_1 \left(\frac{\epsilon_1 - 1}{\epsilon_1 + 2} \right) + f_2 \left(\frac{\epsilon_2 - 1}{\epsilon_2 + 2} \right), \quad (2.8)$$

where

$$f_i = \frac{n_i}{n_1 + n_2}.$$

The Lorentz-Lorenz approximation assumes that the constituents are mixed on an atomic scale. However, in a real composite this is unlikely to be a valid assumption. It is more likely that the material will be formed of regions of one constituent or another. These regions are likely to be large enough to be able to be described by their own permittivity. Taking this into account it is clear that it is not valid to model the material as polarisable points surrounded by a vacuum. Instead, we can adjust the model for this situation by picturing the points surround by a host medium with permittivity ϵ_h (figure 2.3(c)). The effective permittivity of the composite is now given by

$$\frac{\epsilon - \epsilon_h}{\epsilon + 2\epsilon_h} = f_1 \left(\frac{\epsilon_1 - \epsilon_h}{\epsilon_1 + 2\epsilon_h} \right) + f_2 \left(\frac{\epsilon_2 - \epsilon_h}{\epsilon_2 + 2\epsilon_h} \right). \quad (2.9)$$

It is at this point that the MGA and Bruggeman's EMT make different assumptions.

2.2.1.2 Maxwell-Garnett Approximation (MGA)

It is now assumed that there is no separate host medium and that all space is filled by either one or the other constituent. In addition, the assumption is that the concentration of one of the constituents is far greater than the other, in effect becoming the host medium with the particles of the other constituent embedded into it. If we define constituent one as the host medium and constituent two as the dilute medium, (i.e. $\epsilon_h = \epsilon_1$) and substitute this into equation (2.9), we obtain the Maxwell-Garnett Approximation,

$$\frac{\epsilon - \epsilon_h}{\epsilon + 2\epsilon_h} = f \left(\frac{\epsilon_2 - \epsilon_h}{\epsilon_2 + 2\epsilon_h} \right). \quad (2.10)$$

2.2.1.3 Bruggeman's Effective Medium Theory (EMT)

Bruggeman's theory also makes the assumption that there is no separate host medium and that all space is filled with one or other of the constituents. However, it does not make any assumptions regarding the relative concentrations of the constituents. Instead, it makes the 'self-consistent' choice that the host permittivity is the effective permittivity of the composite, i.e. $\epsilon = \epsilon_h$. Therefore, equation (2.9) now becomes

$$0 = f_1 \left(\frac{\epsilon_1 - \epsilon}{\epsilon_1 + 2\epsilon} \right) + f_2 \left(\frac{\epsilon_2 - \epsilon}{\epsilon_2 + 2\epsilon} \right). \quad (2.11)$$

Whilst these may seem relatively small differences in interpretation of the system, they have a marked effect on the results obtained and it is important to choose the correct theory for the material of interest. Figure 3 shows a schematic representation of the difference in interpretation between the two basic methods.

2.2.1.4 Extensions to basic effective medium theories

It is worth emphasising that both MGA and Bruggeman's EMT assume that the inclusions are spherical, non-interacting particles. Of course, in most real composites these are not valid assumptions. Therefore there have been many extensions to the two main effective media approximations. These are often developed for specific systems and it is therefore important to choose the appropriate model for the system under investigation. An in-depth look at all the various extensions is far beyond the scope of this thesis and so a few are mentioned here purely by way of illustration, for further information see [40].

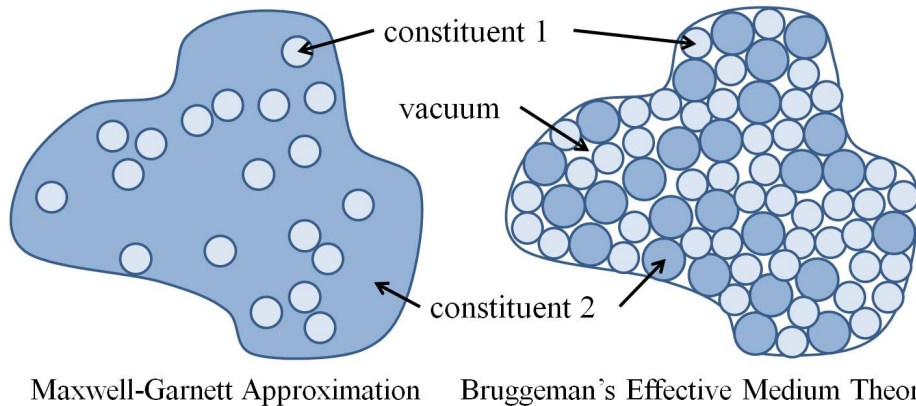


Figure 2.4: *Schematic representation of the difference in interpretation of the composite structure for the Maxwell-Garnett Approximation and Bruggeman's Effective Medium Theory.*

It has long been known that the shape of a particle and its orientation with respect to the incident field has a pronounced effect on its polarisability and consequently its EM field profiles. Interactions between the particles, as well as the shape of the inclusions themselves, also play an important part in the material response. However these parameters are not taken into account in the original equations.

The importance of the particle shape can be understood in terms of ‘screening’ [44]. ‘Screening’ is the term given to the polarisation charge that accumulates at a boundary between the two constituents perpendicular to the incident electric field. The more conductive the material (i.e. the higher the polarisability), the more charge that accumulates and therefore more ‘screening’ results. This charge on the surface of the particle effectively ‘screens’ (or cancels) the electric field from inside the particle (figure 2.5). Therefore the contribution from this particle to the overall field is less than expected. It is relatively simple to see that a ‘needle-like’ particle orientated parallel to the field will have less effect on the field than a flat disc orientated perpendicular to the incident field. There have been many publications extending these theories for different geometries including ellipsoids, discs, needles, cylinders and cuboids [43, 45, 46].

This also leads to an alternative approach in which the value of epsilon is predicted by mathematical bounds. The largest range of these bounds is predicted by the Weiner bounds [31, 44]. These take the two extreme cases of no screening (all boundaries parallel to the incident field) and full screening (all boundaries perpendicular to the incident field). Other limit theorems have also been produced, predicting more stringent limits for certain microstructures [47–49].

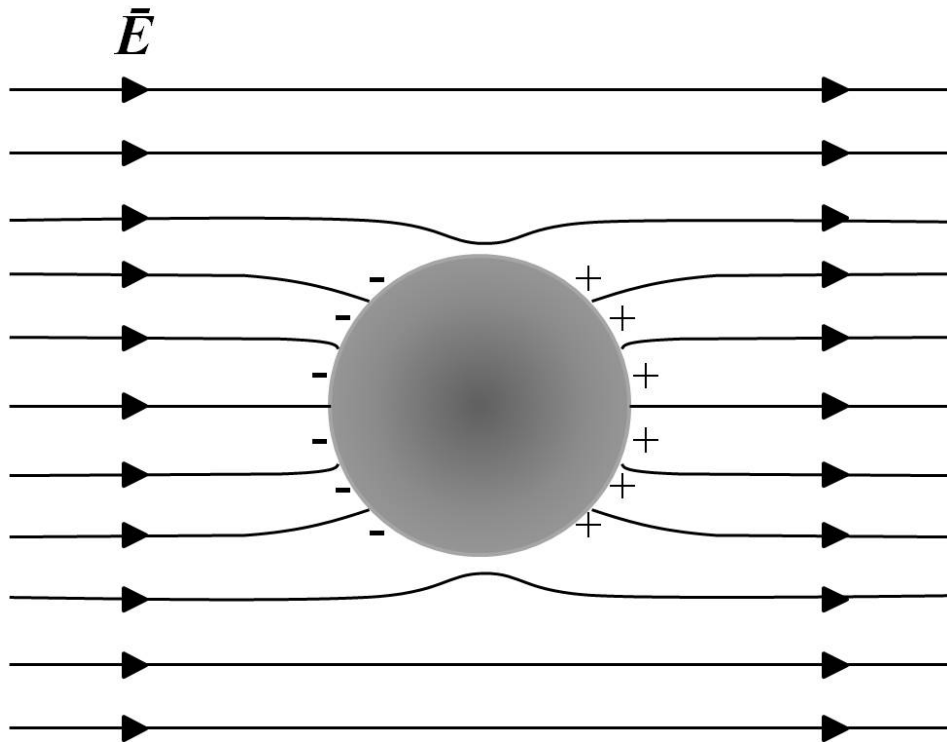


Figure 2.5: *Screening of small metal sphere in a dielectric medium under an applied field (reproduced from [44]).*

Many real random systems exhibit ‘clumping effects’ that are also believed to have a significant effect on the electromagnetic behaviour of the system. There have been several attempts to describe these systems in terms of fractals and then apply effective medium theory to these fractal clusters [50–52].

A very early theory that includes particle interactions was produced by Rayleigh [53]. To the first order, his theory produces the same relationship as the MGA. However, his full theory uses a series expansion and it is these higher orders that account for the interactions between the particles.

Stroud and Pan [54], on the other hand, produced an adaptation of Bruggeman’s EMT to account for the dynamic effects caused by the metal particles in composites. They have extended Bruggeman’s work to systems with propagating waves by including the effect of induced eddy currents which result in increased absorption. However, by their own admission their theory only predicts experimental observations in some specific systems, not on a general basis.

McLachlan [55–58] has produced a large body of work on effective medium theories to describe the conductivity of composite materials. In early work he derives two

equations to describe the conductivity of composites as a function of the volume fraction, space dimension, conductivity of the components and a morphology parameter. He uses Bruggeman's theory as a starting point and then extends it to include percolation effects. He proposes that the exponent used to describe the power law dependence is the fractal dimension of the system.

2.2.2 Wavelength of the same order as the period

In the $\lambda \sim d$ regime, that the majority of this thesis investigates, diffraction is fully evident and produces a wealth of interesting phenomena. Interest in diffraction of light by metal gratings began in earnest with Wood's seminal observation in 1902 of two types of reflection anomalies from metal gratings in the visible regime [59, 60].

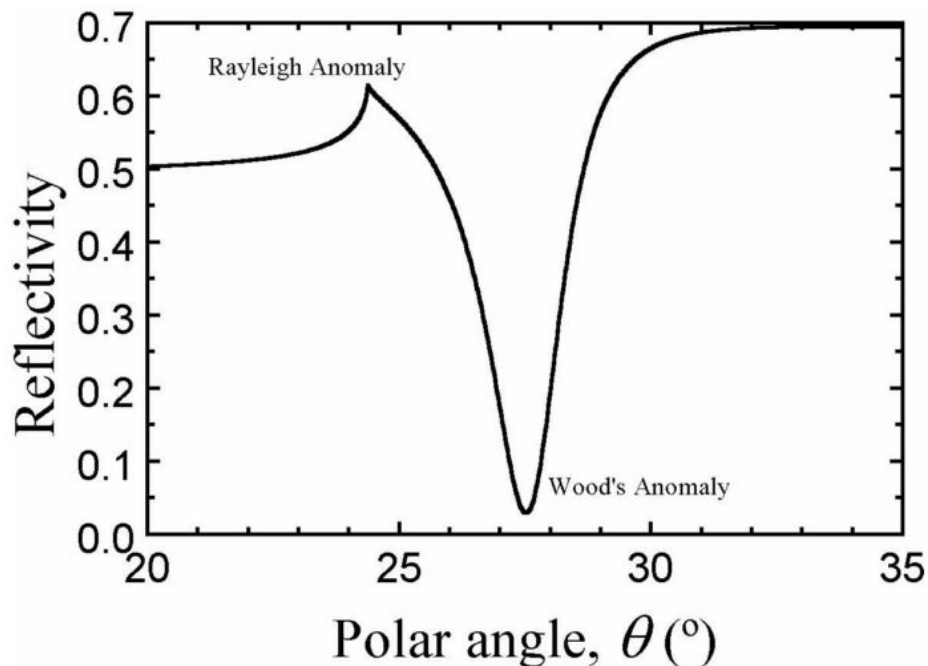


Figure 2.6: *Theoretically derived angle-dependent reflectivity data from a gold coated grating illustrating the bright (Rayleigh) and dark (Wood's) anomalies observed by Wood in 1902 [59, 61].*

In 1907 Lord Rayleigh provided a partial explanation of one of these anomalies in his *Dynamical Theory of Gratings* [62]. He surmised that when a diffracted order became grazing to the grating plane, the order becomes evanescent in nature and the energy associated with that order is distributed amongst the remaining propagating orders resulting in a bright band of high transmission (the Rayleigh Condition). It

wasn't until Fano's [63] work in 1941 however, that full understanding of both of the anomalies was reached. He explained the origin of the observed extended feature of two dark and bright neighbouring bands in terms of a pair of surface waves that travel along the surface of the grating. These waves are bound to the surface and decay exponentially in the direction perpendicular to the grating.

In 1944, Bethe [64] investigated the transmission of light through arrays of small circular holes in perfect conductors. He suggested that in cases when the period was much smaller than the wavelength, transmission would be proportional to $(a/\lambda)^4$ where a is the radius of the hole. It is worth highlighting that this was dependent on the area of the hole and therefore was purely non-resonant transmission. However, it was discovered in 1998 by Ebbesen *et al* [2] that significantly more light than predicted by Bethe could be transmitted by periodic arrays of subwavelength holes at specific frequencies. This phenomenon became known as Extraordinary Optical Transmission (EOT) and has proved to be a seminal result.

In the microwave regime however, the phenomenon of enhanced transmission from an array had been used for decades in frequency selective surfaces. The equivalent seminal discovery for microwave and infra-red frequencies had occurred in 1967 with Ulrich [65, 66]. Using periods smaller than the wavelength, these structures allowed 100% transmission at the resonant frequencies. Due to the extensive applications in the microwave regime, this behaviour continues to attract much interest [67, 68].

2.2.3 Surface plasmons and spoof surface plasmons

Fano suggested that the surface waves he described [63] were a special case of the surface waves suggested by Zenneck and Sommerfeld in 1909 [69, 70]. The momentum of these surface waves is greater than that of the incident radiation and hence incident radiation cannot couple directly to them on a planar interface and they themselves are non-radiative. The two main methods for enhancing the incident photon momentum, and therefore enabling coupling to the surface wave, are prism coupling [71, 72] and grating coupling [73]. It is the periodic nature of the arrays described within this thesis that allows the observed surface modes to be coupled to. Although the focus of the work presented here is solely in the microwave regime, a general understanding of surface plasmons is required before looking at the specifics of this frequency range.

2.2.3.1 The surface plasmon polariton dispersion relation

Surface plasmons are transverse longitudinal oscillations of surface charge density. These oscillations propagate along a metal-dielectric interface with no radiative loss. Transverse magnetic (TM), or p -polarised radiation is required to excite a surface plasmon polariton (SPP) on a planar surface as the incident electric vector needs to have a component normal to the interface in order to generate the required polarisation charge. The dispersion of the SPP follows the light line closely until it approaches the surface plasma frequency at $\omega_{SP} = \omega_P / \sqrt{\epsilon + 1}$ where ω_P is the bulk plasma frequency of the material. Typically for metals the bulk plasma frequency occurs in the ultra-violet part of the spectrum, and below this frequency the real part of the permittivity is negative. The dispersion then asymptotes towards this frequency and curves away from the light line. As the mode curves away, it changes from photon-like to plasmon-like. As microwave frequencies are far below the surface plasma frequency, the surface mode is always close to the light line (i.e. photon-like).

For a planar interface between two semi-infinite homogeneous media, the normal component of the electric displacement \vec{D} must be continuous across the interface. The electric field \vec{E} is related to the electric displacement via

$$\vec{D} = \epsilon_r \epsilon_0 \vec{E}, \quad (2.12)$$

where $\epsilon = \epsilon_0 \epsilon_r$, and ϵ_r is the relative dielectric constant of the medium and ϵ_0 is the permittivity of free space. Therefore in the case where the upper medium is a dielectric (i.e. ϵ_r is positive), and the lower medium is a metal (ϵ_r is large and negative at visible frequencies), the normal component of \vec{E} will have to change direction to fulfill the continuity requirement of \vec{D} . It is this discontinuity in the normal \vec{E} field that ‘traps’ the polarisation charge at the surface.

Figure 2.7 describes p -polarised light propagating with wavevector $\vec{k} = (k_x, k_y, 0)$ incident upon an interface with resultant reflected and transmitted radiation. The electric and magnetic fields are in the form

$$\vec{E} = [E_x, E_y, 0] \exp(i(k_x \hat{x} + k_y \hat{y} - \omega t)) \quad (2.13)$$

and

$$\vec{H} = [0, 0, H_z] \exp(i(k_x \hat{x} + k_y \hat{y} - \omega t)). \quad (2.14)$$

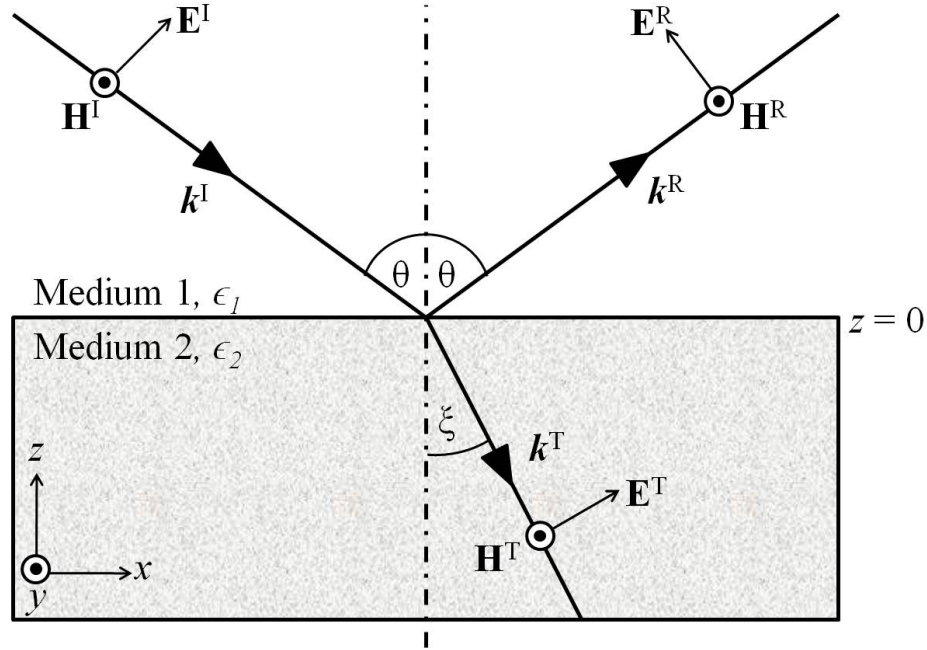


Figure 2.7: The incident, reflected and transmitted fields associated with a p-polarised wave incident on a planar interface between a metal and a dielectric.

Applying Maxwell's equation

$$\nabla \times \vec{H} = \epsilon \frac{\partial \vec{E}}{\partial t}, \quad (2.15)$$

results in

$$H_z = \frac{\epsilon \omega E_x}{k_y} = -\frac{\epsilon \omega E_y}{k_x}. \quad (2.16)$$

Combining this result (equation (2.16)) with the field equations (2.13), (2.14) allows the following expressions for the incident, reflected and transmitted fields to be obtained:

$$\vec{E}^I = E_x^I \left[1, -\frac{k_x}{k_{y1}}, 0 \right] \exp(i(k_x \hat{x} + k_{y1} \hat{y} - \omega t)),$$

$$\vec{E}^R = E_x^R \left[1, \frac{k_x}{k_{y1}}, 0 \right] \exp(i(k_x \hat{x} - k_{y1} \hat{y} - \omega t)),$$

$$\vec{E}^T = E_x^T \left[1, -\frac{k_x}{k_{y1}}, 0 \right] \exp(i(k_x \hat{x} + k_{y1} \hat{y} - \omega t)),$$

$$\vec{H}^I = E_x^I \left[0, 0, \frac{\omega \epsilon_1}{k_{y1}} \right] \exp(i(k_x \hat{x} + k_{y1} \hat{y} - \omega t)),$$

$$\vec{H}^R = E_x^R \left[0, 0, -\frac{\omega \epsilon_1}{k_{y1}} \right] \exp(i(k_x \hat{x} - k_{y1} \hat{y} - \omega t)),$$

and

$$\vec{H}^T = E_x^T \left[0, 0, \frac{\omega \epsilon_1}{k_{y1}} \right] \exp(i(k_x \hat{x} + k_{y1} \hat{y} - \omega t)). \quad (2.17)$$

The SPP is a non-radiative mode (i.e. a ‘trapped’ surface wave) and this property allows either the incident or the reflected field to be arbitrarily set to zero. In this derivation the incident field has been set to zero. In addition, the tangential boundary conditions state that the tangential components of both the electric and the magnetic field must be continuous at the interface. Applying these conditions gives

$$E_x^I = 0, \quad E_x^R = E_x^T, \quad (2.18)$$

and

$$H_z = -E_x^R \frac{\epsilon_1 \omega}{k_{y1}} = E_x^T \frac{\epsilon_2 \omega}{k_{y2}}. \quad (2.19)$$

Combining equations (2.18) and (2.19) results in

$$\frac{\epsilon_1}{k_{y1}} = -\frac{\epsilon_2}{k_{y2}}. \quad (2.20)$$

Conservation of momentum requires $k_{x1} = k_{x2} = k_x$ as expected, since the interface is a planar surface and therefore invariant under translation. Therefore the y -component of the wavevector in the medium j may be expressed as

$$k_{yj} = \sqrt{\epsilon_j k_0^2 - k_x^2}. \quad (2.21)$$

Substitution of equation (2.21) into equation (2.20) followed by rearranging results in an expression for the SPP dispersion relation

$$k_{SPP} = k_x = k_0 \sqrt{\frac{\epsilon_1 \epsilon_2}{\epsilon_1 + \epsilon_2}}. \quad (2.22)$$

It is worth highlighting that the epsilons are complex quantities. This is particularly relevant in the microwave regime where for metals, the imaginary component is positive and larger than the real component by at least several orders of magnitude.

Metals at microwave frequencies are often approximated as perfect conductors (i.e., infinite conductivity implying that $\epsilon_i = +\infty$) meaning that an SPP at microwave frequencies is equivalent to a grazing photon. It is therefore critical that the full complex permittivity value is used in any calculations. It also follows that k_x is also complex. The real component of k_x describes the real wavevector of the SPP at any frequency whilst the imaginary component describes the non-radiative damping of the mode. At microwave frequencies, this surface wave may be considered as an SPP, as despite the long propagation length, as there is still some penetration into the metal. The fields decay exponentially into both the metal and the dielectric, although the fields in the metal decay substantially more rapidly than those in the dielectric leading to a loosely bound mode, as opposed to the tightly bound modes observed at optical frequencies (figure 2.8).

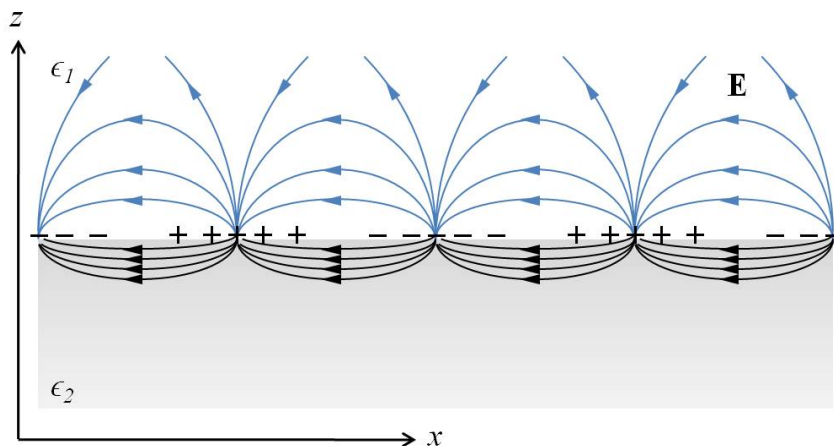


Figure 2.8: *Schematic representation of the polarisation of the surface charge density and associated electric field for the SPP mode. The field decays exponentially into both media penetrating the metal (ϵ_2) to a lesser extent than the dielectric (ϵ_1) (reproduced from [74]).*

A schematic of the SPP dispersion curve is shown in figure 2.9. The lightline corresponds to the wavevector of a grazing photon for any given frequency. The dispersion curve has two asymptotes. The higher asymptote is that of the surface plasma frequency and the lower is the lightline itself, when the behaviour of the metal approaches that of a perfect conductor (as at microwave frequencies). When an electric field is applied to a perfect conductor, an instantaneous response occurs to exactly cancel the applied field, excluding all fields from the metal.

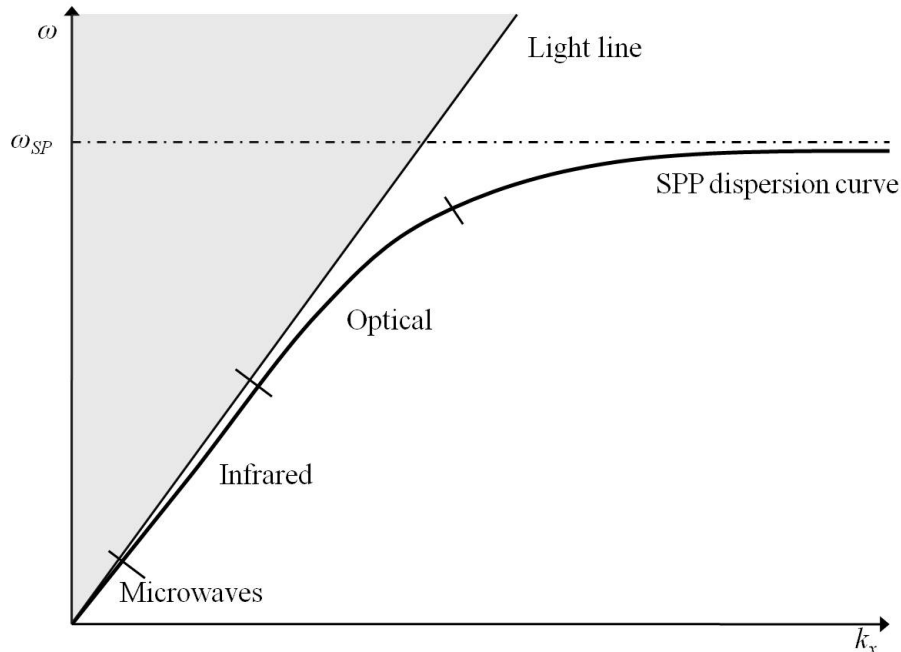


Figure 2.9: Schematic representation of the SPP dispersion curve where ω_{SP} denotes the surface plasma frequency (reproduced from [61]).

2.2.3.2 Spoof Surface Plasmons

In sections 2.2.3 and 2.2.3.1 the non-radiative nature of the SPP mode was introduced along with the requirement of a coupling mechanism. The further away from the lightline the SPP dispersion curve is, the greater the additional momentum required to couple an incident photon to the SPP mode. Figure 2.9 shows that for microwave frequencies, the SPP dispersion curve is very close to the lightline implying that the momentum required to allow an incident photon to couple to this mode is small compared to optical frequencies. In this regime, grating coupling is the most common method. As mentioned in the previous section, at low frequencies metals behave as near-perfect conductors with $\epsilon_i \gg |\epsilon_r|$. The resultant surface wave is photon-like with speeds close to the speed of light and it very loosely bound to the surface; that is the fields only penetrate a fraction of a wavelength into the metal, but extend many wavelengths into the dielectric. A corrugation of the interface is required to bind this mode more tightly to the surface.

Introducing a periodic surface modulation breaks the translational surface symmetry of the interface as shown by Barlow and Cullen's work in 1953 [75], and by Cutler more recently [76]. They considered a metal slab with periodic finite grooves. These

grooves support a resonance at a depth of a quarter of a wavelength. This resonance is analogous to the surface plasma frequency at visible frequencies. Below this resonant frequency, the corrugated surface can support a p -polarised bound surface wave with a cut-off at the resonant frequency of the groove. The breaking of the translational surface symmetry means that the conservation of tangential momentum is no longer required. The periodicity of the surface allows scattering of the incident light in a direction normal to the surface modulation at integer numbers of the grating vector k_g ($k_g = 2\pi/\lambda_g$, where λ_g is the pitch of the grating). These scattered waves are the diffracted orders produced by the surface. If the momentum of a diffracted order is greater than the maximum allowed momentum in the incident medium, the order will not propagate and instead will become evanescent. However, the evanescent fields have greater in-plane momentum and the incident photons are able to excite the surface modes beyond the lightline, giving the following condition:

$$\vec{k}_{SPP} = \vec{k}_0 \sin \theta \pm N \vec{k}_g. \quad (2.23)$$

where θ is the angle of incidence and N is an integer (i.e. $\vec{k}_0 \sin \theta$ is the in-plane wavevector of the incident light (see figure 2.11)). We can represent diffraction as a line of points in reciprocal space with a separation of \vec{k}_g . As integer multiples of \vec{k}_g are added or subtracted, thereby changing the momentum, the light cone and the SPP dispersion curves are displaced by these scattering centres (figure 2.10). Radiative coupling is now possible between p -polarised radiation and the diffracted SPP modes that are between the lightlines as shown by the shaded area in figure 2.10.

The coordinate system used to describe the grating orientation is illustrated in figure 2.11. The polar angle θ is defined as the angle of incidence and is measured normal to the plane of the grating. The azimuth angle ϕ is defined as the angle between the positive x -axis and the grating vector. With respect to the plane of incidence, TM, or p -polarised radiation is defined as having its electric vector in the plane, and TE, or s -polarised radiation as having its electric vector normal to the plane.

For all azimuth angles other than $\phi = 0$, \vec{k}_{SPP} , \vec{k}_0 and \vec{k}_g are no longer collinear and equation (2.23) becomes

$$k_{SPP}^2 = n_1^2 k_0^2 \sin^2 \theta + N^2 k_g^2 \pm 2n_1 N k_g k_0 \sin \theta \cos \phi. \quad (2.24)$$

The two dimensional equivalent of figure 2.10 for all azimuthal angles is shown in figure 2.12.

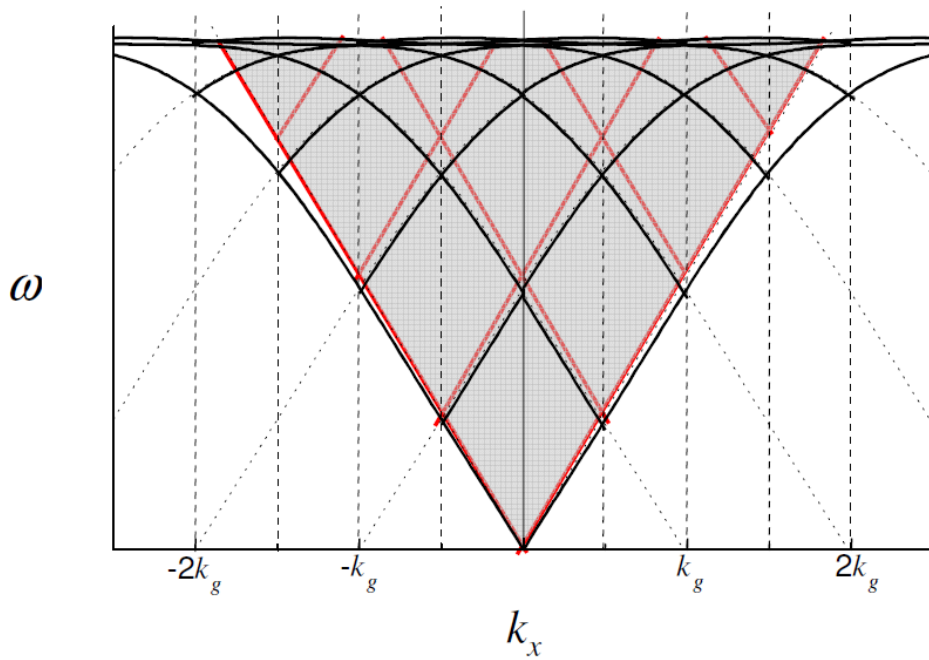


Figure 2.10: Dispersion curve for grating-coupled SPP's reflected at the Brillouin zone boundaries. The light lines are denoted by the red lines and the scattered dispersion curves by the black lines. The scattered dispersion curves between the shaded light lines can be radiatively coupled to [77].

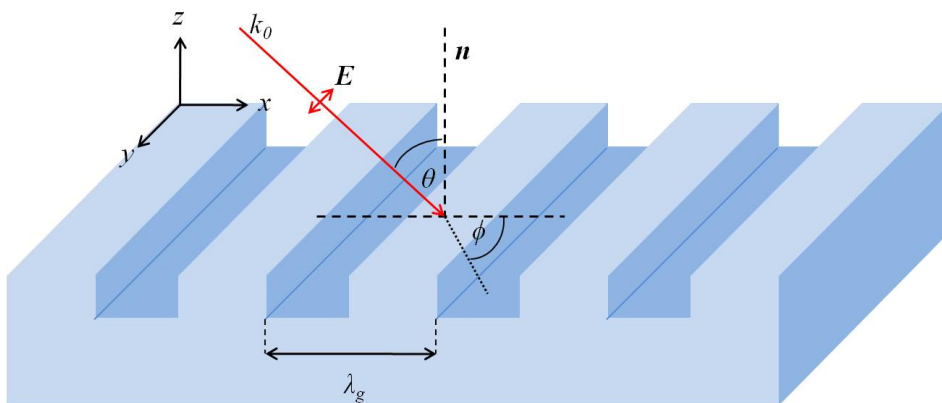


Figure 2.11: Schematic illustrating the coordinate system used to describe the grating orientation. The electric field vector is shown for p-polarised incident radiation.

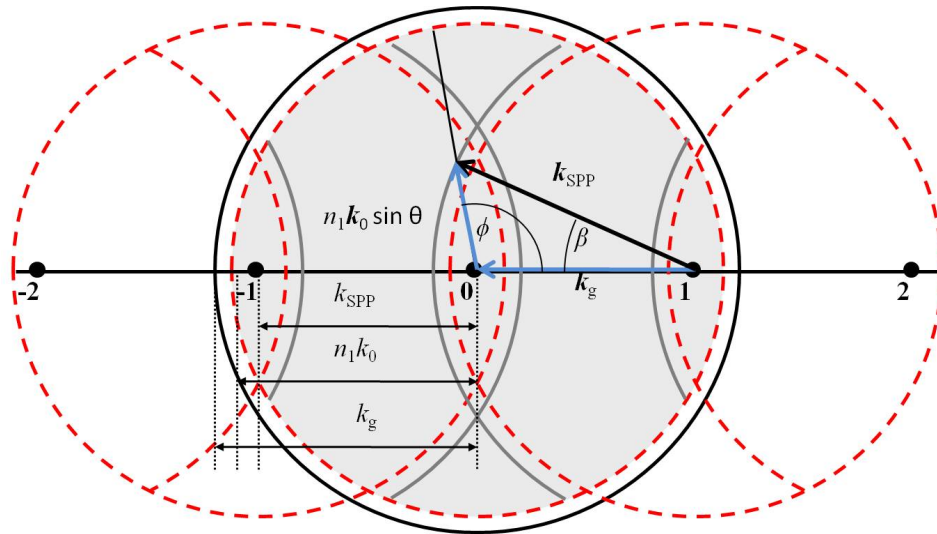


Figure 2.12: A reciprocal space representation in two dimensions of the SPP modes and light circles produced by a grating. The maximum possible momentum in the plane from a photon propagating above the grating is shown by the red dashed circle. The solid circles represent the momentum of the SPP modes; the black one being the zero order mode and the grey arcs the diffracted modes. The arrows represent the coupling between a photon incident at angle θ and azimuth angle ϕ to an SPP that propagates at angle β to the grooves of the grating (reproduced from [61]).

As before, the shaded region indicates the reciprocal space within which modes can be excited. One important consequence of using a periodic grating is that for azimuthal angles between 0° and 90° , both p - and s -polarised radiation will excite an SPP as both have a component of the electric vector normal to the interface.

2.3 Waveguide Modes

In chapter 3 a detailed review of the modelling methods used throughout this thesis are presented. The analytical method (section 3.2.2) used describes the fields throughout the structure in various characteristic forms. One of the structures investigated is a two dimensional hole array in a sheet of perfect electrical conductor (PEC). The fields within the holes can be described in terms of waveguide modes. It is therefore necessary to briefly explain what is meant by a waveguide mode and their underlying physics. The following derivations have been adapted from *Microwave Engineering* by Pozar [78].

2.3.1 Waveguide Modes

The walls of the waveguide are considered to be perfectly conducting and therefore as the conductivity is infinite, all fields are excluded from the conductor. As the tangential E fields must be continuous, within the dielectric the E fields must go to zero at the conducting wall. There are two main types of modes with waveguides; TE (transverse electric) solutions have the entire electric vector transverse to the wave propagation direction (figure 2.13(a)); and TM (transverse magnetic) solutions have the entire magnetic vector transverse to the wave propagation direction (figure 2.13(b)). The fundamental TM mode is sometimes referred to as a TEM (transverse electromagnetic) mode and both the electric and magnetic vectors are entirely transverse to the wave propagation direction (figure 2.13(c)).

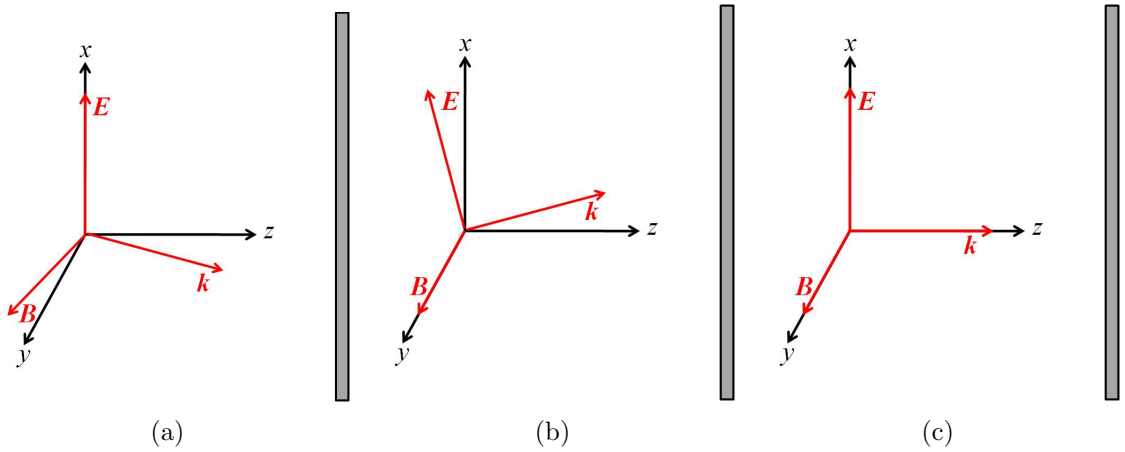


Figure 2.13: *Schematic illustrating the field alignments and plane of incidence for (a) TE polarisation, (b) TM polarisation and (c) TEM polarisation.*

The fields can then be expressed in the form

$$\vec{E} = [\bar{E}(x, y) + \hat{z}E_z(x, y)e^{-ik_z z}] \quad (2.25)$$

and

$$\vec{H} = [\bar{H}(x, y) + \hat{z}H_z(x, y)e^{-ik_z z}], \quad (2.26)$$

where $\bar{E}(x, y)$ and $\bar{H}(x, y)$ represent the transverse components, E_z and H_z are the axial components, $k_z = 2\pi/\lambda_z$ and it is assumed that the fields are harmonic fields with a variation in time of $e^{-i\omega t}$, where all symbols have their usual meaning. The wavelength of the guided wave is given by λ_z . If the waveguide is assumed to be source free it is

true to say

$$\nabla \times \vec{E} = -i\omega\mu\vec{H} \quad (2.27)$$

and

$$\nabla \times \vec{H} = i\omega\epsilon\vec{E}. \quad (2.28)$$

The above relations allow equations 2.25 and 2.26 to be expressed as the following field components:

$$\frac{\partial E_z}{\partial y} + ik_z E_y = -i\omega\mu H_x, \quad (2.29)$$

$$-\frac{\partial E_z}{\partial x} - ik_z E_x = -i\omega\mu H_y, \quad (2.30)$$

$$\frac{\partial E_y}{\partial y} - \frac{\partial E_x}{\partial x} = -i\omega\mu H_z, \quad (2.31)$$

$$\frac{\partial H_z}{\partial y} + ik_z H_y = -i\omega\epsilon E_x, \quad (2.32)$$

$$-\frac{\partial H_z}{\partial x} - ik_z H_x = i\omega\epsilon E_y, \quad (2.33)$$

$$\frac{\partial H_y}{\partial x} - \frac{\partial H_x}{\partial y} = -i\omega\epsilon E_z. \quad (2.34)$$

The above equations can be solved to give the transverse components in terms of the axial components:

$$H_x = \frac{i}{k_c^2} \left(\omega\epsilon \frac{\partial E_z}{\partial y} - k_z \frac{\partial H_z}{\partial x} \right), \quad (2.35)$$

$$H_y = \frac{-i}{k_c^2} \left(\omega\epsilon \frac{\partial E_z}{\partial x} - k_z \frac{\partial H_z}{\partial y} \right), \quad (2.36)$$

$$E_x = \frac{-i}{k_c^2} \left(k_z \frac{\partial E_z}{\partial x} + \omega\mu \frac{\partial H_z}{\partial y} \right), \quad (2.37)$$

$$E_y = \frac{i}{k_c^2} \left(k_z \frac{\partial E_z}{\partial y} + \omega\mu \frac{\partial H_z}{\partial x} \right), \quad (2.38)$$

where

$$k_c^2 = \omega^2 \epsilon \mu - k_z^2 = k_0^2 - k_z^2,$$

is the cutoff wavevector.

2.3.1.1 TE Waves

At the start of the discussion on waveguide modes, the differences between TE and TM modes was discussed. These differences allow us to further simplify equations (2.35) to (2.38) to apply specifically to either TE or TM waves. Looking at TE waves first, there is no axial component of electric field and therefore the field equations reduce to:

$$H_x = -\frac{ik_z}{k_c^2} \frac{\partial H_z}{\partial x}, \quad (2.39)$$

$$H_y = -\frac{ik_z}{k_c^2} \frac{\partial H_z}{\partial y}, \quad (2.40)$$

$$E_x = -\frac{i\omega\mu}{k_c^2} \frac{\partial H_z}{\partial y} \quad (2.41)$$

$$E_y = \frac{i\omega\mu}{k_c^2} \frac{\partial H_z}{\partial x}, \quad (2.42)$$

and the equation for H_z becomes the two dimensional Helmholtz wave equation

$$\left(\frac{\partial^2}{\partial x^2} + \frac{\partial^2}{\partial y^2} + k_c^2 \right) H_z = 0. \quad (2.43)$$

2.3.1.2 TM Waves

A similar process can be applied for TM waves, although in this case there is no magnetic field axial component. This results in the following general equations:

$$H_x = \frac{i\omega\epsilon}{k_c^2} \frac{\partial E_z}{\partial y}, \quad (2.44)$$

$$H_y = -\frac{i\omega\epsilon}{k_c^2} \frac{\partial E_z}{\partial x}, \quad (2.45)$$

$$E_x = -\frac{ik_z}{k_c^2} \frac{\partial E_z}{\partial x}, \quad (2.46)$$

$$E_y = \frac{ik_z}{k_c^2} \frac{\partial E_z}{\partial y}, \quad (2.47)$$

and

$$\left(\frac{\partial^2}{\partial x^2} + \frac{\partial^2}{\partial y^2} + k_c^2 \right) E_z = 0. \quad (2.48)$$

2.3.1.3 Rectangular Waveguide Modes

Before the general equations derived in sections 2.3.1.1 and 2.3.1.2 can be solved, the geometry of the particular waveguide must be considered. There are many different possible geometries for waveguides and each has its characteristic modes. However this thesis is only concerned with arrays of rectangular or square holes and therefore we will restrict our discussion to rectangular waveguides, of which square waveguides are a special case. The geometry of the rectangular waveguide is shown in figure 2.14.

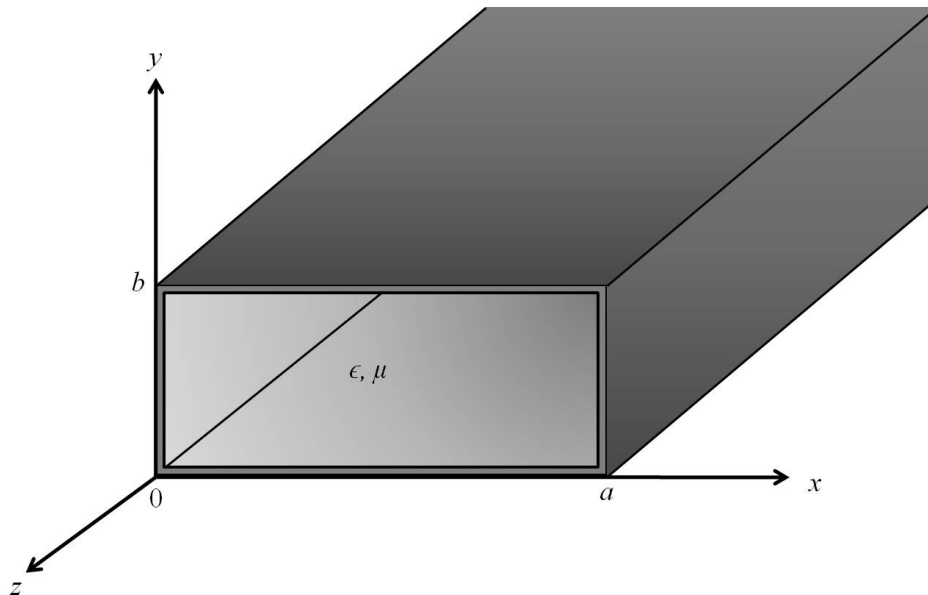


Figure 2.14: *Schematic showing the geometry and coordinate system for the rectangular waveguide (reproduced from [78]).*

The walls of the waveguide are assumed to be perfectly conducting and the waveguide is filled with a lossless dielectric material characterised by permittivity ϵ and permeability μ . The side of the waveguide parallel to the x -axis is denoted by a and the side parallel to the y -axis by b . It is assumed that $a > b$ and that the waveguide is infinitely long and uniform in the z -direction. As before, each polarisation will be considered separately.

TE Modes

By defining $H_z(x, y) = X(x)Y(y)$ we are able to use separation of variables to solve equation (2.43) resulting in

$$\frac{1}{X} \frac{d^2 X}{dx^2} + \frac{1}{Y} \frac{d^2 Y}{dy^2} + k_c^2 = 0. \quad (2.49)$$

Solving this gives a general solution for H_z of

$$H_z(x, y) = (A \cos k_x x + B \sin k_x x)(C \cos k_y y + D \sin k_y y), \quad (2.50)$$

where A , B , C and D are constants and $k_c^2 = k_x^2 + k_y^2$. The boundary conditions state that the tangential electric field components must go to zero at the walls of the waveguide; i.e. $E_x(x, y) = 0$ at $y = 0$ and $y = b$, and $E_y(x, y) = 0$ at $x = 0$ and $x = a$. Using the expression for H_z from equation (2.50) in equations (2.41) and (2.42) gives the following expressions for E_x and E_y ;

$$E_x = -\frac{i\omega\mu k_y}{k_c^2} (A \cos k_x x + B \sin k_x x)(-C \sin k_y y + D \cos k_y y) \quad (2.51)$$

and

$$E_y = -\frac{i\omega\mu k_x}{k_c^2} (-A \sin k_x x + B \cos k_x x)(C \cos k_y y + D \sin k_y y). \quad (2.52)$$

To satisfy the boundary conditions it is clear that $B = D = 0$ and that the final solution for H_z is

$$H_z(x, y, z) = A_{uv} \cos \frac{u\pi x}{a} \cos \frac{v\pi y}{b} e^{-ik_z z}, \quad (2.53)$$

where A_{uv} is an arbitrary amplitude coefficient and u and v are integers. Substituting equation (2.53) into equations (2.39) to (2.42) gives the following expressions for the transverse field components:

$$E_x = \frac{i\omega\mu v\pi}{k_c^2 b} A_{uv} \cos \frac{u\pi x}{a} \sin \frac{v\pi y}{b} e^{-ik_z z}, \quad (2.54)$$

$$E_y = -\frac{i\omega\mu u\pi}{k_c^2 a} A_{uv} \sin \frac{u\pi x}{a} \cos \frac{v\pi y}{b} e^{-ik_z z}, \quad (2.55)$$

$$H_x = \frac{ik_z u\pi}{k_c^2 a} A_{uv} \sin \frac{u\pi x}{a} \cos \frac{v\pi y}{b} e^{-ik_z z}, \quad (2.56)$$

$$H_y = \frac{ik_z v \pi}{k_c^2 b} A_{uv} \cos \frac{u \pi x}{a} \sin \frac{v \pi y}{b} e^{-ik_z z}, \quad (2.57)$$

with a propagation constant of

$$k_z = \sqrt{k_0^2 - k_c^2} = \sqrt{k_0^2 - \left(\frac{u \pi}{a}\right)^2 - \left(\frac{v \pi}{b}\right)^2}. \quad (2.58)$$

When k_0 is greater than the cut-off wavevector (k_c), the propagation constant is real and the mode propagates. The dominant mode is the one with the lowest cut-off frequency, in this case the TE_{10} where 1 and 0 are the values of the integers u and v respectively. Figure 2.15 shows the electric field profiles from the first four TE modes of a rectangular waveguide.

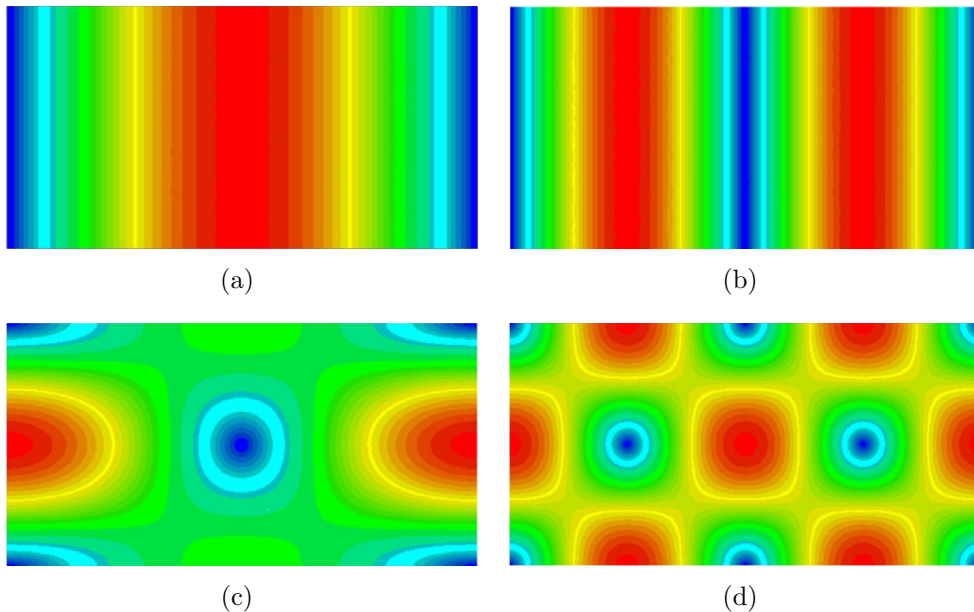


Figure 2.15: *Electric field profiles in the xy -plane corresponding to the eigensolutions of (a) the TE_{10} , (b) TE_{20} , (c) TE_{01} and (d) TE_{11} supported by an air filled perfectly conducting metal waveguide. Red corresponds to a field magnitude of 1 and blue to a magnitude of zero. The waveguide is uniform and infinite in the z -direction [77].*

TM Modes

The same separation of variables method as was used for the TE modes can again be applied to give a general solution to equation (2.48) of

$$E_z(x, y) = (A \cos k_x x + B \sin k_x x)(C \cos k_y y + D \sin k_y y). \quad (2.59)$$

The boundary conditions for the TM case apply directly to E_z giving $E_z(x, y) = 0$ at $x = 0$, $x = a$, $y = 0$ and $y = b$. Satisfying these boundary conditions yields the solution

$$E_z(a, y, z) = B_{uv} \sin \frac{u\pi x}{a} \sin \frac{v\pi y}{b} e^{-ik_z z}, \quad (2.60)$$

where B_{uv} is an arbitrary amplitude constant and u and v are integers. Substituting this expression into equations (2.44) to (2.47) gives the following transverse field components:

$$E_x = -\frac{ik_z u \pi}{k_c^2 a} B_{uv} \cos \frac{u\pi x}{a} \sin \frac{v\pi y}{b} e^{-ik_z z}, \quad (2.61)$$

$$E_y = -\frac{ik_z v \pi}{k_c^2 b} B_{uv} \sin \frac{u\pi x}{a} \cos \frac{v\pi y}{b} e^{-ik_z z}, \quad (2.62)$$

$$H_x = \frac{i\omega \epsilon v \pi}{k_c^2 b} B_{uv} \sin \frac{u\pi x}{a} \cos \frac{v\pi y}{b} e^{-ik_z z}, \quad (2.63)$$

$$H_y = -\frac{i\omega \epsilon u \pi}{k_c^2 a} B_{uv} \cos \frac{u\pi x}{a} \sin \frac{v\pi y}{b} e^{-ik_z z}, \quad (2.64)$$

with a propagation constant of

$$k_z = \sqrt{k_0^2 - k_c^2} = \sqrt{k_0^2 - \left(\frac{u\pi}{a}\right)^2 - \left(\frac{v\pi}{b}\right)^2}. \quad (2.65)$$

The dominant TM mode supported by the rectangular waveguide is TM_{11} where 1 and 0 are the values of the integers u and v respectively as for the TE modes and the electric field profiles for the first four TM modes are illustrated in figure 2.16.

2.4 Summary

This chapter has shown that the study of EM interaction with metal-dielectric composite periodic media is well established with the first investigations being in the mid 17th century with Grimaldi's observations of diffraction patterns through a feather [23] and still flourishing today. A brief overview of the main historical seminal results have been discussed. The use of effective medium theories to describe composite media when the constituent particles are very subwavelength has been introduced and simple derivations given for the Clausius-Mossotti formula, Maxwell Garnett Approximation and Bruggeman's Effective Medium Theory. Most effective medium theories use one of the

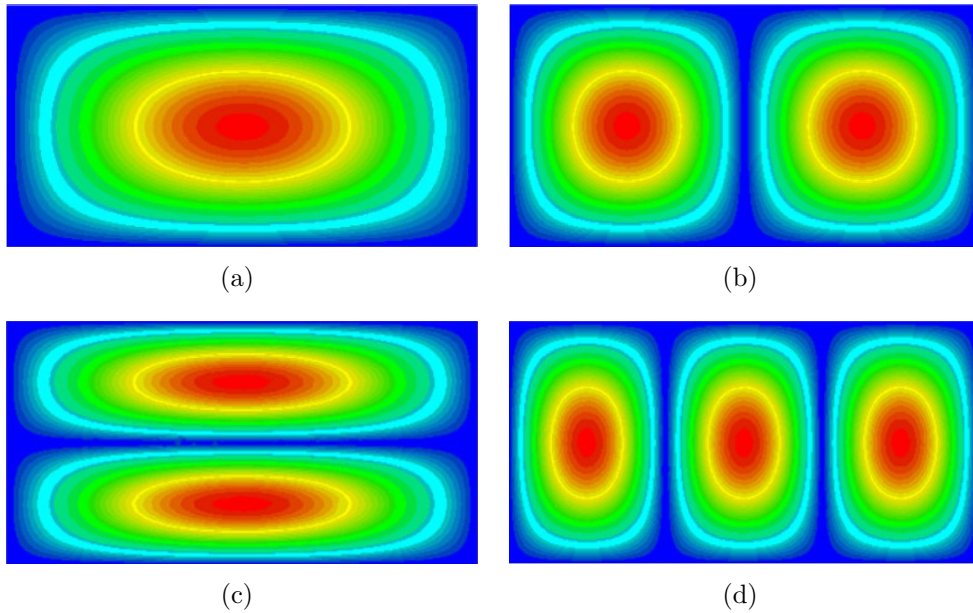


Figure 2.16: *Electric field profiles in the xy -plane corresponding to the eigensolutions of (a) the TM_{11} , (b) TM_{21} , (c) TM_{12} and (d) TM_{31} supported by an air filled perfectly conducting metal waveguide. Red corresponds to a field magnitude of 1 and blue to a magnitude of zero. The waveguide is uniform and infinite in the z -direction [77].*

last two methods as their starting point before extending the application of the theory to include different geometries or allow for particle interactions.

This chapter also introduced the concept of EM surface waves supported at the interface of dissimilar non-magnetic media. These surface waves are supported for frequencies from the microwave regime to the optical regime until the surface plasma frequency of the metal is reached. To tightly bind these waves at low frequencies, surface corrugation is required and the analogies between these ‘spoof’ surface plasmons and the surface plasmon polaritons supported at visible frequencies has been covered. Finally this chapter addressed the various types of waveguide mode supported by a rectangular waveguide and their EM derivation. Rectangular waveguides support both transverse magnetic (TM) and transverse electric (TE) modes and field distributions of the lowest order TE and TM eigenmodes were illustrated.

Chapter 3

Analytical and Numerical Modelling Techniques

3.1 Introduction

As discussed in section 2.1, not only the EM response itself, but the ability to predict the response of periodic metallic media forms an extensive body of research in its own right. There are many different modelling methods available, both numerical and analytical. This chapter will provide a brief description of the most common methods. In addition, it will provide an in-depth look at the two methods utilised throughout the thesis, as well as the advantages and limitations of these methods.

Section 3.2 looks at various different analytical methods. The majority of the work presented in this thesis utilises an analytic modal matching method to gain an understanding of the physics underlying the observed responses. Therefore an in-depth look at the method of modal matching and a brief review is presented in section 3.2.2.

As well as analytical methods, numerical modelling is commonly used to predict the response of structures to EM radiation and there are many publications purely on numerical modelling. An overview of some of the available numerical modelling methods is given in section 3.3. The other modelling method used throughout this thesis is the Finite Element Method (FEM). FEM modelling is a long standing accepted numerical method of modelling the response of structures to EM radiation and there are many commercial packages available. This technique has been used throughout this thesis purely as a tool to verify the veracity of the modal matching methods developed during this research. Section 3.3.1 covers the specifics of the commercially available FEM software used for this verification.

Finally, the chapter concludes in section 3.4 with a summary of the salient points for the modelling methods chosen for this work.

3.2 Analytical Methods

Most recent studies have been dominated by numerical modelling methods, however, of the analytical methods used, the two main methods are transmission line theory [65, 79–84] and modal matching [60, 68, 85–91]. Transmission line theory, or equivalent circuit modelling technique as it is also known, represents the structure in terms of an electric circuit consisting of elements with reactance and resistance equivalent to that of the system.

3.2.1 Equivalent Circuit Modelling

Consider a free standing thin metal mesh of square holes in a square array with pitch d and square hole of side length a where the thickness of the mesh, h , is far less than the width of grid, $(d - a)$, (figure 3.1(a)). For an incident plane wave on this structure, the tangential components of the scattered electric field are continuous across the grid, whilst the tangential magnetic field components are discontinuous. As long as there are no propagating diffracted orders, the system may be represented by the circuit illustrated in figure 3.1(b). Below the onset of diffraction, the zeroth order reflection and the zeroth order transmission are the only propagating contributions of the scattered field. In the non-diffracting regime, the complex amplitude coefficients of these propagating scattered waves are dependent on the incident wavelength and the geometrical parameters of the grid. Ulrich [65] shows how in the infrared regime, where metals can be approximated as PECs with no absorption losses, the reflection and transmission are always 90° out of phase with respect to each other. This is analogous to electrical circuit components in an AC circuit. Each component of the system is represented by a circuit component with equivalent parameters. In this case, free space is represented by a transmission line of unity, and the mesh by a lumped admittance of $2Y$ [65], where admittance is the reciprocal of the impedance of the mesh, i.e. $Y = 1/Z$.

The admittance of the mesh needs to accurately represent the frequency dependent response of the mesh to incident radiation. Ulrich [65] achieves this by combining inductors and capacitors in such a way as to give a frequency dependent response that

3. Analytical and Numerical Modelling Techniques

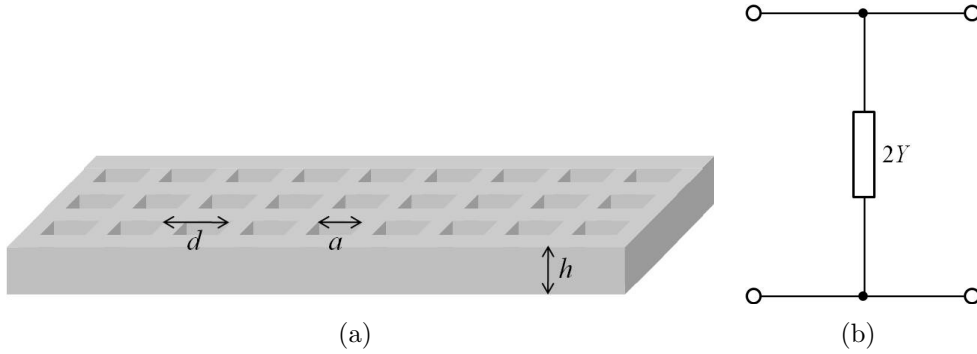


Figure 3.1: (a) Schematic of metal mesh of thickness h with pitch d and square holes of size a ; (b) Equivalent circuit representing the mesh illustrated in figure 3.1(a), reproduced from [65].

is also dependent on the mesh parameters. Using only three components the response of an inductive thin mesh below the onset of diffraction may be represented (figure 3.2).

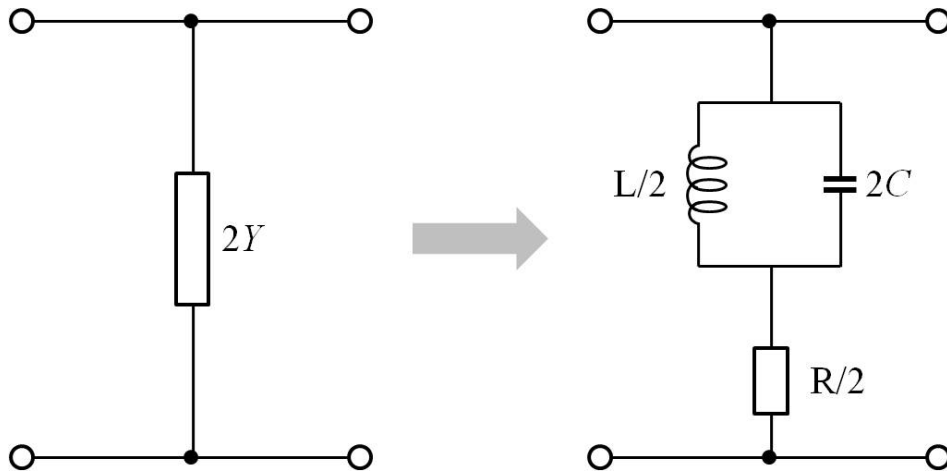


Figure 3.2: Equivalent circuit for a single metal mesh layer detailing the single components required to accurately represent the mesh detailed in figure 3.1(a), reproduced from [65].

Transmission line theory has been used to analyse a variety of systems. Starting from the simple case detailed above, more complex systems can be built up by combining components in series or parallel until the circuit has the equivalent resonance of the system. This approach was clearly illustrated by Sauleau *et al.* in 1998 [92] in their paper investigating the resonant frequency of parallel Fabry-Pérot cavities consisting of partially reflecting metal meshes. They consider two metal meshes of square holes in a square array with pitch d and square hole of side length a (figure 3.3). The scattered

3. Analytical and Numerical Modelling Techniques

fields from this mesh can be represented as a sum of Floquet space harmonics with propagation constants,

$$\gamma_{pq} = \sqrt{k^2 - \left(\frac{2\pi}{a}\right)^2 (p^2 + q^2)} \quad (3.1)$$

where p and q are integers and $k = 2\pi/\lambda_0$, where λ_0 is the free space wavelength.

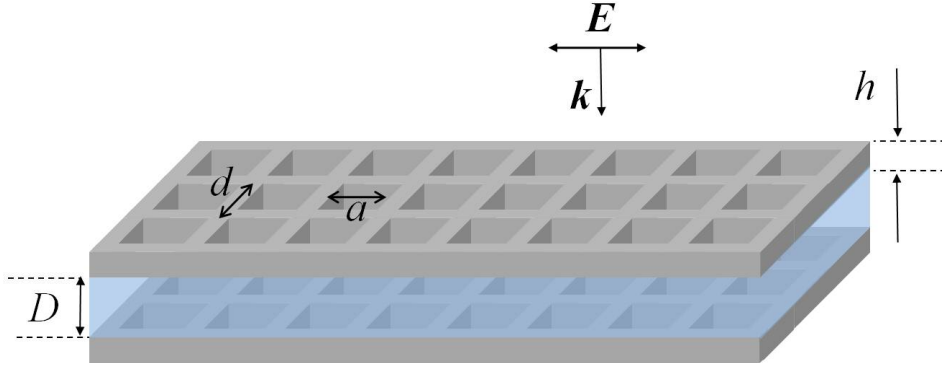


Figure 3.3: Schematic showing a pair of parallel inductive meshes with square apertures.

If the pitch is subwavelength then the only propagating mode is the zeroth order (or (0,0)) mode, as all other modes are evanescent. These evanescent waves are represented by the reactance of the equivalent circuit. Dielectric materials are represented by the wave impedance of the bulk material i.e. $Z_0/\sqrt{\epsilon_r}$ where $Z_0 = 120\pi \Omega$ is the free space impedance. The mesh is represented by an effective impedance, Z_{eq} , which is a function of wavelength and the mesh parameters (a, d). Figure 3.4 illustrates the equivalent circuit for the structure in figure 3.3.

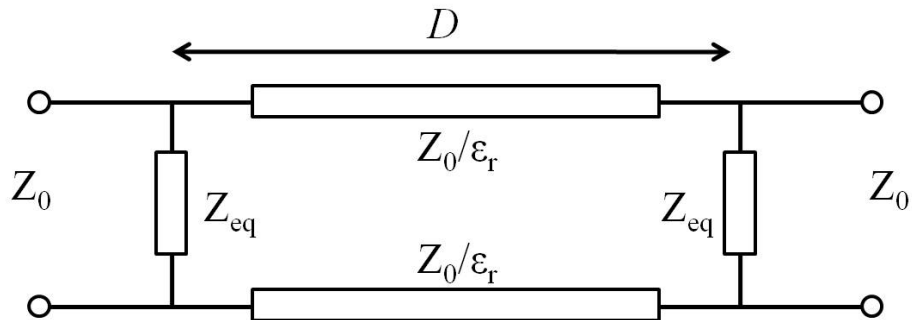


Figure 3.4: Equivalent circuit diagram for the system in figure 3.3 (reproduced from [92]).

In 1951 Marcuvitz [93] published formulae for the effective impedance for inductive

3. Analytical and Numerical Modelling Techniques

(cavity) and capacitive (patch) strip gratings for TE and TM incident radiation respectively. Ulrich [65] further developed this technique to produce formulae for meshes in free space. Inductive meshes are generally reflective, however, they support a resonance at which they transmit at 100%. Ulrich [65] determined the reactance, X , of an inductive mesh to be given by:

$$\frac{X}{Z_0} = -\omega_r \ln \left(\frac{1}{\sin \left(\frac{\pi d}{2a} \right)} \right) \left(\frac{\omega_0}{\omega_r} - \frac{\omega_r}{\omega_0} \right)^{-1} \quad (3.2)$$

where $\omega_0 = a/\lambda_0$ and ω_r is the resonant frequency and is determined by fitting experimental data.

There have been various other circuit models for metal meshes, for example Chen [94] produced a formula for the effective impedance of a mesh from a modal matching method using a single waveguide mode. In 1985, Whitbourn and Compton [79] proposed an equivalent circuit adaptation that accounted for systems involving different refractive indices.

There are however, disadvantages with this method. Interactions between the meshes are not accounted for and therefore this theory is only applicable to widely spaced meshes. In addition, it is important that the hole size is small compared to the pitch and that the pitch is very subwavelength. As the pitch approaches the wavelength, the effects of evanescent diffraction become paramount and the accuracy of the circuit approximation rapidly decreases [92].

3.2.2 Modal matching

A large proportion of the modelling presented in this thesis utilises an analytical modal matching method to gain an understanding of the physics underlying the observed responses. This method is based on the method presented by McPhedran [68] and later adapted by Hendry *et al.* [89]. There are various modal matching methods [85, 86, 88] each with their own idiosyncrasies, however, the primary difference between them and this particular method is that it includes the contributions from multiple-order waveguide modes, propagating and evanescent diffracted waves. It also accounts for finite depth holes in the calculation making it more similar to the approach taken by Mary *et al* [95]. One of the crucial differences between this and some of the other analytical models [85, 86, 90, 91] is that this approach does not involve describing the system in terms of effective material parameters, and therefore the near field interactions

3. Analytical and Numerical Modelling Techniques

that are so significant in this regime can be rigorously represented leading to accurate prediction of the EM response.

In all modal matching methods the electromagnetic fields in each different region of the structure are matched to the fields in the adjacent region at the interface. For example, in the case of a simple three layer system, i.e. superstrate, metallic mesh and substrate, the EM fields of the superstrate are matched to the fields in the mesh at the top interface, and the substrate fields are matched at the bottom interface. By applying the relevant boundary conditions and the continuity constraints of electric and magnetic fields it is possible to obtain analytical expressions for transmission and reflection through the structure. The starting point for the method is to first define the electric fields in all regions.

3.2.2.1 Method

For simplicity we will consider a single sheet of PEC perforated with a square array of square holes. For this structure there are three distinct regions of space to be considered. These are the semi-infinite vacuum regions above (region I) and below (region III) the film, and the composite film itself (region II) (Figure 3.5).

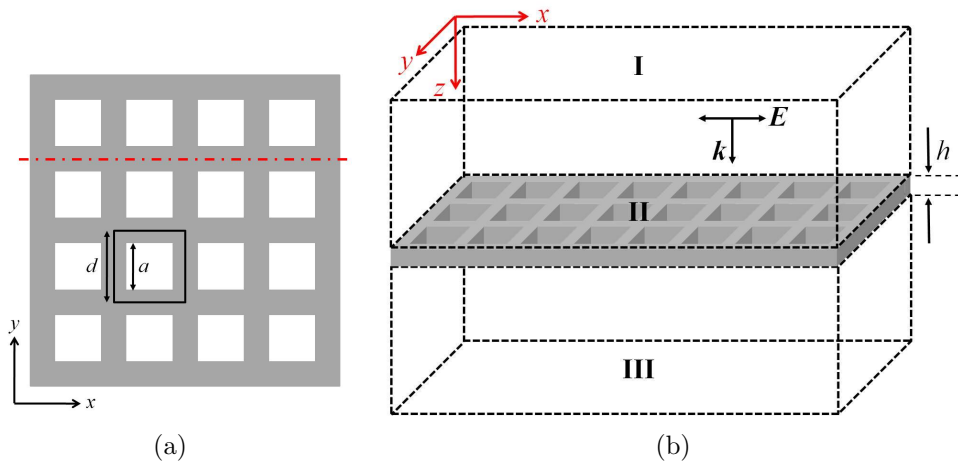


Figure 3.5: Schematic showing (a) investigated system where the shaded area denotes PEC, the unit cell is shown by the solid black line and the red dotted line indicates the plane of incidence; (b) Defined regions (I, II, III) of the system used by the modal matching method.

The electric fields in the vacuum regions above and below the film can be described using a two dimensional Fourier-Floquet expansion of the diffracted orders (equations

3. Analytical and Numerical Modelling Techiques

3.3 - 3.6). Note that the time dependent field component, $\exp(i\omega t)$ where ω is the radial frequency, has been omitted throughout for simplicity.

$$E_x^I = E_x \exp(ik_x x) \exp(ik_z^{0,0} z) + \sum_{m,n} A_x^{m,n} \Psi_1^{m,n}(x, y) \exp(-ik_z^{m,n} z) \quad (3.3)$$

$$E_y^I = E_y \exp(ik_x x) \exp(ik_z^{0,0} z) + \sum_{m,n} A_y^{m,n} \Psi_1^{m,n}(x, y) \exp(-ik_z^{m,n} z) \quad (3.4)$$

$$E_x^{III} = \sum_{p,q} D_x^{p,q} \Psi_1^{p,q}(x, y) \exp(ik_z^{p,q} z) \quad (3.5)$$

$$E_y^{III} = \sum_{p,q} D_y^{p,q} \Psi_1^{p,q}(x, y) \exp(ik_z^{p,q} z) \quad (3.6)$$

where

$$\Psi_1^{m,n}(x, y) = \exp\left[i\left(k_x + \frac{2m\pi}{d}\right)x\right] \exp\left[i\left(k_y + \frac{2n\pi}{d}\right)y\right] \quad (3.7)$$

and

$$k_z^{m,n} = \sqrt{\left(\frac{\omega}{c}\right)^2 - \left(k_x + \frac{2m\pi}{d}\right)^2 - \left(k_y + \frac{2n\pi}{d}\right)^2} \quad (3.8)$$

The diffracted orders in region I are denoted by m and n and region III by p and q , the wave-vector of the diffracted order by k , the period of the array by d and the field amplitude by $A^{m,n}$, $D^{p,q}$ whilst $\Psi_1^{m,n}(x, y)$ describes the diffracted waves. Note that for the vacuum region above the film (region I) there is an additional term for the incident field.

Within the PEC layer, the electric fields are only present in the holes, within which they take the form of waveguide modes, [equations 3.9, 3.10],

$$E_x^{II} = \sum_{u,v} B_x^{u,v} \Psi_2(x, y) \exp(iq_z^{u,v} z) + C_x^{u,v} \Psi_2(x, y) \exp(-iq_z^{u,v} z) \quad (3.9)$$

$$E_y^{II} = \sum_{u,v} B_y^{u,v} \Psi_3(x, y) \exp(iq_z^{u,v} z) + C_y^{u,v} \Psi_3(x, y) \exp(-iq_z^{u,v} z) \quad (3.10)$$

where

$$\Psi_2(x, y) = \cos\left(\frac{u\pi x}{a}\right) \sin\left(\frac{v\pi y}{a}\right) \quad (3.11)$$

3. Analytical and Numerical Modelling Techniques

$$\Psi_3(x, y) = \sin\left(\frac{u\pi x}{a}\right) \cos\left(\frac{v\pi y}{a}\right) \quad (3.12)$$

and

$$q_z^{u,v} = \sqrt{\epsilon_h \left(\frac{\omega}{c}\right)^2 - \left(\frac{u\pi}{a}\right)^2 - \left(\frac{v\pi}{a}\right)^2} \quad (3.13)$$

The order of the waveguide modes are denoted by u and v with the associated propagation constant given by $q_z^{u,v}$, the hole side length by a and the permittivity within the cavity by ϵ_h . The field amplitudes are denoted by $B_i^{u,v}$ and $C_i^{u,v}$.

The tangential electric fields in all three regions have now been defined. Expressions for the corresponding tangential magnetic field components, H_x and H_y , can now be obtained for each region using Maxwell's equations.

$$\nabla \cdot \vec{E} = \frac{\rho}{\epsilon_0}, \quad (3.14)$$

$$\nabla \times \vec{E} = -\frac{\partial \vec{B}}{\partial t}. \quad (3.15)$$

However, as there is no source charge in the system, equation 3.14 reduces to $\nabla \cdot \vec{E} = 0$. Rearranging this provides an expression for E_z :

$$E_z = \int \left(-\frac{\partial E_x}{\partial x} - \frac{\partial E_y}{\partial y} \right) \quad (3.16)$$

Equation 3.16 can be substituted into the rearranged equation 3.15 to give the following expressions for H_x and H_y :

$$H_x = -\frac{1}{i\omega} \left[\frac{\partial E_z}{\partial y} - \frac{\partial E_y}{\partial z} \right], \quad (3.17)$$

$$H_y = -\frac{1}{i\omega} \left[\frac{\partial E_x}{\partial z} - \frac{\partial E_z}{\partial x} \right]. \quad (3.18)$$

The tangential boundary conditions require that the electric field must be continuous at each interface across the entire unit cell, whilst the magnetic field must be continuous across the aperture at each interface. Considering the electric field initially, if the first interface is arbitrarily defined as occurring at $z = 0$, equations 3.3, 3.4, 3.9 and 3.10

3. Analytical and Numerical Modelling Techiques

give the tangential field components as:

$$E_x^I|_{z=0} = E_x \exp(i(k_x x + k_y y)) + \sum_{m,n} A_x^{m,n} \exp\left[i\left(k_x + \frac{2m\pi}{d}\right)x\right] \exp\left[i\left(k_y + \frac{2n\pi}{d}\right)y\right], \quad (3.19)$$

$$E_y^I|_{z=0} = E_y \exp(i(k_x x + k_y y)) + \sum_{m,n} A_y^{m,n} \exp\left[i\left(k_x + \frac{2m\pi}{d}\right)x\right] \exp\left[i\left(k_y + \frac{2n\pi}{d}\right)y\right], \quad (3.20)$$

$$E_x^{II}|_{z=0} = \sum_{u,v} B_x^{u,v} \cos\left(\frac{u\pi x}{a}\right) \sin\left(\frac{v\pi y}{a}\right) + C_x^{u,v} \cos\left(\frac{u\pi x}{a}\right) \sin\left(\frac{v\pi y}{a}\right) \quad (3.21)$$

and

$$E_y^{II}|_{z=0} = \sum_{u,v} B_y^{u,v} \sin\left(\frac{u\pi x}{a}\right) \cos\left(\frac{v\pi y}{a}\right) + C_y^{u,v} \sin\left(\frac{u\pi x}{a}\right) \cos\left(\frac{v\pi y}{a}\right). \quad (3.22)$$

The tangential electric fields in region I and region II must be equal, and continuous, across the entire unit cell. These requirements can be fulfilled by equating the field components in each region, multiplying both sides by the conjugate exponential term and integrating over the unit cell:

$$E_x \sum_{m,n} Q_1^{m,n} + d^2 \sum_{m,n} A_x^{m,n} = \sum_{m,n,u,v} [(B_x^{u,v} + C_x^{u,v}) Q_{2x}^{m,n,u,v}] \quad (3.23)$$

$$E_y \sum_{m,n} Q_1^{m,n} + d^2 \sum_{m,n} A_y^{m,n} = \sum_{m,n,u,v} [(B_y^{u,v} + C_y^{u,v}) Q_{2y}^{m,n,u,v}] \quad (3.24)$$

where

$$Q_1^{m,n} = \int_0^d \int_0^d \exp\left[-i\left(\frac{2m\pi}{d}\right)x\right] \exp\left[-i\left(\frac{2n\pi}{d}\right)y\right] dx dy, \quad (3.25)$$

$$Q_{2x}^{m,n,u,v} = \int_0^d \int_0^d \cos\left(\frac{u\pi x}{a}\right) \sin\left(\frac{v\pi y}{a}\right) \exp\left[-i\left(k_x + \frac{2m\pi}{d}\right)x\right] \exp\left[-i\left(k_y + \frac{2n\pi}{d}\right)y\right] dx dy \quad (3.26)$$

3. Analytical and Numerical Modelling Techniques

and

$$Q_{2y}^{m,n,u,v} = \int_0^d \int_0^d \sin\left(\frac{u\pi x}{a}\right) \cos\left(\frac{v\pi y}{a}\right) \exp\left[-i\left(k_x + \frac{2m\pi}{d}\right)x\right] \exp\left[-i\left(k_y + \frac{2n\pi}{d}\right)y\right] dx dy. \quad (3.27)$$

The same process is applied to the tangential magnetic field components at $z = 0$ and both electric and magnetic field components at the second interface ($z = h$), although the tangential magnetic fields are only continuous across the aperture. This results in four pairs of coupled simultaneous equations in terms of the unknown amplitude coefficients. These equations can be solved to determine an analytical form for the complex transmission and reflection amplitude coefficients,

$$r^{m,n} = \sqrt{(A_x^{m,n})^2 + (A_y^{m,n})^2} \quad (3.28)$$

and

$$t^{p,q} = \sqrt{(D_x^{p,q})^2 + (D_y^{p,q})^2}. \quad (3.29)$$

3.2.2.2 Approximations and Simplifications

It is clear from equations 3.23 and 3.24 that the coupled equations to be solved involve infinite sums of waveguide modes and diffracted orders. However, there are various simplifications and approximations that can be applied to reduce the complexity of these equations. The thickness of the metal mesh is far less than the wavelength and therefore no propagating waveguide modes are supported in the holes. The inclusion of the orders in the calculation is necessary purely as a ‘matching condition’ across the interfaces, and therefore the first order mode is sufficient to provide an accurate representation of the behaviour (i.e., $u = 1$; $v = 0$ for TE and $u = 0$; $v = 1$ for TM). This assumption has been tested and verified by comparing the results including higher orders of waveguide modes in the summation (not shown). The contribution from these higher orders is so negligible there is no discernible affect on the transmission response, proving the validity of this assumption. Purely for illustration purposes, the specific case of normal incidence with the electric field oscillating parallel to the x -axis will be explored, i.e. $k_x = k_y = 0$ and $E_y = 0$, however, the method for the general case is identical. In addition, the amplitude of the incident field, E_x , will be taken to be unity. Including only the first order waveguide mode and as there are only x -components in

3. Analytical and Numerical Modelling Techniques

this system, the simultaneous equations to be solved reduce to:

$$\sum_{m,n} Q_1^{m,n} + d^2 \sum_{m,n} A_x^{m,n} = (B_x + C_x) \sum_{m,n} Q_2^{m,n,0,1}, \quad (3.30)$$

$$d^2 \sum_{p,q} D_x^{p,q} \exp[ihk_z^{p,q}] = (B_x \exp[ihq_z] + C_x \exp[-ihq_z]) \sum_{p,q} Q_2^{p,q,0,1}, \quad (3.31)$$

$$-k_z^{0,0} \frac{2a^2}{\pi} + \sum_{m,n} \left[A_x^{m,n} (Q_2^{m,n,0,1})^* \left(k_z^{m,n} + \frac{4m^2\pi^2}{d^2 k_z^{m,n}} \right) \right] = -(B_x - C_x) q_z \frac{a^2}{2} \quad (3.32)$$

and

$$\sum_{p,q} \left[D_x^{p,q} \exp[ihk_z^{p,q}] (Q_2^{m,n,0,1})^* \left(k_z^{p,q} + \frac{4p^2\pi^2}{d^2 k_z^{p,q}} \right) \right] = (B_x \exp[ihq_z] - C_x \exp[-ihq_z]) q_z \frac{a^2}{2} \quad (3.33)$$

where

$$Q_2^{m,n,0,1} = \int_0^d \int_0^d \sin\left(\frac{\pi y}{a}\right) \exp\left[-i\left(\frac{2m\pi}{d}\right)x\right] \exp\left[-i\left(\frac{2n\pi}{d}\right)y\right] dx dy. \quad (3.34)$$

Rearranging equations 3.30 and 3.31 provides expressions for $A_x^{m,n}$ and $D_x^{p,q}$ which are required for the complex transmission and reflection coefficients,

$$\sum_{m,n} A_x^{m,n} = \frac{(B_x + C_x) \sum_{m,n} Q_2^{m,n,u,v} - \sum_{m,n} Q_1^{m,n}}{d^2} \quad (3.35)$$

and

$$\sum_{p,q} D_x^{p,q} = \frac{(B_x \exp[ihq_z] + C_x \exp[-ihq_z]) \sum_{p,q} Q_2^{p,q,u,v}}{d^2 \exp[ihk_z^{p,q}]}. \quad (3.36)$$

These can be substituted into equations 3.32 and 3.33 resulting in the following pair of simultaneous equations:

$$-k_z^{0,0} \frac{2a^2}{\pi} + \frac{(B_x + C_x)}{d^4} G_1 - \frac{1}{d^4} G_2 = -(B_x - C_x) q_z \frac{a^2}{2} \quad (3.37)$$

and

$$\frac{(B_x \exp[ihq_z] + C_x \exp[-ihq_z])}{d^4} = (B_x \exp[ihq_z] - C_x \exp[-ihq_z]) q_z \frac{a^2}{2}, \quad (3.38)$$

3. Analytical and Numerical Modelling Techniques

where

$$G_1 = \sum_{n,m} \frac{(4m^2\pi^2 + d^2(k_z^{m,n})^2) Q_2^{m,n,0,1} (Q_2^{m,n,0,1})^*}{k_z^{m,n}}, \quad (3.39)$$

$$G_2 = \sum_{n,m} \frac{(4m^2\pi^2 + d^2(k_z^{m,n})^2) Q_1^{m,n} (Q_2^{m,n,0,1})^*}{k_z^{m,n}} \quad (3.40)$$

and

$$H = \sum_{p,q} \frac{(4p^2\pi^2 + d^2(k_z^{p,q})^2) Q_2^{p,q,0,1} (Q_2^{p,q,0,1})^*}{k_z^{p,q}}. \quad (3.41)$$

These can be solved to provide expressions for B_x and C_x :

$$B_x = \frac{C_x \exp[-2ihq_z](2H + a^2d^4q_z)}{a^2d^4q_z - 2H} \quad (3.42)$$

and

$$C_x = \frac{2 \exp[2ihq_z](2H - a^2d^4q_z)(G_2\pi + 2a^2d^4K_z^{0,0})}{\pi [2a^2d^4q_z (1 + \exp[2ihq_z]) (H + G_1) + (\exp[2ihq_z] - 1) (a^2d^4q_z - 4G_1H)]}. \quad (3.43)$$

Substituting these expressions back into equation 3.29 gives the following general equation for the transmission amplitude coefficient:

$$t^{p,q} = \frac{\frac{\omega}{c} (Q_2^{0,0,0,1})^* \sum_{p,q} Q_2^{p,q,0,1}}{\sum_{m,n} \left(\frac{(k_z^{m,n})^2 + \left(\frac{2m\pi}{d}\right)^2}{k_z^{m,n}} \right) (Q_2^{m,n,0,1})^* Q_2^{m,n,0,1}}. \quad (3.44)$$

The manipulation of these equations was done with the aid of Wolfram's Mathematica software [96] and the full calculation is provided in Appendix A.

3.2.2.3 Advantages and Limitations

One of the primary advantages of an analytical model over a numerical one is the increased understanding of EM fields it can provide. As well as a numerical prediction of the EM response, by examining the constituent terms in the equation, the origin of any resonances can be determined. The aim of this thesis is to understand why the examined structures interact with EM radiation as they do and therefore an analytical model is an important tool. The modal matching method provides a more complete solution by allowing any number of diffracted (propagating or evanescent) and waveguide modes to be included in the calculation, although these may be truncated as necessary, as is the case with the waveguide modes. This is an important factor as the frequency range just

3. Analytical and Numerical Modelling Techniques

below the onset of diffraction, where evanescent fields can play a significant role, is of particular interest. This flexibility of the model allows us to gain an understanding of the influence of specific orders on the structure's overall EM response. Another benefit of the model is its fast computation time in comparison to many of the commercially available numerical models.

There are advantages and disadvantages to all models, and modal matching is no exception. There are two main disadvantages to this method. Firstly, there is a limit to the geometries that can be modelled analytically. Finite arrays cannot be solved as a unit cell is required. This limitation also means that random and aperiodic arrays are beyond the scope of the method. In addition, the model requires an analytical form for the waveguide modes within the hole to be available, further limiting the options for the geometry of the hole. The second disadvantage is that each specific structure requires an individual model. Once the model is created, parameter changes can be done and results obtained extremely quickly, but the production of the initial model can be time intensive.

3.3 Numerical Methods

As previously mentioned, the development of efficient modelling tools to predict and quantify the EM response of metamaterials is extremely important. Numerical modelling techniques are often chosen as analytical solutions are only possible for certain specific regular geometries (section 3.2.2.3).

Finite Difference Time Domain (FDTD) is one of the most widely used numerical modelling methods. It is used to solve a wide variety of EM problems including antennas, microwave systems and radar cross section predictions. It was originally derived by Yee [97] in 1966 and solves Maxwell's curl equations in their differential form. The program uses an iterative algorithm to numerically solve the fields in discrete time and spatial steps. The far-field solution is then used to compute the EM properties of the structure [22, 97, 98].

Whilst the FDTD method is known for its versatility, the conventional algorithm cannot deal with complex geometry (such as curved surfaces) and the commercially available software does not allow the user to edit the algorithms used. Therefore, for complex problems, users need to be able to design and manipulate algorithms themselves. Another significant disadvantage is that FDTD develops numerical inaccuracies if evanescent waves are required to be included in the calculation [22].

3. Analytical and Numerical Modelling Techniques

Another ‘family’ of numerical models make use of volume-integral equations. These methods involve introducing a volume current density and thereby converting the homogeneous Helmholtz equation into an inhomogeneous differential equation. This can then be solved by finding the Green’s function and substituting this into the equation for the electric field and performing the volume integral [99, 100]. Two methods that use this approach are the Method of Moments (MoM) and the Discrete Dipole Approximation (DDA). In the MoM approach, the structure is divided up into discrete finite volume elements. These elements must be small enough to realistically assume that the permittivity of each element is homogeneous. The long wavelength approximation is applied to evaluate the electric field from each element, and then summed over the whole volume [101]. The DDA also begins by dividing the structure into volume elements and the volume current density for each element is evaluated. The incident field is then deemed to induce a dipole moment in each element. The far field dipole approximation is then applied and the contribution from each element is summed over the entire volume [101].

3.3.1 Finite Element Method

Another widely used method is the Finite Element Method (FEM). Both FDTD and FEM replace a continuous function by discrete polynomial approximations. The idea of breaking down a difficult problem into smaller ‘finite elements’ that can be approximated is not a new one. The Greek philosopher and mathematician Archimedes used this exact theory to determine formulae for areas and volumes, as well as an extremely accurate approximation of π [102]. In its modern context, the method was (re)instigated by structural engineers. It is suggested that the first uses of it were by Hrennikoff [103] in 1941 and McHenry [104] in 1943 with regards to aircraft design. In time the application of this method to any continuous boundary condition problem that can be described in terms of partial differential equations was realised and the method is now used in a wide range of areas including (but not limited to) heat conduction problems [105], viscous fluid flow [106], biomedical engineering [107] and electromagnetic theory [108]. In electromagnetics, it is a conceptually similar approach to FDTD but in the FEM it is the Helmholtz equation that is spatially discretised. Then all the boundary conditions are solved numerically. In essence, the area is divided into a grid mesh of sufficient detail and then the fields are solved across each grid boundary.

Throughout this thesis the validity of the analytical results from modal matching

3. Analytical and Numerical Modelling Techniques

have been verified by assigning numerical values to the parameters of the structure and comparing the results with those from the commercially available numerical modelling software, which has itself been validated using experimental studies. The software package chosen is Ansoft's High Frequency Structure Simulator (HFSSTM) versions 10 to 13.1 [109]. HFSSTM uses the finite element method to simulate the electromagnetic fields through a structure. This software was chosen primarily as the Microwave Section of the Electromagnetic Materials Group at the University of Exeter have worked with Ansoft's developers for several years now to allow this flexible code to be applied to incident wave problems of complicated structures.

3.3.1.1 Introduction to HFSSTM

Ansoft's HFSSTM is a three dimensional full-wave electromagnetic field simulator and is one of the simulation products produced by parent company ANSYS. HFSSTM was historically used by industrial engineers to design components such as PCB intercepts, antennas, microwave components (including waveguide systems) and biomedical devices as well as calculating the eigenmodes of a given system.

HFSSTM divides the model into a number of smaller sub-regions, known as elements or tetrahedra. These tetrahedra form the mesh and the EM vector field in each element is represented by a function. In order to differentiate between fields at the edges and the faces of the elements, the tangential electric field components of the element edges are stored at the vertices of the element; and the tangential electric field components of the element's faces are stored at the edges. The field throughout the element may then be calculated. The system describes Maxwell's equations in terms of matrices and solves numerically. The number of tetrahedra in a solution (i.e. the mesh resolution) dictates the accuracy of the field solution. In areas of high field gradient the field is changing rapidly and if the individual tetrahedra are too large, the nodal values will not accurately represent the field within the element. However, the larger the number of tetrahedra in the mesh, the more processing power and computational memory is needed. In an attempt to achieve the minimum mesh resolution whilst still obtaining an accurate field solution HFSSTM uses adaptive passes. An initial mesh is generated and successive passes refine the mesh in regions of high field gradient for a user-specified number of passes.

3.3.1.2 Using HFSSTM

HFSSTM contains an integrated computer aided design (CAD) package with which to define the structure. The user constructs a scale drawing of the structure using simple 1-D, 2-D and 3-D geometric objects to build into the complete structure. The parameters of these objects may be defined as variables and either assigned a value or defined as a function of other variables, allowing the geometry to be altered automatically.

HFSSTM contains a large materials database allowing different parts of the geometric model to be assigned accurate material parameters. This database may be added to by the user. The materials within the database are characterised in terms of relative complex permeability (μ), relative complex permittivity (ϵ), bulk conductivity, dielectric loss tangent (ϵ_i/ϵ_r) and magnetic loss tangent (μ_i/μ_r). As metals can be considered as perfect conductors at microwave frequencies, unless otherwise specified, PEC has been used to represent all metal components of each structure. Fields are excluded from within a perfect conductor, therefore HFSSTM only solves at the surface of PEC components.

The software allows the user to specify different types of solution depending on their requirements. The two used in this thesis are the driven modal solution and the eigenmode solution. For the driven modal solution the properties of the incident radiation may be defined to reflect the realities of the physical system: i.e. plane, Gaussian or spherical waves in the incident medium or injected through a port such as a waveguide. The eigenmode solution calculates the eigenmodes of the system purely in terms of the geometry, material parameters and boundary conditions but does not give any information regarding the coupling ability of the mode.

In order to model infinite periodic structures, as in this thesis, periodic boundary conditions (referred to as master-slave boundaries within the software) are used. A single unit cell of the array is drawn and then the field on a particular outer boundary (the slave) is forced to match the field on the opposite boundary (the master) including any phase delay between the two boundaries (figure 3.6). It is particularly important that the unit cell is chosen so that there is no material discontinuity at the master-slave boundaries. For example if there is metal at a specific point on the master boundary, there must be metal on the corresponding point on the slave boundary.

The driven modal solutions used in this thesis use ‘Floquet Ports’ as their method of excitation. These ports are defined on the incident and transmitted faces of the unit cell. The excitation is defined as a plane wave comprising a sum of diffracted modes arising from the periodic structure. As Floquet ports define their fields in terms of diffracted

3. Analytical and Numerical Modelling Techniques

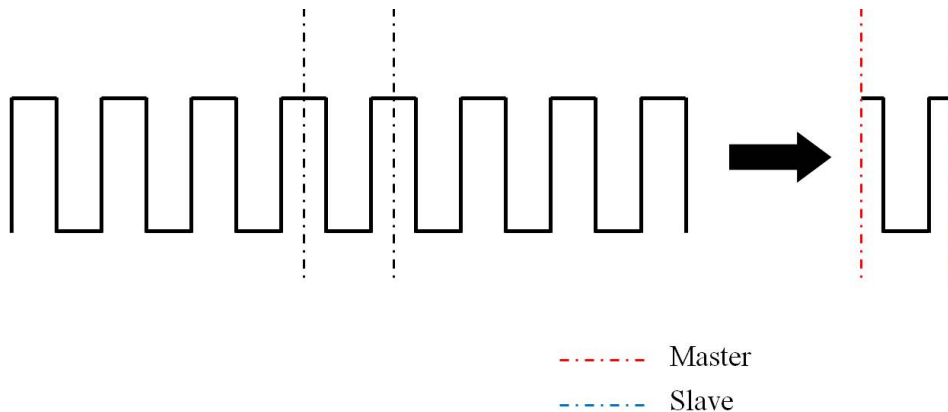
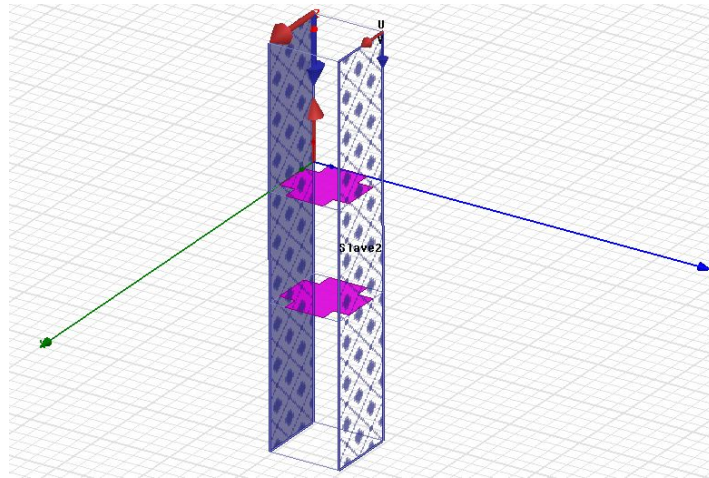


Figure 3.6: *Master-slave boundaries are designed to allow infinite periodic structures or arrays to be represented as a unit cell by forcing the fields at the slave boundary to be identical to those at the master [77].*

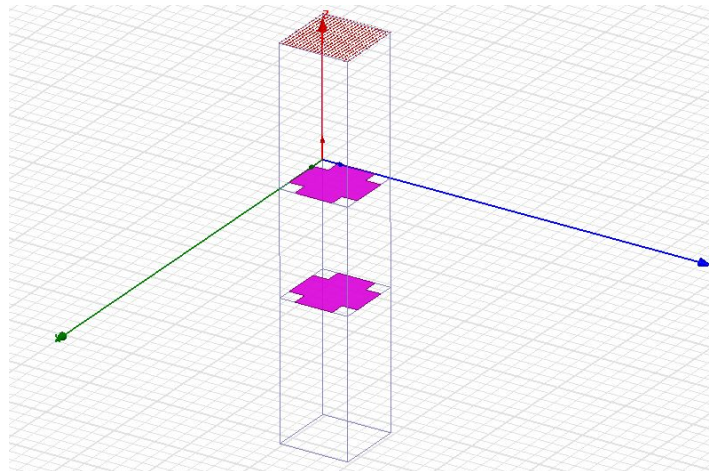
orders, they are only available for exciting periodic structures. Due to the inclusion of the evanescent diffracted orders they produce far more accurate results when modelling close to the onset of diffraction when compared to the results using a simple plane wave excitation. Figure 3.7 illustrates firstly, one set of master-slave boundaries (figure 3.7(a)) and secondly, the top Floquet port (figure 3.7(b)) for a system comprising two layers of a PEC square mesh.

In addition to the automatic iterative meshing process, the mesh may be manually refined. The user specifies either a maximum number of tetrahedra or a maximum tetrahedra size for a specific design object. This is particularly useful for very subwavelength objects to ensure they are adequately represented. Once the mesh has been refined, HFSSTM can be set to ‘step’ through the user specified frequency range analysing the response. Figure 3.8 illustrates the mesh produced on the top face of the unit cell of a hole array.

Once a solution has been obtained, a useful range of tools is available to display and analyse the results. Transmission and reflection plots for changing frequencies, material parameters, geometrical parameters or orientation may be obtained. In addition various field plots are available allowing the user to evaluate the magnetic and electric fields throughout the structure. These are available for both field magnitudes and the vector fields themselves.



(a)



(b)

Figure 3.7: Screen shots from $HFSS^{TM}$ for a system comprising of two layers of a PEC square mesh illustrating (a) one of the master-slave boundaries and (b) the top Floquet Port excitation. A single unit cell is illustrated with the PEC being the highlighted pink areas.

3.3.1.3 Advantages and Limitations

FEM modelling has advantages over some other methods in that it incorporates a CAD (Computer Aided Design) package allowing complex geometries to be modelled and solved. In particular, as mentioned in section 3.2.2.3, each modal matching computation is for a specific geometry. This is true for many analytical models. The CAD package in $HFSS^{TM}$ allows complex models to be quickly and easily constructed using basic geometric shapes.

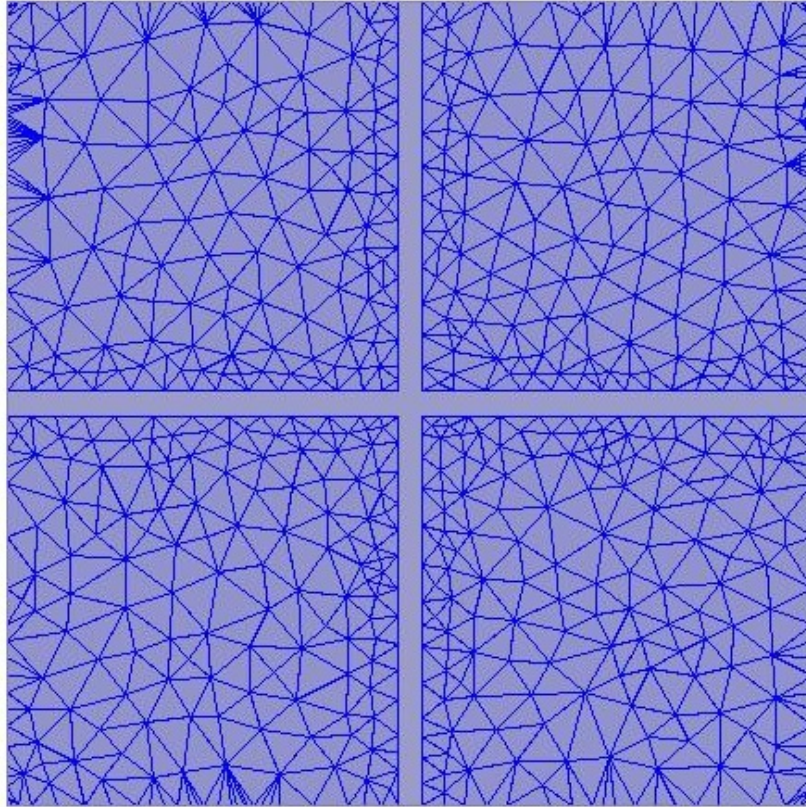


Figure 3.8: A sample mesh produced by HFSSTM on the top face of the unit cell of a hole array.

However, there are disadvantages to this numerical model. The primary drawback of this, and many numerical models, is the large computation time required to solve a model. HFSSTM provides a full-wave solution meaning that the programme makes no approximations whilst solving. In addition, the mesh resolution has an important role to play. The resolution must be fine enough to ensure that electric fields are accurately represented, particularly close to the onset of diffraction and for areas with high field gradients. Consequently, the larger and more complex the model to be solved, the longer the computation time. A limitation of particular relevance to the structures investigated in this thesis, is the difficulty that FEM models have in representing thin mesh layers, i.e. systems where the thickness of the mesh is much less than either the wavelength of the incident radiation or the other dimensions of the structure. In this situation, the number of tetrahedra required in the mesh layer for HFSSTM to accurately describe the EM response is generally too large for the system to handle, causing the software to ‘crash’. If the number of tetrahedra are lower, whilst the software is able to run, the results produced do not represent the true EM response of the system.

3.4 Conclusion

This chapter has reviewed the two main modelling methods used throughout this thesis. The aim of this research is to further develop the understanding of the origin of the observed responses of metal-dielectric periodic media to EM radiation. To achieve this aim, the primary modelling tool used is an analytical modal matching method. The model differs from some alternative modal matching approaches in that it incorporates the effect of multiple order waveguide modes, diffracted waves (both propagating and evanescent) and can be used to model finite depth holes. Due to the analytical nature of the results, it is possible to link observed resonances to specific mathematical terms and hence provide physical understanding. The flexibility of the model allows the waveguide and diffracted orders to be included, or excluded as required. In addition, the fast computation time in comparison to commercial numerical models is of benefit.

The veracity of the results obtained by this analytical method have been verified using a commercially available FEM model. FEM models are a well established, extensively used tool. They divide the structure into discrete spatial areas and then solve Maxwell's equations in differential form in each of these elements. The software used for this verification is Ansoft's three dimensional full-wave electromagnetic field simulator HFSSTM. It was chosen due to its ability to solve complex geometrical systems and the strong knowledge base within the Electromagnetic Group at the University of Exeter.

Chapter 4

The Microwave Response of Square Arrays of Square Elements

4.1 Introduction

This first investigative chapter studies the EM response of one of the most simple examples of a bigrating; a square array of square holes in a sheet of PEC, and its complementary structure of a square array of perfectly conducting square patches. The transmissive properties of patterned thin metallic films has generated much interest in recent years in both the optical regime [2, 110, 111] and at radio frequencies [112–115].

The arrays are modelled utilising the modal matching technique described in section 3.2.2 and employing Babinet’s Principle (see section 4.2.2). At frequencies close to, but below, the onset of diffraction, a near-complete reflection condition is predicted for the patch arrays, even for low metal filling fractions: conversely, for high metal filling fractions a near-complete transmission condition results for hole arrays. These resonance phenomena are associated with evanescent diffraction and the complementary nature of the responses of the two types of array, as predicted by Babinet’s Principle, is confirmed. In other words, the dispersion of the predicted modes for the hole array is different to that of the patch array for the same incident polarisation. Using mathematical analysis the reason for the dominant coupling to a particular grating vector for each array and polarisation is explained.

Studies into random structures have suggested that the electrical connectivity of the structure is paramount in determining its transmissivity [116]. Therefore, a connected structure such as a hole array would demonstrate a markedly different response to that of an unconnected structure, such as a patch array. For the initial structure

4. The Microwave Response of Square Arrays of Square Elements

explored within this chapter, the patch array remains unconnected until 100% metal occupancy is reached; and conversely, the hole array remains a connected structure until the metal occupancy reaches 0%. To investigate the changes in the EM response of a connected and unconnected structure, the elements in the square array are rotated by 45° with respect to the lattice (section 4.6). A connected structure is therefore reached for metal filling fractions of 50% and above, whilst the structure is unconnected for metal filling fractions of less than 50%. Although it would be expected that once electrical connectivity has been established, the array would switch from transmitting on resonance to reflecting on resonance, for frequencies approaching the diffraction edge, this is not the case. The evanescent diffraction discussed in the previous section (section 4.5) is resonantly enhanced to such an extent that the expected step change in transmission is reversed; i.e., a connected structure demonstrates increased transmission with increasing filling fraction.

Frequency selective surfaces (FSSs) have been used by microwave engineers for many years, particularly to screen-out unwanted radiation from sensitive locations. These specifically designed surfaces use metallic elements to produce the desired response over a particular frequency range [83]. Bigratings are often used as FSSs and the type of bigrating dictates the response. Hole arrays are inductive meshes and are used to filter out low frequencies (i.e., they are good reflectors at low frequencies), whilst patch arrays are capacitive meshes and are used to filter out high frequency radiation (i.e., they are good transmitters at low frequencies). For the inductive mesh, as it is a connected structure, the electrons in the metal can travel across the entire mesh upon application of an electric field. The mesh is inductive due to its ability to support the flow of current. At low frequencies the electrons travel a large distance across the mesh before reversing direction. The electrons re-emit the radiation 180° out-of-phase with respect to the incident radiation resulting in low transmission. For the complementary capacitive mesh, the electrons are confined to the metal patches. Due to the confinement of the patches, a net charge builds up on the edges of the patches in the direction of the incident field leading to capacitance between neighbouring patches. For low frequencies, the electrons are trapped at the edge of the patch (i.e. stationary) for much of the period of the EM wave. This leads to high transmission due to the inability of the electrons to respond to the incident field. It is worth noting that due to the 2D nature of the bigrating, the response of these meshes is polarisation independent. There is a large body of research concerning the EM response of these surfaces [65, 66, 83, 117, 118]. However, this has focused on the subwavelength regime where an inductive surface will

4. The Microwave Response of Square Arrays of Square Elements

support a TM surface mode, whilst the complementary capacitive structure will support a TE surface mode.

The work presented in this chapter also has analogies to work undertaken in the field of metallic photonic crystals [119, 120]. Metallic photonic crystals are materials specifically designed in the same way as dielectric photonic crystals, but using metals. Their properties are controlled by periodically structuring the material to a scale that is comparable to the wavelength of interest. Although much work has been done at optical frequencies, there has been some investigation into metallic photonic crystals at microwave frequencies to produce materials with a negative permeability [121, 122].

There have been many studies into gratings close to the onset of diffraction. However, the vast majority of these studies have involved connected structures, such as grooved metal surfaces [69, 75, 86, 123] or hole arrays [2, 60, 67, 110, 124–128].

4.2 Background

Chapter 2 discussed spoof surface plasmons and their associated SPP dispersion curves (section 2.2.3.2) for a monograting (one-dimensional grating). However, an array is periodic in two directions and is therefore known as a bigrating, or two-dimensional grating (figure 4.1).

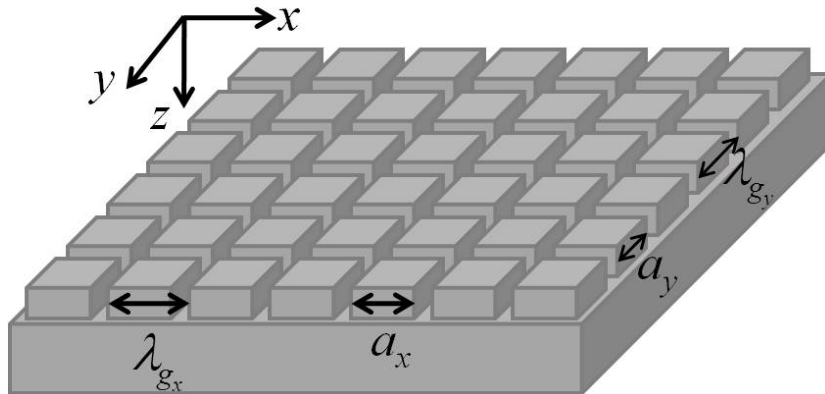


Figure 4.1: Schematic of a bigrating with two orthogonal grating periods λ_{g_x} and λ_{g_y} with elements with side lengths a_x and a_y .

There are two orthogonal grating periods, λ_{g_x} and λ_{g_y} parallel to the x -axis and y -axis respectively. In the case of a square bigrating, ($\lambda_{g_x} = \lambda_{g_y}$), the onset of diffraction corresponding to the x and y periodicity will occur at the same frequency for normal

incidence. In addition, the grating has four-fold symmetry. For a rectangular bigrating, ($\lambda_{g_x} \neq \lambda_{g_y}$), the grating has only two-fold symmetry and the onset of diffraction for each periodicity will occur at different frequencies.

4.2.1 Bigrating dispersion

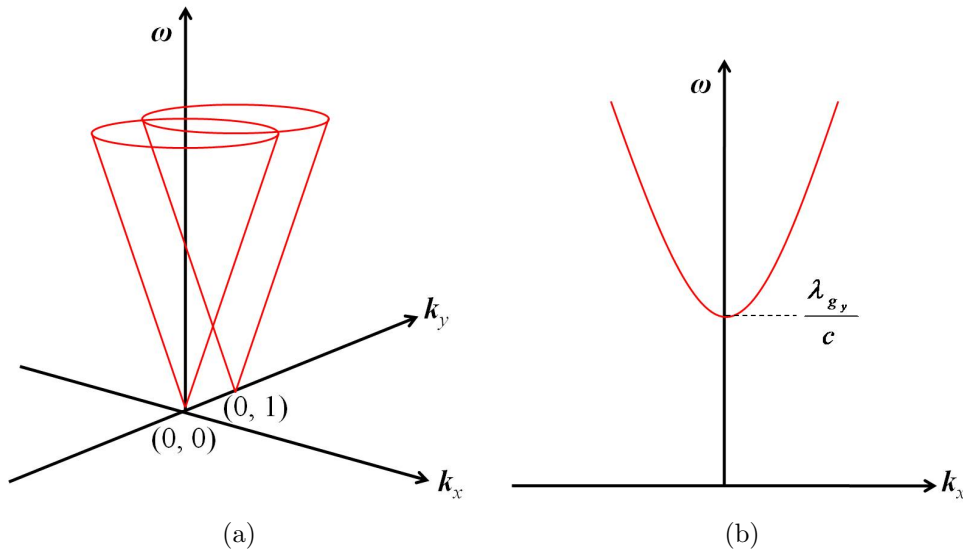


Figure 4.2: Schematic illustrating (a) the intersection of light cones centred on $(0, 0)$ and $(0, 1)$ and (b) their projection onto the k_x axis forming a parabolic diffracted light line for the $k_y = 0$ plane (reproduced from [129]).

The presence of two grating vectors results in the possibility of scattering occurring both in the plane of incidence and out of the plane of incidence. For diffraction out of the plane of incidence, the light line is parabolic. For example, the light cone centred on $(0, k_{g_y})$ intersects with the $k_y = 0$ plane as a parabola (figure 4.2).

The reciprocal space representation for a bigrating is similar to that for a monograting (figure 2.12) but with a two dimensional lattice of scattering centres (figure 4.3).

The dispersion curves for SPP's coupled from a bigrating are shown in figure 4.4 and the shaded area indicates SPP's that can be radiatively coupled to. It is clear from this diagram that the dispersion curves greatly differ depending on whether the diffraction is in or out of the plane of incidence. What is not clear however, is which modes should be most strongly coupled to for a specific polarisation.

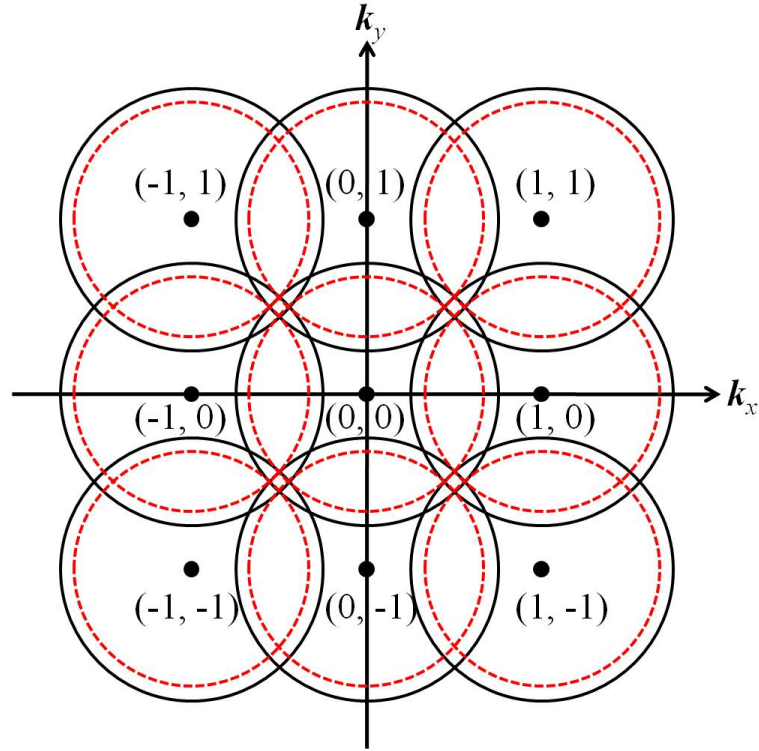


Figure 4.3: A reciprocal space representation of a bigrating for a fixed frequency. The scattering centres are represented by the points, the momentum of the surface modes by the solid black circles and the available momentum from an incident photon by the red dashed circles (reproduced from [129]).

4.2.2 Babinet's Principle

In 1837, Babinet [131] derived a principle relating the transmission through a screen and its complement with the transmission when no screen is present. Babinet's Principle states that the sum of the transmission through an infinitely thin perforated screen, with the transmission through the complementary structure rotated by 90° about the normal to its plane, is equal to unity. It is worth noting that, in the context of the present work (i.e., in the non-diffracting regime and with $\theta = 0$), this is equivalent to a rotation of the incident polarisation with no rotation of the structures. The study of complementary structures by application of Babinet's Principle has numerous precedents [60, 66, 91, 132–134]. Babinet's Principle was originally derived in scalar form, however, in 1946 Booker [135] derived a vector form for electromagnetic radiation. There are two primary assumptions made by Babinet's Principle that are worth drawing attention to. The first assumption is that there is no absorption by the screen, hence the requirement for a PEC

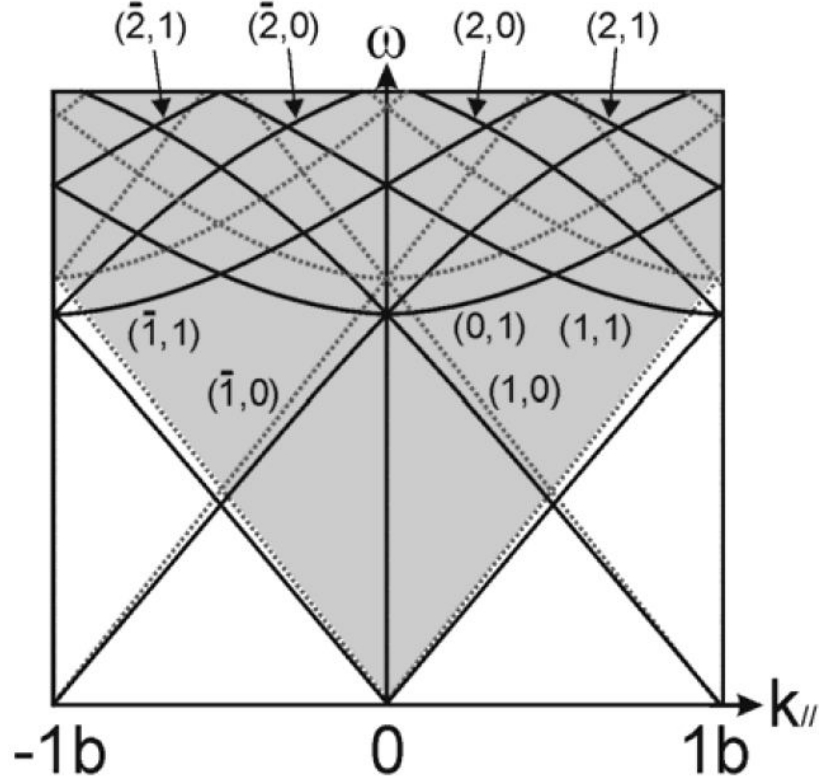


Figure 4.4: Schematic diagram illustrating the scattered light lines (dotted) and SPP modes (solid) for a square grating. Negative values of m and n are represented by \bar{m} and \bar{n} and k_g is represented by b in this diagram. Reproduced from [130]

screen. The second assumption is that there is no phase change through the screen, leading to the condition that the screen must be infinitely thin. The consequences of these assumptions are that whilst it is valid to assume that metals at microwave frequencies behave as perfect conductors, this is not valid for higher frequencies where the finite conductivity of metals has a significant role to play in the response of the metal to EM radiation. The validity of Babinet's Principle for finite thickness systems is explored in section 4.4.1.2.

4.2.3 Derivation of Babinet's Principle

This derivation is for the vector form of Babinet's Principle and is adapted from the derivation in *Principles of Optics* by M. Born and E. Wolf [136]. Figure 4.5 illustrates a 2D PEC sheet perforated by a rectangular hole and its complement of a rectangular PEC patch. The incident EM wave is propagating in the z -direction. Note that the

4. The Microwave Response of Square Arrays of Square Elements

polarisation of the incident electric field on the patch is rotated by 90° with respect to the incident field on the aperture. This can also be described as a transformation from $\vec{E} \rightarrow \vec{H}$.

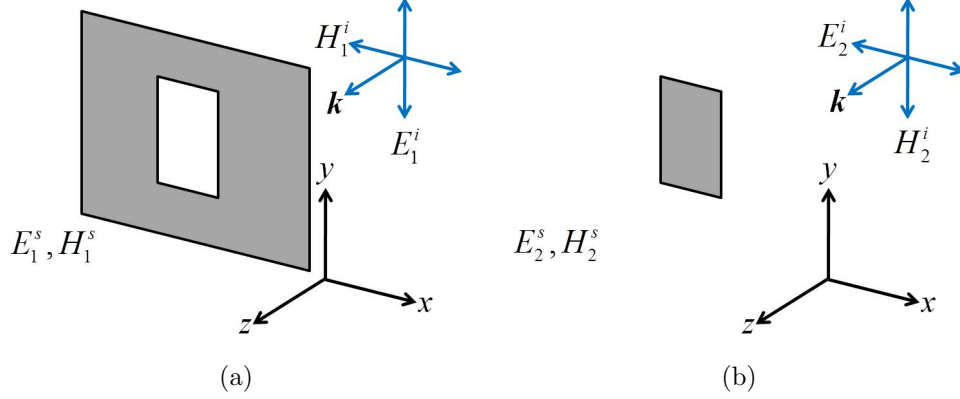


Figure 4.5: Schematic showing the coordinate system, incident and scattered fields for (a) a rectangular hole in a PEC sheet, and (b) a rectangular PEC patch where the superscripts ‘i’ and ‘s’ denote incident and scattered fields respectively (reproduced from [129]).

On the PEC regions, the boundary conditions determine that the tangential electric fields must go to zero; whereas the tangential \vec{H} fields go to zero on the aperture as there are no induced currents within it (equation 4.1):

$$E_x^i + E_x^s = E_y^i + E_y^s = 0 \quad (\text{PEC regions}); \quad H_x^s = H_y^s = 0 \quad (\text{aperture}). \quad (4.1)$$

Considering the case of the aperture first and redefining the incident field as $\vec{E}_1^i = \vec{F}^i$ where the suffix 1 denotes the aperture screen, applying the boundary conditions described in equation 4.1, results in

$$F_x^i + E_{1x}^s = F_y^i + E_{1y}^s = 0 \quad \Rightarrow \quad E_{1x}^s = -F_x^i, \quad E_{1y}^s = -F_y^i, \quad (4.2)$$

for the PEC regions, and

$$H_{1x}^s = H_{1y}^s = 0 \quad (4.3)$$

for the aperture.

For the patch array (denoted by the suffix 2), the incident field is now defined by $\vec{H}_2^i = \vec{F}^i$ and the application of the boundary conditions, in terms of the total field

4. The Microwave Response of Square Arrays of Square Elements

gives

$$E_{2x} = E_{2y} = 0 \quad (4.4)$$

for the aperture, and

$$H_{2x} = F_x^i, \quad H_{2y} = F_y^i, \quad (4.5)$$

for the PEC regions.

Maxwell's equations are invariant in free space for the transformations $\vec{E} \rightarrow \vec{H}$ and $\vec{H} \rightarrow -\vec{E}$. Comparing equation 4.2 with equation 4.5, and equation 4.3 with equation 4.4, it can be concluded that

$$\vec{H}_2 = -\vec{E}_1^s, \quad (4.6)$$

The total electric field from the aperture screen, \vec{E}_1 , is the sum of the incident and scattered fields, i.e., $\vec{E}_1^i + \vec{E}_1^s$, which can also be written as

$$\vec{E}_1 = \vec{F}^i - \vec{H}_2. \quad (4.7)$$

Rearranging equation 4.8 produces the required form of Babinet's Principle

$$\vec{E}_1 + \vec{H}_2 = \vec{F}^i. \quad (4.8)$$

Therefore, the sum of the transmission through an infinitely thin perforated screen, with the transmission through the inverse structure rotated by 90° about the normal to its plane, is equal to the incident field, i.e. unity (figure 4.6). For a non-absorbing structure, it is consequently also true to state that the transmission through a 2D screen is equal to the reflection from the complementary structure rotated by 90° .

4.3 Method

The system investigated comprises a square array of square holes in a sheet of perfect electrical conductor (PEC) (structure A) and its complementary system (structure A*) of a square array of square PEC patches (figure 4.7).

The modal matching formalism is identical to that presented in the previous chapter (section 3.2.2) and using the defined regions of the system as per figure 3.5(b). The system is simplified by considering a two dimensional (2D) mesh layer i.e., $h = 0$, and

4. The Microwave Response of Square Arrays of Square Elements

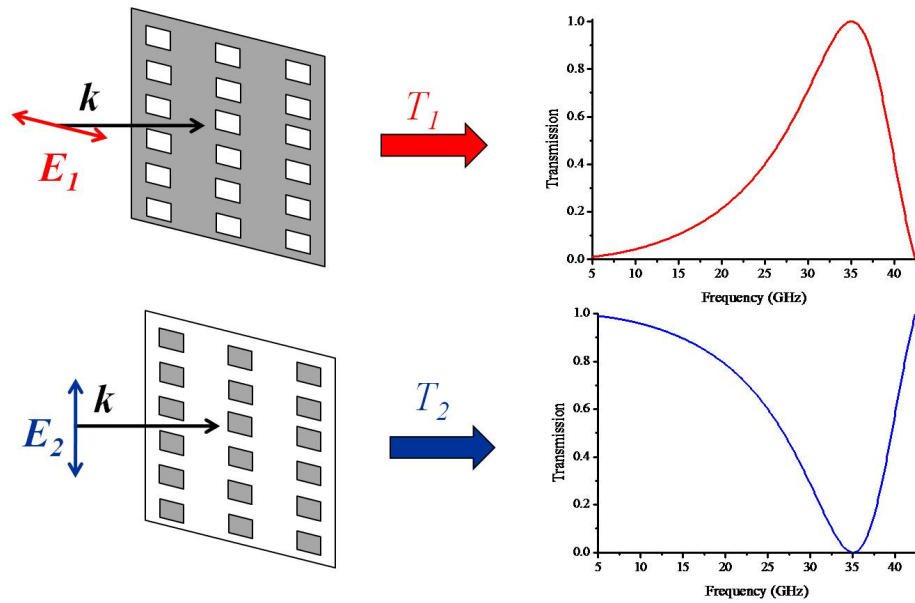


Figure 4.6: Graphical illustration of Babinet's Principle showing the transmission through an arbitrary hole array and the transmission through its complementary patch array for the orthogonal polarisation. At all points, the sum of the transmission through both arrays is equal to unity.

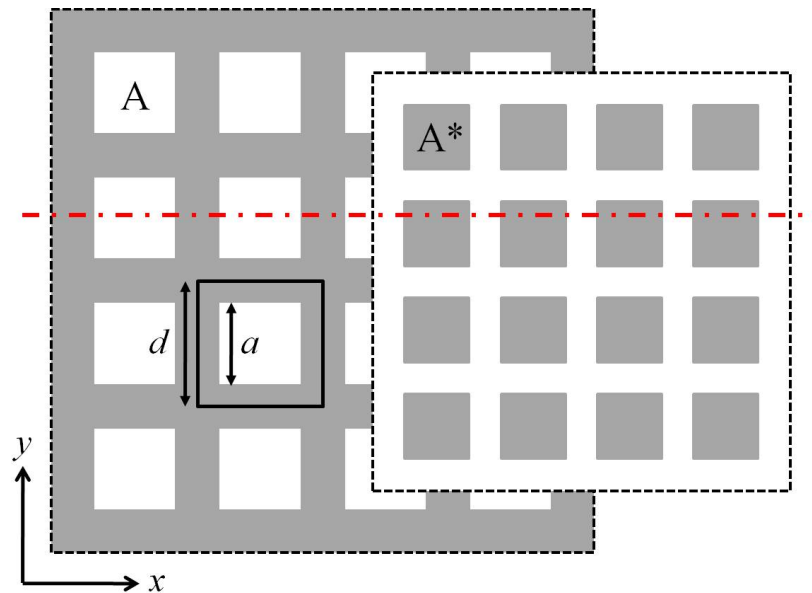


Figure 4.7: Schematic showing the investigated structure A and its complementary structure A^* . Grey areas denote PEC and white areas air. The array has pitch d and square elements of side length a . The black solid line indicates the unit cell and the red dashed line the xz -plane of incidence.

4. The Microwave Response of Square Arrays of Square Elements

assuming that the electric field is parallel to the x -axis, i.e., $E_y = 0$, and that the plane of incidence is the xy -plane (i.e., $k_y = 0$). These considerations mean that the complex amplitude coefficient for transmission (equation 3.44) is of the form

$$t^{p,q} = \frac{\frac{(\frac{\omega}{c})^2}{\sqrt{(\frac{\omega}{c})^2 - (k_x)^2}} (Q_2^{0,0,0,1})^* \sum_{p,q} Q_2^{0,0,0,1}}{\sum_{m,n} \left(\frac{(k_z^{m,n})^2 + (k_x + \frac{2m\pi}{d})^2}{k_z^{m,n}} \right) (Q_2^{m,n,0,1})^* Q_2^{m,n,0,1}}. \quad (4.9)$$

The resonance of the array occurs in the non-diffracting region and therefore only the specular transmission is required (i.e., $p = q = 0$). The resulting expression for the transmission is given by

$$t^{0,0} = \frac{\frac{(\frac{\omega}{c})^2}{\sqrt{(\frac{\omega}{c})^2 - (k_x)^2}} (Q_2^{0,0,0,1})^* Q_2^{0,0,0,1}}{\sum_{m,n} \left(\frac{(k_z^{m,n})^2 + (k_x + \frac{2m\pi}{d})^2}{k_z^{m,n}} \right) (Q_2^{m,n,0,1})^* Q_2^{m,n,0,1}}. \quad (4.10)$$

4.4 Results

Figure 4.8 compares numerical results using the modal matching method (including the first three diffracted orders) with the HFSSTM solution for the transmission through a hole array with pitch (d) of 10 mm and hole side (a) of 3 mm illuminated at normal incidence where the incident field vector is polarised along the hole side. There is very close agreement with the results from HFSSTM, with the modal matching transmission values within 0.4% of those produced by HFSSTM, verifying the validity of the model matching method.

At a frequency of ≈ 29.5 GHz, just below the onset of diffraction at 30 GHz, a peak of complete transmission is observed despite the system being a well-connected structure with a metal filling fraction of 91%; i.e., a structure that perhaps would conventionally be assumed to be a low pass FSS (purely reflecting at microwave frequencies). However, this response is expected as hole array resonances have been well documented as discussed earlier [85, 88, 89, 138]. Correspondingly, the complementary structure of metal patches (structure A*) exhibits enhanced reflection on resonance (not illustrated) despite very low metal occupancy.

Figure 4.9 illustrates the use of Babinet's Principle with this method. Babinet's Principle (section 4.2.2) has been applied to the transmission results from the hole array to produce the transmission results for the complementary patch array. These are then

4. The Microwave Response of Square Arrays of Square Elements

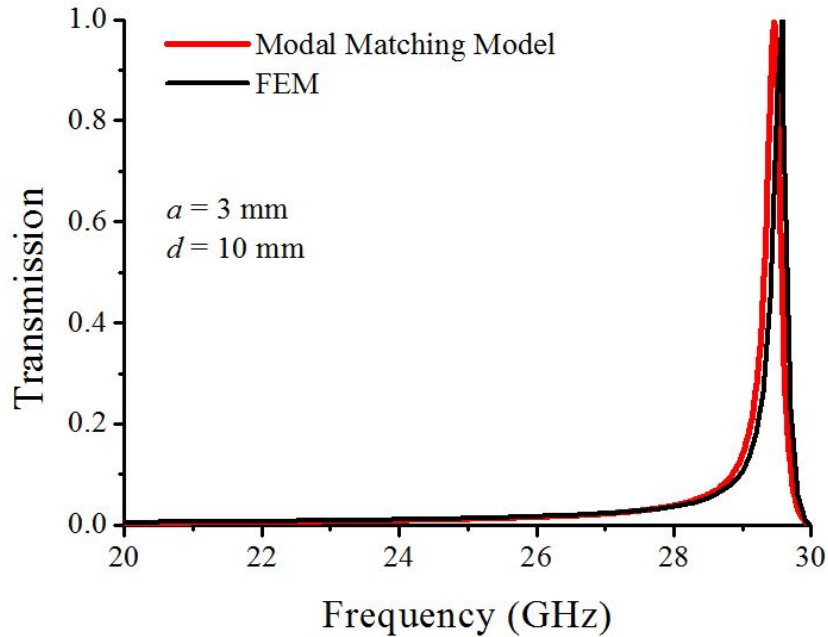


Figure 4.8: Comparison between the modal matching model with up to and including the third family of evanescent orders in the calculation, and the HFSSTM solution for structure A (figure 4.7) with $d = 10 \text{ mm}$, $a = 3 \text{ mm}$ and $h = 0 \text{ mm}$ at normal incidence [137]. The diffraction edge is at 30 GHz.

compared to the full solution produced by HFSSTM. The agreement is excellent and thus gives confidence in the use of this analytical technique which is far less computationally intensive than full solver, numerical methods. Furthermore, as previously discussed in chapter 3, the primary advantage of this technique is that it allows further investigation of the form of the fields and the EM response observed resulting in an improved physical understanding of the response.

The modal matching method provides a complete solution by allowing any number of diffracted (propagating or evanescent) and waveguide modes to be included in the calculation. As discussed in section 3.2.2.2, the first order waveguide mode only is required to represent the behaviour accurately and as we are interested in the frequency range below the diffraction edge, there are no propagating diffracted orders. However, the number of evanescent diffracted orders included in the summation is important: too few and the near fields are not accurately represented resulting in incorrect EM responses; too many and the computational resources and run-time are adversely affected. Figure 4.10 illustrates the effect on the transmission response when the number of included evanescent diffracted orders is increased. For this simple structure, three

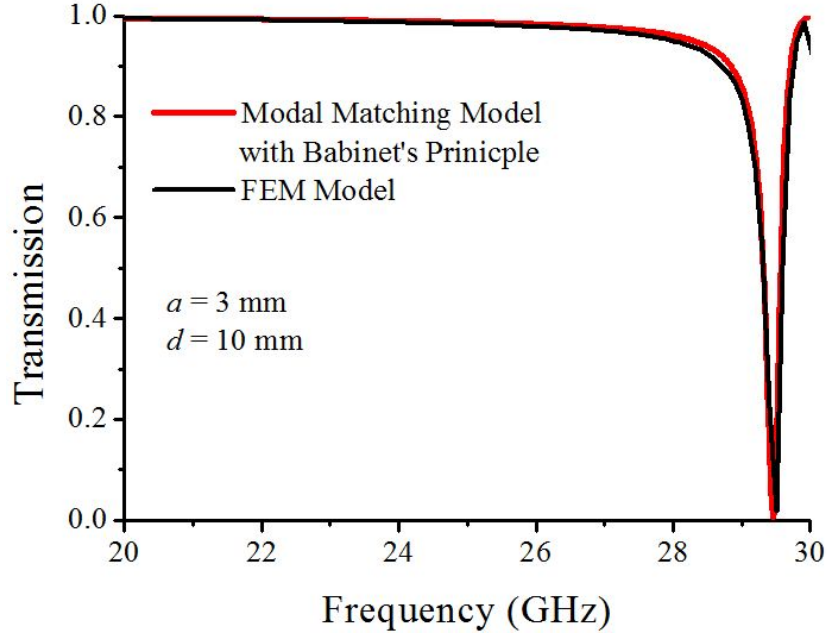


Figure 4.9: Comparison between the modal matching model data after application of Babinet's Principle and the HFSSTM solution for structure A^* (figure 4.7) at normal incidence with $d = 10$ mm, $a = 3$ mm and $h = 0$ mm [137].

orders are sufficient to represent the transmission response accurately. Whilst additional orders can be included in the calculation, there is no noticeable change in the transmission line plot with these higher orders included.

4.4.1 Geometric Parameter Variations

The three main structure parameters that can be changed are pitch d , length of hole side a and the mesh thickness h . So far the results have pertained to 2D meshes ($h = 0$) as Babinet's Principle is only applicable for infinitely thin screens. However, in section 4.4.1.2 the effect on transmission and the application of Babinet's Principle for meshes of varying finite thickness is explored. Section 4.4.1.1 looks at the role that the pitch and the size of the element plays in the EM response of 2D meshes.

4.4.1.1 Variations in Pitch and Element Size

Figure 4.11(a) shows the transmission response for a hole array (structure A) for varying hole sizes and pitch of 10 mm. In addition, the transmission as predicted by Bethe (section 2.2.2) is also plotted to provide an indication of the degree of transmission

4. The Microwave Response of Square Arrays of Square Elements

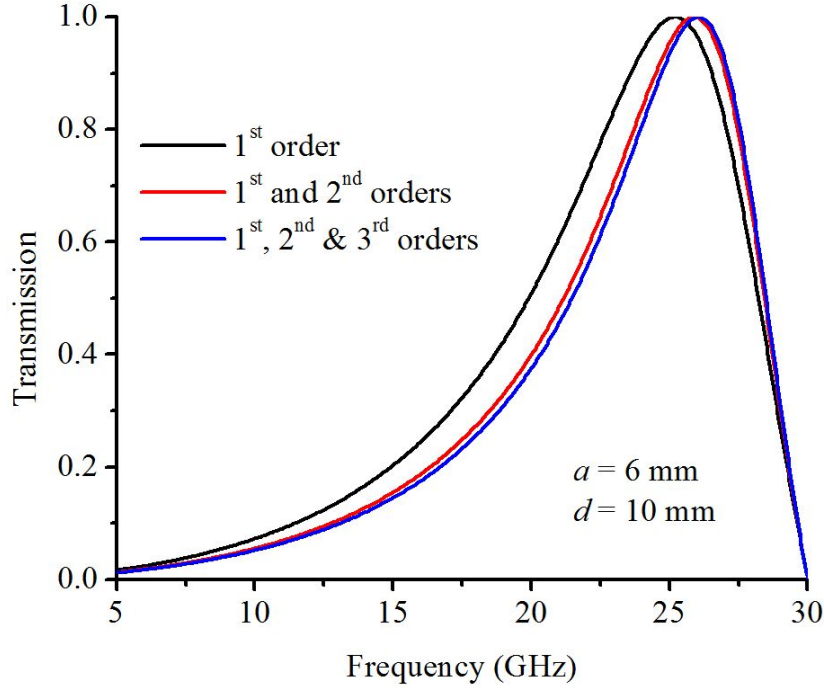
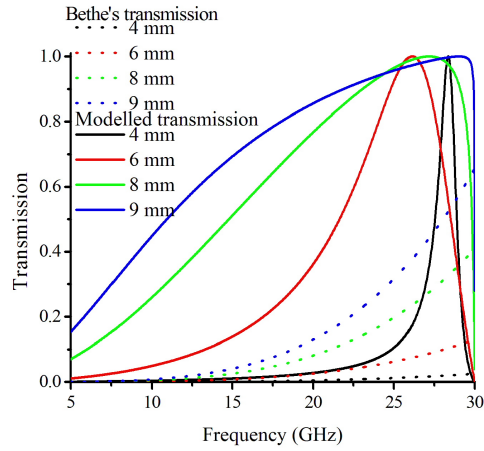


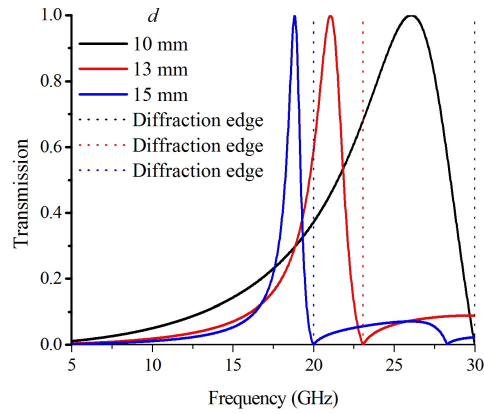
Figure 4.10: *The varying transmission response for structure A (figure 4.7) with $d = 10$ mm, $a = 6$ mm and $h = 0$ mm at normal incidence as a result of increasing the number of evanescent diffracted orders included in the calculation.*

enhancement around the resonance. The predicted transmission by Bethe is the non-resonant contribution, but there is a resonant contribution resulting from the evanescent diffraction allowing resonant interactions between adjacent holes (or patches). In addition, there is a third contribution arising from interference between the two channels. There is a clear transmission enhancement for all hole sizes and as the hole size increases the resonance broadens. As the transmission is enhanced, there is clearly more than one transmission channel present in the system. These three transmission contributions comprise the observed Fano-like [139] transmission response. As well as the broadening of the resonance, as the hole (patch) side length increases, the resonant frequency decreases due to the relative significance of the contribution from each transmission channel on the overall transmission response. For small hole (patch) sizes, the non-resonant transmission channel has little significance and the majority of the transmission response is due to the resonant channel. This results in a characteristic sharp resonant feature close to the onset of diffraction. For large holes (patches) however, this is no longer the case. The non-resonant transmission channel forms a much larger part of the overall transmission response and this, combined with the EM coupling

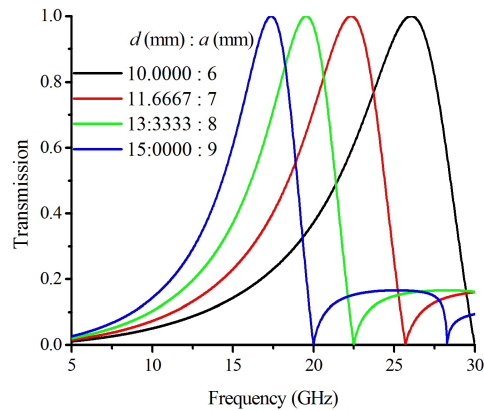
4. The Microwave Response of Square Arrays of Square Elements



(a)



(b)



(c)

Figure 4.11: Normal incidence transmission for a 2D hole array (structure A) with: (a) pitch $d = 10$ mm and varying hole sizes, including Bethe's predicted transmission of $(a/\lambda)^4$ for the corresponding hole sizes; (b) square holes with side length $a = 6$ mm with varying array pitch; (c) pitch to hole side length ratio, $d:a$ of 5:3.

4. The Microwave Response of Square Arrays of Square Elements

of the resonant surface-like mode to radiative modes leads to a substantially broader resonance at lower frequencies. This observation echoes that of Bravo-Abad *et al.* in 2007 [88].

Figure 4.11(b) illustrates the numerical results for the modal matching model at normal incidence for a hole array with squares of side length 6 mm for varying array pitch. As the pitch increases, the diffraction edge moves to lower frequencies according to the relation c/λ_g where c is the speed of light. The resonant transmission peak is therefore pushed up closer to the diffraction edge. In figure 4.11(c) the transmission response of four different arrays, all with the same pitch to hole side length ratio are shown. The response for each mesh is almost identical albeit shifted down in frequency due to the changes in the onset of diffraction. The fact that the resonance always appears below the onset of diffraction is evidence of the diffractive excitation of the mode. It implies a surface wave nature of the resonance as coupling is only achieved via evanescent fields associated with diffraction. It is apparent that the periodicity is a far more dominant parameter than the element size with regards to the resonant frequency. In addition, it is evident that the Q factor (or width) of the resonance is also affected by the period of the array; the closer the diffraction edge to the resonant frequency, the higher the Q factor of the mode, i.e., the sharper the mode.

4.4.1.2 Variations in Mesh Thickness

Up until this point, all the structures have been infinitely thin to enable the application of Babinet's Principle in calculating the EM response of the patch array (structure A*). Although for finite thickness systems Babinet's Principle is no longer exact, it can still be used to guide our understanding [140]. The transmissivity of hole arrays of increasing thickness are shown in figure 4.12.

The resonant frequency occurs at ≈ 26 GHz for all thicknesses. As the thickness of the cavity increases, it is able to support propagating waveguide modes, as in the 1 mm thick array. Figure 4.13 compares the HFSSTM solution for the patch array with various finite thicknesses with the modal matching solution for the finite thickness holes after Babinet's Principle has been applied. Whilst it is clear that Babinet's Principle is not exact for finite thickness systems, the complementary nature of the response is apparent, as suggested by Rockstuhl *et al.* [140].

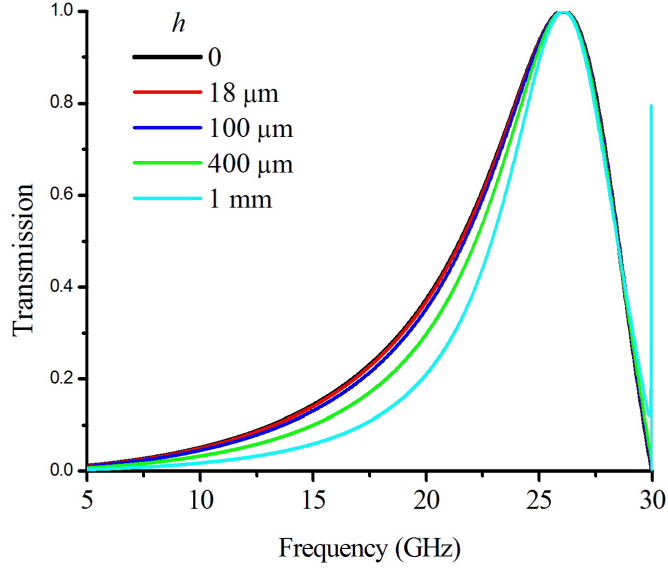
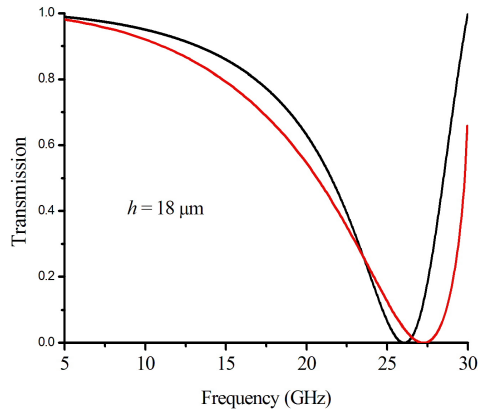


Figure 4.12: *The transmission response for a hole array with $d = 10$ mm, $a = 6$ mm at normal incidence for increasing values of mesh thickness, h .*

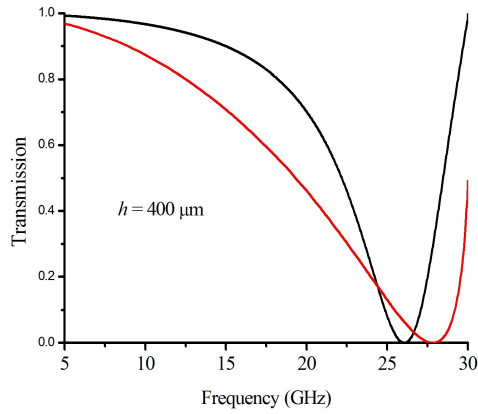
4.4.2 Dispersion Plots

As described by Babinet's Principle a complementary relationship exists between the transmission response of a 2D PEC screen and its inverse. The analytical data shown in figure 4.14 indicates that for different polarisations in each array, the incident radiation preferentially scatters more strongly from one grating. In the patch array, for p -polarisation the mode closely follows the in-plane $(0, 1)$ and $(0, -1)$ diffracted light lines whilst for s -polarisation, it follows the $(-1, 0)$ and $(1, 0)$ light lines out of the plane. The complementary nature is clearly evident in the non-diffracting region below the light line of figure 4.14. Figure 4.14 illustrates the zeroth order transmission and therefore after the onset of diffraction the dispersion plots do not include any of the propagating diffracted orders and hence no relationship can be inferred above the diffracted light lines.

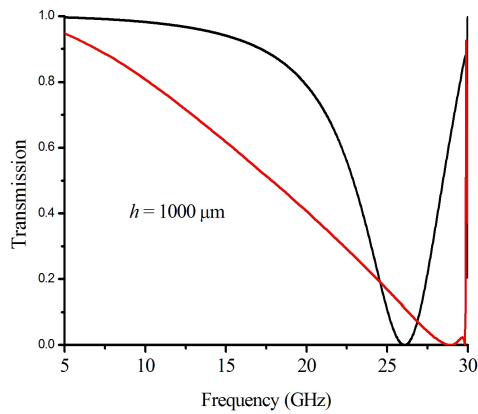
4. The Microwave Response of Square Arrays of Square Elements



(a)



(b)



(c)

Figure 4.13: Comparison for normal incidence transmission between the modal matching transmission data (black line) for the finite depth hole arrays after application of Babinet's Principle with the HFSSTM solution (red line) for finite depth patch arrays for depths of (a) $18 \mu\text{m}$, (b) $400 \mu\text{m}$ and (c) $1000 \mu\text{m}$.

4. The Microwave Response of Square Arrays of Square Elements

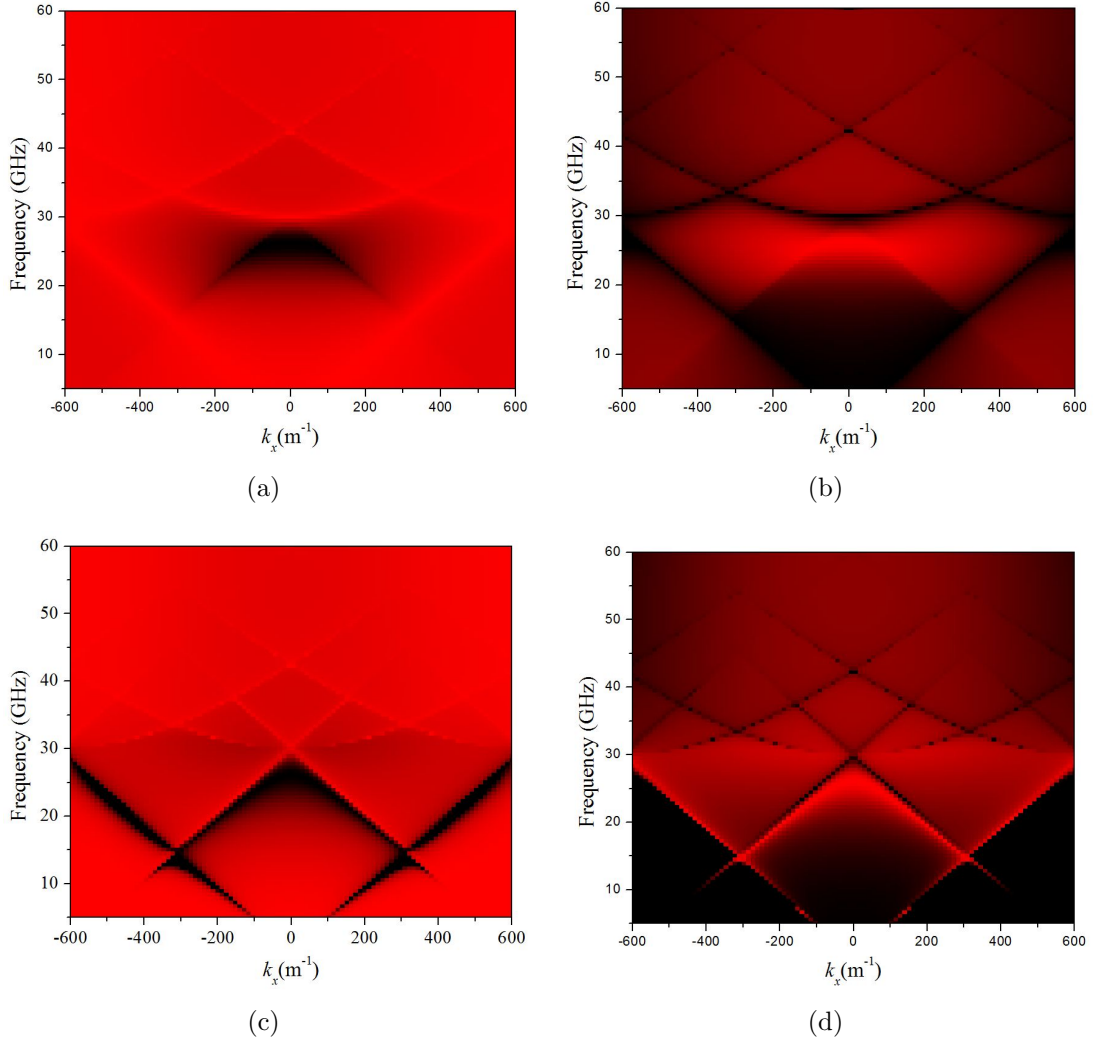


Figure 4.14: *Dispersion plots using the modal matching model for the transmission for; (a) s-polarisation for structure A, (b) p-polarisation for structure A*, (c) p-polarisation for structure A, (d) s-polarisation for structure A* (figure 4.7) with $d = 10$ mm, $a = 6$ mm and $h = 0$ mm [137]. Red signifies a transmission value of 0 and black a transmission value of 1.*

4.5 Discussion

4.5.1 Mathematical Analysis

Analysis of the resulting equations for the transmission and reflection coefficients shows the dominance of scattering from a particular grating vector, as also reported by Bravo-Abad *et al* [90]. However, further analysis is needed to understand the reason for this dominance. Examination of equation 4.10 shows that the transmission reaches a maximum when equation 4.11 is a minimum.

$$L = \frac{(k_z^{m,n})^2 + \left(k_x + \frac{2m\pi}{d}\right)^2}{k_z^{m,n}} \quad (4.11)$$

By substituting the explicit expression for $k_z^{m,n}$ and differentiating, the turning points of equation 4.11 can be determined. The differential of equation 4.11 with respect to ω results in

$$\frac{\partial L}{\partial \omega} = \frac{w \left(1 - \frac{\left(k_x + \frac{2m\pi}{d}\right)^2}{\frac{\omega^2}{c^2} - \frac{4n^2\pi^2}{d^2} - \left(k_x + \frac{2m\pi}{d}\right)^2} \right)}{c^2 \sqrt{\frac{\omega^2}{c^2} - \frac{4n^2\pi^2}{d^2} - \left(k_x + \frac{2m\pi}{d}\right)^2}}. \quad (4.12)$$

The solution of $\partial L/\partial \omega = 0$ provides the condition that equation 4.11 is a minimum when

$$\frac{\omega}{c} = \sqrt{2k_x^2 + \frac{8m\pi}{d} \left(k_x + \frac{m\pi}{d}\right) + \frac{4n^2\pi^2}{d^2}}. \quad (4.13)$$

It is clear from examination of equation 4.13 that this condition occurs for $[m, 0]$ orders and $[0, n]$ orders when

$$\frac{\omega}{c} = \sqrt{2} \left(k_x + \frac{2m\pi}{d}\right) \quad (4.14)$$

and

$$\frac{\omega}{c} = \sqrt{2k_x^2 + \frac{4n^2\pi^2}{d^2}} \quad (4.15)$$

respectively. Further investigation reveals that for p -polarised incident radiation, the $[m, 0]$ orders dominate the effect, as predicted, due to the associated overlap integrals, $Q^{m,n,u,v}$, also being large under this condition; whilst for s -polarised incident radiation, the $Q^{m,n,u,v}$ terms are large for the $[0, n]$ orders.

The electric field on the surface of the mesh (i.e., $h = 0$) in region III (equation 3.5)

4. The Microwave Response of Square Arrays of Square Elements

is described by

$$E^{III} = \sum_{m,n} t^{m,n} \exp \left[i \left(k_x + \frac{2m\pi}{d} \right) x \right] \exp \left[i \left(\frac{2n\pi}{d} \right) y \right]. \quad (4.16)$$

At the resonant condition for p -polarised incident radiation, this \vec{E} field is dominated by the $t^{m,0} \exp \left[i \left(k_x + \frac{2m\pi}{d} \right) x \right]$ term. This term describes a surface plane wave component propagating in the x -direction with wavevector $\left(k_x + \frac{2m\pi}{d} \right)$. Using the same approach, it can be shown that for incident s -polarisation, the dominant term is given by $t^{0,n} \exp \left[i \left(\frac{2n\pi}{d} \right) y \right]$ describing a surface plane wave component propagating in the y -direction with wavevector $\left(\frac{2n\pi}{d} \right)$.

Conversely, for the patch array (structure A*), Babinet's Principle predicts that it is the p -polarisation that will result in a dominant surface plane wave component propagating in the y -direction and the s -polarisation is required to produce a dominant component propagating in the x -direction.

4.5.2 Physical meaning

These field components can be interpreted by considering an incident electric field upon a patch array (structure A*), that induces a dipolar response in the patches. Each of these dipoles radiate and the strong radiated fields are in a plane orthogonal to the orientation of the dipoles. This dipolar interpretation is well known and has been used to describe the system in the small-patch limit [91, 141]. This leads to regions of enhanced electric fields in the spaces between the patches orthogonal to the polarisation direction. The resultant large modulation in electric field reflects the fact that scattering from the grating vector perpendicular to the polarisation dominates the response (figure 4.15(a)). Figures 4.15(b) and 4.15(c) show the electric field enhancement for the patch array (figure 4.7), produced using the modal matching model. Close to the film, there is strong modulation in both directions (figure 4.15(b)), however, exploring the fields further away shows that the scattering from the grating vector parallel to the incident field decays very quickly with distance, and the scattering from the grating vector perpendicular to the incident dominates (figure 4.15(c)).

Dipoles are also induced in the hole array upon application of an electric field; however, these are not discrete dipoles as this is a connected structure and therefore supports real surface currents. These surface currents run parallel to the \vec{E} field, but due to the presence of the holes, there is enhancement of the surface current density at

4. The Microwave Response of Square Arrays of Square Elements

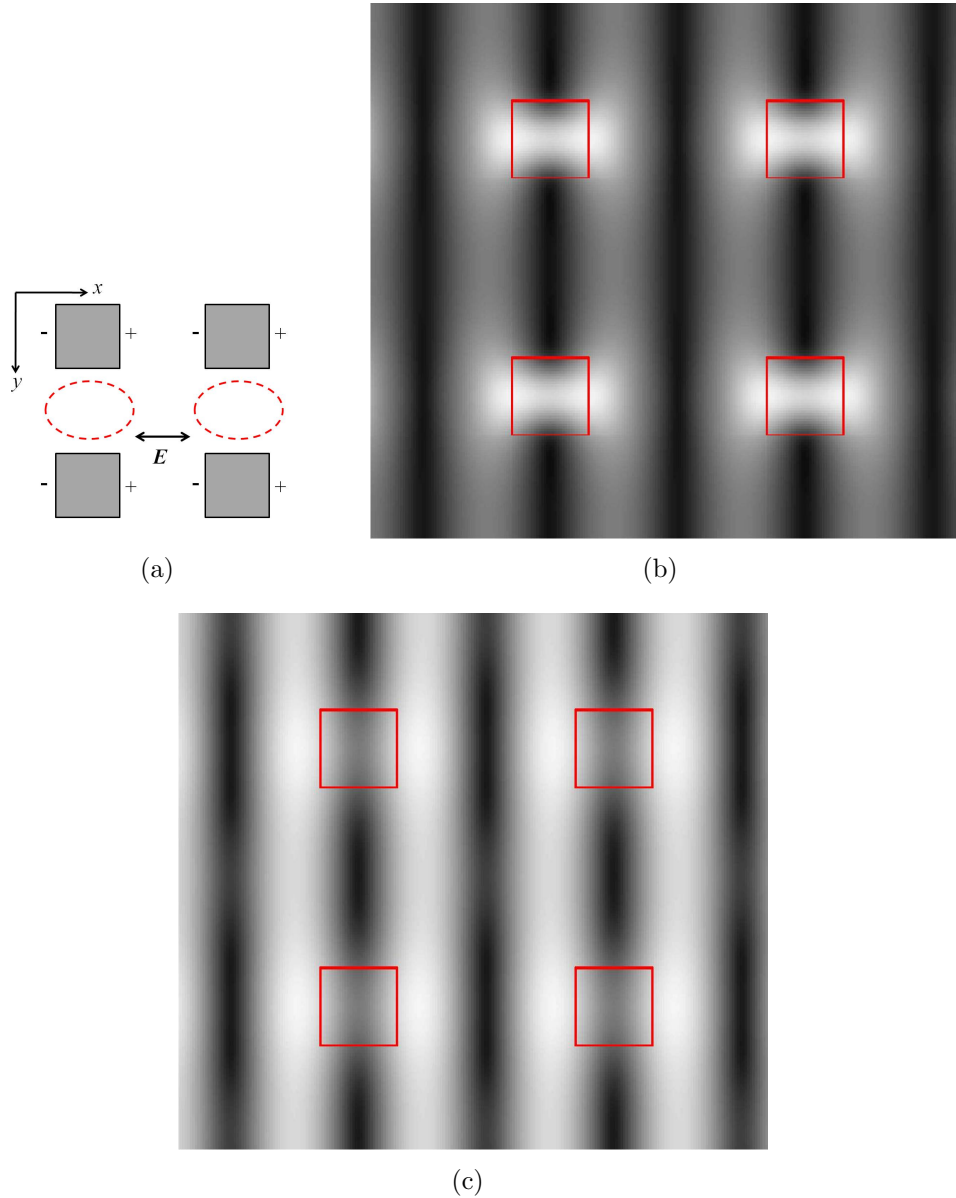


Figure 4.15: (a) Schematic of dipole array description showing the regions of enhanced \vec{E} field, indicated by red dashed line for a square array of square PEC patches; \vec{E} field plots produced from the modal matching model for a patch array with pitch of 10 mm and patch side of length 3 mm showing the \vec{E} field enhancement with the incident \vec{E} field polarised along the x -axis for (b) 0.5 mm below the structure and (c) 4 mm below the structure showing the dominance of the scattering from the $(0, k_g)$ grating. Black denotes low transmission and white high transmission.

the narrowest point (between the holes). This results in regions of enhanced magnetic (\vec{H}) fields orthogonal to the surface current direction. Similarly to the patch array, it is these regions of enhanced field and the resultant field modulation that leads to the scattering from the grating vector *parallel* to the polarisation dominating the response (figure 4.16).

4.6 Rotated holes and patches

The complementary relationship between the observed enhanced responses of hole and patch arrays raises the interesting question as to how the response will behave as the metal fill fraction of a patch array increases to the point at which the system becomes electrically connected. Consider a square array of square holes in a sheet of PEC rotated by 45° about their centre (structure B) and its inverse (structure B*) as illustrated in figure 4.17. This somewhat unconventional geometry results in electrical continuity being established for metal fill fractions of 50% and above for both structure B and B*. This is markedly different from the conventional square array, where for structure A electrical connectivity does not terminate until 0% metal fill fraction and structure A* where connectivity is not established until 100% metal fill fraction. Whilst the response of films as a function of fill fractions has been investigated before [88], these investigations tend to be on either electrically connected or disconnected systems such as structure A and A*. The self-similarity that results for the arrays of rotated elements (structures B and B*) allows the microwave response of both systems for the entire range of filling fractions to be predicted by only considering filling fractions between 0% and 50% for one of the structures and employing Babinet's Principle to predict the response of the complementary structure.

4.6.1 Method

The modal matching method is now applied to analyse the response of structure B. The general method follows the same process as detailed in section 4.3, however the equations need to be altered to account for the geometry changes in the unit cell. Although the electric fields in regions I and III can still be described by a 2D Fourier-Floquet expansion of the diffracted orders of the form described in equations 3.3 - 3.6,

4. The Microwave Response of Square Arrays of Square Elements

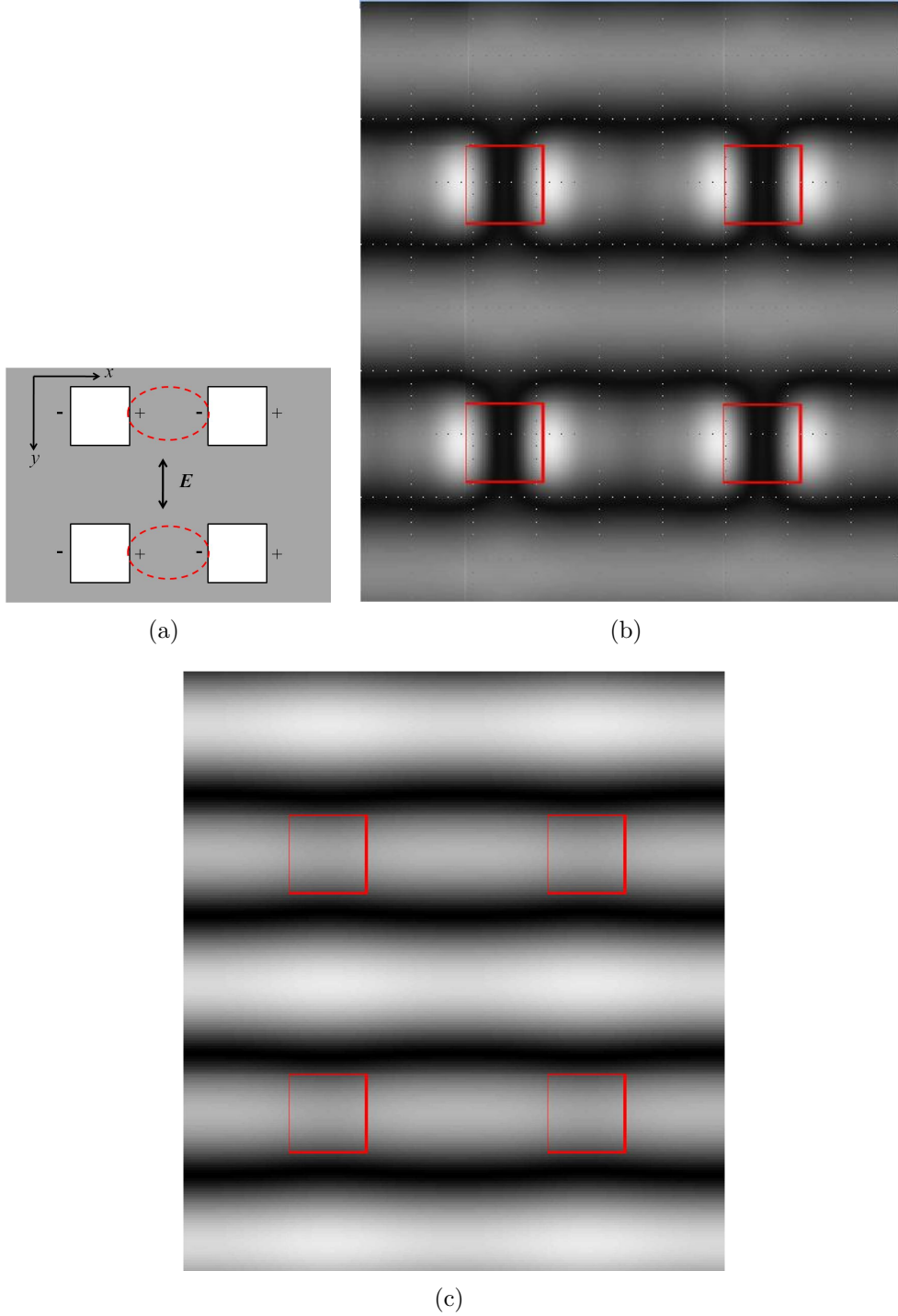


Figure 4.16: (a) Schematic of surface current description showing the regions of enhanced \vec{H} field, indicated by red dashed line for a square array of square holes in a PEC sheet; \vec{H} field plots produced from the modal matching model for a hole array with pitch of 10 mm and hole side of length 3 mm showing the \vec{H} field enhancement with the incident \vec{E} field polarised along the y-axis for (b) 0.5 mm below the structure and (c) 4 mm below the structure showing the dominance of the scattering from the $(k_g, 0)$ grating. Black denotes low transmission and white high transmission.

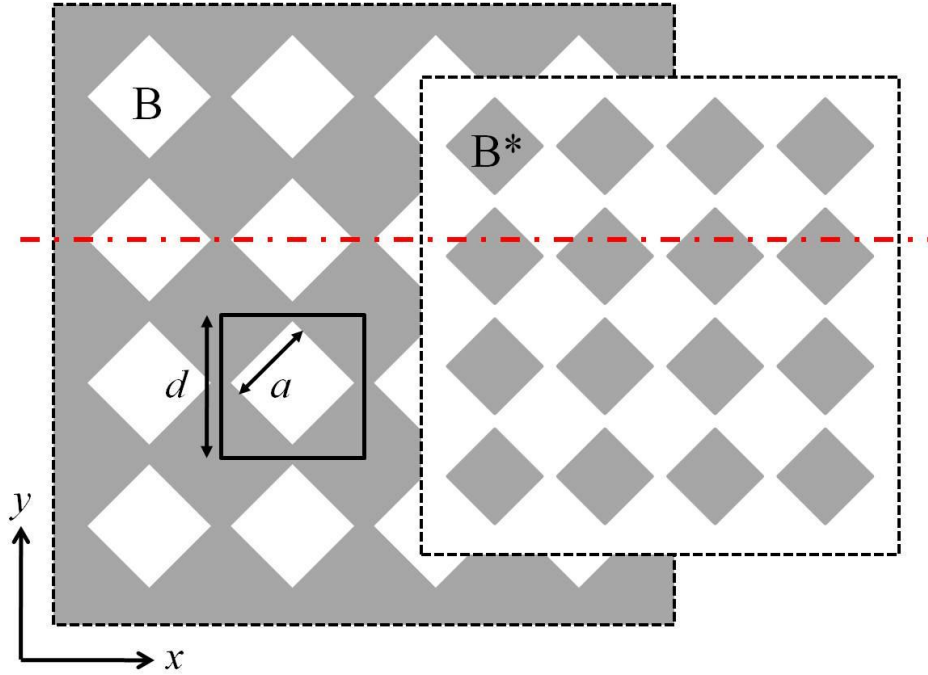


Figure 4.17: *Schematic of the modified structure of a square array of square holes rotated by 45° with respect to the coordinate system in a PEC sheet and its complementary system of a square array of rotated square PEC patches structures B and B^* respectively (reproduced from [137])*

$\Psi_1^{m,n}(x, y)$ now takes the form

$$\Psi_1^{m,n}(x, y) = \exp \left[i \frac{2m\pi}{d} \left(\frac{x+y}{\sqrt{2}} \right) \right] \exp (ik_x x) \exp \left[i \frac{2n\pi}{d} \left(\frac{y-x}{\sqrt{2}} \right) \right] \exp (ik_y y). \quad (4.17)$$

where all symbols have the same meaning as defined before. The equations describing the waveguide modes are unchanged; however, care must be taken when applying the orthogonality and boundary conditions to ensure that the boundaries are defined correctly with respect to the rotated geometry of the hole.

4.6.2 Results and Discussion

As for the regular square array, both the rotated hole and the patch arrays exhibit a resonant feature close to the onset of diffraction due to the hybridisation of the array resonance of the mesh with the dipolar mode of the element. Due to the rotated geometry, structures with a metal fill fraction of $M\%$ are the exact inverse of those

4. The Microwave Response of Square Arrays of Square Elements

with a metal fill fraction of $(100 - M\%)$. Assuming that these meshes are infinitely thin, Babinet's Principle can be applied and the transmissivity (T_1) of one mesh will be the complement of the other mesh, $(1 - T_1 = T_2)$.

Considering the square array of PEC rotated patches (structure B*), for low frequencies a 'step change' from high to low transmissivity occurs when electrical continuity is established (for structure B* this is at 50% metal occupancy). At DC this change would be a perfect step function, however as the frequency is increased this step change is expected to be 'softened'. This 'softening' is due to the restraints on electron movements caused by the finite frequency of the incident radiation. For metal occupancy of greater than 50%, currents are able to propagate throughout the connected metal. The 13 GHz data of figure 4.18 illustrates this 'softened' response.

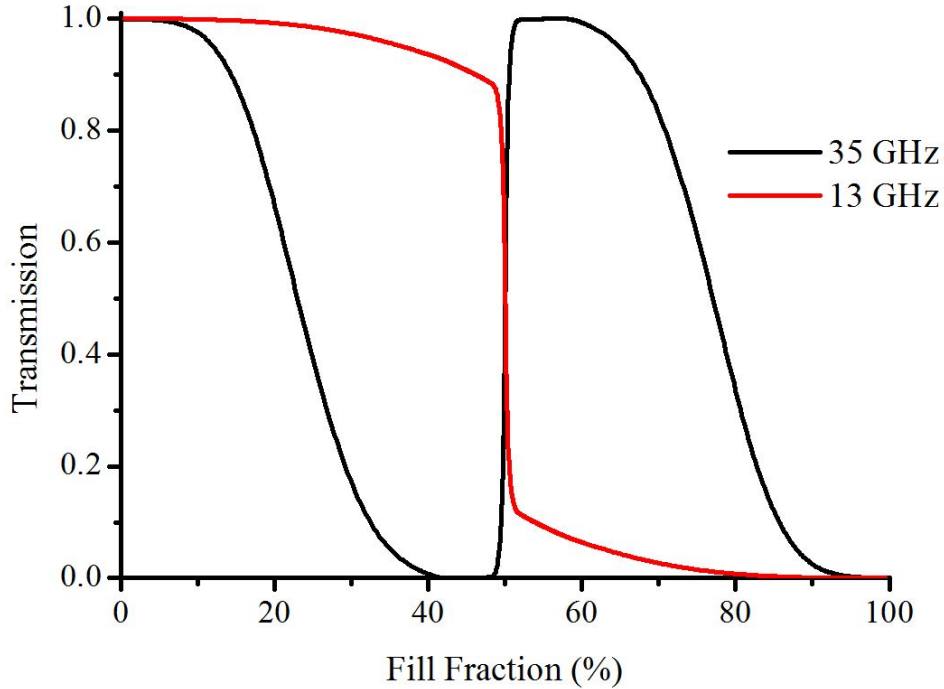


Figure 4.18: *Transmission through a square array of rotated square holes in a PEC sheet with a pitch of 7 mm at normal incidence as a function of metal filling fraction for 13 and 35 GHz (reproduced from [137])*

The closer the incident wavelength is to the pitch of the grating, λ_g , the greater the perturbation due to the resonance. As the frequency becomes more comparable to the onset of diffraction, the strength of the evanescent diffraction is such that the resulting resonance perturbs the response so strongly that the step change is completely reversed

4. The Microwave Response of Square Arrays of Square Elements

as shown by the 35 GHz data of figure 4.18. As the frequency is increased for a particular metal occupancy, intuition would imply that the transmission would decrease due to the inability of the electrons to respond to the increased frequency. However, figure 4.18 illustrates that the structure actually reaches 100% transmission *past* the point of electrical connectivity due to the strong resonance of the structure. It is also worth noting that both transmission curves illustrated in figure 4.18 have inversion symmetry about the point of 50% metal fill fraction. This is due to the complementary nature between the two types of meshes. This extraordinary result has also been observed experimentally [142].

4.7 Summary

In conclusion, using a modal matching method, a complete analytical solution for the reflectance and transmission from a thin PEC-dielectric film has been presented, demonstrating the possibility of enhanced reflectance from low metal occupancy structures and enhanced transmission from high metal occupancy structures. The original film explored comprised a square array of square elements orientated parallel to the axes of the coordinate system. The method allows for fast calculations and its flexibility means that successively higher evanescent diffracted and waveguide orders can be included separately, allowing for detailed mathematical analysis to be undertaken to confirm the origin of observed features. The response to EM radiation of these arrays is due to a combination of resonant and non-resonant transmission channels. The resonant channel results from the near-field interaction of array elements mediated by the evanescent diffraction associated with the array geometry. Babinet's Principle has been derived and employed, and as predicted, the response of each structure and its inverse has been shown to have a complementary relationship. Exploration of the analytical expressions obtained for the transmission through each structure explains the origin of the observed resonances and demonstrates their complementary nature. For different polarisations in each array, the incident radiation preferentially scatters more strongly from one grating than the other.

To further explore the transmission response for systems with and without electrical connectivity, a square array of rotated square elements was investigated. The importance of the role of the evanescent diffraction has been illustrated, showing that it can perturb the response to such an extent that the expected step change in transmission at electrical connectivity can be completely reversed. The modal matching method has

4. The Microwave Response of Square Arrays of Square Elements

been used to explore one of the most simple systems, a square array of square elements. The analytical nature of the solution has allowed mathematical verification of the origin of the transmission response to be extracted resulting in an improved understanding of the physics underlying the phenomenon.

Chapter 5

The Aspect Ratio Dependence of the Microwave Response of Hole Arrays

5.1 Introduction

The previous chapter presented an analytical solution for the reflectance and transmission through a thin PEC-dielectric film. The structure consisted of a square array of square elements providing four-fold symmetry in both the array and the geometry of the elements. This chapter extends that initial investigation by exploring the dependence of the EM response on the aspect ratio of the elements and the symmetry of the array. This creates an additional tuneability of the structure by independently altering the EM response from each orthogonal axis. It will be shown that the resonant frequency of the array is dictated by both the fundamental resonance of an individual element and the interaction of the evanescent diffractive fields with this elemental mode.

Following the seminal work by Ebbesen *et al* [2], the resurgence of interest in the EM response of periodic media, amongst other things, investigated the effect the hole shape had on the observed response [143–152]. In 2007, Mary *et al* [95] investigated the interaction between the localised hole resonance of a rectangular aperture with the excitation of the SPPs that facilitate extraordinary transmission in an array of holes in a real metal at optical frequencies. They reported that the array resonance was a hybrid resonance and it was not possible to separate the two contributions. This agreed with the earlier work of van der Molen *et al* [147], and has also been reported by Zhao

5. The Aspect Ratio Dependence of the Microwave Response of Hole Arrays

et al in their numerical modelling paper investigating the polarisation dependence of the EM response of hole arrays [153].

Periodicity plays an important role in the EM response of these structures due to the possibility of incident radiation scattering from both orthogonal gratings. Rectangular arrays provide an additional opportunity to ‘tune’ the response of the bigrating by independently altering the periodicity along the orthogonal axes [154].

Section 4.4 established the complementary nature of the response of hole and patch arrays and thus, as the complementary array’s response can be trivially deduced, throughout this chapter the described arrays only refer to arrays of holes in a PEC sheet. In the next section (section 5.2), the adaptations made to the modal matching formulation are detailed for each specific geometry. Following this, section 5.3 analyses the results for each investigated geometry separately including a numerical comparison using HFSSTM as verification of the accuracy of the model. The first of these geometries (section 5.3.1) is a regular square array of rectangular holes in a sheet of PEC; the second geometry (section 5.3.2) comprises a rectangular array, i.e. differing orthogonal pitches, of square holes in a sheet of PEC; and lastly, section 5.3.3 discusses transmission results for a rectangular array of rectangular holes. The conclusions of these explorations are summarised in section 5.4.

5.2 Method

In all investigated systems the modelling method is unchanged from that detailed in section 3.2.2. What has changed however, are the initial equations describing the fields in each region. Whilst they are of the same form as the square array of square holes, the parameters need to be altered to reflect the change in geometry.

5.2.1 Square Array of Rectangular Holes

The investigated system is illustrated in figure 5.1 and consists of a sheet of PEC with a square array of rectangular holes. For simplicity, only normal incidence is considered and the incident \vec{E} field is parallel to the x -axis. There is no change in the symmetry of the array, only in the symmetry of the hole, therefore it is only the form of the fields (equations 3.9 and 3.10) within the holes that need amending.

$$E_x^{II} = \sum_{u,v} B_x^{u,v} \Psi_2(x, y) \exp(iq_z^{u,v} z) + C_x^{u,v} \Psi_2(x, y) \exp(-iq_z^{u,v} z) \quad (5.1)$$

5. The Aspect Ratio Dependence of the Microwave Response of Hole Arrays

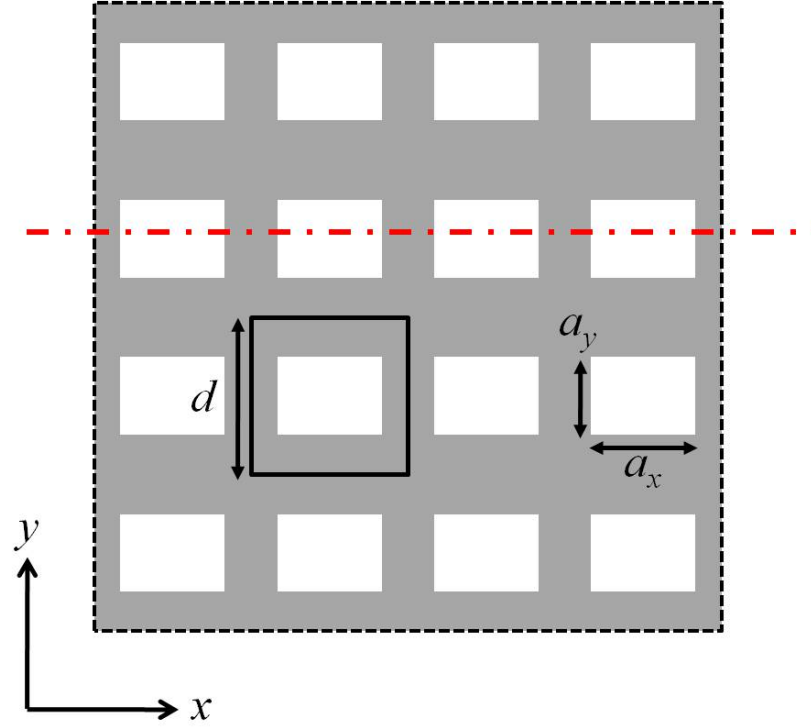


Figure 5.1: Schematic of a regular square array of rectangular holes in a PEC sheet. Grey areas denote PEC and white areas vacuum. The array has pitch d and rectangular holes of side length a_x and a_y parallel to the axes of the coordinate system. The black solid line indicates the unit cell and the red dashed line the xz -plane of incidence.

and

$$E_y^{II} = \sum_{u,v} B_y^{u,v} \Psi_3(x, y) \exp(iq_z^{u,v} z) + C_y^{u,v} \Psi_3(x, y) \exp(-iq_z^{u,v} z), \quad (5.2)$$

where

$$\Psi_2(x, y) = \cos\left(\frac{u\pi x}{a_x}\right) \sin\left(\frac{v\pi y}{a_y}\right), \quad (5.3)$$

$$\Psi_3(x, y) = \sin\left(\frac{u\pi x}{a_x}\right) \cos\left(\frac{v\pi y}{a_y}\right) \quad (5.4)$$

and

$$q_z^{u,v} = \sqrt{\epsilon_h \left(\frac{\omega}{c}\right)^2 - \left(\frac{u\pi}{a_x}\right)^2 - \left(\frac{v\pi}{a_y}\right)^2}. \quad (5.5)$$

As before, the order of the waveguide modes are denoted by u and v with the associated propagation constant given by $q_z^{u,v}$, the hole side length parallel to the x -axis by a_x , the

5. The Aspect Ratio Dependence of the Microwave Response of Hole Arrays

hole side length parallel to the y -axis by a_y and the permittivity within the cavity by ϵ_h . The field amplitudes are denoted by $B_i^{u,v}$ and $C_i^{u,v}$.

5.2.2 Rectangular Array of Square Holes

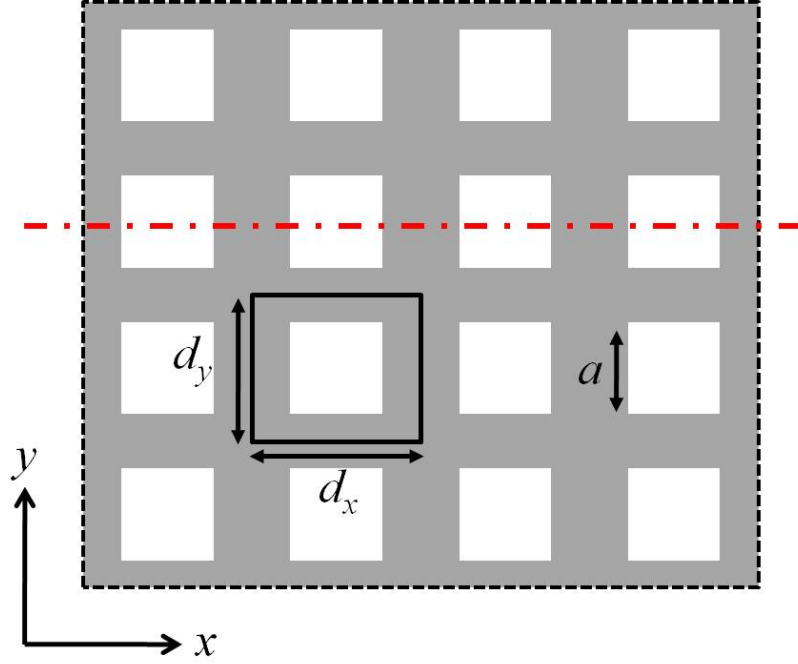


Figure 5.2: Schematic of a regular rectangular array of square holes in a PEC sheet. Grey areas denote PEC and white areas vacuum. The pitch of the array is d_x and d_y parallel to the axes of the coordinate system and square holes of side length a . The black solid line indicates the unit cell and the red dashed line the xz -plane of incidence.

The investigated system is illustrated in figure 5.2 and consists of a sheet of PEC with a rectangular array of square holes. For simplicity, only normal incidence is considered and the incident \vec{E} field is parallel to the x -axis. In this case, it is the symmetry of the array that is broken, whilst the hole still has four-fold symmetry and therefore the form of the fields above and below the mesh (equations 3.3 - 3.6) needs to be amended.

$$E_x^I = E_x \exp(ik_x x) \exp(ik_z^{0,0} z) + \sum_{m,n} A_x^{m,n} \Psi_1^{m,n}(x, y) \exp(-ik_z^{m,n} z), \quad (5.6)$$

5. The Aspect Ratio Dependence of the Microwave Response of Hole Arrays

$$E_y^I = E_y \exp(ik_x x) \exp(ik_z^{0,0} z) + \sum_{m,n} A_y^{m,n} \Psi_1^{m,n}(x, y) \exp(-ik_z^{m,n} z), \quad (5.7)$$

$$E_x^{III} = \sum_{p,q} D_x^{p,q} \Psi_1^{p,q}(x, y) \exp(ik_z^{p,q} z), \quad (5.8)$$

and

$$E_y^{III} = \sum_{p,q} D_y^{p,q} \Psi_1^{p,q}(x, y) \exp(ik_z^{p,q} z), \quad (5.9)$$

where

$$\Psi_1^{m,n}(x, y) = \exp \left[i \left(k_x + \frac{2m\pi}{d_x} \right) x \right] \exp \left[i \left(k_y + \frac{2n\pi}{d_y} \right) y \right] \quad (5.10)$$

and

$$k_z^{m,n} = \sqrt{\left(\frac{\omega}{c} \right)^2 - \left(k_x + \frac{2m\pi}{d_x} \right)^2 - \left(k_y + \frac{2n\pi}{d_y} \right)^2}. \quad (5.11)$$

The diffracted orders in region I are denoted by m and n and region III by p and q , the wave-vector of the diffracted order by k , the period of the array by d_x and d_y parallel to the x - and y -axes respectively and the field amplitude by $A^{m,n}$, $D^{p,q}$ whilst $\Psi_1^{m,n}(x, y)$ describes the diffracted waves. For the vacuum region above the film (region I) there is an additional term for the incident field.

5.2.3 Rectangular Array of Rectangular Holes

The investigated system is illustrated in figure 5.3 and consists of a sheet of PEC with a rectangular array of rectangular holes. Again only normal incidence is considered and the incident \vec{E} field is parallel to the x -axis. In the final investigated structure, neither the array nor the holes have retained their four-fold symmetry resulting in the equations describing the fields in all three regions having to be altered to reflect the geometrical changes.

The electric fields in the vacuum regions above and below the film (regions I and III)

5. The Aspect Ratio Dependence of the Microwave Response of Hole Arrays

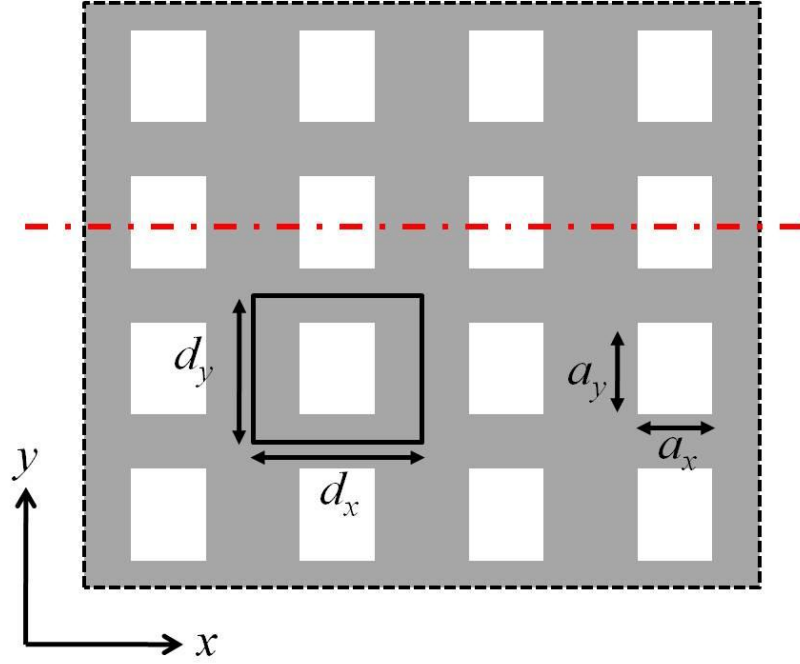


Figure 5.3: Schematic of a regular rectangular array of rectangular holes in a PEC sheet. Grey areas denote PEC and white areas vacuum. The array has pitch d_x and d_y and rectangular holes of side length a_x and a_y parallel to the axes of the coordinate system. The black solid line indicates the unit cell and the red dashed line the xz -plane of incidence.

are described by two dimensional Fourier-Floquet expansions of the diffracted orders.

$$E_x^I = E_x \exp(ik_x x) \exp(ik_z^{0,0} z) + \sum_{m,n} A_x^{m,n} \Psi_1^{m,n}(x, y) \exp(-ik_z^{m,n} z), \quad (5.12)$$

$$E_y^I = E_y \exp(ik_x x) \exp(ik_z^{0,0} z) + \sum_{m,n} A_y^{m,n} \Psi_1^{m,n}(x, y) \exp(-ik_z^{m,n} z), \quad (5.13)$$

$$E_x^{III} = \sum_{p,q} D_x^{p,q} \Psi_1^{p,q}(x, y) \exp(ik_z^{p,q} z), \quad (5.14)$$

and

$$E_y^{III} = \sum_{p,q} D_y^{p,q} \Psi_1^{p,q}(x, y) \exp(ik_z^{p,q} z), \quad (5.15)$$

5. The Aspect Ratio Dependence of the Microwave Response of Hole Arrays

where

$$\Psi_1^{m,n}(x, y) = \exp \left[i \left(k_x + \frac{2m\pi}{d_x} \right) x \right] \exp \left[i \left(k_y + \frac{2n\pi}{d_y} \right) y \right] \quad (5.16)$$

and

$$k_z^{m,n} = \sqrt{\left(\frac{\omega}{c} \right)^2 - \left(k_x + \frac{2m\pi}{d_x} \right)^2 - \left(k_y + \frac{2n\pi}{d_y} \right)^2}, \quad (5.17)$$

where all symbols have their previously defined meanings.

Within the PEC layer, the electric fields take the form of waveguide modes within the holes.

$$E_x^{II} = \sum_{u,v} B_x^{u,v} \Psi_2(x, y) \exp(iq_z^{u,v}z) + C_x^{u,v} \Psi_2(x, y) \exp(-iq_z^{u,v}z) \quad (5.18)$$

and

$$E_y^{II} = \sum_{u,v} B_y^{u,v} \Psi_3(x, y) \exp(iq_z^{u,v}z) + C_y^{u,v} \Psi_3(x, y) \exp(-iq_z^{u,v}z), \quad (5.19)$$

where

$$\Psi_2(x, y) = \cos \left(\frac{u\pi x}{a_x} \right) \sin \left(\frac{v\pi y}{a_y} \right), \quad (5.20)$$

$$\Psi_3(x, y) = \sin \left(\frac{u\pi x}{a_x} \right) \cos \left(\frac{v\pi y}{a_y} \right) \quad (5.21)$$

and

$$q_z^{u,v} = \sqrt{\epsilon_h \left(\frac{\omega}{c} \right)^2 - \left(\frac{u\pi}{a_x} \right)^2 - \left(\frac{v\pi}{a_y} \right)^2}. \quad (5.22)$$

All symbols have their previously defined meanings and the analytical solution now follows the same method as detailed in section 3.2.2.1.

5. The Aspect Ratio Dependence of the Microwave Response of Hole Arrays

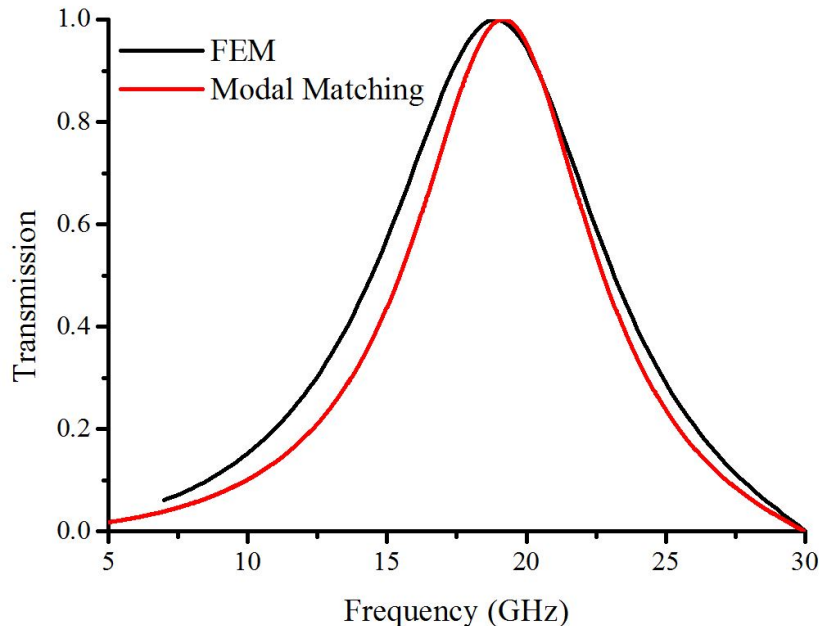


Figure 5.4: Comparison between the modal matching model and the solution derived using a finite element method model for a square array of rectangular holes in a PEC sheet at normal incidence with $d = 10$ mm, $a_x = 3$ mm and $a_y = 8$ mm.

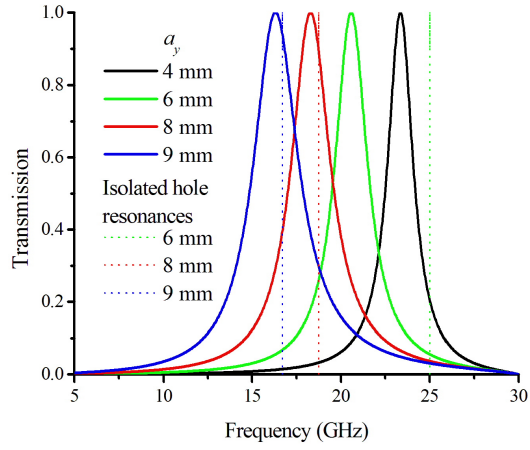
5.3 Results and Discussion

5.3.1 Square Array of Rectangular Holes

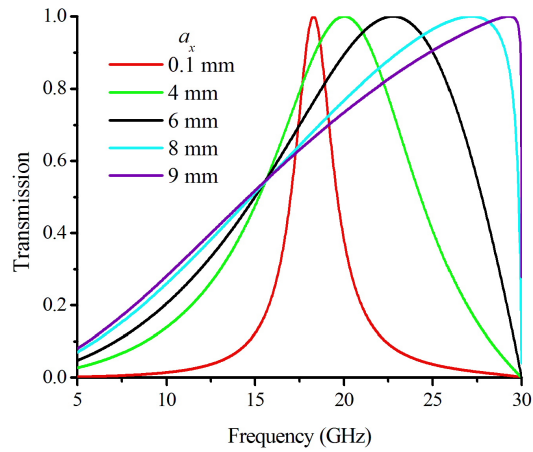
A comparison between the FEM solution and the modal matching approach for a square array of pitch 10 mm of rectangular holes of side lengths 3 mm and 8 mm parallel to the x - and y -axes respectively where the incident field is polarised parallel to the x -axis is illustrated in figure 5.4, verifying the validity of the model. The modal matching results are within 2% of those FEM model and this is due to the finite mesh resolution of the FEM model and the truncation of the Fourier sum in the modal matching model (not shown).

Figure 5.5 illustrates the EM response for a square array of rectangular holes: in figure 5.5(a), the sides of the rectangular hole parallel to the incident radiation are fixed, and the two perpendicular sides are varied in length; and vice versa in figure 5.5(b). As a_y increases in length, the frequency of the transmission resonance decreases due to the associated decrease in the resonant frequency of the fundamental waveguide mode (figure 5.5(a)). This trend was also reported for optical frequencies in 2005 by van der Molen [147]. For large values of a_y , the frequency of the transmission

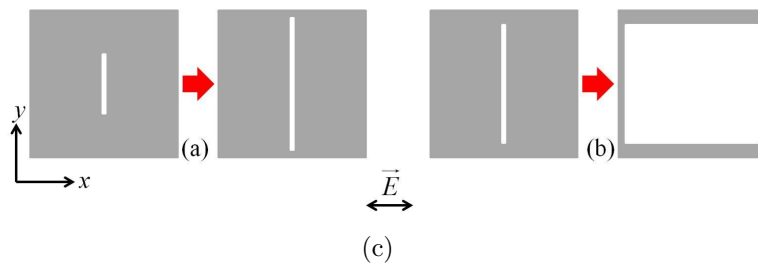
5. The Aspect Ratio Dependence of the Microwave Response of Hole Arrays



(a)



(b)



(c)

Figure 5.5: Transmission response for a square array of rectangular holes in a PEC sheet with pitch 10 mm for (a) $a_x = 0.1$ mm, (b) $a_y = 8$ mm, at normal incidence with the incident radiation polarised parallel to the x -axis, and (c) a scale schematic of the change in unit cell illustrated in graph.

5. The Aspect Ratio Dependence of the Microwave Response of Hole Arrays

resonance approaches that of the fundamental dipolar mode of the hole, and the role of evanescent diffraction becomes less significant. As the mode is quantised perpendicular to the polarisation of incident radiation, intuition may suggest that little dependence on the value of a_x would be seen. However, as figure 5.5(b) shows, this is not the case. Instead, as a_x increases in length, the modelled resonance broadens and the peak moves to higher frequencies. In addition, the resonance becomes asymmetrical as the EM response is perturbed by the evanescent diffractive fields. This behaviour is explained in the following section.

5.3.1.1 Analysis of results

The complex amplitude coefficient expression for the transmission is of the same form as for the square array of square holes (equation 4.10), however, the overlap integrals are changed due to the geometrical changes to the hole, i.e., from square to rectangular,

$$Q_2^{m,n,0,1} = \int_0^{a_y} \int_0^{a_x} \sin\left(\frac{\pi y}{a_y}\right) \exp\left[-i\left(\frac{2m\pi}{d}\right)x\right] \exp\left[-i\left(\frac{2n\pi}{d}\right)y\right] dx dy \quad (5.23)$$

and

$$(Q_2^{m,n,0,1})^* = \int_0^{a_y} \int_0^{a_x} \sin\left(\frac{\pi y}{a_y}\right) \exp\left[i\left(\frac{2m\pi}{d}\right)x\right] \exp\left[i\left(\frac{2n\pi}{d}\right)y\right] dx dy. \quad (5.24)$$

From equations 5.23 and 5.24 it is clear that there is a dependence on both a_x and a_y as suggested by figure 5.5. The asymmetry of the response is a direct result of this dual dependence, with the extent of the asymmetry being determined by the relative significance of each of the parameters. However, the significance of each parameter perhaps cannot be envisaged as clearly. For $[0, n]$ diffracted orders, equations 5.23 and 5.24 become:

$$Q_2^{0,n,0,1} = \frac{a_x a_y d^2 \left(1 + \exp\left[-\frac{2ia_y n \pi}{d}\right]\right)}{(d^2 - 4a_y^2 n^2)\pi} \quad (5.25)$$

and

$$(Q_2^{0,n,0,1})^* = \frac{a_x a_y d^2 \left(1 + \exp\left[\frac{2ia_y n \pi}{d}\right]\right)}{(d^2 - 4a_y^2 n^2)\pi}; \quad (5.26)$$

5. The Aspect Ratio Dependence of the Microwave Response of Hole Arrays

whilst for all other diffracted orders, i.e. $[m, n]$ where $m \neq 0$, they are given by

$$Q_2^{m,n,0,1} = -\frac{ia_y d^3 \exp\left[-\frac{2i(a_x m + a_y n)\pi}{d}\right] \left(\exp\left[\left(\frac{2ia_x m\pi}{d}\right)\right] - 1\right) \left(1 + \exp\left[\left(\frac{2ia_y n\pi}{d}\right)\right]\right)}{2m(d^2 - 4a_y^2 n^2)\pi^2} \quad (5.27)$$

and

$$(Q_2^{m,n,0,1})^* = -\frac{ia_y d^3 \left(\exp\left[\left(\frac{2ia_x m\pi}{d}\right)\right] - 1\right) \left(1 + \exp\left[\left(\frac{2ia_y n\pi}{d}\right)\right]\right)}{2m(d^2 - 4a_y^2 n^2)\pi^2}. \quad (5.28)$$

Further examination of equations 5.25 to 5.28 reveals that in all cases, for incident radiation polarised along the x -axis, it is the length of the hole orthogonal to the polarisation, i.e., parallel to the y -axis (a_y), that is the dominant parameter. As expected from the results from the previous chapter, the greater the size of the hole, the larger the overlap integrals; and therefore increasing either hole side will increase the overlap integral. However, increasing a_y results in the numerator increasing and the denominator decreasing creating a significant change in the overlap integral, whilst the overlap integral has a linear relationship with a_x . The broadening of the mode observed in figure 5.5(b) is similar to the broadening seen in figure 4.11(a) due to the non-resonant transmission channel becoming more dominant for larger holes. This description can now be clarified by the statement that it is a_x that determines the significance of the non-resonant channel whilst a_y determines the significance of the resonant transmission channel.

If this array is considered in terms of an LC circuit model, the influence of a_x and a_y on the position of the resonance is perhaps clearer to see. Although hole arrays are considered as inductive FSSs [135, 155] (section 4.1), they have both an inductive and capacitive contribution when considered in terms of an equivalent circuit [65, 83], as illustrated by figure 5.6 and figure 3.2. The hole geometry will affect both the inductance and capacitance of the equivalent circuit. If the incident radiation is polarised parallel to the x -axis, a capacitance will exist between the sides of the hole parallel to the y -axis (a_y). These will act as a parallel plate capacitor and therefore the capacitance, C , will be proportional to the plate area ($a_y h$) divided by the distance between them (a_x). The inductance, L , is given by the integral of the surface current density and consequently is proportional to the area of the conductor ($a_y(d - a_x)$). Therefore, looking at a_y first, both the capacitance and the inductance are directly proportional to a_y , i.e. $C \propto a_y$ and $L \propto a_y$. As a_y increases, so will both the inductance and capacitance of the equivalent

5. The Aspect Ratio Dependence of the Microwave Response of Hole Arrays

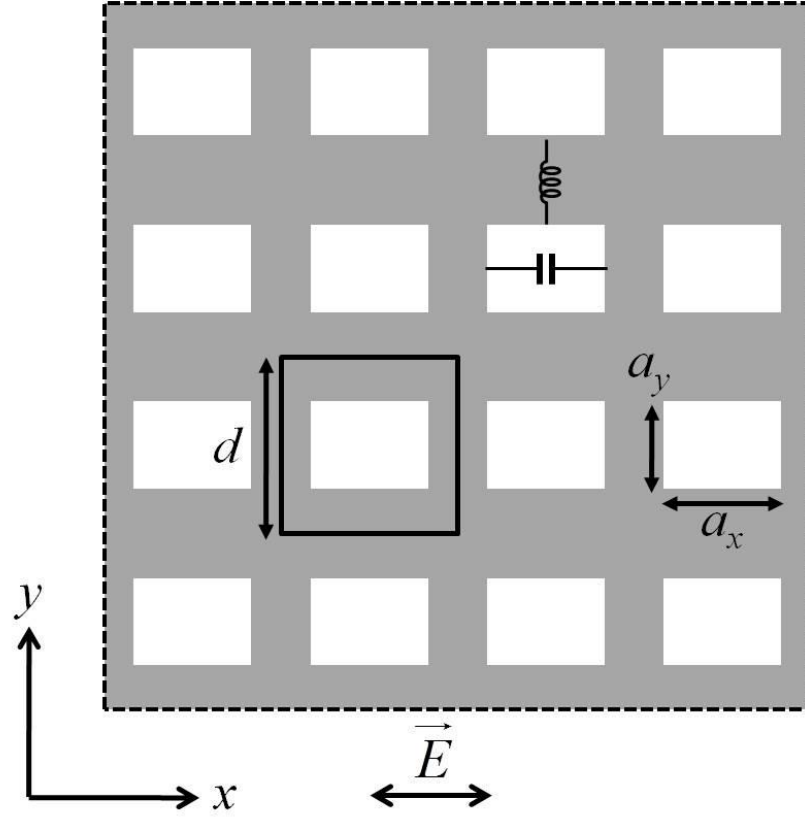


Figure 5.6: Schematic of a square array of rectangular holes showing the capacitive and inductive components.

circuit. As equation 5.29 shows, this means that as a_y increases, the resonant frequency will decrease.

$$\omega = \frac{1}{\sqrt{LC}} \propto \frac{1}{\sqrt{a_y^2}} \propto \frac{1}{a_y}. \quad (5.29)$$

By contrast, for a_x , the capacitance is inversely proportional to a_x while the inductance is still directly proportional to the period minus a_x (i.e. $C \propto \frac{1}{a_x}$ and $L \propto (d - a_x)$). Consequently as a_x increases, so will the resonant frequency (equation 5.30).

$$\omega = \frac{1}{\sqrt{LC}} \propto \sqrt{\frac{a_x}{d - a_x}}. \quad (5.30)$$

5.3.2 Rectangular Array of Square Holes

Figure 5.7 shows the comparison between the HFSSTM solution and the modal matching approach for a rectangular array with pitch of 10 mm and 8 mm parallel to the x - and

5. The Aspect Ratio Dependence of the Microwave Response of Hole Arrays

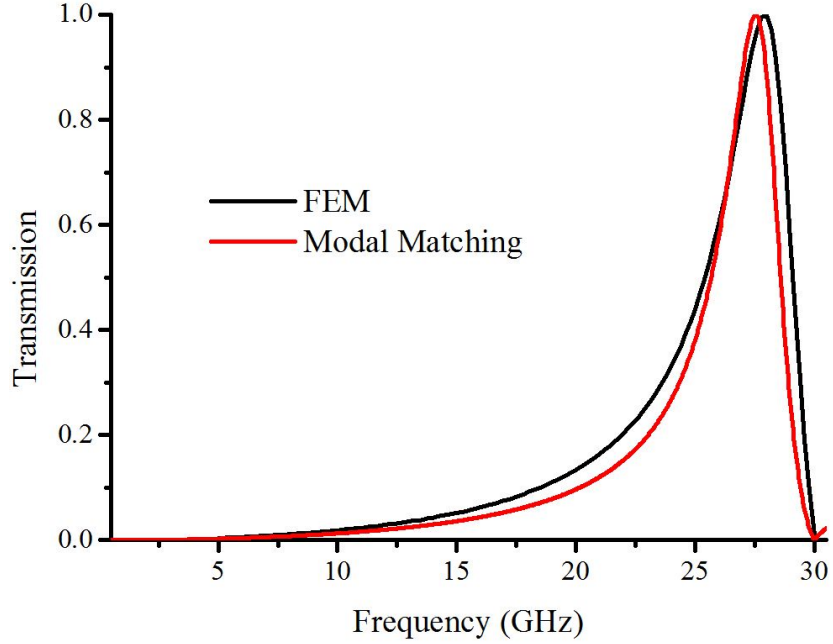


Figure 5.7: Comparison between the modal matching model and the solution derived using a FEM model for a rectangular array of square holes in a PEC sheet at normal incidence with $d_x = 10$ mm, $d_y = 8$ mm and $a = 4.5$ mm, with the incident radiation polarised along the x -axis.

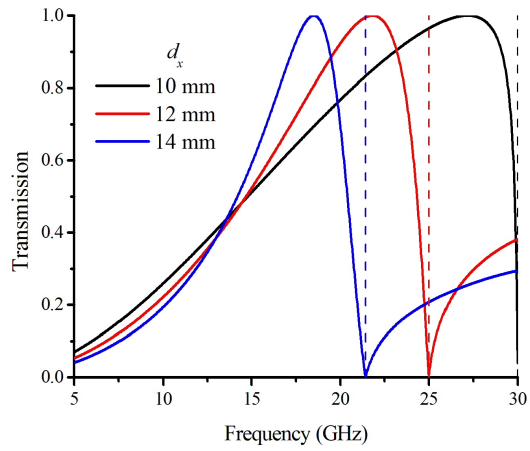
y -axes respectively and square holes of side length 4.5 mm where the incident field is polarised parallel to the x -axis, providing verification of the model's validity.

Figure 5.8 illustrates the EM response for a rectangular array of square holes: in figure 5.8(a), the pitch perpendicular to the polarisation of the incident radiation is fixed, and the pitch parallel to the polarisation of the incident radiation is varied; whilst in figure 5.8(b), it is the pitch *parallel* to the polarisation of the incident radiation that is fixed and the perpendicular pitch that varies. As d_x increases, the associated onset of diffraction moves down in frequency, resulting in the transmission resonance correspondingly moving to lower frequencies as expected (figure 5.8(a)). Variation of d_y also has a significant effect on the predicted EM response (figure 5.8(b)). A sharp transmission peak is observed as the onset of diffraction associated with d_y moves below the onset of diffraction associated with d_x .

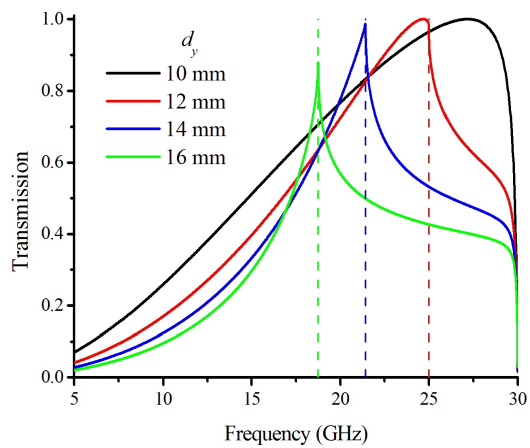
5.3.2.1 Analysis of results

Whilst it is of the same form, the equation for the complex amplitude transmission coefficient (equation 4.10) has changed to account for the changes in the pitch geometry

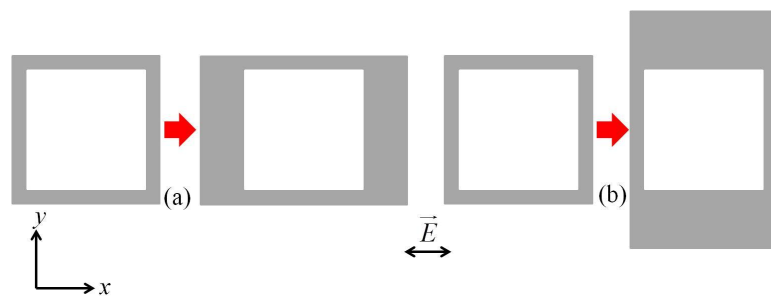
5. The Aspect Ratio Dependence of the Microwave Response of Hole Arrays



(a)



(b)



(c)

Figure 5.8: Transmission response for a rectangular array of square holes in a PEC sheet with side length 8 mm for (a) $d_y = 10$ mm, (b) $d_x = 10$ mm, at normal incidence with the incident radiation polarised parallel to the x-axis, and (c) a scale schematic of the change in unit cell for each graph. The onset of diffraction is indicated by the dashed lines.

5. The Aspect Ratio Dependence of the Microwave Response of Hole Arrays

of the unit cell. These changes also affect the overlap integrals resulting in the following equations:

$$t^{0,0} = \frac{\frac{(\frac{\omega}{c})^2}{\sqrt{(\frac{\omega}{c})^2 - (k_x)^2}} (Q_2^{0,0,0,1})^* Q_2^{0,0,0,1}}{\sum_{m,n} \left(\frac{(k_z^{m,n})^2 + (k_x + \frac{2m\pi}{d_x})^2}{k_z^{m,n}} \right) (Q_2^{m,n,0,1})^* Q_2^{m,n,0,1}}, \quad (5.31)$$

$$Q_2^{m,n,0,1} = \int_0^a \int_0^a \sin\left(\frac{\pi y}{a}\right) \exp\left[-i\left(\frac{2m\pi}{d_x}\right)x\right] \exp\left[-i\left(\frac{2n\pi}{d_y}\right)y\right] dx dy \quad (5.32)$$

and

$$(Q_2^{m,n,0,1})^* = \int_0^a \int_0^a \sin\left(\frac{\pi y}{a}\right) \exp\left[i\left(\frac{2m\pi}{d_x}\right)x\right] \exp\left[i\left(\frac{2n\pi}{d_y}\right)y\right] dx dy. \quad (5.33)$$

As suggested by figure 5.8, equations 5.32 and 5.33 show a dependence on both d_x and d_y . As in section 5.3.1.1, they can be described as follows: for $[0, n]$ diffracted orders, equations 5.32 and 5.33 become:

$$Q_2^{0,n,0,1} = \frac{a^2 d_y^2 \left(1 + \exp\left[-\frac{2ian\pi}{d_y}\right]\right)}{(d_y^2 - 4a^2 n^2)\pi} \quad (5.34)$$

and

$$(Q_2^{0,n,0,1})^* = \frac{a^2 d_y^2 \left(1 + \exp\left[\frac{2ian\pi}{d_y}\right]\right)}{(d_y^2 - 4a^2 n^2)\pi}; \quad (5.35)$$

whilst for all other diffracted orders, i.e. $[m, n]$ where $m \neq 0$, they are given by

$$Q_2^{m,n,0,1} = -\frac{iad_x d_y^2 \exp\left[-\frac{2ia(d_y m + d_x n)\pi}{d_x d_y}\right] \left(\exp\left[\frac{2iam\pi}{d_x}\right] - 1\right) \left(1 + \exp\left[\frac{2ian\pi}{d_y}\right]\right)}{2m(d_y^2 - 4a^2 n^2)\pi^2} \quad (5.36)$$

and

$$(Q_2^{m,n,0,1})^* = -\frac{iad_x d_y^2 \left(\exp\left[\frac{2iam\pi}{d_x}\right] - 1\right) \left(1 + \exp\left[\frac{2ian\pi}{d_y}\right]\right)}{2m(d_y^2 - 4a^2 n^2)\pi^2}. \quad (5.37)$$

The consequence of this is that the incident radiation will no longer simply preferentially scatter more strongly from one grating than the other for different polarisations. Now, in addition, the orthogonal pitches of the array will significantly influence the

5. The Aspect Ratio Dependence of the Microwave Response of Hole Arrays

predicted response.

5.3.3 Rectangular Array of Rectangular Holes

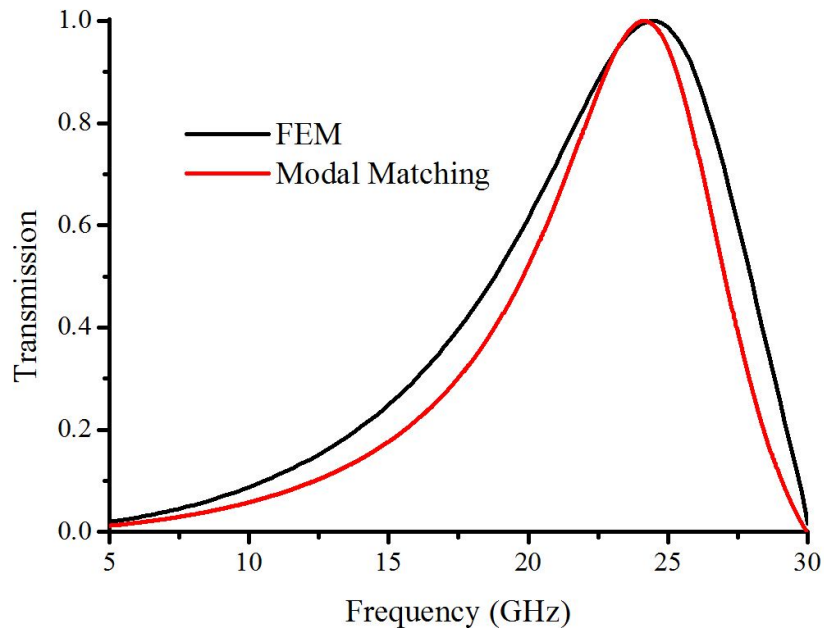


Figure 5.9: Comparison between the modal matching model and the solution derived using a FEM model solution for a rectangular array of rectangular holes in a PEC sheet at normal incidence with $d_x = 10$ mm, $d_y = 8$ mm, $a_x = 4.5$ and $a_y = 6$ mm, with the incident radiation polarised parallel to the x -axis.

Figure 5.9 compares the transmission plots for the FEM solution and the modal matching approach for a rectangular array with pitch of 10 mm and 8 mm parallel to the x - and y -axes respectively and rectangular holes of side lengths 4.5 mm and 6 mm parallel to the x - and y -axes respectively, where the incident field is polarised parallel to the x -axis, verifying that the model is valid.

Figure 5.10 illustrates the effect on the EM response when different geometric parameters are varied, for a rectangular array of rectangular holes. For figures 5.10(a) and 5.10(b) the pitch parallel to the incident polarisation is 7 mm and the pitch perpendicular to the polarisation of the incident radiation is 10 mm. In each case, one side length is fixed whilst the other is varied. The onset of diffraction at 30 GHz is associated with the grating vector perpendicular to the polarisation of the incident radiation, whilst the onset of diffraction associated with the grating parallel to the incident radiation polarisation is at higher frequencies (≈ 43 GHz) and therefore is not within

5. The Aspect Ratio Dependence of the Microwave Response of Hole Arrays

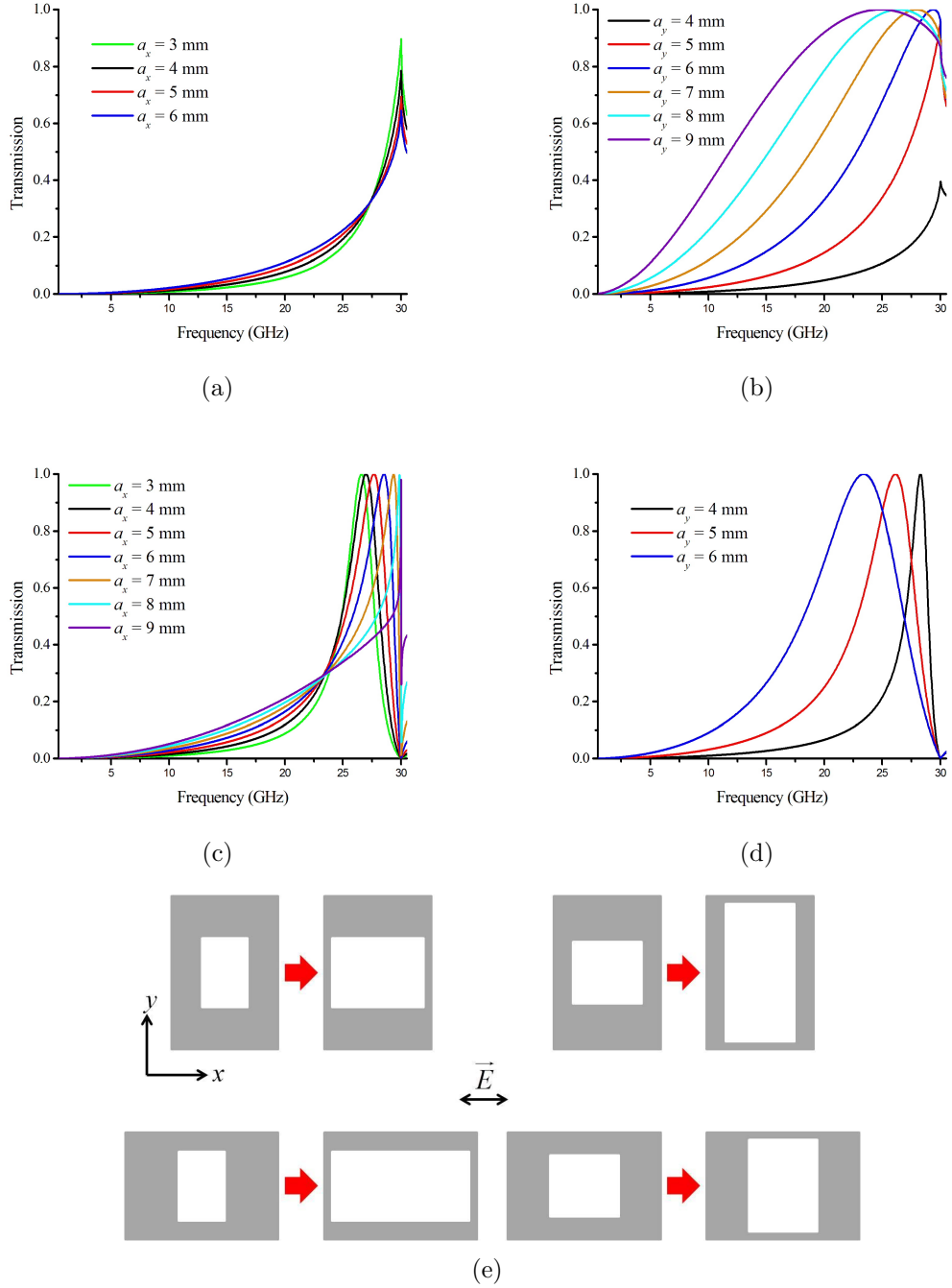


Figure 5.10: Transmission response for a rectangular array of rectangular holes in a PEC sheet for varying hole sizes with fixed pitch. The first two transmission graphs have a pitch of $d_x = 7$ mm and $d_y = 10$ mm with (a) $a_y = 4.5$ mm, and (b) $a_x = 4.5$ mm respectively. The last two graphs have a pitch of $d_x = 10$ mm and $d_y = 7$ mm with (c) $a_y = 4.5$ mm, and (d) $a_x = 4.5$ mm. In all cases the incident radiation is at normal incidence and polarised parallel to the x -axis. A scale schematic of the change in unit cell for each graph is provided in (e).

5. The Aspect Ratio Dependence of the Microwave Response of Hole Arrays

the range of the graph. As a_x increases in value, the resonance moves closer to the onset of diffraction at 30 GHz, whereas when a_y is increased the resonance broadens and moves to lower frequencies. The resonance broadens due to the influence of the evanescent diffraction below the onset of diffraction at 30 GHz and the movement to lower frequencies is associated with the resonant frequency of the fundamental dipolar mode of the hole decreasing as a_y increases (section 2.3.1.3). The pitch parallel to the incident radiation polarisation is 10 mm and the pitch perpendicular to the polarisation of the incident radiation is 7 mm for figures 5.10(c) and 5.10(d), and therefore the diffraction edge situated at 30 GHz is now associated with the grating vector *parallel* to the incident radiation polarisation. The same trend is apparent, with a_x moving to higher frequencies and a_y moving to lower frequencies as their values are increased.

Figure 5.11 also presents the EM response for a rectangular array of rectangular holes, however, it is the effect on the transmission due to a variation in pitch that is illustrated. For figures 5.11(a) and 5.11(b) the hole side lengths are 6 mm parallel to the polarisation of the incident radiation and 4.5 mm perpendicular to the incident radiation polarisation. In each case, one pitch is fixed whilst the other is varied. In figure 5.11(a), the diffraction edge associated with the grating perpendicular to the polarisation of the incident radiation, d_y , is at 30 GHz for all pitch variations. As d_x increases, the onset of diffraction moves to lower frequencies; consequently for the first three traces, the only diffraction edge evident is the edge associated with d_y , until the fourth trace when they are both at the same frequency. As d_x increases, the resonant feature broadens and moves further from the onset of diffraction perpendicular to the polarisation at 30 GHz. From the results in section 4.4.1.1, this is to be expected; as the resonant frequency of the array moves further from the onset of diffraction, the lower the Q factor of the mode becomes due to the decreased significance of the evanescently diffracted orders. Figure 5.11(b) illustrates the opposing situation, where the onset of diffraction associated with d_x is fixed at 30 GHz and as the value of d_y increases, the associated onset of diffraction moves from higher frequencies down to 30 GHz. The resonance condition moves closer to the onset of diffraction at 30 GHz and sharpens as d_y increases. The same behaviour is seen in figures 5.11(c) and 5.11(d), the side length parallel to the polarisation of the incident radiation is 4.5 mm and the side length perpendicular to the incident radiation polarisation is 6 mm.

5. The Aspect Ratio Dependence of the Microwave Response of Hole Arrays

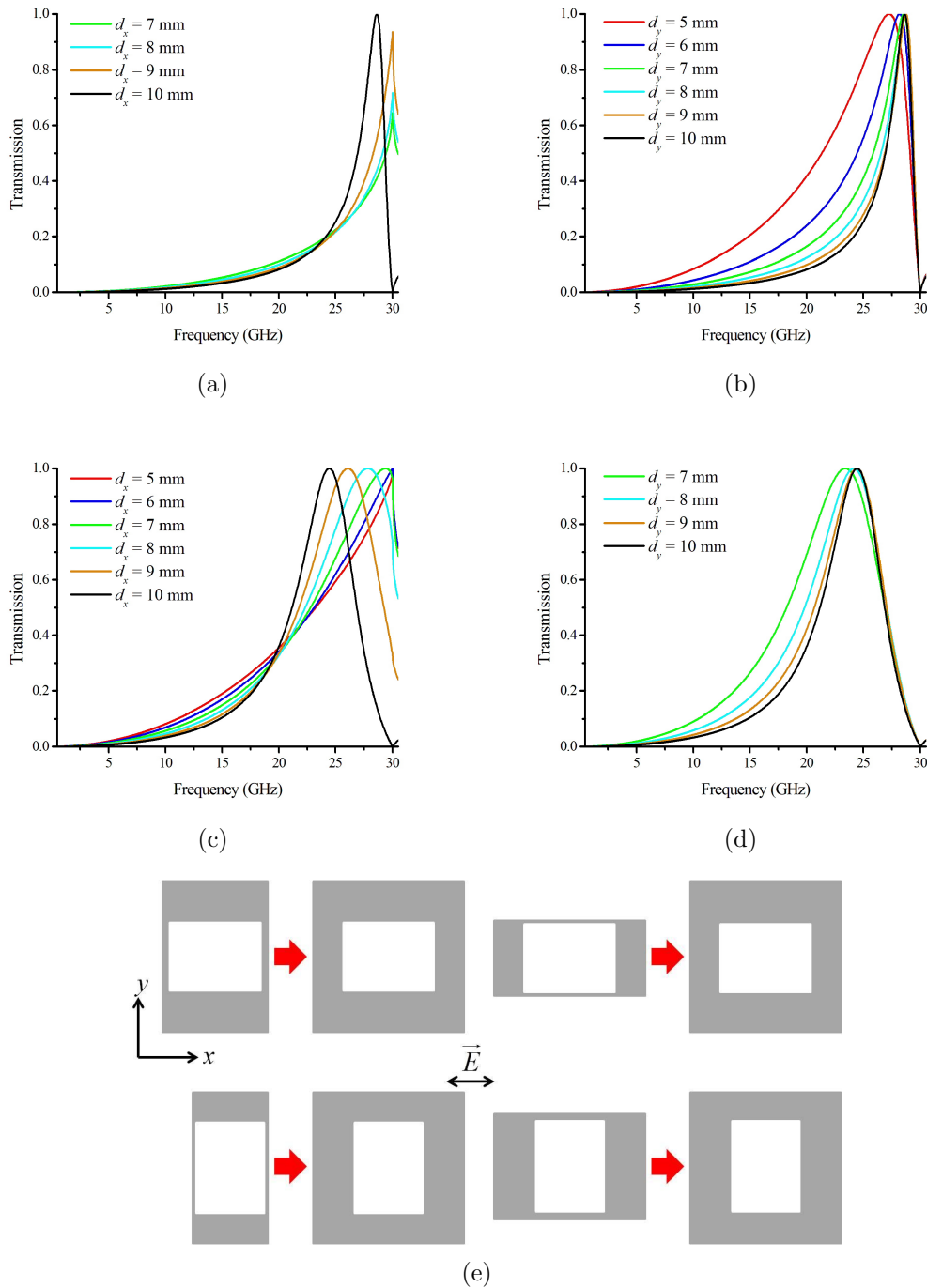


Figure 5.11: Transmission response for a rectangular array of rectangular holes in a PEC sheet for varying pitches with fixed hole sizes. The first two transmission graphs have holes of side length $a_x = 6$ mm and $a_y = 4.5$ mm with (a) $d_y = 10$ mm, and (b) $d_x = 10$ mm. The last two graphs have holes of side length $a_x = 4.5$ mm and $a_y = 6$ mm with (c) $d_y = 10$ mm, and (d) $d_x = 10$ mm. In all cases the incident radiation is at normal incidence and polarised parallel to the x -axis. A scale schematic of the change in unit cell for each graph is provided in (e).

5. The Aspect Ratio Dependence of the Microwave Response of Hole Arrays

5.3.3.1 Analysis of results

The equation for the complex amplitude transmission coefficient (equation 4.10) is the same as for the rectangular array of square holes (equation 5.31). However, the overlap integrals are further adapted to account for the changes in geometry for the geometry of both the unit cell and the hole:

$$Q_2^{m,n,0,1} = \int_0^{a_y} \int_0^{a_x} \sin\left(\frac{\pi y}{a_y}\right) \exp\left[-i\left(\frac{2m\pi}{d_x}\right)x\right] \exp\left[-i\left(\frac{2n\pi}{d_y}\right)y\right] dx dy \quad (5.38)$$

and

$$(Q_2^{m,n,0,1})^* = \int_0^{a_y} \int_0^{a_x} \sin\left(\frac{\pi y}{a_y}\right) \exp\left[i\left(\frac{2m\pi}{d_x}\right)x\right] \exp\left[i\left(\frac{2n\pi}{d_y}\right)y\right] dx dy. \quad (5.39)$$

The results in figures 5.10 and 5.11 indicate a complex interplay between all four geometrical parameters (d_x , d_y , a_x and a_y). As in the previous sections (sections 5.3.1.1 and 5.3.2.1), for $[0, n]$ diffracted orders, equations 5.38 and 5.39 can also be written as:

$$Q_2^{0,n,0,1} = \frac{a_x a_y d_y^2 \left(1 + \exp\left[-\frac{2ia_y n \pi}{d_y}\right]\right)}{(d_y^2 - 4a_y^2 n^2)\pi} \quad (5.40)$$

and

$$(Q_2^{0,n,0,1})^* = \frac{a_x a_y d_y^2 \left(1 + \exp\left[\frac{2ia_y n \pi}{d_y}\right]\right)}{(d_y^2 - 4a_y^2 n^2)\pi}; \quad (5.41)$$

whilst for all other orders, i.e. $[m, n]$ where $m \neq 0$, they are given by

$$Q_2^{m,n,0,1} = -\frac{ia_y d_x d_y^2 \exp\left[-\frac{2i(a_x d_y m + a_y d_x n)\pi}{d_x d_y}\right] \left(\exp\left[\frac{2ia_x m \pi}{d_x}\right] - 1\right) \left(1 + \exp\left[\frac{2ia_y n \pi}{d_y}\right]\right)}{2m(d_y^2 - 4a_y^2 n^2)\pi^2} \quad (5.42)$$

and

$$(Q_2^{m,n,0,1})^* = -\frac{ia_y d_x d_y^2 \left(\exp\left[\frac{2ia_x m \pi}{d_x}\right] - 1\right) \left(1 + \exp\left[\frac{2ia_y n \pi}{d_y}\right]\right)}{2m(d_y^2 - 4a_y^2 n^2)\pi^2}. \quad (5.43)$$

The similarities in equations 5.40 to 5.43 explain the similarities in figures 5.10 and 5.11 with the results in sections 5.3.1 and 5.3.2. As before, an increase in a_y moves the resonant feature to lower frequencies, whilst an increase in a_x moves the resonance to higher frequencies due to changes in the inductance and capacitance of the array.

5. The Aspect Ratio Dependence of the Microwave Response of Hole Arrays

Changes in the orthogonal pitches of the array are responsible for the shift in the onset of diffraction as would be expected.

5.4 Conclusion

To conclude, the modal matching method introduced in chapter 4 has been extended to explore the EM response to three new structures: a square array of rectangular holes, a rectangular array of square holes and a rectangular array of rectangular holes in a PEC sheet and orientated parallel to the axes of the coordinate system. For the square array of rectangular holes it was shown that the breaking of the four-fold symmetry of the hole resulted in a change in the relative proportions of the resonant and non-resonant transmission channels. The hole side length perpendicular to the direction of the incident radiation is the dominant parameter and is related to the resonant transmission channel; whilst the hole side length parallel to the incident radiation has a linear relationship with the overlap integral. This can be also be described as changes in the effective inductive and capacitive elements of the equivalent circuit describing the mesh.

Regarding the rectangular array of square holes, by breaking the four-fold symmetry of the unit cell, the onset of diffraction with respect to the orthogonal grating vectors occurs at different frequencies, unlike in a square array when they both occur at the same frequency. For $[0, n]$ diffracted orders, the overlap integrals are only dependent on the pitch orthogonal to the direction of the incident radiation, i.e., d_y in the example given. However, for all other diffracted orders, whilst the orthogonal pitch is still the dominant parameter, the pitch parallel to the incident radiation also has a contribution and is therefore able to affect the EM response of the mesh. For the rectangular array of rectangular holes, both elements of the previous two structures combine. Although all these elements combine depending on the parameters involved in the specific array, in broad, general terms, it can be seen that the geometric parameters of the hole influence the Q factor of the resonance, with a_y being the significant parameter dictating the resonant frequency, and a_x the sharpness of the mode. Whilst the periodicity of the array dictates the extent to which this resonance is perturbed by the evanescent diffractive orders. The closer the resonance to the onset of diffraction, the more significant the perturbation.

Chapter 6

The Microwave Response of Closely Spaced Metal Meshes

6.1 Introduction

Section 2.2.3 introduced the fact that a planar metal dielectric interface can support a surface plasmon polariton [63]. However, the momentum of these surface waves is greater than that of the incident photon (i.e., $k_{spp} > k_0$) and so incident radiation cannot directly couple to an SPP on a planar interface. One method of coupling to the surface mode is via diffractive grating coupling, for example, corrugation of the surface or by introducing a periodic structure as in metal meshes [2, 65]. The periodic meshes studied in this chapter also support plasmon-like surface-bound modes [86, 124] that can be diffractively coupled to by the incident radiation enabling enhanced transmission through the hole array.

The modal matching method described in section 3.2.2 and employed previously for a single layer (chapter 4) has been extended and applied to a double-layered system where each layer consists of a square array of square holes in a PEC sheet. Investigation of the single mesh layer showed that there is a strong transmission resonance due to a resonantly excited surface wave located at a frequency slightly below the onset of diffraction [137]. Here a double mesh layer is studied with particular emphasis on unravelling the influence of evanescent coupling on the effect on the transmission of translational displacement of one mesh relative to the other.

Although most studies into the EM response of metal meshes have concentrated on single mesh layers, there have been some investigations into double mesh structures. In 2000, Yu *et al* created a reflective polariser using a double layer of metal monogratings

at optical frequencies [156]. Another optical investigation studied double layer meshes where the small separation between the layers allows coupling of the SPPs supported by each mesh leading to extraordinary optical transmission, even when the layers are laterally misaligned with respect to each other [157]. The effect of lateral displacement on double mesh layers in the visible regime was studied by Cheng *et al* in 2007 [158]. He *et al* conducted a near identical study to that presented in this chapter albeit at optical frequencies reaching similar conclusions [159], as did Miyamaru and Hangyo in the terahertz regime [160]. A common motivation behind the study of double mesh layer structures in the optical regime appears to be the creation of negative index materials [156, 157, 161].

Section 6.2 introduces Fabry-Pérot etalons and the modes associated with them. The following section (6.3) details the extensions and adaptations to the basic modal matching model necessary to mathematically represent the transmission through a double mesh structure. Section 6.4 presents the effect of parameter variations and discusses the results. Mathematical analysis is utilised to develop a further understanding of why this structure responds to EM radiation as it does. Both aligned and misaligned structures are investigated, where the alignment of one mesh relative to the other is varied. The meshes are translated in a single direction parallel and perpendicular to the axis of polarisation. The final section (section 6.5) provides a summary of the key conclusions of this exploration into the EM response of two PEC meshes separated by a dielectric.

6.2 Background

6.2.1 Fabry-Pérot Modes

Fabry-Pérot modes are resonant transmission cavity modes. They were proposed in 1899 by Fabry and Pérot [162] and used in the design of their interferometer. A Fabry-Pérot etalon comprises of a pair of highly reflecting parallel plates (but not 100% reflecting) a distance, l , apart (figure 6.1). Transmitted radiation through the etalon is made up of radiation directly transmitted and radiation that has undergone multiple reflections between the plates before being transmitted.

For a transmission peak to occur, the transmitted light has to interfere constructively, i.e., all contributions need to be transmitted in phase. Fabry and Pérot discovered that this occurs when the distance between the plates is, to first order, a half-wavelength

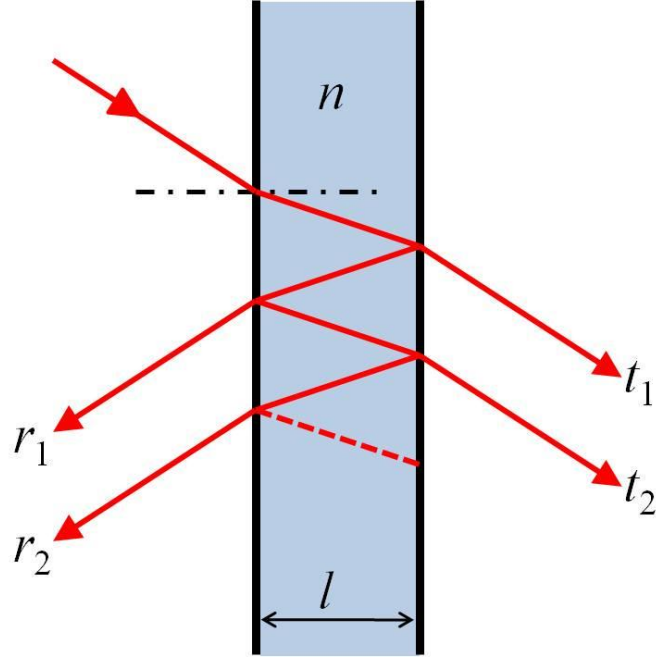


Figure 6.1: *Schematic of a Fabry-Pérot etalon comprising a pair of highly reflecting parallel surfaces a distance d apart filled with a dielectric with refractive index n . Light enters the etalon and undergoes multiple internal reflections.*

multiple (for normal incidence), i.e.,

$$l = \frac{m\lambda}{2} \quad m = 1, 2, 3 \dots \quad (6.1)$$

Conversely, a reflection peak occurs when the contributions are exactly out of phase. The modelled \vec{E} field profiles for the first four Fabry-Pérot transmission resonances of an arbitrary etalon are illustrated in figure 6.2.

6.3 Method

Chapter 4 considered a single mesh layer comprising a square array of square holes in a sheet of PEC. This structure is now extended by considering two mesh layers; each mesh layer comprises a two dimensional (2D) square array of square holes in a sheet of PEC of thickness h . The two meshes, which share common orthogonal axes along the sides of the square holes, are separated by a dielectric layer of thickness g , with b_i denoting the lateral displacement of the meshes with respect to each other (figure 6.3) along the polarisation axis of the normally incident radiation.

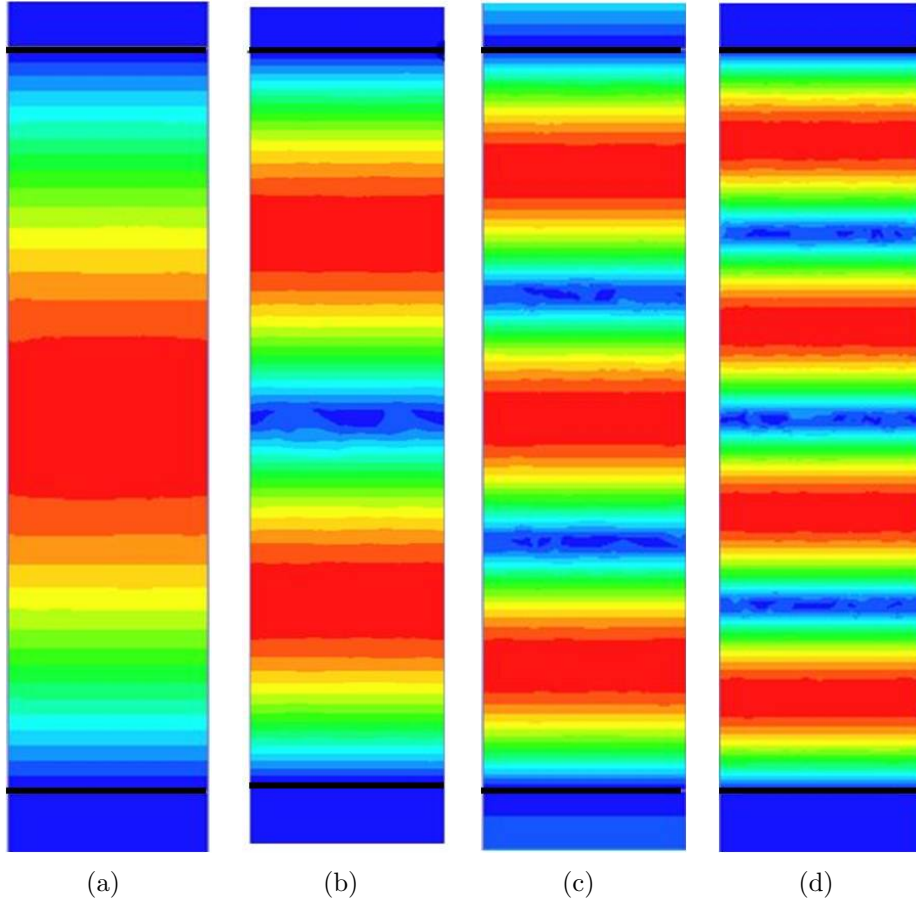


Figure 6.2: \vec{E} Field profiles corresponding to the eigensolutions of the first four Fabry-Pérot modes supported by a pair of perfectly conducting square metal meshes, with holes much smaller than the wavelength, separated by an air gap. Red corresponds to a time-averaged arbitrary field magnitude of 1 and blue to a magnitude of zero.

The theoretical formalism is the same as utilised previously for the single mesh layer (section 4.3), with the electric fields in the regions above and below the mesh layer described by a two dimensional Fourier-Floquet expansion of the diffracted orders, [equations 3.3 - 3.6]. As before, within the mesh layer, the electric fields are only present in the square holes, and they may be expanded as a sum of waveguide modes, [equations 3.9, 3.10].

The method is extended for the double mesh system by describing the electric fields in the additional regions (figure 6.4) in the same way, with the fields in the holes of the second mesh layer (region IV) also expanded as a sum of waveguide modes, while in the region between the meshes (region III) the fields are represented as a Fourier-Floquet expansion of the diffracted orders. To account for the multiple reflections between the

6. The Microwave Response of Closely Spaced Metal Meshes

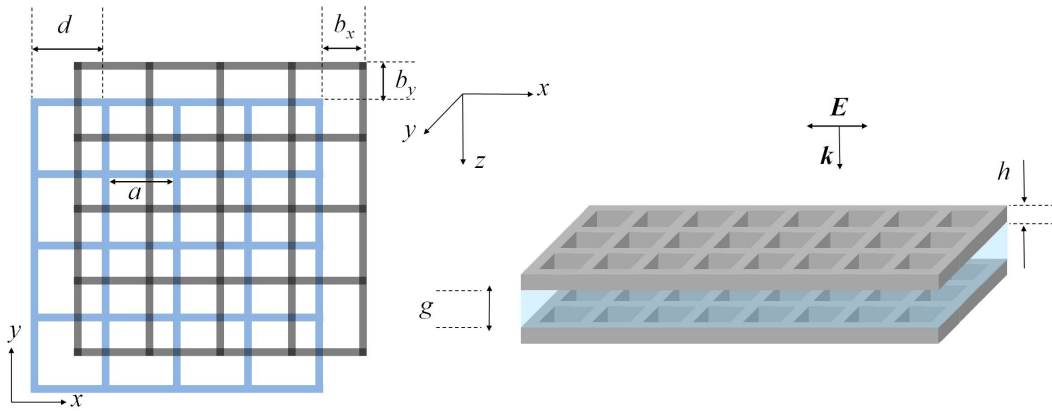


Figure 6.3: Schematic of the investigated geometry comprising two layers of a square array with pitch d of holes of length side a (unshaded) in a PEC sheet (shaded) of thickness h . The sheets are separated by a dielectric layer of thickness g and the translational displacement of the meshes relative to each other is denoted by b_i .

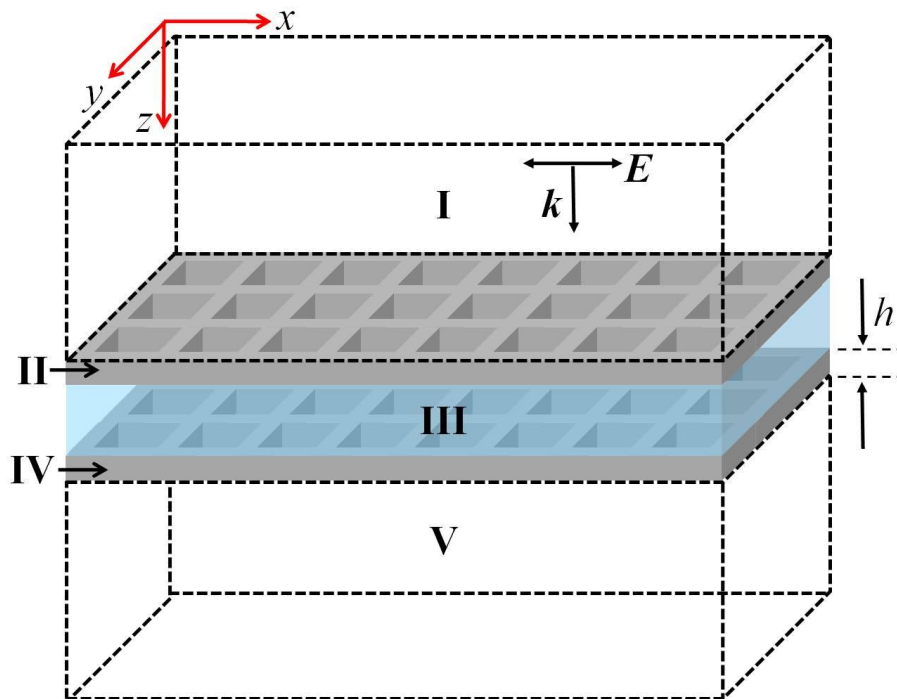


Figure 6.4: Schematic showing the defined regions for the double mesh layer structure.

6. The Microwave Response of Closely Spaced Metal Meshes

meshes, two expansions are needed in this dielectric cavity (i.e., both an $\exp[-ik_z z]$ and an $\exp[ik_z z]$ sum). For the dielectric regions (I, III and V), the expressions for region I are unchanged (equations 3.3 and 3.4), for region III equations 3.5 and 3.6 are replaced by equations 6.2 and 6.3 respectively and the fields in region V are described by equations 6.4 and 6.5:

$$E_x^{III} = \sum_{p,q} D_x^{p,q} \Psi_1^{p,q}(x, y) \exp(ik_z^{p,q} z) + \sum_{p,q} F_x^{p,q} \Psi_1^{p,q}(x, y) \exp(-ik_z^{p,q} z), \quad (6.2)$$

$$E_y^{III} = \sum_{p,q} D_y^{p,q} \Psi_1^{p,q}(x, y) \exp(ik_z^{p,q} z) + \sum_{p,q} F_y^{p,q} \Psi_1^{p,q}(x, y) \exp(-ik_z^{p,q} z), \quad (6.3)$$

$$E_x^V = \sum_{\alpha,\beta} D_x^{\alpha,\beta} \Psi_1^{\alpha,\beta}(x, y) \exp(ik_z^{\alpha,\beta} z), \quad (6.4)$$

and

$$E_y^V = \sum_{\alpha,\beta} D_y^{\alpha,\beta} \Psi_1^{\alpha,\beta}(x, y) \exp(ik_z^{\alpha,\beta} z). \quad (6.5)$$

where Ψ_1 and k_z have the same definitions as before (equations 3.7 and 3.8). Similarly, the equations for region II are unchanged (equations 3.9 and 3.10) and the fields in region IV are described by

$$E_x^{IV} = \sum_{\iota,\kappa} L_x^{\iota,\kappa} \Psi_2(x, y) \exp(iq_z^{\iota,\kappa} z) + M_x^{\iota,\kappa} \Psi_2(x, y) \exp(-iq_z^{\iota,\kappa} z) \quad (6.6)$$

and

$$E_y^{IV} = \sum_{\iota,\kappa} L_y^{\iota,\kappa} \Psi_3(x, y) \exp(iq_z^{\iota,\kappa} z) + M_y^{\iota,\kappa} \Psi_3(x, y) \exp(-iq_z^{\iota,\kappa} z), \quad (6.7)$$

where Ψ_2 , Ψ_3 and q_z have the same respective definitions as in equations 3.11, 3.12 and 3.13.

After the corresponding tangential magnetic field components have been obtained, the boundary conditions and continuity requirements are then applied at each boundary, resulting in pairs of coupled simultaneous equations. Due to the additional two boundaries, this results in twice as many pairs of simultaneous equations as for the single mesh structure. The limits for the overlap integrals need to be adjusted to reflect any translational displacement between the mesh layers. If the origin and unit cells

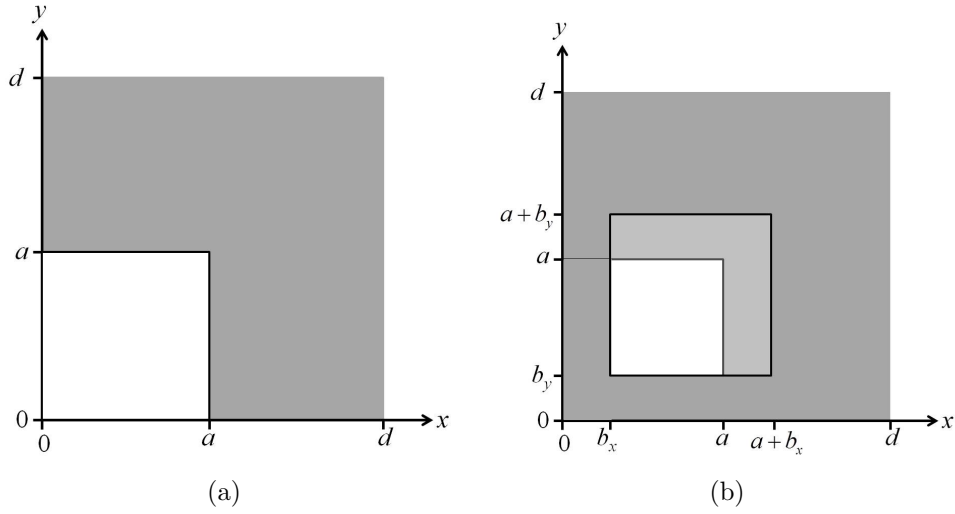


Figure 6.5: Schematic defining the unit cell and the origin for the double mesh layers as used in the analytical formulation for (a) the upper mesh layer and (b) the lower mesh layer.

are arbitrarily defined as illustrated in fig 6.5, the overlap integral (equation 3.34) is replaced by the following equations for the upper and lower mesh respectively;

$$Q_{2top}^{m,n,0,1} = \int_0^a \int_0^a \sin\left(\frac{\pi y}{a}\right) \exp\left[-i\left(\frac{2m\pi}{d}\right)x\right] \exp\left[-i\left(\frac{2n\pi}{d}\right)y\right] dx dy \quad (6.8)$$

and

$$Q_{2bot}^{m,n,0,1} = \int_{b_y}^{a+b_y} \int_{b_x}^{a+b_x} \sin\left(\frac{\pi y}{a}\right) \exp\left[-i\left(\frac{2m\pi}{d}\right)x\right] \exp\left[-i\left(\frac{2n\pi}{d}\right)y\right] dx dy. \quad (6.9)$$

The simultaneous equations are then solved, as before, to provide equations for the unknown amplitude coefficients. The method is essentially the same as for the single layer, albeit more computationally laborious.

6.4 Results and Discussion

6.4.1 Lateral displacement parallel to the incident polarisation

Analysis of the mathematical expression for the transmission and reflection coefficients shows that the relationship between the resonance of each mesh, the resonance of the

6. The Microwave Response of Closely Spaced Metal Meshes

cavity between the meshes and the relative alignment of the meshes is a complex one. However, despite the complexity of the equation, it is still possible to extract further insight into these relationships. For simplicity here we have only considered incident radiation polarised parallel to the displacement direction, although the method can equally be used to consider radiation perpendicular to it. From the analysis of a single mesh layer in section 4.5.1 it is known that the transmission maximum for each mesh individually occurs for the $[0, n]$ diffracted orders when $\frac{\omega}{c} = \sqrt{2k_x^2 + \frac{4n^2\pi^2}{d^2}}$ (equation 4.15). At normal incidence this reduces to $\frac{\omega}{c} = \frac{2n\pi}{d}$. As in the single mesh case, only the first order waveguide modes need to be included in the calculation as it is purely a ‘matching condition’ across the interfaces, and therefore the first order mode is sufficient to provide an accurate representation of the behaviour. This assumption ceases to be valid for finite thickness films. In addition, since the resonances occur in the non-diffracting regime, only the specular propagating beam (zero-order) in transmission below the second mesh need be considered. Applying these conditions gives the following general equation for the transmission amplitude coefficient

$$t^{0,0} = \frac{4a^2 G_x \exp[i(g+2h)q_z]}{d^2 \pi}, \quad (6.10)$$

where G_x is the complex amplitude coefficient incorporating the ‘overlap integrals’ describing the boundary and orthogonality conditions and the alignment of the meshes. By further examination of this amplitude coefficient, we are able to isolate the terms involving the misalignment of the meshes, b , and the separation between them, g ,

$$G_x = \left(\frac{k_z^0 \frac{4a^2}{\pi} + C_x \left(q_z \frac{a^2}{2} - F_1 + \exp[-2ihq_z] \right)}{\exp[i(h+g)q_z] \left(q_z \frac{a^2}{2} - H_1 + H_3 - \frac{\exp[2ihq_z] \left(q_z \frac{a^2}{2} - I_1 \right) \left(q_z \frac{a^2}{2} + H_1 - H_3 \right)}{I_1 + q_z \frac{a^2}{2}} \right)} \right) \frac{2H_4 \exp[ihq_z]}{q_z \frac{a^2}{2} + F_1}, \quad (6.11)$$

where

$$F_1 = \sum_{m,n} K \left(Q_{top}^{m,n,1,0}, (Q_{top}^{m,n,1,0})^* \right), \quad (6.12)$$

$$H_1 = \sum_{p,r} K \left(\frac{Q_{bot}^{p,r,1,0}, (Q_{bot}^{p,r,1,0})^* \exp[2igk_z^{p,r}]}{\exp[2igk_z^{p,r}] - 1} \right), \quad (6.13)$$

6. The Microwave Response of Closely Spaced Metal Meshes

$$H_3 = - \sum_{p,r} K \left(\frac{Q_{bot}^{p,r,1,0}, (Q_{bot}^{p,r,1,0})^*}{\exp [2igk_z^{p,r}] - 1} \right), \quad (6.14)$$

$$H_4 = \sum_{p,r} K \left(\frac{Q_{top}^{p,r,1,0}, (Q_{bot}^{p,r,1,0})^* \exp [-igk_z^{p,r}]}{\exp [-2igk_z^{p,r}] - 1} \right), \quad (6.15)$$

and

$$I_1 = \sum_{u,v} K \left(Q_{bot}^{u,v,1,0}, (Q_{bot}^{u,v,1,0})^* \right), \quad (6.16)$$

and the overlap integral components, Q_i , are given by

$$Q_{top}^{m,n,1,0} = \int_0^a \int_0^a \sin \left(\frac{\pi y}{a} \right) \exp \left[-i \left(\frac{2m\pi}{d} \right) x \right] \exp \left[-i \left(\frac{2n\pi}{d} \right) y \right] dx dy, \quad (6.17)$$

and

$$Q_{bot}^{m,n,1,0} = \int_{b_y}^{a+b_y} \int_{b_x}^{a+b_x} \sin \left(\frac{\pi y}{a} \right) \exp \left[-i \left(\frac{2m\pi}{d} \right) x \right] \exp \left[-i \left(\frac{2n\pi}{d} \right) y \right] dx dy; \quad (6.18)$$

where

$$K = k_z^{m,n} + \frac{4m^2\pi^2}{d^2 k_z^{m,n}}. \quad (6.19)$$

Examination of equation 6.11 shows that it is the H_4 term that contains the overlap integral components that describe the interaction between the two meshes via the evanescent fields, i.e., this term (equation 6.15) is affected by the relative misalignment of the meshes. The separation of the meshes, g , is clearly a dominant parameter within G_x . In particular, as g increases terms H_1 and H_3 will increase rapidly. In other words, as the denominator (separation term) increases, the numerator (alignment term) becomes less dominant.

Figure 6.6 compares normal incidence transmission plots for both aligned and misaligned arrangements of two identical meshes for three different mesh separations. The meshes have a pitch of 10 mm and the sides of the holes are 4.5 mm. For the misaligned geometry, a translational displacement of 5 mm parallel to the polarisation vector orientation is illustrated (i.e. $b_x = 5$ mm, $b_y = 0$).

6. The Microwave Response of Closely Spaced Metal Meshes

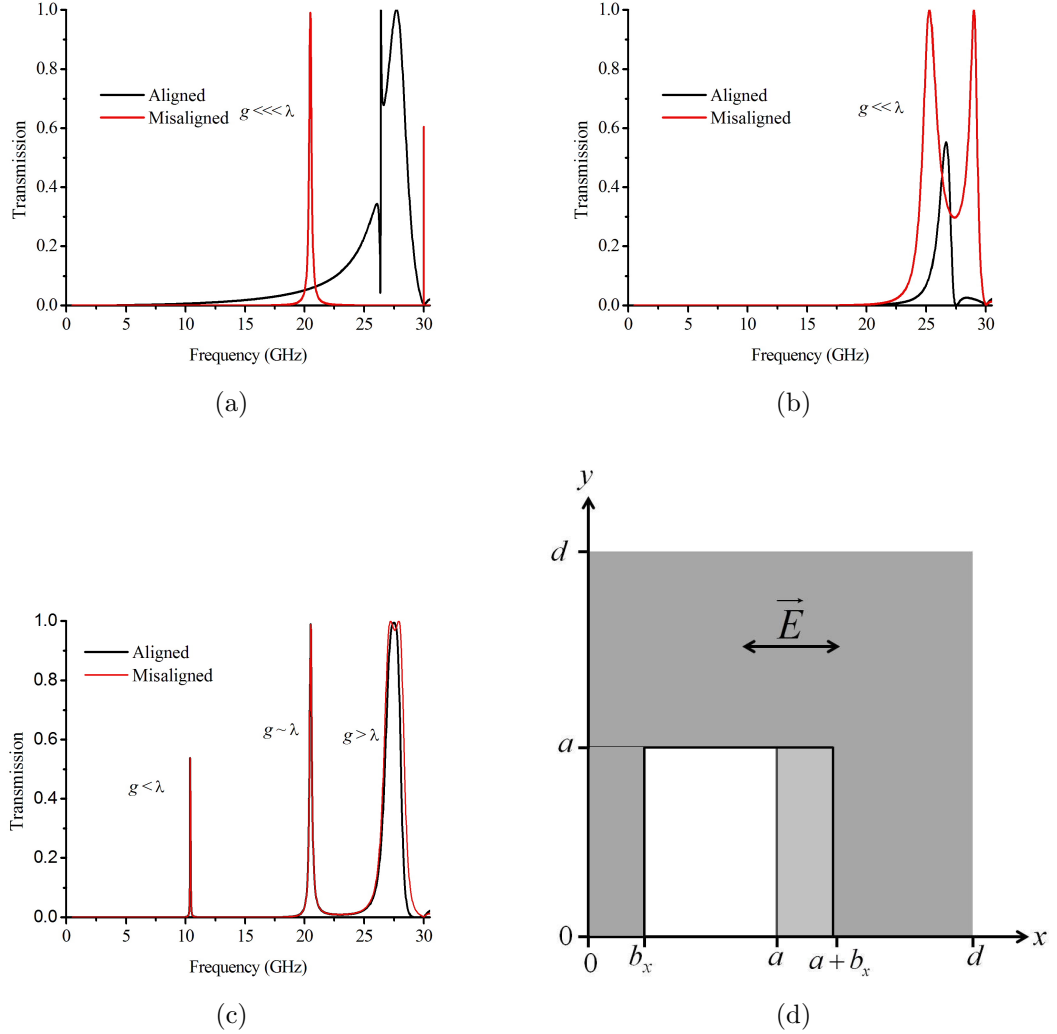


Figure 6.6: Transmission plots for the double mesh arrangement with pitch $d = 10$ mm, holes of side length $a = 4.5$ mm in a PEC sheet where the separation between the meshes is (a) $g = 0.1$ mm, (b) $g = 4$ mm and (c) $g = 14$ mm. A schematic showing the polarisation vector and displacement is illustrated in (d). Each graph shows the transmission profile for both the aligned system and when the meshes are laterally displaced by 5 mm (half a pitch) with respect to each other along the polarisation axis and the onset of diffraction occurs at 30 GHz.

6. The Microwave Response of Closely Spaced Metal Meshes

It is clear that when the separation of the meshes, g , is smaller than the wavelength, λ , there is a significant difference between the transmission of the aligned and misaligned systems. In the aligned case when $g = 0.1$ mm (figure 6.6(a)), the Fano-shaped resonance around 26.5 GHz is in the wings of a coupled surface wave mode at ~ 28 GHz. The former is a symmetric cosh-like mode, whilst the latter is an antisymmetric sinh-like mode (figure 6.7). By contrast, for the 5 mm misaligned case, the cosh-like (symmetric) mode is present at 20 GHz, and the sinh-like mode has pushed up in frequency to just below the onset of diffraction at 30 GHz. Both of the modes supported by the double mesh structures arise from an interaction between a (symmetric / antisymmetric) pair of coupled surface waves and either the cavity's standing-wave resonance or the single mesh resonance to form a hybrid mode. In the long wavelength limit, each hybrid mode has strong Fabry-Pérot characteristics and approaches the frequency where, in an ideal system, the optical path length between each partial mirror (mesh) is equal to an integer number of half-wavelengths. Conversely, in the short wavelength limit, each hybrid mode is dominated by the single mesh resonance and displays strong surface wave characteristics, as will be shown later.

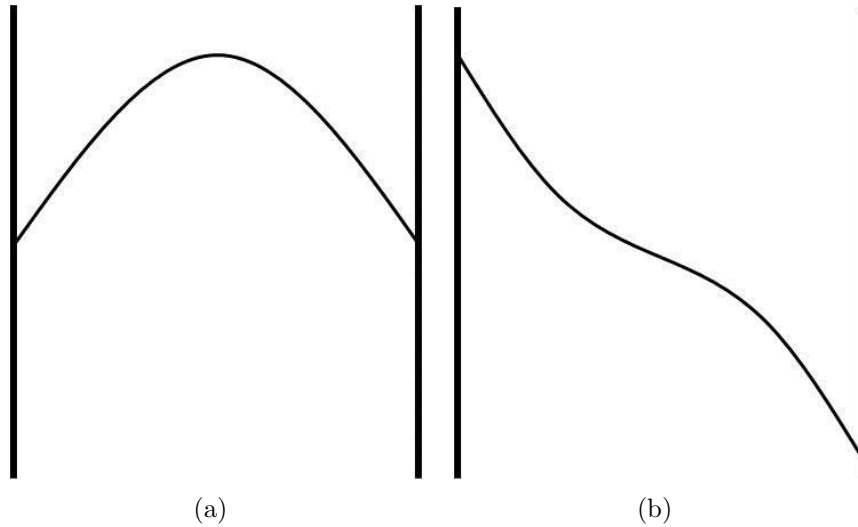


Figure 6.7: *Schematic showing (a) cosh-like symmetric \vec{E} field and (b) sinh-like anti-symmetric \vec{E} field. The mesh layers are indicated by the thick black vertical lines.*

As the separation between the meshes increases to approach the wavelength, the responses for both the aligned and misaligned systems become increasingly similar as shown by figures 6.6(b) and 6.6(c). Figure 6.6(c) shows reasonable qualitative agreement for the region where $g > \lambda$ and we might anticipate that the similarity between the

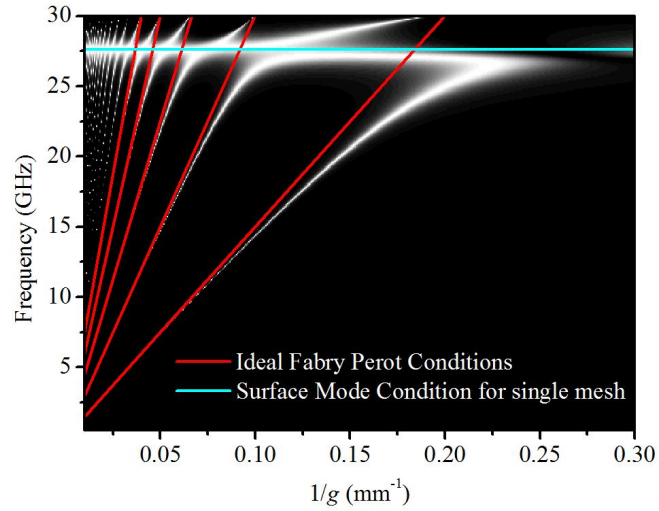
6. The Microwave Response of Closely Spaced Metal Meshes

aligned and misaligned responses would worsen for lower frequencies as the wavelength increases to become comparable to and then greater than the separation. However, this regime, where the wavelength is greater than the separation, is far from the onset of diffraction and evanescent diffraction has little significance. Thus, with no real propagating diffracted orders, the microscopic details describing the subwavelength structure are not conveyed from one layer to the other, including any misalignment of the meshes with respect to each other, and therefore this misalignment has little effect on the response of the system. In other words, each mesh can be effectively described as a homogeneous medium. This will be further explored in chapter 7 and in particular at what distance the separation between the meshes becomes too small to allow this homogeneous medium description to be applicable.

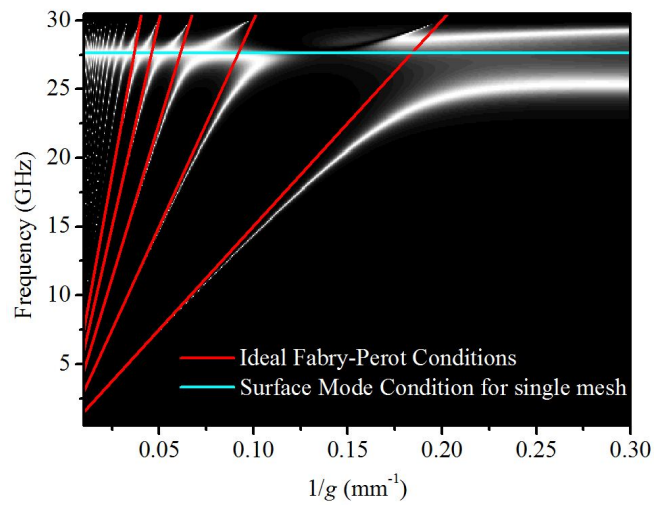
Figure 6.8 shows a more extensive, greyscale plot of the normal incidence transmission as a function of frequency and mesh separation, again for both aligned and misaligned systems. A family of modes between the two meshes can be clearly observed. At low frequencies each mode is Fabry-Pérot-like, however, as the frequency approaches that of the surface mode supported by a single mesh layer of identical geometry, hybridization occurs, as is strongly evidenced by the perturbation of the modes from the simple half-integer wavelength condition of the ideal Fabry-Pérot resonance for perfect electrical mirrors.

In figure 6.9, the transmission is plotted as a function of frequency and misalignment for separations of 14 mm and 0.1 mm (figure 6.9(a) and 6.9(b) respectively). Figure 6.9(b) shows the behaviour of the two modes as the misalignment between two meshes with squares of side length 4.5 mm is increased. When the two meshes are exactly aligned ($b_x = 0$ mm, $b_y = 0$ mm), a broad mode is seen at approximately 26.5 GHz, with a much sharper mode slightly lower in frequency at 25.5 GHz. As the lateral misalignment increases, the modes cross, with the sharper mode approaching the onset of diffraction at 30 GHz, and the broad mode decreasing in frequency to approximately 20 GHz at maximum lateral misalignment ($b_x = 5$ mm, $b_y = 0$ mm). Exploration of the magnitude of the electric fields (\vec{E}_z), calculated using the modal matching method, both between and outside the meshes as the misalignment varies, reveals that while the fields outside of the meshes remain reasonably constant, the fields between the meshes show greater enhancement as the misalignment is increased (not shown). The electric

6. The Microwave Response of Closely Spaced Metal Meshes



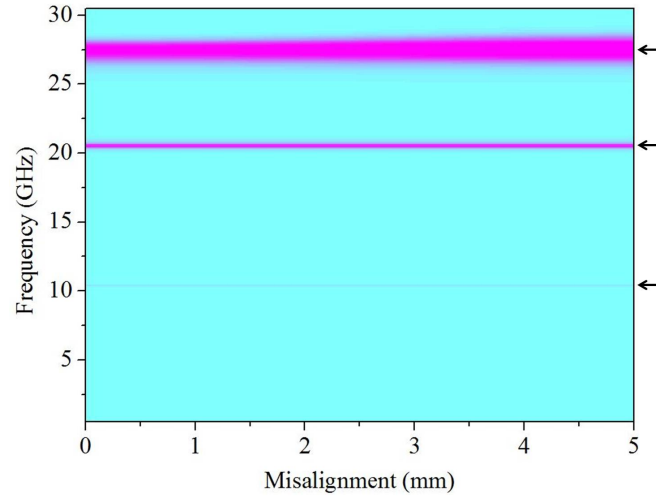
(a)



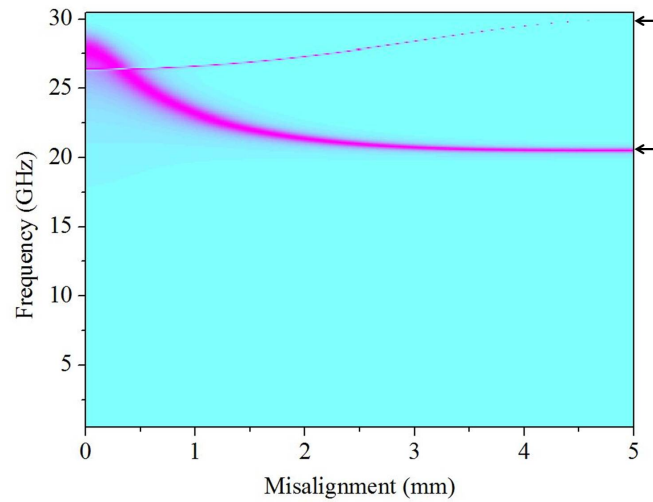
(b)

Figure 6.8: Greyscale plot of the normal incidence transmission as a function of frequency and mesh separation with pitch of 10 mm and holes of side length 4.5 mm for (a) $b_x = 0$ mm, $b_y = 0$ mm and (b) $b_x = 5$ mm, $b_y = 0$ mm. The ideal Fabry-Pérot conditions refer to the half-wavelength condition (i.e., $\lambda = 2g/n$ for $n = 1, 2, 3, \dots$).

6. The Microwave Response of Closely Spaced Metal Meshes



(a)



(b)

Figure 6.9: Colour-scale plot of the normal incidence transmission as a function of frequency and lateral misalignment parallel to the incident polarisation with pitch $d = 10$ mm and holes of side length $a = 4.5$ mm for (a) mesh separation $g = 14$ mm and (b) mesh separation $g = 0.1$ mm. The transmission resonances are highlighted by arrows.

6. The Microwave Response of Closely Spaced Metal Meshes

field between the two mesh layers is given by

$$\vec{E}_z^{III} = \sum_{p,r} (F_x^{p,r}(G_x) \Psi_1^{p,r}(x, y) \exp(-ik_z^{p,r} z) - D_x^{p,r}(G_x) \Psi_1^{p,r}(x, y) \exp(ik_z^{p,r} z)), \quad (6.20)$$

where $F_x^{p,r}$ and $D_x^{p,r}$ describe complex amplitude coefficients and are functions of G_x (equation 6.11).

The field enhancement is expected to be greatest at the edges of the holes due to the evanescent diffraction. At zero misalignment, the holes in both meshes are directly in line with each other and the field enhancement between the meshes is localised in a small area at the edge of the holes (figures 6.10(a) and 6.10(c)). As the misalignment between the meshes gradually increases, the alignment terms in G_x (H_4) start to become dominant, increasing the field enhancement between the meshes, which in turn increases the coupling to the resonance on the opposite mesh (figures 6.10(b) and 6.10(d)).

By considering the charge distribution for the simpler, well understood, case of a similarly spaced pair of identical metal slot arrays (i.e. one dimensional ‘grids’), further physical understanding of these modes can be gained. In this simpler case, there are two possible charge configurations; symmetric and antisymmetric (figure 6.11). In the case where the grids are in exact alignment with respect to each other (figure 6.11(a)), the symmetric charge configuration produces an antisymmetric (sinh-like) electric field configuration between the layers and can be considered as surface-mode-like due to the high electric fields being bound along the interfaces. In contrast, the antisymmetric charge configuration results in a symmetric (cosh-like) electric field configuration between the layers and the high electric fields occur within the cavity between the two meshes and are not bound to the surfaces and therefore can be considered as Fabry-Pérot-mode-like. When the slot arrays are laterally misaligned with respect to each other these charge configurations begin to be perturbed. The surface-mode-like configuration develops Fabry-Pérot-like characteristics, and vice versa (figure 6.11(b)). The greater the misalignment, the more the charge configuration is perturbed. At maximum misalignment there are still two possible configurations but they both have the same energy and have both cosh-like and sinh-like characteristics (figure 6.11(c)). However, for the double mesh system investigated here, when the holes are laterally misaligned, the four-fold symmetry of the aligned unit cell is reduced to a single plane of symmetry. In addition, there are regions of the unit cell that are unaffected by the lateral misalignment and therefore, for this structure, the two configurations are not equal in energy.

6. The Microwave Response of Closely Spaced Metal Meshes

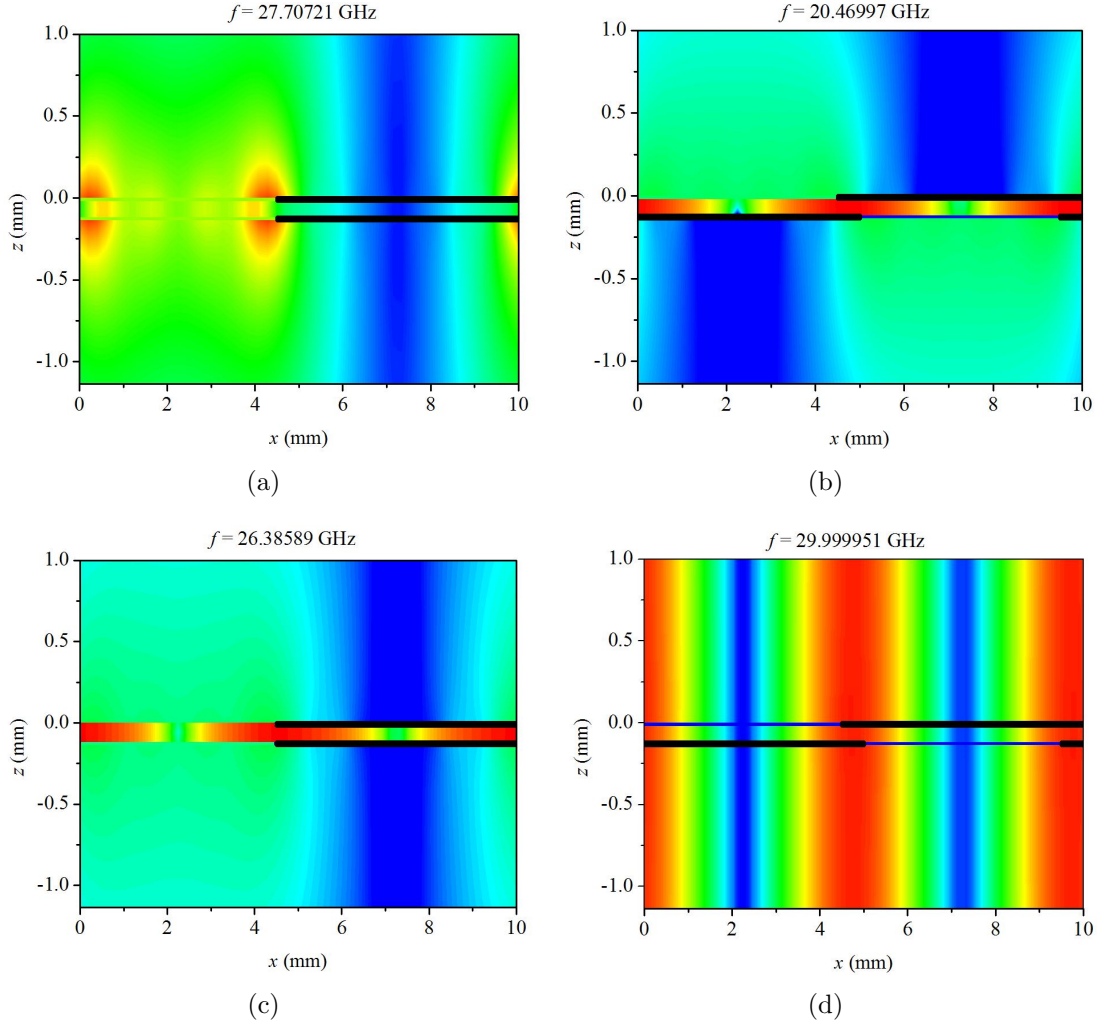


Figure 6.10: Complex magnitude \vec{E} field plots in the xz -plane for a double mesh layer system with pitch $d = 10 \text{ mm}$, square holes of side length $a = 4.5 \text{ mm}$ and mesh separation $g = 0.1 \text{ mm}$ at: (a) $f \approx 27.7 \text{ GHz}$ with misalignment $b_x = 0 \text{ mm}$, $b_y = 0 \text{ mm}$; (b) $f \approx 20.4 \text{ GHz}$ with misalignment $b_x = 5 \text{ mm}$, $b_y = 0 \text{ mm}$; (c) $f \approx 25.5 \text{ GHz}$ with misalignment $b_x = 0 \text{ mm}$, $b_y = 0 \text{ mm}$; (d) $f \approx 29.9 \text{ GHz}$ with misalignment $b_x = 5 \text{ mm}$, $b_y = 0 \text{ mm}$. The metal meshes are represented by thick black lines and the colour scale ranges from blue for a high negative field and red for a high positive field.

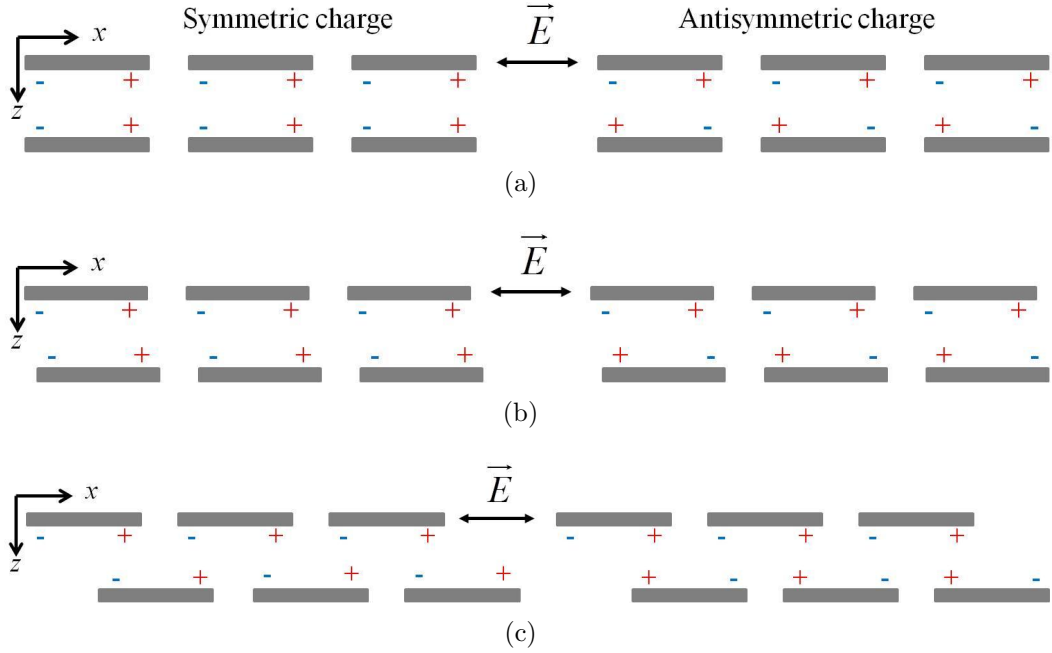


Figure 6.11: *Schematic of possible charge distributions for a double layer of identical metal slit arrays (i.e., one dimensional grids) when: (a) the layers are exactly aligned with respect to each other; (b) slightly laterally misaligned with respect to each other, and; (c) at maximum lateral misalignment with respect to each other.*

Figure 6.12 shows the directional electric fields in region III (between the two meshes) for the structure with 1 mm separation between the meshes. When the meshes are aligned, the symmetric charge configuration (cosh-like mode) is evident for the sharp mode (figure 6.12(a)), whilst the antisymmetric configuration of the surface like mode is shown for the broad mode (figure 6.12(b)). When the meshes are laterally misaligned with respect to each other by 5 mm, the hybrid symmetric (with respect to the charge configuration) mode (figure 6.12(c)) and the antisymmetric hybrid mode (figure 6.12(d)) corresponding to the charge configurations in figure 6.11(c) are illustrated.

6.4.2 Lateral displacement perpendicular to the incident polarisation

Comparison of the transmission response for the maximum lateral displacement of the two meshes relative to each other, both parallel and perpendicular to the incident polarisation, illustrates that the direction of the displacement relative to the polarisation has a significant effect on the EM response of the structure (figure 6.13). As the sepa-

6. The Microwave Response of Closely Spaced Metal Meshes

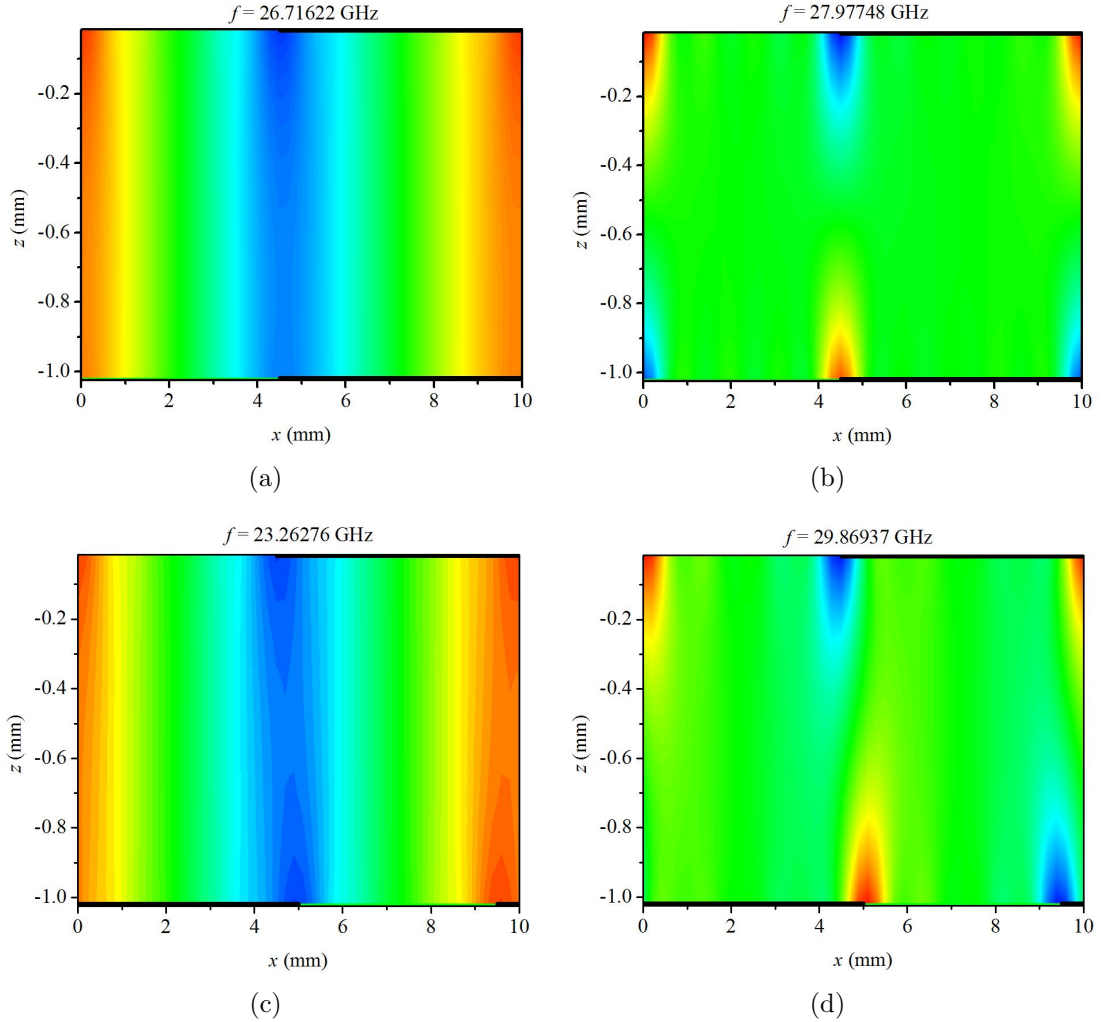


Figure 6.12: Directional \vec{E} field plots in the xz -plane in the region between the two meshes for a double mesh layer system of pitch $d = 10$ mm, square holes of side length $a = 4.5$ mm and mesh separation $g = 1$ mm at: (a) $f \approx 26.7$ GHz with misalignment $b_x = 0$ mm, $b_y = 0$ mm; (b) $f \approx 28.0$ GHz with misalignment $b_x = 0$ mm, $b_y = 0$ mm; (c) $f \approx 23.3$ GHz with misalignment $b_x = 5$ mm, $b_y = 0$ mm; (d) $f \approx 29.9$ GHz with misalignment $b_x = 5$ mm, $b_y = 0$ mm. The metal meshes are represented by thick black lines and the colour scale ranges from blue for a high negative field and red for a high positive field.

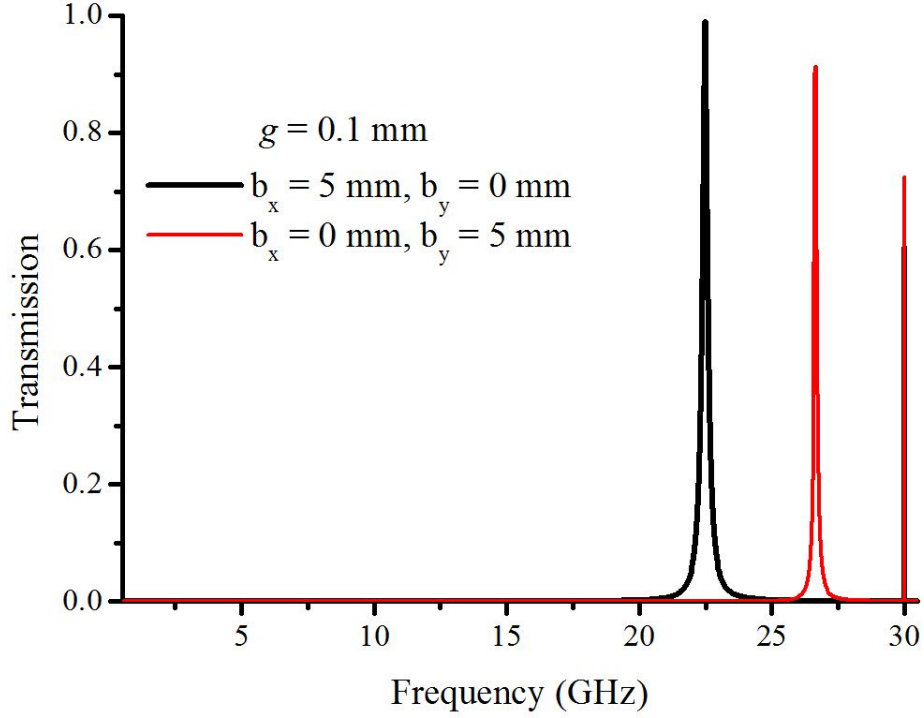
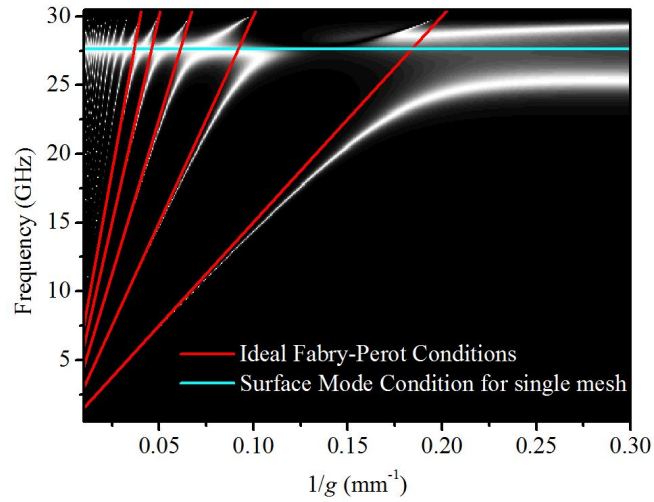


Figure 6.13: *Transmission response for two meshes laterally misaligned relative to each other both parallel (black line) and perpendicular to (red line) the incident polarisation at normal incidence. Both meshes have a pitch of $d = 10$ mm and square hole of side length $a = 4.5$ mm. The red line represents relative misalignment of $b_x = 0$ mm, $b_y = 5$ mm and the black line represents relative misalignment of $b_x = 5$ mm, $b_y = 0$ mm. The incident radiation is polarised parallel to the x -axis.*

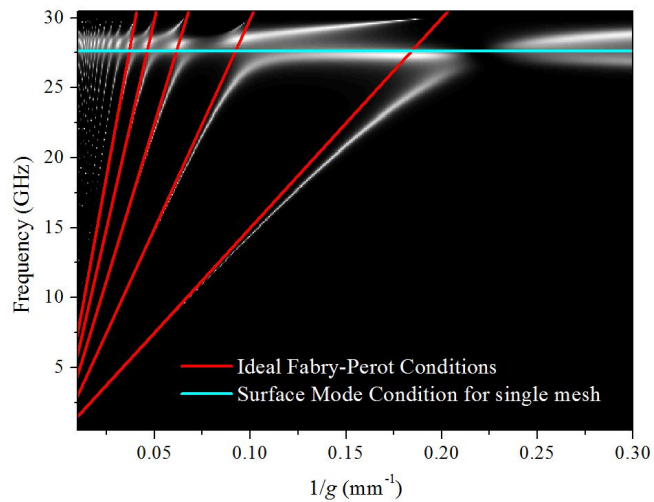
ration between the meshes increases, the near-field effects become less significant and the response of the perpendicular laterally misaligned structure approaches that of the parallel laterally misaligned structure and the aligned structure as explained in section 6.4.1 and figure 6.6 (i.e., the layers can be approximated as an effective homogeneous media).

The difference in the EM responses between the two incident polarisation directions is even more apparent in figure 6.14, which compares how the transmission resonance varies as a function of mesh separation for misalignment both parallel and perpendicular to the incident polarisation vector. As expected, when the separation between the meshes is small, there is significant differences between the transmission responses for each polarisation direction. However, perhaps what is more surprising is that there are still evident differences when the mesh separation is greater than the wavelength, i.e. $g > \lambda$.

6. The Microwave Response of Closely Spaced Metal Meshes



(a)



(b)

Figure 6.14: *Greyscale plot of the normal incidence transmission as a function of frequency and mesh separation with pitch of $d = 10$ mm and holes of side length $a = 4.5$ mm for (a) $b_x = 5$ mm, $b_y = 0$ mm and (b) $b_x = 0$ mm, $b_y = 5$ mm. The ideal Fabry-Pérot conditions refer to the half-wavelength condition (i.e., $\lambda = 2g/n$ for $n = 1, 2, 3, \dots$).*

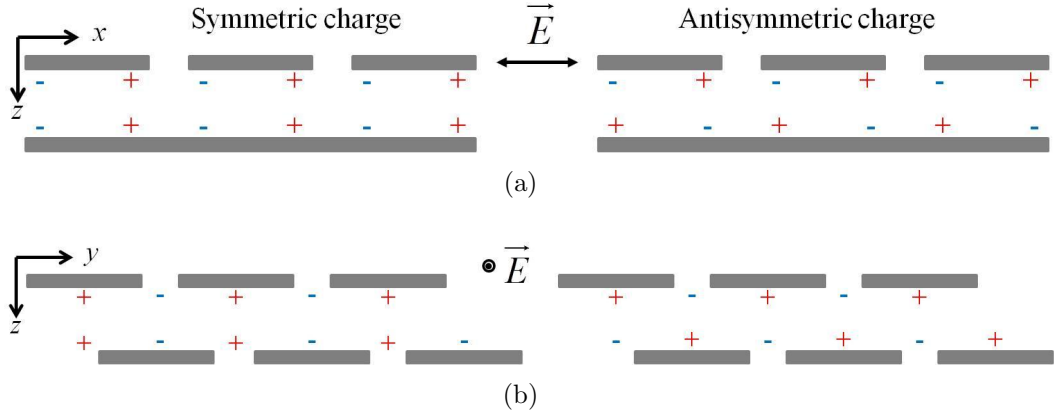


Figure 6.15: *Schematic of possible charge distributions for a double layer metal grids at maximum misalignment with respect to each other where the misalignment is perpendicular to the incident radiation for; (a) xz -plane and (b) yz -plane.*

Considering the possible charge distributions in the same manner as for the parallel misalignment case (section 6.4.1) it is clear that a different field distribution is to be expected as illustrated in figure 6.15. Along the x -axis of the structure, the second layer is continuous metal below the hole due to the unit cell being misaligned perpendicular to the incident radiation. As with the parallel misalignment, there are two possible configurations and as before, they are not equal in energy. However, the energy levels for the antisymmetric charge configurations (symmetric field profile) are different for each polarisation. The field plots between the two metal layers are illustrated in figure 6.16. The fields in the holes are in the form of waveguide modes and in this case, as the incident radiation is polarised parallel to the x axis, are therefore quantised in the y -direction. The effect of misaligning the two holes perpendicular to the incident field is clearly seen in the perturbation of the fields in figure 6.16(c).

6.5 Summary

The electromagnetic transmittance of a double layer of identical square arrays of square holes (mesh) in a perfectly conducting sheet has been analytically modelled using a modal matching technique. The structure supports families of standing wave modes together with surface modes that, close to the onset of diffraction, interact with each other. For frequencies below the onset of diffraction it is the strength of this interaction mediated by evanescent diffraction in the near fields that dictates the electromagnetic response, which is studied as a function of mesh separation and the lateral misalignment

6. The Microwave Response of Closely Spaced Metal Meshes

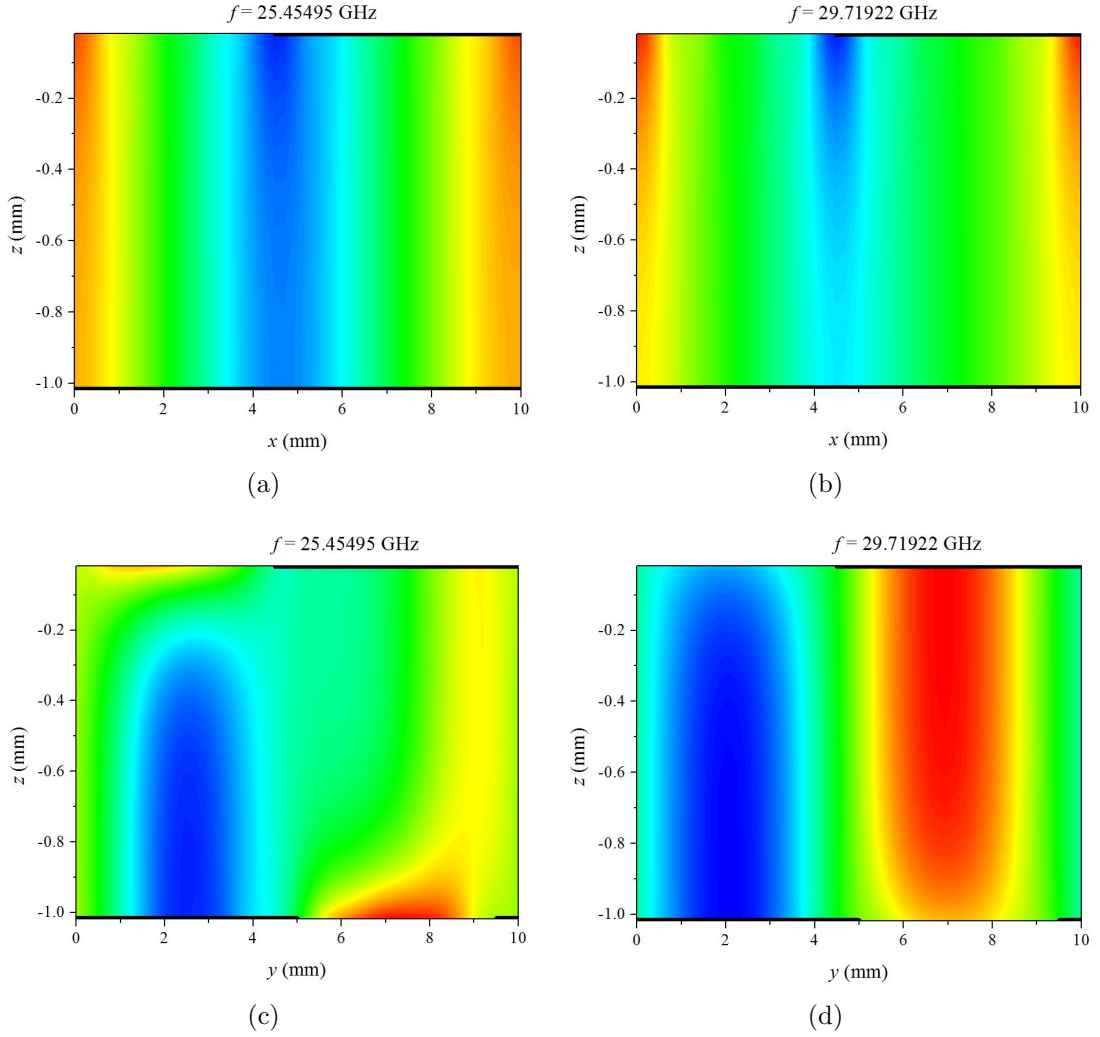


Figure 6.16: \vec{E} field plots in the region between the two meshes for a double mesh layer system of pitch $d = 10 \text{ mm}$, square holes of side length $a = 4.5 \text{ mm}$ and mesh separation $g = 1 \text{ mm}$ with misalignment $b_x = 0 \text{ mm}$, $b_y = 5 \text{ mm}$ at: (a) $f \approx 25.5 \text{ GHz}$ in the xz -plane; (b) $f \approx 29.7 \text{ GHz}$ in the xz -plane; (c) $f \approx 25.5 \text{ GHz}$ in the yz -plane; (d) $f \approx 29.7 \text{ GHz}$ in the yz -plane. The metal meshes are represented by thick black lines and the colour scale ranges from blue for a high negative field and red for a high positive field.

6. The Microwave Response of Closely Spaced Metal Meshes

between the meshes.

In conclusion, using an adapted modal matching method, a complete analytical solution for transmission through a double layer of PEC mesh with dielectric spacing has been developed by extending a previous method. Examination of the numerical results and analytic equations shows that the EM response of the system is highly dependent on the strength of the evanescent diffraction. Families of modes are supported and at low frequencies these are Fabry-Pérot-like. However, as the frequency approaches that of the surface mode supported by a single mesh layer as described in chapter 4, the modes are perturbed becoming more surface mode-like in character. The solution shows that it is the separation between the mesh layers that is the critical parameter; whilst the misalignment of the meshes with relation to one another is only significant in the regime where the separation is less than the wavelength. Exploration of the analytical expressions obtained for the transmission through the structure and the field profiles gives an insight into the behaviour of the observed resonances by determining the conditions in which the alignment terms become dominant. In particular in the case of closely spaced layers, as the lateral misalignment of the meshes with respect to each other increases, the perturbation of the charge distributions on each mesh causes greater enhancement of the electric field between the two meshes.

The exploration of this structure has been confined to the case where the lateral displacement is in one direction only, either parallel or perpendicular to the direction of polarisation. As originally discussed in chapter 5 and illustrated again in this chapter, in systems with two-fold symmetry (as here) as opposed to four-fold symmetry, the choice of incident polarisation can have a marked effect on the EM response of the system. This raises the question as to what the expected response would be to lateral two-dimensional translation of one mesh with respect to the other. This possibility is briefly explored in chapter 8.

Chapter 7

The Microwave Response of Finite Multilayer Stacks of Alternating Metal Meshes

7.1 Introduction

Multilayer structures have been the focus of an extensive body of research over many years [163–170]. Conventional multilayer structures consist of dielectric-dielectric stacks [166] (generally referred to as Bragg stacks) where each dielectric layer is the same thickness and the refractive indices of the layers, n_1, n_2 are altered with one dielectric having a high refractive index and the other a low index. When illuminated by radiation with a wavelength of the order of the layer thickness, resonant features are observed at wavelengths that are multiples of the layer thickness, comprising of band-pass and band-gap regions. However, in 1939 Geffcken [171] investigated thin film stacks comprising metal-dielectric layers. The observed resonant transmission features were found to be far narrower than those observed in conventional Bragg stacks. By altering the thickness of the layers, the frequency of the band-pass and band-gap regions can be altered, or ‘tuned’. This ‘tuneability’ has led to applications in electromagnetic shielding, perfect lenses and non-linear photonics [163–165, 172]. Although the majority of the studies have been in the visible regime, there have been some recent studies at microwave frequencies [173–175].

This chapter looks at the highly interesting response of multilayer stacks consisting of layers of metal mesh and dielectric where the mesh layers contain two different

7. The Microwave Response of Finite Multilayer Stacks of Alternating Metal Meshes

alternating meshes. The motivation for exploring multilayer systems with this particular geometry was provided by two presentations by Timothy Atherton [176, 177] based on previous work by Moore and Balents on topological insulators in two dimensional magnetic systems [178]. Their initial theoretical work into the existence of topological insulators in one dimensional systems had suggested that analogies to these states may be physically observable in 1D photonic crystal systems [176].

The word topology is derived from the Greek $\tau\omicron\pi\omicron\zeta$ (meaning place) and $\lambda\omicron\gamma\omicron\alpha$ (meaning study) [179]. This area of study is believed to have started in 1736 with Euler's paper on the Seven Bridges of Königsberg [180], although the term topology was not coined until far later by Listing in 1847 [181, 182]. Topology in its current form is heavily based on Cantor's set theory with the seminal work coming from Poincaré in 1895 [183]. Topology has applications in a wide range of subjects, from biological systems [184, 185] to social networking models [186] to physical systems [187, 188] and astrophysics [189].

The next section 7.2 provides a brief discussion of the physics governing the response of multilayer systems, beginning with the Fresnel coefficients for reflection and transmission (7.2.1). Conventional Bragg stack responses are then summarised (7.2.2), followed by a brief introduction to topology (7.2.3). Section 7.3 details the methods used to model the response of metal mesh and dielectric stacks, looking at both modal matching models and effective medium approaches. The results of this modelling and the implications of these results is discussed in section 7.4. The section is separated into two main parts: the first part (7.4.1) considers a double mesh structure with differing meshes and compares the modal matching model with an effective medium approach; whilst the second section is concerned with the response of multilayer structures of the same alternate mesh configuration for larger numbers of layers (7.4.2). This section presents the emergence of a topological mode for certain configurations. Finally the chapter finishes with a summary of the salient results in section 7.5.

7.2 Background

7.2.1 Fresnel Equations

When light is incident upon an interface between dissimilar media a proportion is reflected with the remainder being transmitted. In multilayer structures this happens at each interface (figure 7.1).

7. The Microwave Response of Finite Multilayer Stacks of Alternating Metal Meshes

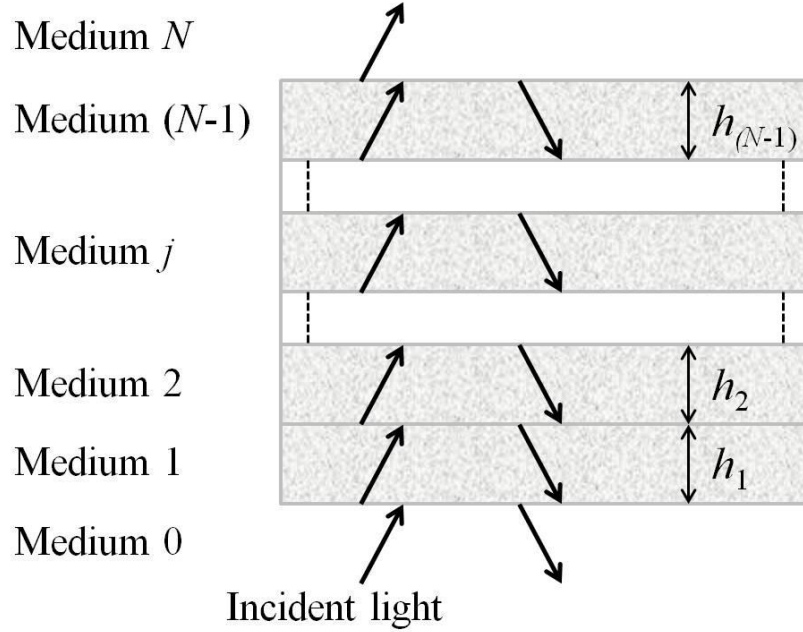


Figure 7.1: Schematic of light propagating through a planar multilayer structure with $(N-1)$ layers.

7.2.1.1 Single Interface Fresnel Equations

The following derivation is adapted from that by Born and Wolf [136]. Consider a single interface as shown in figure 7.2 between two media, labelled 1 and 2, with characteristic relative permittivities ϵ_1 , ϵ_2 and the assumption that the media are non-magnetic and therefore the relative permeabilities μ_1 , μ_2 are both equal to 1. The magnitude of the wavevectors in the media are assigned the variables k_1 and k_2 respectively.

The free space wavevector k_0 is defined as

$$k_0 = \frac{2\pi}{\lambda_0}, \quad (7.1)$$

where λ_0 is the wavelength of light in free space. The wavevector k_i in a medium i is given as

$$k_i = \sqrt{\epsilon_i} k_0, \quad (7.2)$$

where ϵ_i is the relative permittivity of the medium i .

Defining the axes as in figure 7.2 and the angle between k_i and the z -axis as being θ , the magnitude of the wavevector is related to the magnitudes of its components by

7. The Microwave Response of Finite Multilayer Stacks of Alternating Metal Meshes

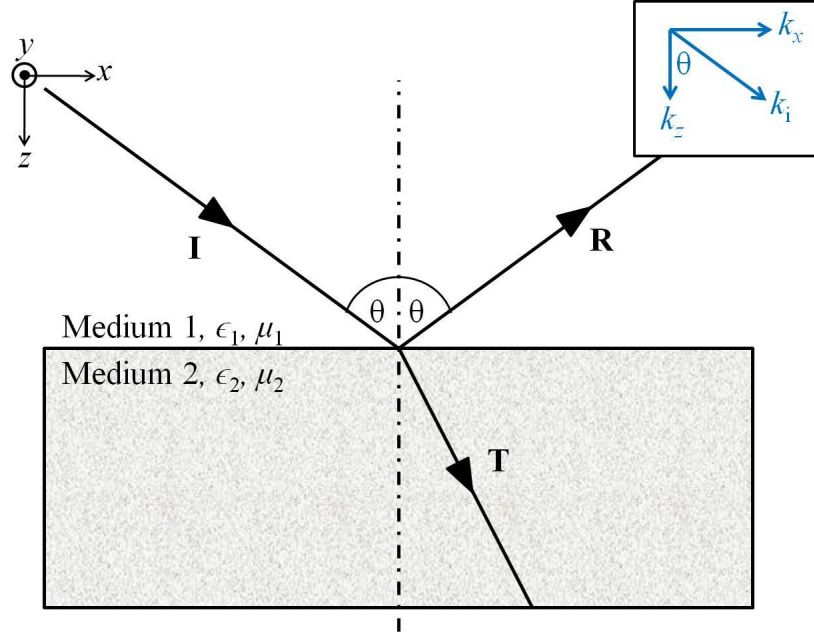


Figure 7.2: Schematic showing the reflection (R) and transmission (T) of incident light (I) at a single interface between two different media. The Cartesian coordinates of the wavevector in medium i are shown in the inset.

the following relations:

$$k_i = \sqrt{k_x^2 + k_z^2}; \quad \cos \theta = \frac{k_z}{k_i}; \quad \sin \theta = \frac{k_x}{k_i}. \quad (7.3)$$

p-Polarisation

The reflection and transmission coefficients of an interface are determined by applying the boundary conditions that the tangential EM field components must be continuous across the interface. Firstly propagation directions need to be chosen for the incident, reflected and transmitted fields and the components present depend on the incident polarisation. For *p*-polarisation, \vec{E} is in the plane of incidence and the propagation vector, \vec{k}^I , has been defined as propagating in the positive x -direction. At the interface the propagation vector, \vec{k}^R , for the reflected \vec{E} field has also been chosen to be propagating in the positive x -direction. The chosen field directions are illustrated in figure 7.3.

The tangential boundary conditions give us the following relationship between the incident, reflected and transmitted components of E_x :

$$\vec{E}_I \cos \theta_I - \vec{E}_R \cos \theta_R = \vec{E}_T \cos \theta_T. \quad (7.4)$$

7. The Microwave Response of Finite Multilayer Stacks of Alternating Metal Meshes

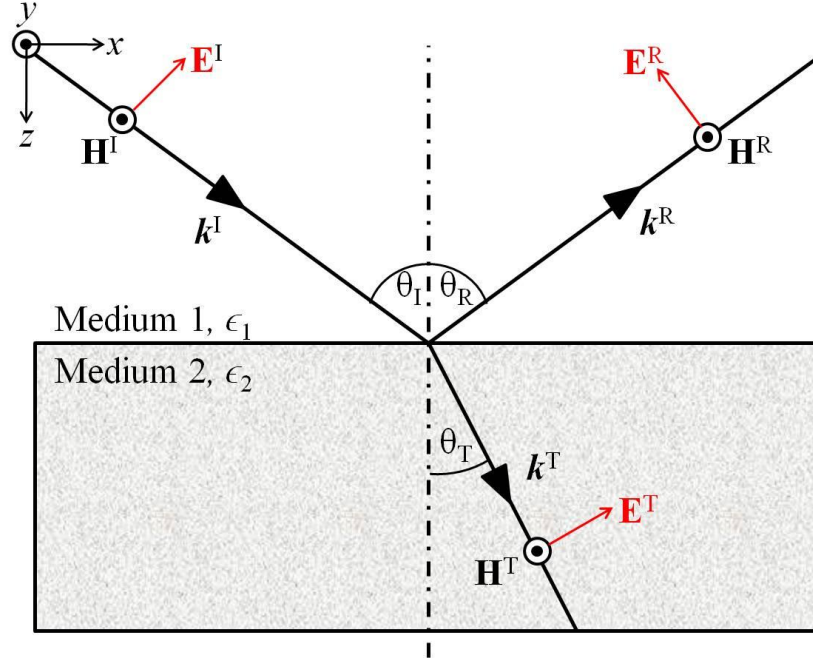


Figure 7.3: *The incident, reflected and transmitted fields associated with a p-polarised wave incident on a planar interface between two different media.*

Using the relation stated in equation 7.3, this can be written in terms of k-vectors:

$$\left(\vec{E}_I - \vec{E}_R\right) \frac{k_{1z}}{k_1} = \vec{E}_T \frac{k_{2z}}{k_2}. \quad (7.5)$$

The continuity requirement for tangential \vec{E} , also gives us the relation

$$\vec{H}_I + \vec{H}_R = \vec{H}_T. \quad (7.6)$$

This can be written as

$$\left(\vec{E}_I + \vec{E}_R\right) k_1 = \vec{E}_T k_2, \quad (7.7)$$

using Maxwell's equation

$$\frac{\vec{E}}{\vec{H}} = \frac{\omega}{k_i}, \quad (7.8)$$

where ω is the angular frequency. Equations 7.5 and 7.7 can be rearranged to give an expression for \vec{E}_T , which can then be eliminated by combining the resultant expressions to give

$$\left(\vec{E}_I - \vec{E}_R\right) \frac{k_{1z}k_2}{k_{2z}k_1} = \left(\vec{E}_I + \vec{E}_R\right) \frac{k_1}{k_2}. \quad (7.9)$$

7. The Microwave Response of Finite Multilayer Stacks of Alternating Metal Meshes

Using the definition of k_i given in equation 7.3 and rearranging results in

$$\vec{E}_R \left(\frac{k_{1z}\sqrt{\epsilon_2}}{k_{2z}\sqrt{\epsilon_1}} + \frac{\sqrt{\epsilon_1}}{\sqrt{\epsilon_2}} \right) = \vec{E}_I \left(\frac{\sqrt{\epsilon_1}}{\sqrt{\epsilon_2}} - \frac{k_{1z}\sqrt{\epsilon_2}}{k_{2z}\sqrt{\epsilon_1}} \right). \quad (7.10)$$

The amplitude reflection coefficient is the ratio of the reflected and initial field components,

$$\frac{\vec{E}_R}{\vec{E}_I} = r_p = \frac{(k_{1z}\epsilon_2 - k_{2z}\epsilon_1)}{(k_{1z}\epsilon_2 + k_{2z}\epsilon_1)}. \quad (7.11)$$

Equations 7.5 and 7.7 can also be rearranged to eliminate \vec{E}_R instead. This gives the relation

$$\vec{E}_I - \vec{E}_T \left(\frac{k_{2z}k_1}{k_{1z}k_2} \right) = \vec{E}_T \left(\frac{k_2}{k_1} \right) - \vec{E}_I. \quad (7.12)$$

Using the same method as before, the amplitude transmission coefficient is the ratio of the transmitted and initial field components and is given by:

$$\frac{\vec{E}_T}{\vec{E}_I} = t_p = \frac{(2k_{1z}\sqrt{\epsilon_1\epsilon_2})}{(k_{2z}\epsilon_1 + k_{1z}\epsilon_2)}. \quad (7.13)$$

s-Polarisation

There is again a choice to be made for the direction of propagation of the waves. As before, the propagation vector \vec{k}^I is defined as propagating in the positive x and z -direction as illustrated in figure 7.4.

Tangential E and H must be conserved, giving the following two equations:

$$\frac{k_{1z}}{k_{2z}}(\vec{E}_I - \vec{E}_R) = \vec{E}_T \quad (7.14)$$

and

$$(\vec{E}_I + \vec{E}_R) = \vec{E}_T. \quad (7.15)$$

Using equation 7.15 for \vec{E}_T and substituting this into the conservation requirement gives

$$(\vec{E}_I + \vec{E}_R) = (\vec{E}_I - \vec{E}_R) \frac{k_{1z}}{k_{2z}}. \quad (7.16)$$

Rearranging this gives us the amplitude reflection coefficient,

$$\frac{\vec{E}_R}{\vec{E}_I} = r_s = \frac{k_{1z} - k_{2z}}{k_{1z} + k_{2z}}. \quad (7.17)$$

7. The Microwave Response of Finite Multilayer Stacks of Alternating Metal Meshes

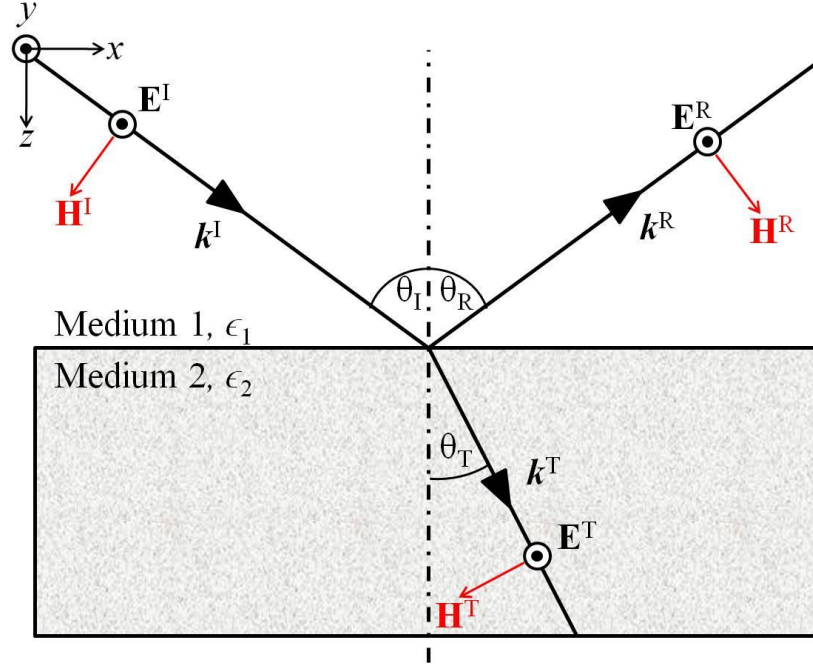


Figure 7.4: *The incident, reflected and transmitted fields associated with a s-polarised wave incident on a planar interface between two different media.*

Rearranging equation 7.15 and using the conservation requirement to eliminate \vec{E}_T , and rearranging the resulting expression gives us an equation for the amplitude transmittance coefficient of

$$\frac{\vec{E}_T}{\vec{E}_I} = t_s = \frac{2k_{1z}}{k_{1z} + k_{2z}}. \quad (7.18)$$

7.2.1.2 Recursive Fresnel Equations

Now consider a system with three different media. The incident wave will be partially reflected and partially transmitted at the first interface. The transmitted part will continue to propagate through the media until it reaches the second interface. Again, part of the wave will be transmitted through the interface to medium 3 and part of the wave will be reflected. When this reflected wave reaches the interface between media 2 and 1, it will again be partially reflected and partially transmitted, and so on. Using the Fresnel coefficients above, the fraction reflected and transmitted at each interface can be calculated. All the contributions can then be added together to calculate the net wave reflected back into medium 1 and the net wave transmitted into medium 3. The important point to remember is that the phase differences between the different

7. The Microwave Response of Finite Multilayer Stacks of Alternating Metal Meshes

contributions must be accounted for.

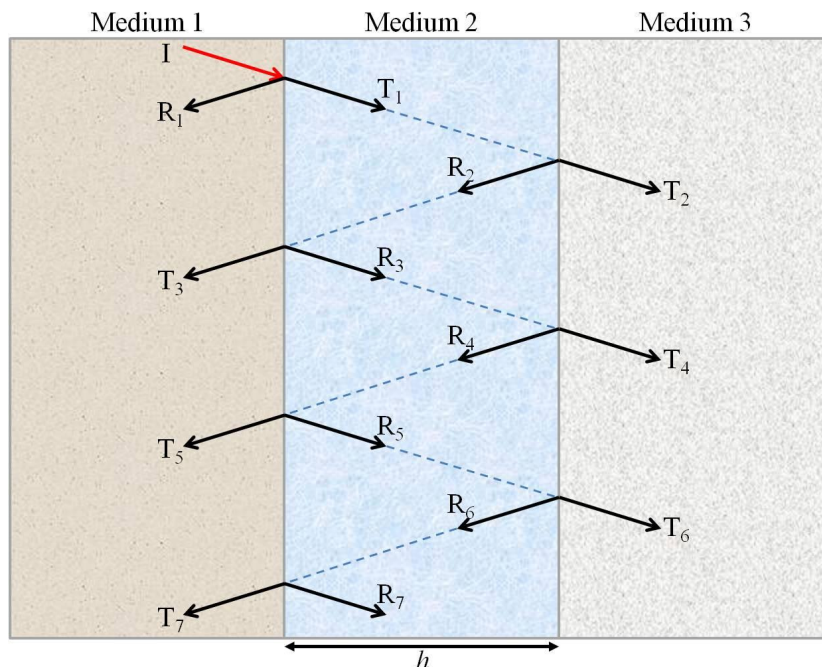


Figure 7.5: *Schematic of EM waves propagating in a three media system.*

Figure 7.5 illustrates a wave propagating in a three media system. The net reflected wave at the first interface is the sum of all the different contributions. Defining the net reflected wave as R and r_{ij} as the reflection amplitude coefficient between media i and j , and using the notation in figure 7.5, we have the following two relations for R :

$$R = Ir_{13} \quad (7.19)$$

and

$$R = R_1 + T_3 + T_5 + T_7 + \dots \quad (7.20)$$

From figure 7.5 we have the following equations for each contribution:

$$R_1 = Ir_{12},$$

$$T_3 = It_{12}t_{21}r_{23} \exp 2\beta,$$

$$T_5 = It_{12}t_{21}(r_{23})^2r_{21} \exp 4\beta$$

7. The Microwave Response of Finite Multilayer Stacks of Alternating Metal Meshes

and

$$T_7 = It_{12}t_{21}(r_{23})^3(r_{21})^2 \exp 6\beta, \quad (7.21)$$

where the phase change on propagation through the media is given by

$$\beta = ik_z h. \quad (7.22)$$

By combining these relations, R can be eliminated to produce an equation for the net reflection coefficient,

$$r_{13} = r_{12} + t_{12}t_{21}r_{23} \exp 2\beta(1 + r_{23}r_{21} \exp 2\beta + (r_{23})^2(r_{21})^2 \exp 4\beta + \dots). \quad (7.23)$$

This is a simple geometric series and therefore applying the standard result for the sum of geometric series gives

$$r_{13} = r_{12} + \frac{t_{12}t_{21}r_{23} \exp 2\beta}{1 - r_{23}r_{21} \exp 2\beta}. \quad (7.24)$$

Making use of the following relations

$$r_{21} = -r_{12}; \quad t_{12}t_{21} = (t_{12})^2; \quad (r_{12})^2 + (t_{12})^2 = 1, \quad (7.25)$$

gives an equation for the reflection amplitude coefficient of

$$r_{13} = \frac{r_{12} + r_{23} \exp 2\beta}{1 + r_{12}r_{23} \exp 2\beta}. \quad (7.26)$$

The same process can be applied to determine the transmission coefficient,

$$t_{13} = \frac{t_{12}t_{23} \exp \beta}{1 + r_{12}r_{23} \exp 2\beta}. \quad (7.27)$$

It is important to remember that the results are different for p - and s -polarisations. The single interface Fresnel coefficients for the relevant polarisation must be used. This theory can be expanded to account for any number of different media. In a system with N media, firstly the Fresnel coefficients for each of the interfaces are calculated. Then the last three media are considered (N , $N - 1$ and $N - 2$) and the Fresnel coefficients calculated for these interfaces using equations 7.26 and 7.27. This provides a formula for the reflection and transmission coefficient between layers $N - 2$ and N (i.e., $r_{(n-2)n}$ and $t_{(n-2)n}$). Equations 7.26 and 7.27 are used again to provide the coefficients for

7. The Microwave Response of Finite Multilayer Stacks of Alternating Metal Meshes

layers $N - 3$ and N and this process is repeated recursively until all the interfaces are considered.

7.2.2 Bragg Stacks and Metal-Dielectric Stacks

As described in section 7.1, a Bragg stack is a multilayer system consisting of alternating layers of dielectric material with differing refractive indices [166, 171]. The width of the each layer is such that it is one quarter of a specific wavelength, and these structures are often known as quarter-wave stacks. The transmission through the stack can be calculated using the recursive Fresnel equations described in the previous section. The reflected and transmitted components interfere with each other, with the interference between the layers dictating whether the structure transmits or reflects at a particular frequency. When the transmitted radiation interferes constructively, the multilayer structure shows enhanced transmission features [190] forming a band pass region; and conversely, when the interference is destructive, a band gap region is formed within which light is ‘forbidden’ to propagate as illustrated in figure 7.6. These band gap regions where the majority of the incident radiation is reflected occur around the specific wavelength related to the width of each layer. By altering the width of the layers, the frequencies where the band gaps occur can be chosen.

The electromagnetic response of metal-dielectric stacks also comprises band pass and band gap regions. The band pass regions (high transmission) correspond to exponential fields within the metal layer facilitating coupling between near standing wave resonances within each dielectric layer [191]. With the use of periodic metal meshes, these metal-dielectric stacks can be extended to operate in the lower frequency microwave and infrared regimes [174].

7.2.3 Topology

Topology is a branch of mathematics that studies properties that are unchanged by continuous transformations: for example, a sphere is topologically identical to an ellipsoid. A particularly clear example is given by the mathematical joke that asks what a topologist is, as illustrated in figure 7.7 [192].

However, topology is not restricted to geometrical objects, it is also used to describe movement of an electron gas [193], phase spaces and symmetry groups. In broad terms it is the study of qualitative properties that are invariant under certain transformations, or the study of continuity and connectivity. Another example of this is given by the

7. The Microwave Response of Finite Multilayer Stacks of Alternating Metal Meshes

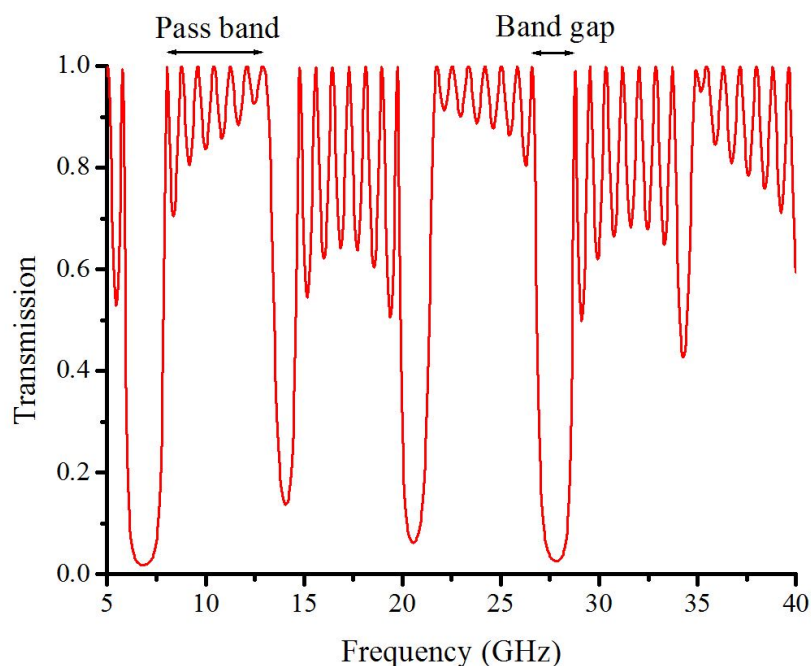


Figure 7.6: *Transmission through a multilayer Bragg stack of 16 layers of alternating dielectric with relative permittivity of 2 and 4. Each dielectric layer is 6.35 mm thick.*

Hilbert cube (figure 7.8), which is defined as a topological product of the intervals $[0, 1/p]$ for $p = 1, 2, 3, 4, \dots$. This can also be thought of as a cuboid where the lengths of the edges form the infinite sequence $1/p$ where $p \in \text{natural numbers}$. As the cube can also be constructed by an infinite number of unit cubes, it is topologically identical to a unit cube of infinite dimension. There are countless other examples of topology, however, these are beyond the scope of this thesis.

7.3 Methods

7.3.1 Adaptation of the Modal Matching Method for a Double Mesh Structure with Different Mesh Layers

Chapter 6 explored the EM response of a double mesh structure with two identical metal meshes. To adapt the method for use with a double mesh structure comprising two differing meshes is a relatively simple alteration. The general method is identical, however the parameters pertaining to the second mesh are used in the initial electric field equation for region IV (the mesh layer) as defined in figure 6.4. It is worth commenting on the limiting conditions on the mesh parameters. A unit cell for the structure

7. The Microwave Response of Finite Multilayer Stacks of Alternating Metal Meshes

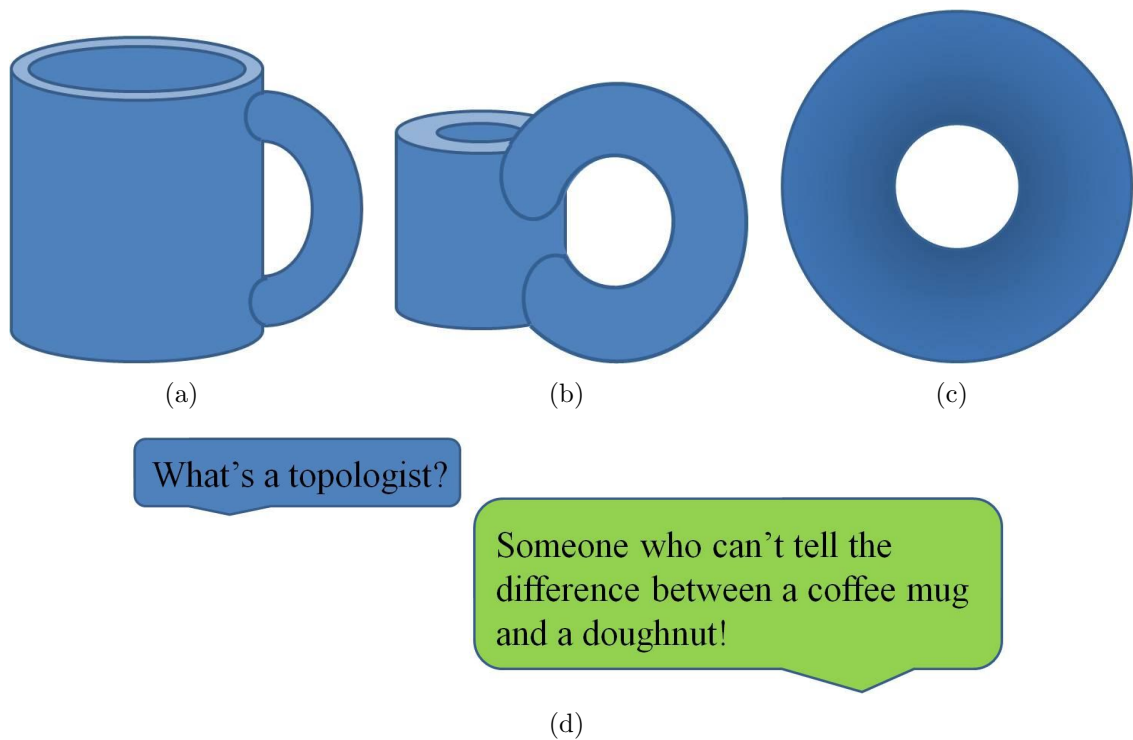


Figure 7.7: Schematic illustrating a mathematical joke regarding the identical topology of a coffee mug and a doughnut: (a) - (c) snapshots of the coffee cup deforming into the doughnut; (d) the original joke [192].

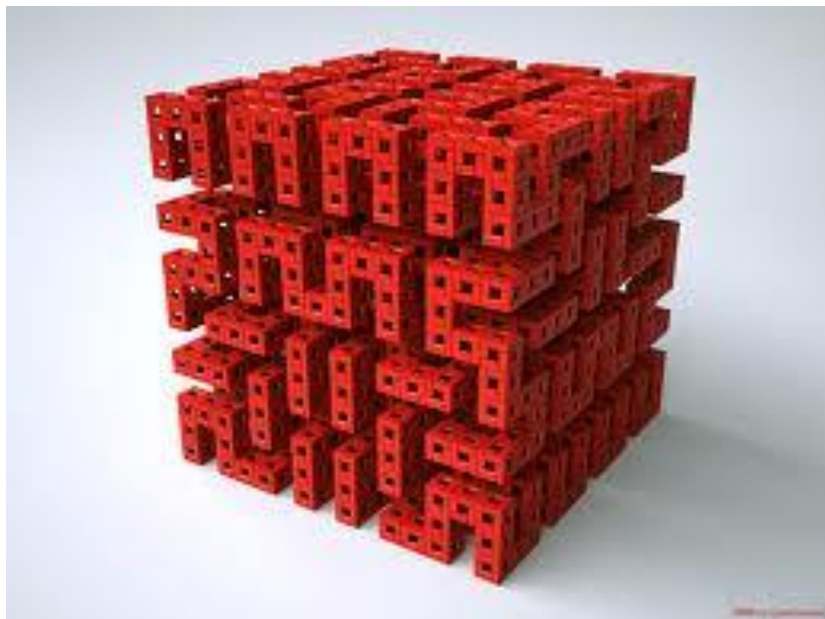


Figure 7.8: A Hilbert Cube [1].

7. The Microwave Response of Finite Multilayer Stacks of Alternating Metal Meshes

as a whole is required and therefore the period of each mesh must be the same or commensurate; this means that the only variable parameters between the two meshes are the hole size and mesh thickness. With that in mind, the overlap integrals for the upper and lower meshes (equations 6.8 and 6.9) become;

$$Q_{2top}^{m,n,0,1} = \int_0^{a_t} \int_0^{a_t} \sin\left(\frac{\pi y}{a_t}\right) \exp\left[-i\left(\frac{2m\pi}{d}\right)x\right] \exp\left[-i\left(\frac{2n\pi}{d}\right)y\right] dx dy \quad (7.28)$$

and

$$Q_{2bot}^{m,n,0,1} = \int_0^{a_b} \int_0^{a_b} \sin\left(\frac{\pi y}{a_b}\right) \exp\left[-i\left(\frac{2m\pi}{d}\right)x\right] \exp\left[-i\left(\frac{2n\pi}{d}\right)y\right] dx dy. \quad (7.29)$$

The simultaneous equations are solved providing expressions for the unknown amplitude coefficients.

7.3.2 Description of a Metal Mesh using an Effective Medium Approach

The description of a mesh layer as an effective homogeneous medium under certain conditions was introduced in section 6.4.1. The required conditions were that the meshes had to be far enough apart for the evanescent diffracted orders to be of little significance, i. e., the mesh separation must be greater than the incident wavelength. In these conditions, the microscopic details of the subwavelength structure are not communicated from one layer to the other. Using a technique detailed by Smith *et al*, the effective impedance, Z_{eff} , and the effective refractive index, n_{eff} can be determined from the reflection and transmission coefficients of the mesh [194]. The relationship between the normalised transmission amplitude coefficient, t , Z_{eff} , and n_{eff} is given as

$$t = \left(\cos [n_{eff} kd] - \frac{i}{2} \left(Z_{eff} + \frac{1}{Z_{eff}} \sin [n_{eff} kd] \right) \right), \quad (7.30)$$

where $k = \omega/c$. This relation is linked to the normalised reflection amplitude coefficient by

$$\frac{r}{t} = -\frac{1}{2}i \left(\cos [n_{eff} kd] - \frac{i}{2} \left(Z_{eff} + \frac{1}{Z_{eff}} \sin [n_{eff} kd] \right) \right). \quad (7.31)$$

7. The Microwave Response of Finite Multilayer Stacks of Alternating Metal Meshes

Equations 7.30 and 7.31 can be rearranged to give

$$\cos [n_{eff}kd] = \frac{1}{t} + \frac{i}{2} \left(Z_{eff} + \frac{1}{Z_{eff}} \right) \sin [n_{eff}kd] \quad (7.32)$$

and

$$\sin [n_{eff}kd] = \left(\frac{2iZ_{eff}}{Z_{eff}^2 - 1} \right) \left(\frac{r}{t} \right) \quad (7.33)$$

respectively. Equation 7.33 can be substituted into equation 7.32 and the trigonometric identity $\cos^2 [A] + \sin^2 [A] = 1$ used to obtain the relation

$$\left(\frac{r^2}{t^2} \right) \left(\frac{2iZ_{eff}}{Z_{eff}^2 - 1} \right)^2 + \frac{1}{t^2} \left(1 - r \left(\frac{Z_{eff}^2 + 1}{Z_{eff}^2 - 1} \right) \right)^2 = 1. \quad (7.34)$$

Solving equation 7.34 with respect to the effective impedance results in the following solution:

$$Z_{eff} = \pm \sqrt{\frac{1 + 2r + r^2 - t^2}{1 - 2r + r^2 - t^2}}. \quad (7.35)$$

Equation 7.33 can be rearranged to give a solution for n_{eff} in terms of Z_{eff} :

$$n_{eff} = \frac{c}{\omega d} \sin^{-1} \left(\frac{2iZ_{eff}}{Z_{eff}^2 - 1} \right) \left(\frac{r}{t} \right). \quad (7.36)$$

Therefore the mesh has now been described in terms of homogeneous effective parameters.

7.3.3 Application of the Effective Medium Approach to Multilayer Systems

Once a metal mesh has been described as an effective homogeneous medium, it is a relatively trivial matter to describe the transmission or reflection response for a multilayer system in terms of the recursive Fresnel coefficients. The structure investigated in this chapter is illustrated in figure 7.9 and comprises ‘N’ repeats of an ‘ACBC’ arrangement, where A and B are PEC meshes with different mesh parameters and C is a dielectric spacer. The dielectric for this system is air.

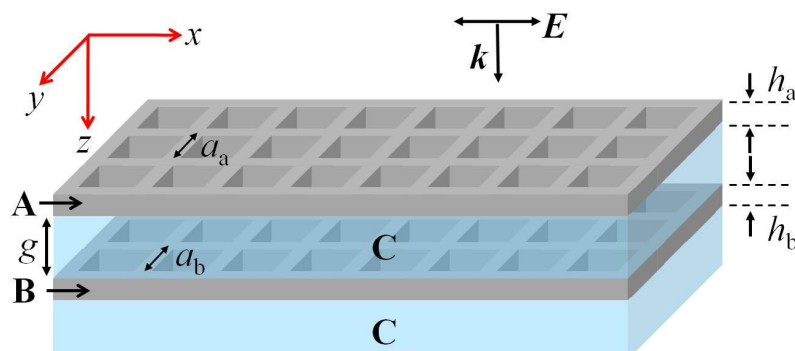


Figure 7.9: Schematic of the unit cell in the z -direction of an ‘ACBC’ multilayer arrangement. A and B are PEC meshes with square holes of side length a_a and a_b and mesh thickness of h_a and h_b respectively. C is a dielectric spacer layer of air. The mesh layers are a distance g apart.

7.4 Results and Discussion

The results and discussion section of the chapter has been separated into two main sections: The first section concerns a single unit cell in the z -direction, i.e. two mesh layers, one of mesh A and one of mesh B . The second section considers multiple unit cells in the z -direction.

7.4.1 Double Mesh Structure with Different Mesh Layers

To verify the veracity of the results gained using the effective medium approximation, the transmission response for a double mesh structure, with a pitch of $d = 5$ mm and a hole size of $a = 4.85$ mm with the meshes a distance $g = 6$ mm apart, was predicted using the effective medium approximation detailed in sections 7.3.2 and 7.3.3. This was then compared with the response from the modal matching approach for a double mesh structure as discussed in chapter 6 and the results are illustrated in figure 7.10.

7.4.1.1 Comparison of Effective Medium Approach with Modal Matching Method

Figure 7.10 shows that the predicted transmission response using the effective medium approximation is identical to that of the modal matching approach. This shows clearly that the mesh layer can be represented by an effective homogeneous medium and that little microscopic information regarding the subwavelength structure is communicated. The pitch of the meshes is 5 mm and therefore the onset of diffraction occurs at 60

7. The Microwave Response of Finite Multilayer Stacks of Alternating Metal Meshes

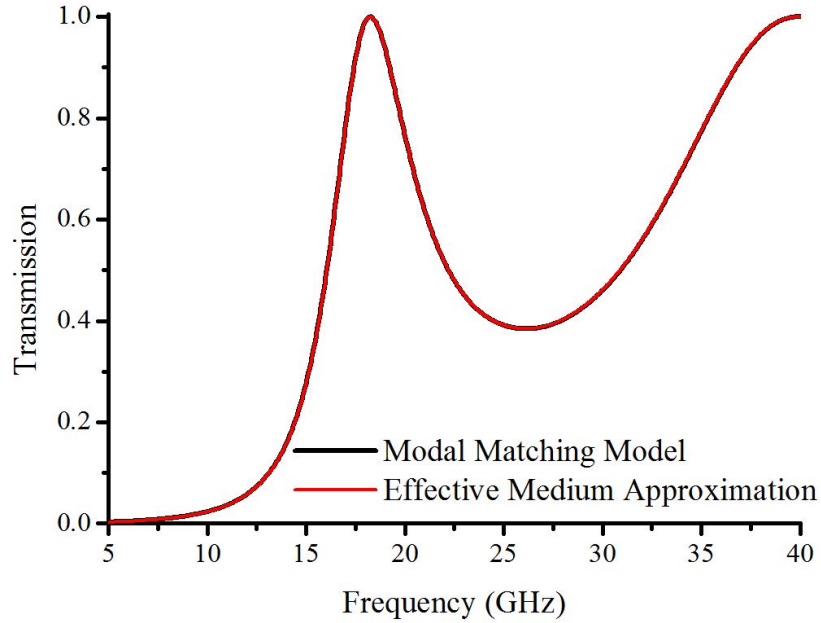


Figure 7.10: *Transmission response at normal incidence for a double mesh structure comparing the modelled response from an effective medium approximation with that from a modal matching model. The PEC meshes have a pitch $d = 5$ mm and a hole side length of 4.85 mm and are a distance $g = 6$ mm apart.*

GHz. Figure 7.10 illustrates the EM response of the structure between 5 GHz and 40 GHz, far from the onset of diffraction. The transmission peaks correspond to near-standing-wave resonances within the dielectric layer and replicate the behaviour of metal-dielectric structures in the visible regime [191, 195, 196]. As described by Butler *et al* the fields within the sub-cutoff holes of the mesh decay exponentially, with the decay length being determined by the geometry of the mesh [174], with a larger pitch corresponding to a shorter decay length. This implies that if the separation between the mesh layers, g , was decreased, there would come a point where the decay length of the fields would overlap allowing the meshes to couple together via their near fields, thereby perturbing the response of the structure. At this point, the effective medium approximation would be unable to describe the EM response of the structure accurately. Figure 7.11 illustrates the transmission response of the double mesh structure for the same mesh parameters as in figure 7.10 as the separation, g , is decreased for both the modal matching technique and the effective medium approximation.

In figure 7.11(a), both methods give near identical responses; however, differences between the modelled responses are beginning to appear at a separation of 3 mm between the meshes (figure 7.11(b)), although both methods give qualitatively similar

7. The Microwave Response of Finite Multilayer Stacks of Alternating Metal Meshes

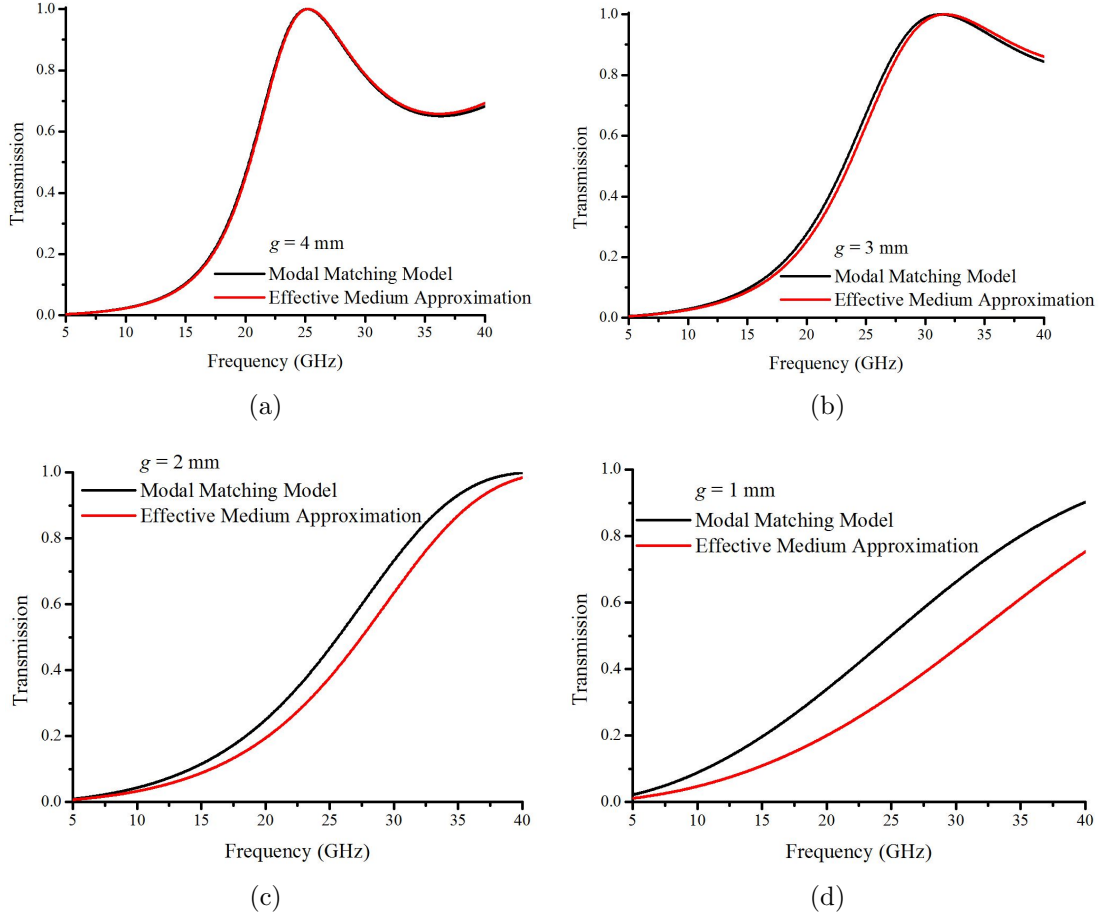


Figure 7.11: Transmission response at normal incidence for a double mesh structure comparing the modelled response from an effective medium approximation with that from a modal matching model for different mesh separations. The PEC meshes have a pitch $d = 5$ mm and a hole side length of 4.85 mm and are a distance; (a) $g = 4$ mm, (b) $g = 3$ mm, (c) $g = 2$ mm, (d) $g = 1$ mm apart.

results. As the separation between the meshes is decreased further, the discrepancy between the results becomes greater, until the effective medium approximation is no longer able to describe the EM response of the meshes with any degree of accuracy (figure 7.11(d)). As described in section 6.4, as the separation between the two meshes decreases, the observed resonance increases in frequency due to being perturbed by the hybrid structure resonance as it approaches the onset of diffraction. The decay length of the first order field component is illustrated in figure 7.12 for the relevant frequency range indicating a decay length of approximately 1 mm, as reported by Butler *et al* for the same pitch mesh [174], where the decay length, τ is given by $1/k_z^{m,n}$.

From the discussion of the results in chapter 6 (section 6.4.1) it has been shown that

7. The Microwave Response of Finite Multilayer Stacks of Alternating Metal Meshes

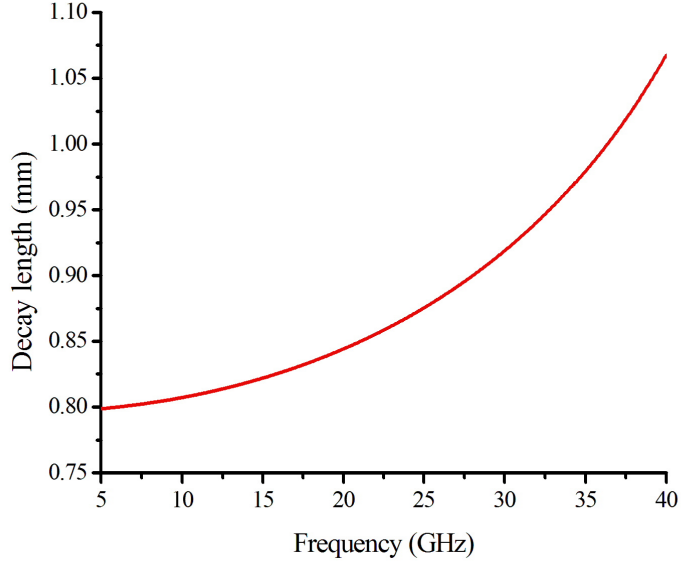


Figure 7.12: *Decay length of the fields for a mesh with period $d = 5$ mm for the frequency range 5 - 40 GHz.*

the separation between the meshes is a dominant parameter in determining the transmission response of the structure, with the resonant features arising from diffractively coupled surface waves. In particular, any relative misalignment between the layers is of little significance if the layers are far apart. The explanation was that close to the onset of diffraction, the evanescent fields are at their strongest and this was responsible for coupling of the surface waves between the meshes. In the present case, the pitch is extremely subwavelength and therefore evanescent diffraction would have a far less significant role as the onset of diffraction occurs at a much higher frequency (60 GHz). The resonant features in this structure are not due to diffractively coupled surface waves but due to standing waves in the dielectric layers coupled via the evanescent fields within the mesh layer [174].

Examination of equations 6.11 to 6.19 provide further insight into the role of the decay length. Using the decay length, τ , equation 6.19 can be written as

$$K = \frac{a}{\tau} + \tau \left(\frac{2m\pi}{d} \right)^2. \quad (7.37)$$

Equation 7.37 indicates a clear relationship between the decay length and the significance of the evanescent diffracted orders on the EM response. If τ is large, then the term containing the diffracted orders will dominate K , whilst if τ is small, the first term

7. The Microwave Response of Finite Multilayer Stacks of Alternating Metal Meshes

dominates and the evanescent diffracted orders term becomes insignificant. As $k_z^{m,n}$ is a function of both the frequency and the pitch of the mesh (equation 3.8) the decay length can be increased by either increasing the frequency of the incident radiation or decreasing the pitch. Therefore the effective medium approach can be used in the regime where $\tau \ll g$; however as τ approaches g , it is no longer a valid approximation due to an inability to describe the near-fields accurately.

7.4.2 Multilayer Structures

As discussed in the introduction to this chapter (section 7.1), the EM response of multilayer metal-dielectric structures has been a topic of interest for many years, building on the work of Geffcken in 1939 [171]. Section 7.4.1 looked at the response of a single unit cell (ACBC) as described in figure 7.9. This section looks at the response of structures comprising N unit cells where $N > 1$. In addition, structures with $N+$ unit cells are explored where the $+$ refers to an additional final layer of mesh A resulting in a symmetric structure in the z -direction. The transmission response of a 4 unit cell ($N = 4$) structure where $A = B$ is illustrated in figure 7.13.

The structure in figure 7.13 could equally well be described as an eight unit cell stack with an AC unit cell where A is the PEC mesh layer and C is the dielectric spacer. For multilayer stacks that are periodic in the direction of propagation (z -direction in this case), the number of observed resonances is given by $N - 1$, where N is the number of unit cells. This is due to the resonances arising from coupling between the standing-waves supported within each cavity; in a structure with N unit cells, there are $N - 1$ cavities. Therefore figure 7.13 shows 7 transmission peaks followed by a band gap before a second family of 7 transmission peaks, as would be expected. The resonances are due to resonant Fabry-Pérot modes in the dielectric layers coupled via the evanescent fields within the mesh layers. This response is analogous to the response of metal-dielectric stacks in the visible regime. In the visible regime, series of transmission peaks are separated by photonic band gaps (regions of low transmission). The peaks arise from Fabry-Pérot resonances in the dielectric layers coupled via exponentially decaying fields within the metal layers. At microwave frequencies the periodic subwavelength mesh produces effective electromagnetic parameters that can mimic plasmonic metals such as silver in the visible regime [86, 174]. Within the mesh layer the fields are evanescent and therefore equivalent to those in a real metal [92, 197].

7. The Microwave Response of Finite Multilayer Stacks of Alternating Metal Meshes

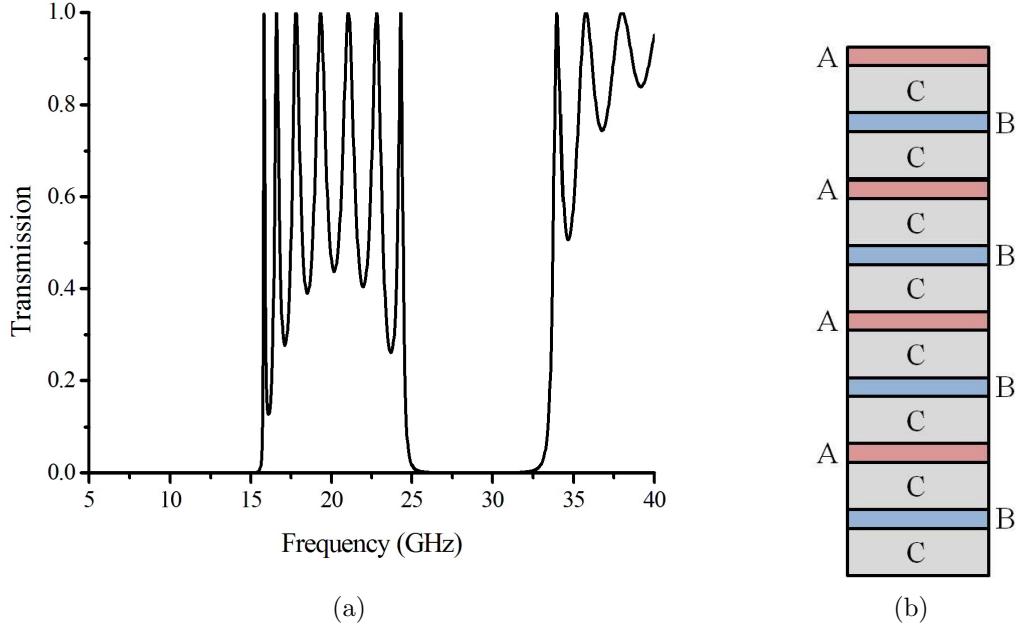


Figure 7.13: (a) Transmission response for a 4 unit cell geometry where each cell is comprised of an ACBC structure. Layers A and B are identical PEC mesh layers of thickness $h = 18 \mu\text{m}$ with pitch $d = 5 \text{ mm}$ and hole side of $a = 4.5 \text{ mm}$. Layer C is a dielectric spacer of thickness $g = 6 \text{ mm}$ with a permittivity of 1 (i.e. air). The incident radiation is orientated parallel to the x -axis and is at normal incidence; (b) schematic of the structure.

7.4.2.1 Varying Multilayer System Parameters

The unit cell of particular interest is that of an ACBC arrangement and the effect that alternating mesh layers will have on the EM response of the structure. In figure 7.14, the parameters of one mesh are kept the same whilst the hole size in the other mesh is varied. The pitch and mesh thickness of both meshes are identical and fixed ($d = 5 \text{ mm}$ and $h = 18 \mu\text{m}$). Whilst the structure producing the results in figure 7.14 has 4 complete unit cells, it is not a symmetrical system. By altering the structure by the removal of the last mesh B layer however, the structure becomes symmetrical. The transmission response for a 3+ unit ACBC structure, where ‘+’ denotes the additional final layer of mesh A, is presented in figure 7.15 for the same parameters as figure 7.14.

In figure 7.14 there are 4 unit cells in the stack; in figure 7.14(a), $a_A > a_B$, whilst in figure 7.14(b) the situation is reversed with $a_A < a_B$. In other words, in figure 7.14(a), the first mesh in the unit cell is more highly transmitting than the second mesh and vice versa in figure 7.14(b). However, it is immediately noticeable that despite the

7. The Microwave Response of Finite Multilayer Stacks of Alternating Metal Meshes

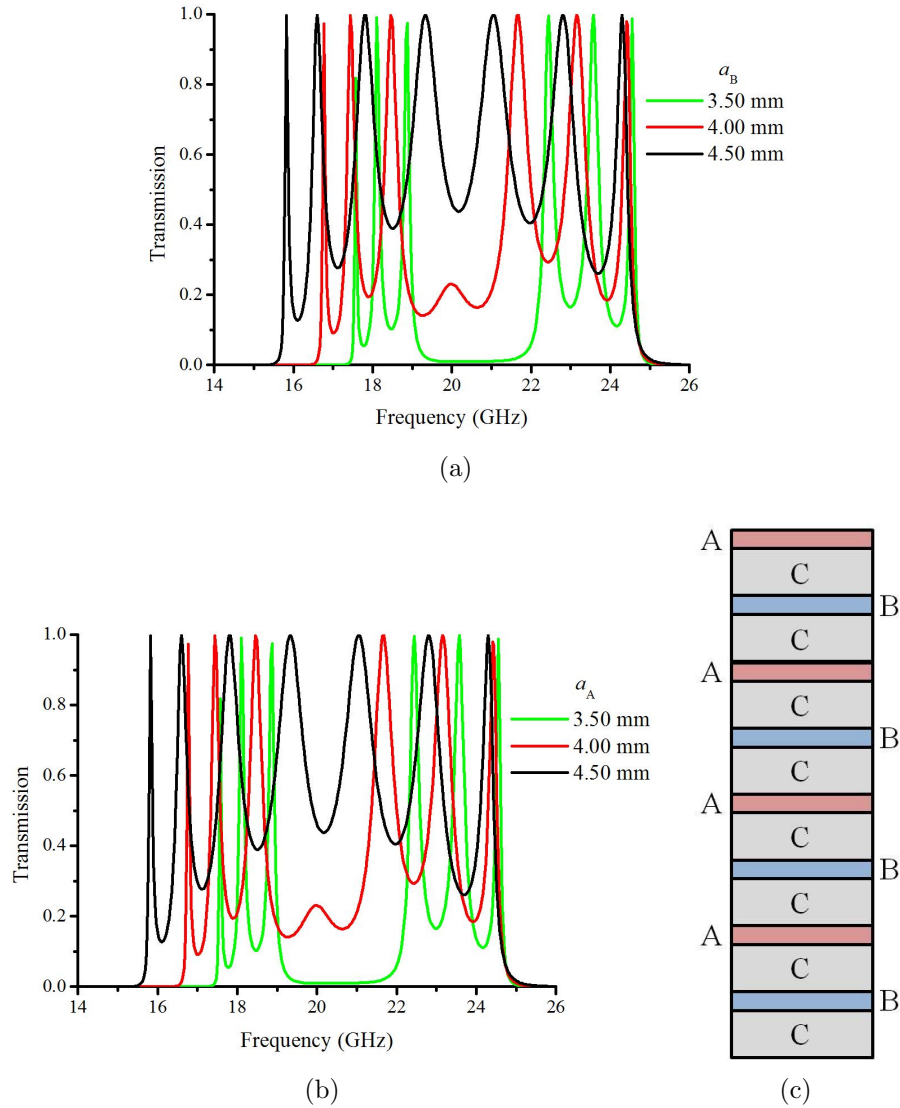


Figure 7.14: *Transmission response at normal incidence for a 4 unit cell geometry where each cell is comprised of an ACBC structure. Both PEC meshes have thickness $h = 18 \mu\text{m}$ and pitch $d = 5 \text{ mm}$: (a) the hole side length for mesh A are fixed ($a_A = 4.5 \text{ mm}$) whilst the hole side length for mesh B are varied and (b) the hole side length for mesh A are varied whilst the hole side length for mesh B are fixed ($a_B = 4.5 \text{ mm}$). C is a dielectric spacer (air) layer of thickness $g = 6 \text{ mm}$. (c) A schematic of the structure.*

7. The Microwave Response of Finite Multilayer Stacks of Alternating Metal Meshes

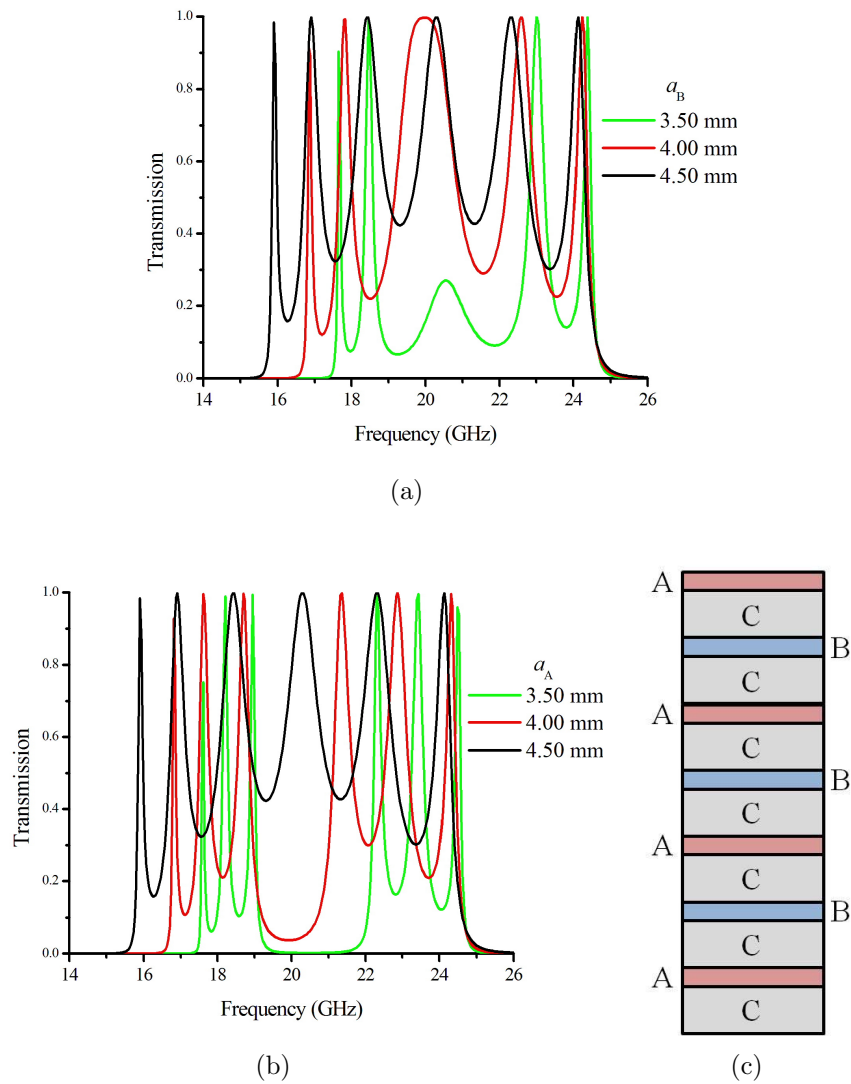


Figure 7.15: Transmission response at normal incidence for a 3+ unit cell geometry where each cell is comprised of an ACBC structure. Both PEC meshes have thickness $h = 18 \mu\text{m}$ and pitch $d = 5 \text{ mm}$: (a) the hole side length for mesh A are fixed ($a_A = 4.5 \text{ mm}$) whilst the hole side length for mesh B are varied and (b) the hole side length for mesh A are varied whilst the hole side length for mesh B are fixed ($a_B = 4.5 \text{ mm}$). C is a dielectric spacer (air) layer of thickness $g = 6 \text{ mm}$. (c) A schematic showing the structure.

7. The Microwave Response of Finite Multilayer Stacks of Alternating Metal Meshes

difference in unit cells, the transmission responses are identical. When the hole side lengths in both mesh A and B are equal ($a_A = a_B = 4.5$ mm), as indicated by the black trace on the graphs, there are 7 transmission peaks in this first band pass region as a result of the structure containing 8 unit cells. However, as the hole size in one of the meshes is changed, and the meshes are no longer identical, the number of unit cells in the structure reduces to four. This results in two band pass regions, containing 3 transmission resonances each separated by a new band gap (green trace on the graphs). When the difference between the two mesh parameters is slight and the new band gap is partially formed, an intermediate stage exists as indicated by the red trace. The red trace in figure 7.14 implies that the two central modes for the structure where mesh A and B are identical (black trace) merge together and then this merged mode reduces in intensity as the band gap forms. This supposition will be examined further in the following section (7.4.2.2).

For the transmission response of the 3+ unit cell structure illustrated in figure 7.15, varying the mesh parameters results in markedly different behaviour. Figure 7.15(a) illustrates the situation when mesh A is more highly transmitting than mesh B (i.e., $a_A > a_B$). In both graphs in figure 7.15, when mesh A and B are identical (black trace) there are 7 unit cells and therefore 6 transmission peaks. As the meshes begin to differ, based on the behaviour of the previous mesh in figure 7.14, it would be expected that as the system changed to 3+ unit cells, the middle two modes would merge and then this new mode would weaken as a band gap formed between the band pass regions containing 2 resonant modes. Figure 7.15(a) appears to support this expectation, although it is worth noting that the ‘strength’ of the central mode is stronger than in the 4 unit cell case. What is unusual, however, is the response when mesh B is more highly transmitting than mesh A (i.e., $a_A < a_B$) as illustrated in figure 7.15(b). Once the meshes begin to differ, the band gap forms more quickly and in addition, there are 3 resonant modes in each band pass region. The inference from figure 7.15(b) is that as the meshes begin to differ, the central two modes move away from each other (i.e., the lower frequency mode moves to lower frequencies and the higher frequency mode moves to higher frequencies) and the new band gap forms between them.

7.4.2.2 Topological Modes

To explore the evolution of the modes as the structure changes, figure 7.16 shows a grayscale plot of transmissivity as a function of frequency and the side length of the hole in mesh B for a fixed hole side length for mesh A. There are four plots in total, the

7. The Microwave Response of Finite Multilayer Stacks of Alternating Metal Meshes

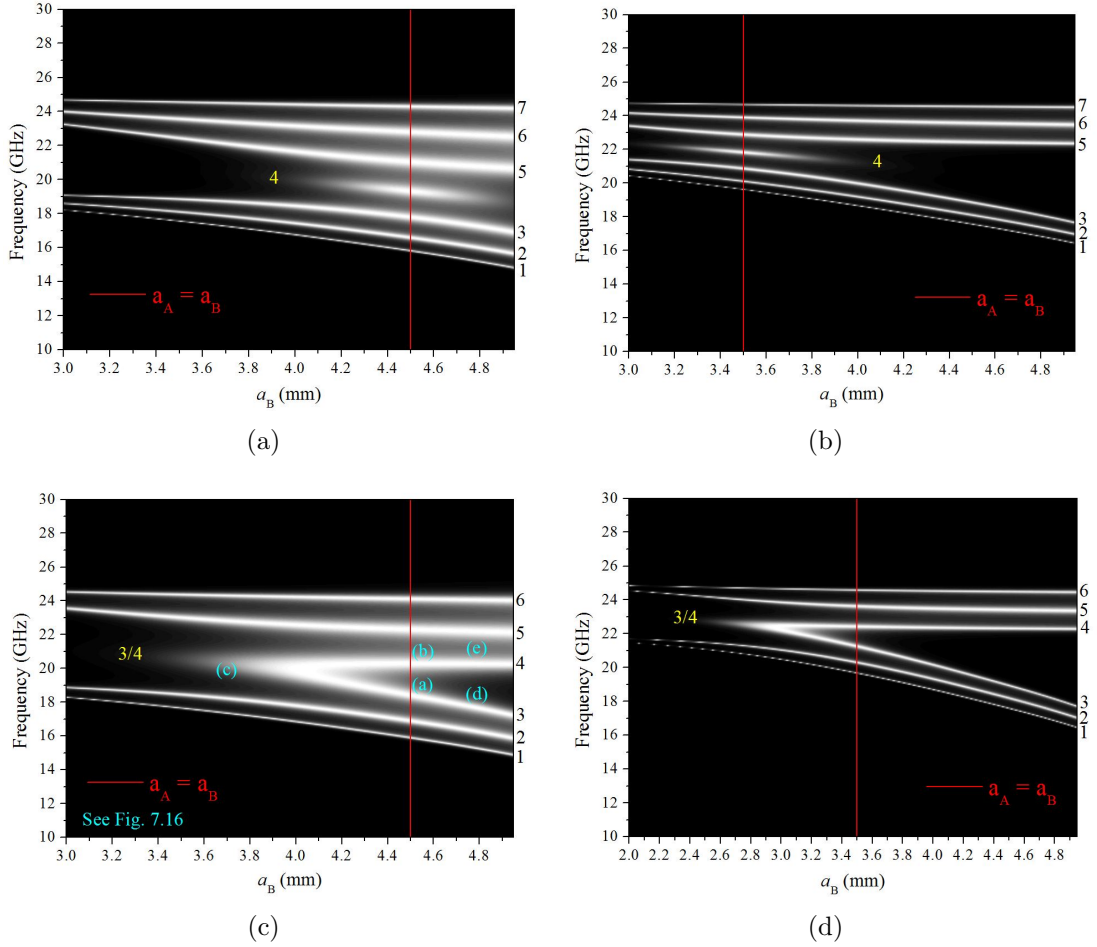


Figure 7.16: Grayscale plot of normal incidence transmission as a function of frequency and mesh B hole side length (a_B) for an ACBC structure where A and B are PEC mesh layers of thickness $h = 18 \mu\text{m}$ and C is a dielectric spacer layer of thickness $g = 6 \text{ mm}$. For mesh A hole side length of: (a) $a_A = 4.5 \text{ mm}$ and 4 unit cells; (b) $a_A = 3.5 \text{ mm}$ and 4 unit cells; (c) $a_A = 4.5 \text{ mm}$ and 3+ unit cells; (d) $a_A = 3.5 \text{ mm}$ and 3+ unit cells. The transmission scale ranges from 0 (black) to a normalised transmission of 1 (white). Arbitrary mode numbers have been assigned for identification purposes.

first two relating to the 4 unit cell structure for two different hole side lengths in mesh A, and the last two for the same two parameters for mesh A, but for the 3+ unit cell structure. As would be expected, small holes in mesh A result in sharper resonances (section 4.4). In all four plots, when $a_A = a_B$, $N - 1$ modes are visible, where N is the number of unit cells. However there are marked differences between the grayscales for 4 unit cells and 3+ unit cells. In figures 7.16(a) and 7.16(b), the mode that exists when $a_A = a_B$ quickly dies off as a_B either increases or decreases; whilst in figures 7.16(c) and 7.16(d), as a_B decreases, the two central resonances of the A=B structure merge to

7. The Microwave Response of Finite Multilayer Stacks of Alternating Metal Meshes

form an additional mode that decreases in intensity as the difference between the two mesh parameters increases. However, as a_B increases, the two central modes separate in frequency as the new band gap forms resulting in an additional mode in each band pass region.

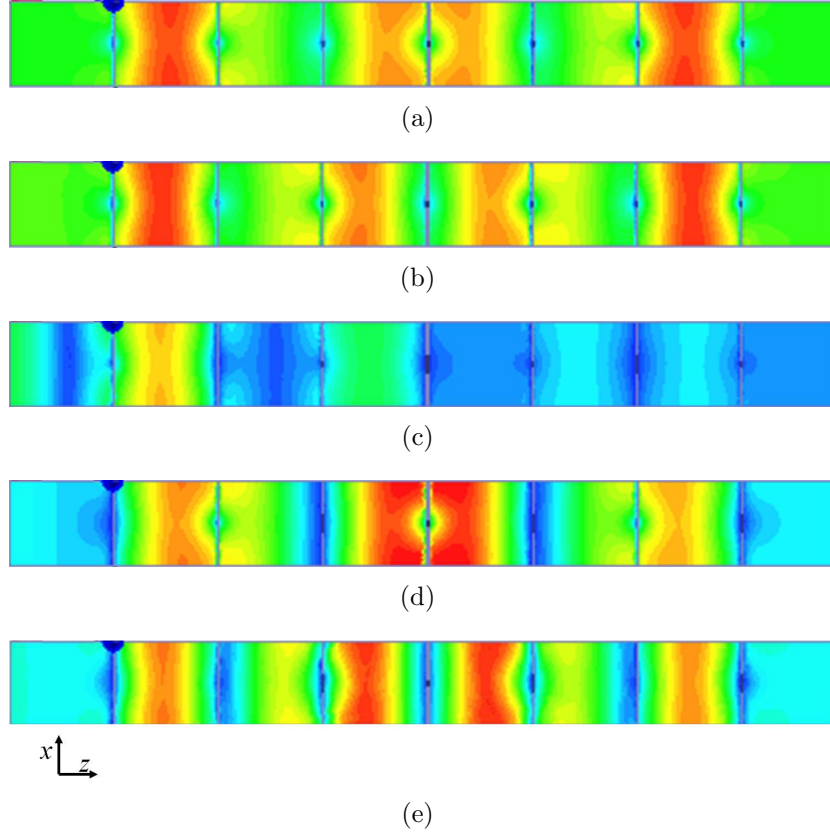


Figure 7.17: Field plot showing time averaged \vec{E}_z fields through the structure normalised to an incident field of unity. The field is propagating from the left for an ACBC structure where A and B are PEC mesh layers of thickness $h = 18 \mu\text{m}$ and C is a dielectric spacer layer of thickness $g = 6 \text{ mm}$. The structure has $3+$ unit cells and mesh A has a hole side length of $a_A = 4.5 \text{ mm}$. The illustrated modes are: (a) the 3rd mode at $\approx 19 \text{ GHz}$ for $a_B = 4.5 \text{ mm}$; (b) the 4th mode at $\approx 21 \text{ GHz}$ for $a_B = 4.5 \text{ mm}$; (c) the 3rd mode at $\approx 20.5 \text{ GHz}$ for $a_B = 3.7 \text{ mm}$; (d) the 3rd mode at $\approx 18 \text{ GHz}$ for $a_B = 4.8 \text{ mm}$; (e) the 4th mode at $\approx 21 \text{ GHz}$ for $a_B = 4.8 \text{ mm}$, where the mode numbers and plot references correspond to those in figure 7.16(c).

Figure 7.17 illustrates field plots through the $3+$ unit cell structure for the modes of interest: the first two plots refer to the case when mesh A and mesh B are identical (i.e., a 7 unit AC structure) for the two central modes (modes 3 and 4 respectively); the third plot illustrates the merging of the two central modes and the emergence of

7. The Microwave Response of Finite Multilayer Stacks of Alternating Metal Meshes

the mode in what would be expected to be a band gap region when mesh A is more transmissive than mesh B; and the final two plots refer to the case when mesh A is less transmissive than mesh B and for the two modes either side of the newly formed band gap (modes 3 and 4 respectively). Figure 7.17(c) shows a markedly different field distribution than the other four plots. It is characterised by strong fields localised in the first dielectric spacer (C) that then decay through the structure. It is proposed that this mode is the physical manifestation of a topological mode.

As introduced in section 7.2.3, topological states are mathematical sets of conditions. Topological states arise from edge effects in finite systems [176, 177, 198] and involve a continuous mapping of points within the Brillouin zone to Bloch-Hamiltonian space [178]. The topological argument is somewhat beyond the scope of this thesis mathematically, but a brief explanation is that it is the symmetry class of the transfer matrix associated with these modes that determines the mode to be of topological origin [178, 198, 199]. In particular the symmetry operator involved in the mapping of the points in the Brillouin zone must commute or anti-commute with the Hamiltonian at particular points [178].

7.4.2.3 Tunnel Barrier Analogy

The comparison of metal layers or metal meshes to tunnel barriers is not new: Hooper *et al* [200] and Gadsdon *et al* showed that for metal-dielectric films in the optical regime [201], the thin metal film acts as a tunnel barrier, as did Martín-Moreno *et al* [110], and this analogy was also used by Butler *et al* to explain the form of the coupling of the fields in the microwave regime for similar structures [174]. Conversely, Wang *et al*'s letter in Nature in 2009 concerned a photonic analogy of a Quantum Hall system [198], whilst in 1992, Martin and Landauer presented an analogy between quantum tunneling and evanescent electromagnetic waves [202]. It is a useful analogy and in this case particularly applicable. The structure referred to in figure 7.13 can be thought of as a quantum mechanical system with 8 identical tunnel barriers as illustrated in figure 7.18. In this case, mesh A is equal to mesh B and therefore the structure is an eight unit cell AC structure.

Continuing the analogy between the quantum mechanical system and the electromagnetic system, the EM 'potential' and the incident energy are given by $-n^2k_0^2$ and $-k_z^2$ respectively, where n is the refractive index and k_z is the normal component of the wavevector in the medium [200]. For simplicity, only normal incidence is explored in this study and this gives the relation

7. The Microwave Response of Finite Multilayer Stacks of Alternating Metal Meshes

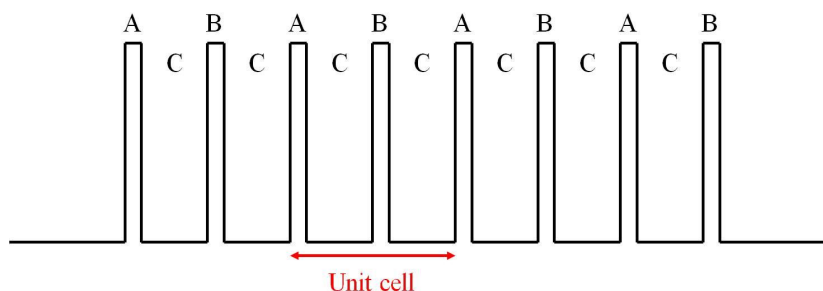


Figure 7.18: *Schematic illustrating quantum mechanical analogy for the 4 unit ACBC structure, where $A = B$, in terms of 8 potential barriers.*

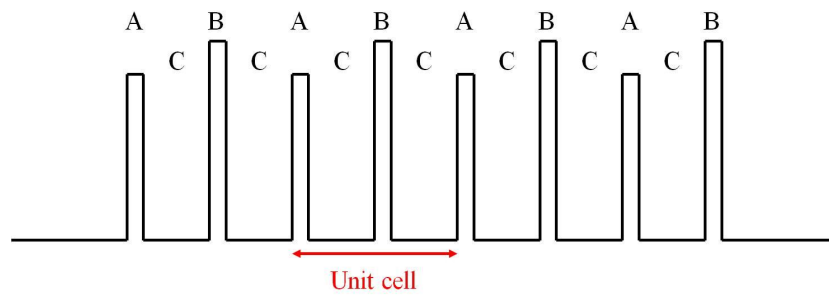
$$k_z^2 = n^2 k_0^2. \quad (7.38)$$

In the schematic in figure 7.18, the incident radiation has an energy of unity. When considering a mesh layer, the transmissivity is inversely proportional to the barrier height, which is determined by hole size; or in other words, the higher the transmissivity, the lower the potential barrier and vice versa.

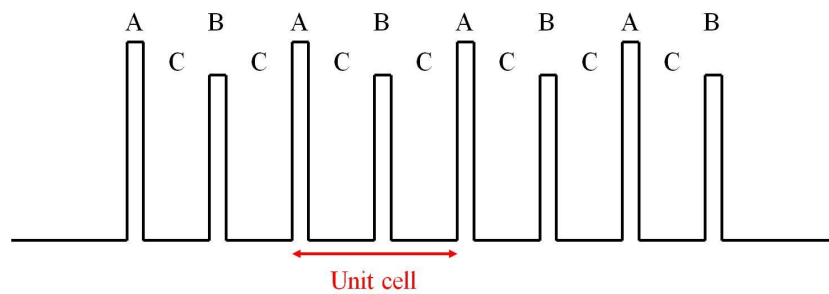
In terms of the mesh parameters, for the 4 unit cell when $a_A > a_B$, this can be represented by the schematic in figure 7.19(a) and figure 7.19(b) represents the case when $a_A < a_B$, whilst the 3+ unit cell structure for the same conditions are illustrated in figures 7.19(c) and 7.19(d) respectively.

The ‘topological’ mode is observed for the structure illustrated in figure 7.19(c), and it is noticeable that this is the only configuration with an ‘attractive potential’ at both ends of the structure, i.e., the lower tunnel barrier of the two followed by a higher tunnel barrier. An ‘attractive potential’ was hypothesised by Atherton and Mathur as necessary to observe a topological mode physically [176, 177] and this seems to be upheld by these initial results. It is worth noting that changing the hole size of the meshes is not the only way to create different height tunnel barriers; using meshes with the same size holes, but different mesh thicknesses (h) would have the same result due to the exponential nature of the fields within the holes. The barrier height would be proportional to the mesh thickness, i.e., a thicker mesh would represent a higher tunnel barrier and vice versa. Filling the holes with a media with differing refractive indices would be another way of altering the height of the tunnel barriers.

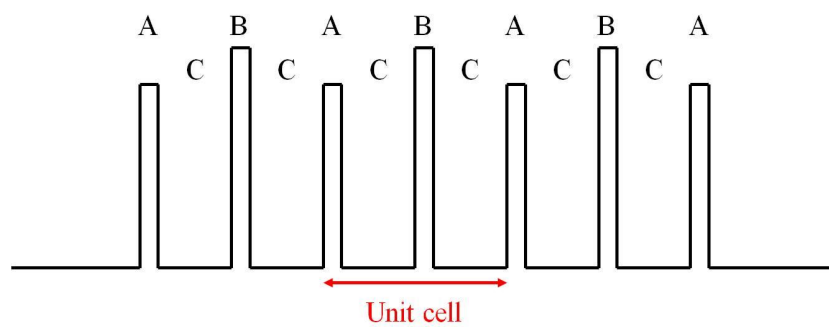
7. The Microwave Response of Finite Multilayer Stacks of Alternating Metal Meshes



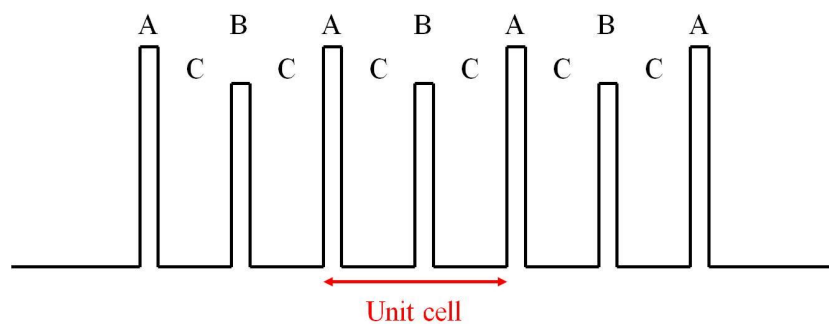
(a)



(b)



(c)



(d)

Figure 7.19: Schematic illustrating quantum mechanical analogy for; (a) the 4 unit ACBC structure, where $a_A > a_B$, (b) the 4 unit ACBC structure, where $a_A < a_B$, (c) the 3+ unit ACBC structure, where $a_A > a_B$ and (d) the 3+ unit ACBC structure, where $a_A < a_B$, in terms of potential barriers.

7.5 Conclusion

This chapter has presented investigations into the EM responses of multilayer metal-dielectric stacks comprising combinations of two different PEC meshes. The comparatively large spacing between the mesh layers allowed the subwavelength mesh to be described as an effective homogeneous layer. The use of the effective medium approach detailed in the method section of the chapter (7.3) allows structures containing more than two mesh layers to be easily modelled without recourse to the mathematically intensive modal matching method.

The first part of this investigation explored the response of multilayer stacks made up of two layers of differing PEC meshes separated by a dielectric, concentrating in particular on comparing the modal matching approach with the effective medium approximation. As the frequency range of interest was far from the onset of diffraction, it was expected that evanescent diffraction would have an insignificant role in the response of this structure. However it was shown that this is only true as long as the decay length of the evanescent fields within the mesh layers is less than half the separation between the mesh layers. At this point, the subwavelength detail of the mesh is described via the near-fields and the effective medium approximation is no longer able to describe the response accurately.

The second part of the investigation focused on multilayer stacks involving more unit cells with particular interest in predicting the existence of an observable topological mode. The transmission responses of 3+ and 4 unit cell structures were studied. Multilayer stacks of ACBC configuration were shown to form an additional band gap region within a previous pass band when compared with an equivalent ACAC structure. However, when the ACBC multilayer stack was symmetrised by the addition of a final layer of metal mesh A, unexpected results were obtained. In particular, when an ‘attractive potential’ was created at both ends of the stack, produced by mesh A being more transmissive than mesh B, a topological mode was observed within the aforementioned newly formed band gap. The topological mode is characterised by high localised electric fields in the first dielectric layer of the system that then decay in intensity through the stack. This extremely interesting topological mode does not appear to emerge when a ‘negative potential’ exists at both ends of the stack.

Chapter 8

Conclusions and Future Work

8.1 Introduction

The work contained within this thesis represents analytical investigations into the electromagnetic response for a variety of metal-dielectric composite structures with a view to enhancing the understanding of the physics underlying the resonant phenomena exhibited by such structures. It is assumed that the metal in these structures can be modelled as a perfect electrical conductor and that the meshes are thin in comparison to the incident wavelength. The initial part of this chapter summarises the conclusions of these investigations. This is followed by a brief discussion of some ideas for future work based on the results of the explorations contained within the thesis. The chapter concludes with a list of publications and conference presentations arising from these studies in reverse chronological order.

Although numerical models are a widely used and flexible tool used to predict the EM response of complex geometries, they offer little in the way of understanding the predicted response of these structures; however, this increased understanding is possible using an analytical model. The understanding gained of the phenomena described in this thesis would not have been reached using a conventional numerical modelling approach. As well as a numerical prediction of the EM response, by examining the constituent terms in the equation, the origin of any resonances can be determined. The aim of this thesis is to understand why the examined structures interact with EM radiation as they do and therefore an analytical model is an important tool. The modal matching method provides a more complete solution by allowing any number of diffracted (propagating or evanescent) and waveguide modes to be included in the calculation, although these may be truncated as necessary, as is the case with the waveguide modes.

This is an important factor as the frequency range just below the onset of diffraction, where evanescent fields play a significant role, is of particular interest. This flexibility of the model allows us to gain an understanding of the influence of specific orders on the structure's overall EM response. Another benefit of the model is its fast computation time in comparison to many of the commercially available numerical models.

8.2 Summary of Thesis

The thesis began with a brief overview of the historical development and seminal results in the key areas (chapter 2) aimed at providing a general background to the thesis and to put the current work in context. It was established that explorations into electromagnetic interactions with metal-dielectric composite periodic media began in the middle part of the 17th century and are still continuing today. Metamaterials are artificial composite materials whose properties are a result of their subwavelength structure as opposed to their chemical composition. One of the key results discussed related to effective medium theories. These are used when the constituent particles are so subwavelength that it is possible to describe the material as a homogeneous medium. In particular, derivations were given for the Clausius-Mossotti formula, Maxwell Garnett Approximation and Bruggeman's Effective Medium Theory. The next significant theory discussed was the concept of electromagnetic surface waves that are supported at the interface of dissimilar non-magnetic media. Although the range of frequencies within which these waves can be supported covers a wide range up to the limit of the surface plasma frequency for the particular metal, it is frequencies far from this limit that are of interest in this body of work. Surface periodicity is required to tightly bind the waves at these low frequencies and this enables analogous behaviour between these surface waves and the surface plasmon polaritons supported at visible frequencies. Whereas sample dimensions have been chosen in this thesis that provide the potential for experimentation in the microwave regime, the work is nonetheless valid as long as the PEC approximation holds. This assumption simplifies the mathematical modelling used throughout the thesis due to the resultant conclusion that no electric fields can exist within the metal. The final part of this chapter introduced the rectangular waveguide and derived the form of the resonant waveguide mode supported. This chapter laid the groundworks for the thesis by explaining the necessary theories that these explorations have utilised.

Chapter 3 introduced the most common modelling methods and reviewed the two

main modelling methods used within the thesis to predict the EM response of the chosen structures. The key advantage of the chosen method is the ability to extract understanding from the analytical formulation as resonant phenomena can be linked to specific mathematical terms in the solution. It was shown that the chosen modal matching approach provided a thorough description of the structure with the inclusion of the effect from multiple order waveguide modes and diffracted waves (both propagating and evanescent). The model allows all geometrical parameters to be varied, including the modelling of finite depth holes. In addition the number of waveguide and diffracted orders included in the modelling can be chosen. Another benefit of the model is the fast computation time in comparison to commercial numerical models. A numerical model is also utilised throughout the thesis as verification of the veracity of the results obtained using the analytical modal matching method. The commercially available FEM model used for this verification is Ansoft's three dimensional full-wave electromagnetic field simulator HFSSTM. The choice of this particular software was dictated by the well established use of it within the Electromagnetic Group at the University of Exeter and its applicability to electromagnetic problems involving periodic systems.

The first structure explored was a single layer PEC bigrating comprising a square array of square elements. Chapter 4 investigated the electromagnetic response of two configurations of this structure; a 'hole array' and its complement, a 'patch array'. The response of the patch array can be determined from that of the hole array by the application of Babinet's Principle, and this is shown to be valid for this structure with the assumption of infinitely thin PEC. Enhanced transmission resonances are supported by the hole array and enhanced reflection resonances by the patch array. These resonances occur at frequencies just below the onset of diffraction due to the strength of the evanescent diffraction. This strength is represented within the analytical solution by the overlap integrals. It was illustrated that even for high metal occupancy (i.e., very small holes) a 100% transmission resonance is supported, and accordingly a 100% reflection resonance is supported by the patch array, even for very low metal occupancy. A mathematical examination of the analytical solution concluded that the enhanced transmission phenomena was a combination of both resonant and non-resonant transmission channels. The evanescent diffraction from the array geometry allows near-field interaction between the elements of the array, resulting in an enhanced resonant response. As the array is a bigrating, it has two associated grating vectors, orthogonal to each other and in this case parallel to the coordinate axes. It was shown

that for a particular array the incident radiation preferentially scatters more strongly from one grating vector than the other depending on the incident polarisation. The significance of the role played by the evanescent diffraction was illustrated by investigating a square array of square elements rotated by 45° with respect to the axes of the unit cell. At 50% metal occupancy and above, this structure becomes electrically connected and would therefore be expected to exhibit low transmissivity. However, it was shown that the strength of the evanescent diffraction allows this structure to transmit at 100%.

The study of single layer bigrating systems was continued in Chapter 5 with the exploration of three new structures and the effect that breaking the four-fold symmetry inherent in the square array of square elements structure had on the predicted electromagnetic response. The first structure was again a square array, but with rectangular holes, with the result that breaking the symmetry of the hole geometry altered the relative proportions of the inductive and capacitive elements of the array. The next two structures were rectangular arrays, the first with square holes and the second with rectangular holes. Changes in the unit cell geometry caused corresponding changes in the frequency of the onset of diffraction with respect to the orthogonal grating vectors. For the rectangular array of rectangular holes, the four-fold symmetry of both the periodicity and the hole geometry has been broken and consequences of the break in symmetry combine with relative significance depending on the parameters involved in the specific geometry of the array. For example, when the incident polarisation is parallel to the x -axis, it was concluded that the hole geometry influences the Q factor of the resonance, with the hole side length parallel to the y -axis, a_y , being the significant parameter dictating the resonant frequency, and the hole side length parallel to the x -axis, a_x , the sharpness of the mode. Whereas it is the periodicity of the array that dictates the extent of the perturbation by the evanescent diffractive orders to the resonance. The closer the resonance is to the onset of diffraction, the stronger the evanescent diffraction and the greater the perturbation.

The previous two chapters concentrated on the exploration of single layer meshes. In chapter 6, the understanding gained from the earlier chapters was applied to more complex double layer structures. The modal matching method was adapted by extending the initial model to account for the complex near-field interactions and multiple reflections between the mesh layers. The structure consisted of a double layer of identical square arrays of square holes (mesh) in a perfectly conducting sheet separated by a dielectric spacer of air. For the single layer structures it had been shown that the resonant phenomena were due to resonant excitation of surface waves via evanescent diffraction.

It was concluded that the structure supports families of standing wave modes together with surface modes and that close to the onset of diffraction these modes interact with each other. As with the single layer structures, the electromagnetic response of this structure is highly dependent on the strength of the evanescent diffraction as shown by examination of the role of the overlap integrals within the analytic equations. At low frequencies the resonant modes are Fabry-Pérot-like. However, the modes become more surface mode-like in character as the frequency increases and approaches that of the surface mode supported by a single mesh layer. A particular focus of this chapter was the effect on the transmission of lateral translation of one mesh relative to the other and the role that evanescent diffraction played in this. The analysis shows that it is the separation of the mesh layers that is the critical parameter; whilst the misalignment of the meshes with relation to one another is only significant in the regime where the separation of the layers is less than the wavelength.

The final and most exciting investigative chapter, Chapter 7, presented explorations into the electromagnetic response of multiple layer stacks consisting of alternating metal mesh and dielectric layers. Multilayer structures have been of interest to the scientific community for many years, however, it is the periodic combination of two different meshes within the structure that makes this study different from previous studies. The meshes used are subwavelength, and this coupled with the comparatively large spacing between the mesh layers allowed an effective medium approach to be used to describe the mesh layers. There were two specific foci for the investigation into this system. The first concentrated on comparing the validity of the effective medium approach with the modal matching model for a double mesh system where each mesh has differing parameters and determining when this approximation was no longer appropriate. The structure consisted of multilayer stacks made up of two layers of differing PEC meshes separated by a dielectric layer of air for simplicity. The results of this study concluded that for the effective medium approach to be applicable, the decay length of the evanescent fields within the mesh layers must be less than half the separation of the dielectric spacer layer. If the decay length is greater than this, then near fields coupling occurs and therefore the response is no longer accurately described by an effective medium approach. This near field coupling of the evanescent diffracted fields was shown to exist even at frequencies far below the onset of diffraction. The second focus of the work was on the electromagnetic response of the alternating mesh multilayer stack configuration involving more unit cells with the aim of determining the existence of an observable topological mode. The unit cell had an ACBC configuration where A and B

were PEC meshes with differing parameters and C was a dielectric spacer layer. Both 3+ and 4 unit cell structures were studied where ‘+’ denotes the addition of a final layer of mesh A resulting in a symmetric stack. When compared with an equivalent ACAC structure, the ACBC multilayer stacks formed an additional band gap within a previous pass band region. The conclusion of this investigation was that a topological mode could be observed within the newly formed band gap when an attractive potential was created at both ends of the stack. An analogy was made with a basic quantum mechanical system in one dimension, where the mesh layers equate to tunnel barrier and a mesh with high transmissivity represents a low tunnel barrier. Therefore the topological mode was supported in the 3+ unit cell structure when the holes in mesh A were larger than those in mesh B. The fields of this topological mode were shown to have high localised electric fields in the first dielectric layer of the system that then decay in intensity through the stack. This result is exciting as it was previously thought that 1D topological modes could not be observed in a physical system.

8.3 Future Work

This thesis has presented a series of analytical investigations into periodic metal-dielectric composite structures and the factors that govern their interaction with electromagnetic radiation. A range of structures and models have been discussed and there are many areas into which this work can be extended. In this section, a brief discussion of a few of these suggestions will be undertaken.

8.3.1 Extension of the Modal Matching Model for Real Metals

In the introduction to the thesis (chapter 1), the scope was identified as being limited to frequency regimes where the simplification that infinite conductivity would give was valid. An obvious extension to this work would be to extend the method to enable accurate modelling of real metals at a wider range of frequencies. This would involve a frequency dependent definition of permittivity for the specific metal and describing the fields within the metal itself. In other works this has been achieved by utilising an effective surface impedance boundary condition [203–205] that replicates the effect of the finite conductivity of the metal but negates the need to describe the fields within the metal. Numerical calculations using the multiple multipole technique has also been attempted [206]. This would have the benefit of extending the validity of the model to

higher frequencies.

8.3.2 Bilateral Displacement in Double Mesh Structures

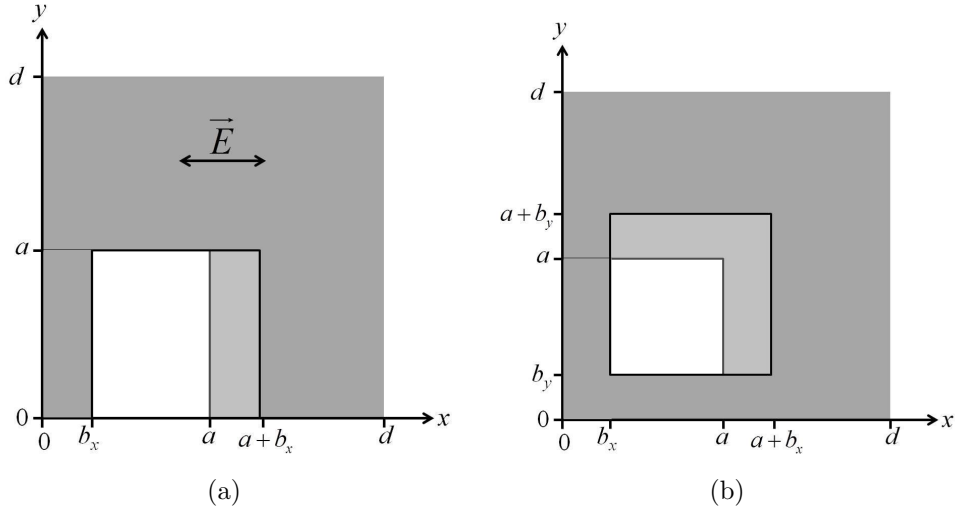


Figure 8.1: Schematic defining the unit cell and the origin for a double mesh structure illustrating lateral displacement in (a) one direction and (b) two directions.

The exploration of the double mesh structure in chapter 6 considered lateral displacement in one direction only (figure 8.1(a)), either parallel or perpendicular to the direction of polarisation. Both this structure and those investigated in chapter 5 illustrated that for systems with two-fold symmetry (as here) as opposed to four-fold symmetry, the electromagnetic response can be markedly different depending on the choice of incident polarisation. Lateral two-dimensional translation of one mesh with respect to the other would remove the remaining symmetry from the unit cell (figure 8.1(b)). Most of the investigations into the effect of lateral displacement only involve displacement in a single direction. Although there are a few studies on bilateral displacement [159, 207] there is little understanding of the underlying physics.

8.3.3 Experimental Determination of a One Dimensional Topological Mode in a Real System

Another extensive area of future study concerns the multilayer alternating mesh layer structures studied in chapter 7. With the prediction that topological modes are supported by the $N+$ unit cell configurations when an attractive potential exists at both

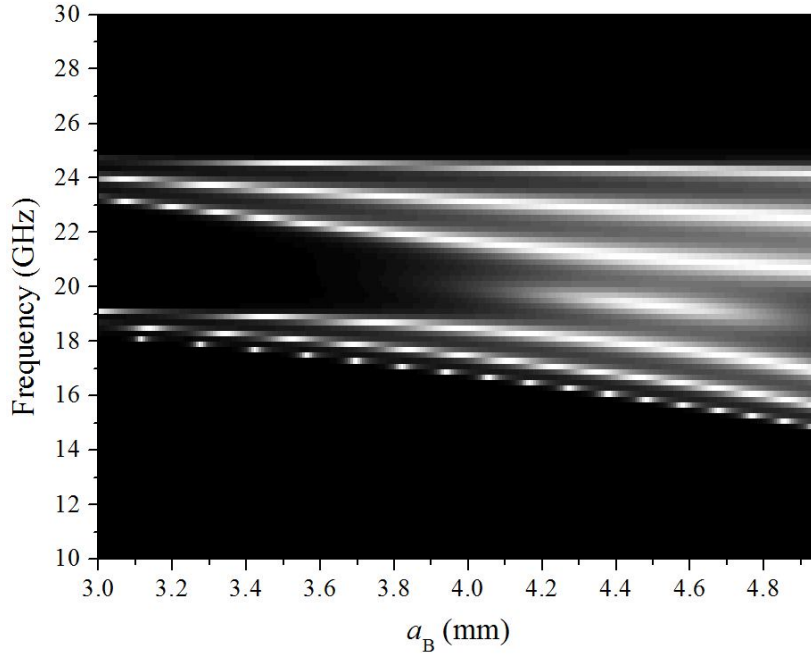


Figure 8.2: Greyscale plot of normal incidence transmission as a function of frequency and mesh B hole side length (a_B) for an ACBC structure where A and B are PEC mesh layers of thickness $h = 18 \mu\text{m}$ and C is a dielectric spacer layer of thickness $g = 6 \text{ mm}$. Mesh A has a hole side length of $a_A = 4.5 \text{ mm}$ and the structure consists of 4 unit cells in the z -direction.

ends of the structure, the corresponding experiment should be conducted to determine whether the predicted modes can be exhibited experimentally. In order to ease the experimental setup it is suggested that different thicknesses of the same mesh are used to create the difference in tunnel barrier heights as opposed to different size meshes. In addition further modelling needs to be conducted to gain understanding into these modes. For example, with reference to the central mode that appears briefly in the N unit cell arrangements (figure 8.2) when mesh $A \approx$ mesh B , is this also a topological mode, or just a normal eigenmode of the system with a coupling intensity that quickly decays away from the equilibrium condition? This is an exciting new area with many questions and possibilities that should be explored further.

8.3.4 Random and Quasi-Random Systems

This thesis has investigated periodic structures, however many systems, especially industrial systems, involve random and quasi-random structures. Whilst modal matching requires a unit cell to exist, it may be possible to achieve an approximation of the EM

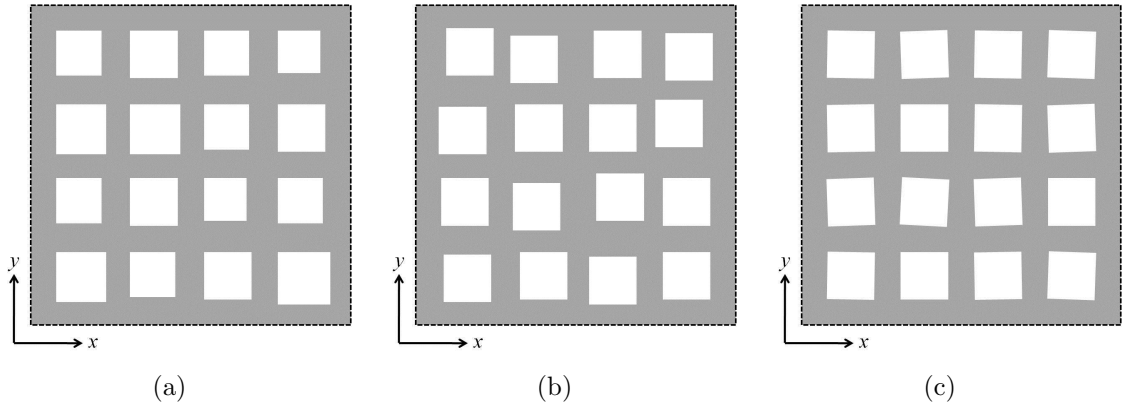


Figure 8.3: Schematic illustrating three possible randomisations of a square lattice using a small random perturbation of: (a) the size of the hole, (b) the lattice position of the hole and (c) the orientation of the hole.

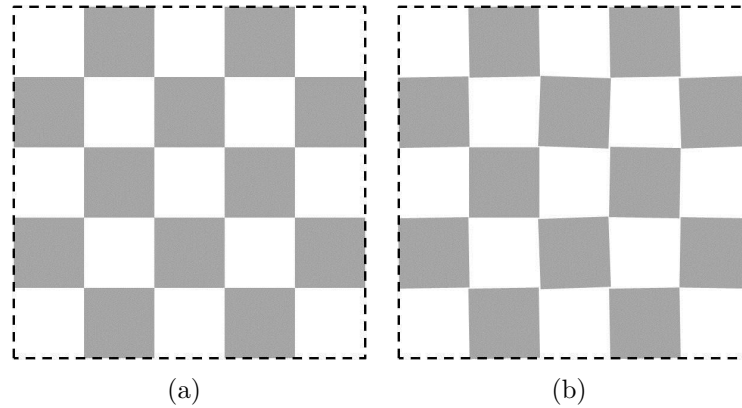


Figure 8.4: Schematic illustrating the effect of perturbing the orientation in a square ‘checkerboard’ lattice: (a) 50% metal fill fraction with each hole orientated at 45° to the coordinate axes and (b) the lattice following a random small perturbation of the hole orientation illustrating the loss of electrical connectivity.

response using perturbation theory for systems with a small degree of ‘randomness’. Figure 8.3 illustrates three examples of such systems. A potentially interesting effect may be observed in a square array of square holes orientated at 45° to the coordinate axes as described in section 4.6. At the point when the metal fill fraction is exactly 50%, a ‘checkerboard’ effect is obtained and the structure reaches electrical connectivity at that point (figure 8.4(a)). If the orientation of the holes is perturbed, even by a infinitesimal amount, that electrical connectivity is broken, providing an ‘instant switch’ effect (figure 8.4(b)).

8.4 Publications and Conference Presentations

8.4.1 Publications

- **M. C. Taylor**, A. P. Hibbins and J.R. Sambles *Microwave Response of Closely Spaced Metal Meshes* Accepted for publication by Physical Review B, October 2011
- **M. C. Taylor**, J. D. Edmunds, E. Hendry, A. P. Hibbins and J.R. Sambles *Microwave Response of Hole and Patch Arrays* Physical Review B **82**, 155105, 2010
- J. D. Edmunds, **M. C. Taylor**, A. P. Hibbins, J.R. Sambles and I. J. Youngs *Babinet's Principle and the band structure of surface waves on patterned metal arrays* Journal of Applied Physics **107**, 103108, 2010

8.4.2 Conference Presentations

- A. P. Hibbins, **M. C. Taylor**, C. Butler, and J.R. Sambles *Evanescent Coupling Between Closely Spaced Metal Meshes* Nanometa 2011, Seefeld, Austria (Poster Presentation)
- J. D. Edmunds, **M. C. Taylor**, A. P. Hibbins, J.R. Sambles and I. J. Youngs *Babinet's Principle and the dispersion of surface waves on complementary patterned metal arrays* Meta'10, Cairo, Egypt (Oral Presentation)
- **M. C. Taylor**, C. Butler, A. P. Hibbins and J.R. Sambles *Evanescent Coupling Between Closely Spaced Metal Meshes* PECS IX 2010, Granada, Spain (Poster Presentation)
- **M. C. Taylor**, A. P. Hibbins and J.R. Sambles *Aspect Ratio Dependence of Microwave Response of Hole Arrays* Royal Society Thio Murphy International Science Meeting 2010, Chicheley, United Kingdom (Poster Presentation)
- **M. C. Taylor**, J. D. Edmunds, E. Hendry, A. P. Hibbins and J.R. Sambles *Enhanced Reflection and Transmission of Structured Metal Films* Metamaterials 2009, London, United Kingdom (Poster Presentation)

8. Conclusions and Future Work

- **M. C. Taylor**, J. D. Edmunds, A. P. Hibbins and J.R. Sambles *Model of the Electromagnetic Response of a Two-Dimensional Metal-Dielectric Composite* Nanometa 2009, Seefeld, Austria (Poster Presentation)

Appendix A

Full Modal Matching Calculation

A.1 Introduction

Section 3.2.2.1 detailed the equations employed within the modal matching method. The manipulation of these equations was done with the aid of Wolfram's Mathematica software [96] and is shown in section A.2.1 and the full solution is provided below in section A.2.2. This is the basic method for the simple structure comprising a square array of square holes in a PEC sheet.

A.2 Wolfram Mathematica File

A.2.1 Manipulation of Equations and Workings

```
Off[General::spell];
```

```
Off[General::spell1];
```

```
Exvac1 = Exp[i * kz0 * z]
```

```
+ Amx * Exp[i * (2 * m1 * pi/d) * x] * Exp[i * (2 * m2 * pi/d) * y] * Exp[-i * kzm * z];
```

```
Eyvac1 = Amy * Exp[i * (2 * m1 * pi/d) * x] * Exp[i * (2 * m2 * pi/d) * y] * Exp[-i * kzm * z];
```

```
Ezvac1 = Integrate[-D[Exvac1, x] - D[Eyvac1, y], dz];
```

```
Hxvac1 = -1/(i*w) * Simplify[(D[Ezvac1, y] - D[Eyvac1, z])]
```

```
Exp[2i*pi*(m1*x+m2*y)/d - ikzm*z] * (Amy*d^2*kzm^2 + 4*Amx*m1*m2*pi^2 + 4*Amy*m2^2*pi^2)
```

```
Exp[-ikzm*z] * (d^2*kzm * (Exp[i*(kz0+kzm)*z] * kz0 - Amx * Exp[2i*pi*(m1*x+m2*y)/d] * kzm) - 4 * Exp[2i*pi*(m1*x+m2*y)/d] * m1 * (Amx*m1 + Amy*m2) * pi^2)
```

```
Excav = Bx * Sin[pi * y/a] * Exp[i * qz * z] - Cx * Sin[pi * y/a] * Exp[-i * qz * z];
```

$$E_{ycav} = 0;$$

$$E_{zcav} = \int (-D[Excav, x] - D[Eycav, y]) dz;$$

$$H_{xcav} = -\frac{1}{i*w} \text{Simplify}[(D[Ezcav, y] - D[Eycav, z])]$$

$$H_{ycav} = -\frac{1}{i*w} * \text{Simplify}[(D[Excav, z] - D[Ezcav, x])]$$

$$0$$

$$-\frac{e^{-iqzz} (C_x + B_x e^{2iqzz}) qz \sin\left[\frac{\pi y}{a}\right]}{w}$$

$$E_{xvac2} = D_{xn} * \text{Exp}[i * (2 * n1 * \pi/d) * x] * \text{Exp}[i * (2 * n2 * \pi/d) * y] * \text{Exp}[i * kzn * z];$$

$$E_{yvac2} = D_{yn} * \text{Exp}[i * (2 * n1 * \pi/d) * x] * \text{Exp}[i * (2 * n2 * \pi/d) * y] * \text{Exp}[i * kzn * z];$$

$$E_{zvac2} = \int (-D[E_{xvac2}, x] - D[E_{yvac2}, y]) dz;$$

$$H_{xvac2} = -\frac{1}{i*w} * \text{Simplify}[(D[E_{zvac2}, y] - D[E_{yvac2}, z])]$$

$$H_{yvac2} = -\frac{1}{i*w} * \text{Simplify}[(D[E_{xvac2}, z] - D[E_{zvac2}, x])]$$

$$\frac{e^{i\left(\frac{2\pi(n1x+n2y)}{d} + kznz\right)} (d^2 D_{yn} kzn^2 + 4n2(D_{xn} n1 + D_{yn} n2)\pi^2)}{d^2 kzn w}$$

$$-\frac{e^{i\left(\frac{2\pi(n1x+n2y)}{d} + kznz\right)} (d^2 D_{xn} kzn^2 + 4n1(D_{xn} n1 + D_{yn} n2)\pi^2)}{d^2 kzn w}$$

*****Matching E fields*****

$$z = 0;$$

$$E_{xvac1}$$

$$E_{yvac1}$$

$$E_{xcav}$$

$$E_{ycav}$$

$$1 + A_{mx} e^{\frac{2i m1 \pi x}{d} + \frac{2i m2 \pi y}{d}}$$

$$A_{my} e^{\frac{2i m1 \pi x}{d} + \frac{2i m2 \pi y}{d}}$$

$$B_x \sin\left[\frac{\pi y}{a}\right] - C_x \sin\left[\frac{\pi y}{a}\right]$$

$$0$$

$$Q1[m1, m2] := \int_0^d \int_0^d \text{Exp}[-i * (2 * m1 * \pi/d) * x] \text{Exp}[-i * (2 * m2 * \pi/d) * y] dx dy;$$

$$Q2[m1, m2] := \int_0^a \int_0^a \sin\left[\frac{\pi y}{a}\right] * \text{Exp}[-i * (2 * m1 * \pi/d) * x] \text{Exp}[-i * (2 * m2 * \pi/d) * y] dx dy;$$

$$Q1[m1, m2] + A_x[m1, m2] * d^2 = (B_x - C_x) * Q2[m1, m2]$$

A. Full Modal Matching Calculation

$$z = h;$$

$$\text{Exvac2}$$

$$\text{Eyvac2}$$

$$\text{Excav}$$

$$\text{Eycav}$$

$$D_{Xn} e^{ihkzn + \frac{2in1\pi x}{d} + \frac{2in2\pi y}{d}}$$

$$D_{Yn} e^{ihkzn + \frac{2in1\pi x}{d} + \frac{2in2\pi y}{d}}$$

$$-C_x e^{-ihqz} \text{Sin} \left[\frac{\pi y}{a} \right] + B_x e^{ihqz} \text{Sin} \left[\frac{\pi y}{a} \right]$$

$$0$$

$$Q2[n1, n2] := \int_0^a \int_0^a \text{Sin} \left[\frac{\pi y}{a} \right] * \text{Exp}[-i * (2 * n1 * \pi / d) * x] * \text{Exp}[-i * (2 * n2 * \pi / d) * y] dx dy;$$

$$Dx[n1, n2] e^{ihkz[\text{Eps}, n1, n2]} d^2 = (B_x e^{ihqz} - C_x e^{-ihqz}) * Q2[n1, n2]$$

*****Matching H fields*****

$$z = 0;$$

$$\text{Expand}[\text{Hxvac1}]$$

$$\text{Expand}[\text{Hyvac1}]$$

$$\text{Hxcav}$$

$$\text{Hycav}$$

$$\begin{aligned} & - \frac{A_{my} e^{\frac{2i\pi(m1x+m2y)}{d}}}{w} k_{zm} - \frac{4A_{mx} e^{\frac{2i\pi(m1x+m2y)}{d}}}{d^2 k_{zm} w} m1 m2 \pi^2 - \frac{4A_{my} e^{\frac{2i\pi(m1x+m2y)}{d}}}{m2^2 \pi^2} \\ & - \frac{kz0}{w} + \frac{A_{mx} e^{\frac{2i\pi(m1x+m2y)}{d}}}{w} k_{zm} + \frac{4A_{mx} e^{\frac{2i\pi(m1x+m2y)}{d}}}{d^2 k_{zm} w} m1^2 \pi^2 + \frac{4A_{my} e^{\frac{2i\pi(m1x+m2y)}{d}}}{d^2 k_{zm} w} m1 m2 \pi^2 \end{aligned}$$

$$0$$

$$\frac{(B_x + C_x) q_z \text{Sin} \left[\frac{\pi y}{a} \right]}{w}$$

$$Q4[m1, m2] := \int_0^a \int_0^a \text{Exp}[i * (2 * m1 * \pi / d) * x] * \text{Exp}[i * (2 * m2 * \pi / d) * y] \text{Sin} \left[\frac{\pi y}{a} \right] dx dy;$$

$$- \frac{kz[0]}{w} \frac{2a^2}{\pi} + \sum_m \left(\frac{A_x[m1, m2] k_z[m1, m2]}{w} * Q4[m1, m2] + \frac{4A_x[m1, m2] m1^2 \pi^2}{d^2 k_z[m1, m2] w} * Q4[m1, m2] \right)$$

A. Full Modal Matching Calculation

$$= -\frac{(Bx+Cx)qz}{w} \frac{a^2}{2} - kz[0] \frac{2a^2}{\pi} + \sum_m Ax[m1, m2] * Q4[m1, m2] * \left(kz[m1, m2] + \frac{4 m1^2 \pi^2}{d^2 kz[m1, m2]} \right) = -(Bx + Cx)qz \frac{a^2}{2}$$

$$z = h;$$

Expand[Hxvac2]

Expand[Hyvac2]

Hxcav

Hycav

$$\frac{D_{yn} e^{i \left(h k_{zn} + \frac{2\pi(n1 x + n2 y)}{d} \right)} k_{zn}}{w} + \frac{4 D_{xn} e^{i \left(h k_{zn} + \frac{2\pi(n1 x + n2 y)}{d} \right)} n1 n2 \pi^2}{d^2 k_{zn} w} + \frac{4 D_{yn} e^{i \left(h k_{zn} + \frac{2\pi(n1 x + n2 y)}{d} \right)} n2^2 \pi^2}{d^2 k_{zn} w} - \frac{D_{xn} e^{i \left(h k_{zn} + \frac{2\pi(n1 x + n2 y)}{d} \right)} k_{zn}}{w} - \frac{4 D_{xn} e^{i \left(h k_{zn} + \frac{2\pi(n1 x + n2 y)}{d} \right)} n1^2 \pi^2}{d^2 k_{zn} w} - \frac{4 D_{yn} e^{i \left(h k_{zn} + \frac{2\pi(n1 x + n2 y)}{d} \right)} n1 n2 \pi^2}{d^2 k_{zn} w}$$

0

$$- \frac{e^{-i h qz} (Cx + Bx e^{2i h qz}) qz \sin \left[\frac{\pi y}{a} \right]}{w}$$

$$Q4[n1, n2] := \int_0^a \int_0^a \text{Exp}[i * (2 * n1 * \pi/d) * x] * \text{Exp}[i * (2 * n2 * \pi/d) * y] \sin \left[\frac{\pi y}{a} \right] dx dy;$$

$$\sum_n Dx[n1, n2] * e^{i(h kz[Eps, n1, n2])} * Q4[n1, n2] * \left(kz[Eps, n1, n2] + \frac{4n1^2 \pi^2}{d^2 kz[Eps, n1, n2]} \right) = (Bx e^{ih qz} + Cx e^{-ih qz}) qz * \frac{a^2}{2}$$

*****Finding Solution*****

$$Q1[m1, m2] + Ax[m1, m2] * d^2 = (Bx - Cx) * Q2[m1, m2]$$

$$Dx[n1, n2] e^{ih kz[Eps, n1, n2]} d^2 = (Bx e^{ih qz} - Cx e^{-ih qz}) * Q2[n1, n2]$$

$$-kz[0] \frac{2a^2}{\pi} + \sum_m Ax[m1, m2] * Q4[m1, m2] * \left(kz[m1, m2] + \frac{4 m1^2 \pi^2}{d^2 kz[m1, m2]} \right) = -(Bx + Cx)qz \frac{a^2}{2}$$

$$\begin{aligned} & \sum_n Dx[n1, n2] * e^{i(hkz[Eps,n1,n2])} * Q4[n1, n2] * \left(kz[Eps, n1, n2] + \frac{4n1^2\pi^2}{d^2kz[Eps,n1,n2]} \right) \\ & = (Bx e^{ihqz} + Cx e^{-ihqz}) qz * \frac{a^2}{2} \end{aligned}$$

$$\begin{aligned} Ax[m1, m2] &= \frac{(Bx-Cx)*Q2[m1,m2]-Q1[m1,m2]}{d^2} \\ Dx[n1, n2] &= \frac{(Bx e^{ihqz} - Cx e^{-ihqz}) * Q2[n1,n2]}{e^{ihkz[Eps,n1,n2]} d^2} \\ & - kz[1, 0, 0] \frac{2a^2}{\pi} + \\ & \sum_m \left(\frac{(Bx-Cx)*Q2[m1,m2]-Q1[m1,m2]}{d^2} * \left(kz[1, m1, m2] + \frac{4m1^2\pi^2}{d^2kz[1,m1,m2]} \right) * Q4[m1, m2] \right) \\ & = -(Bx + Cx)qz \frac{a^2}{2} \\ & \sum_n \frac{(Bx e^{ihqz} - Cx e^{-ihqz}) * Q2[n1,n2]}{d^2} * Q4[n1, n2] * \left(kz[Eps, n1, n2] + \frac{4n1^2\pi^2}{d^2kz[Eps,n1,n2]} \right) \\ & = (Bx e^{ihqz} + Cx e^{-ihqz}) qz * \frac{a^2}{2} \end{aligned}$$

$$\begin{aligned} & -kz[1, 0, 0] \frac{2a^2}{\pi} + \frac{(Bx-Cx)}{d^4} \sum_m \frac{(4m1^2\pi^2+d^2kz[1,m1,m2]^2)*Q2[m1,m2]*Q4[m1,m2]}{kz[1,m1,m2]} - \\ & \frac{1}{d^4} \sum_m \frac{(4m1^2\pi^2+d^2kz[1,m1,m2]^2)*Q1[m1,m2]*Q4[m1,m2]}{kz[1,m1,m2]} = -(Bx + Cx)qz * \frac{a^2}{2} \\ & \frac{(Bx e^{ihqz} - Cx e^{-ihqz})}{d^4} \sum_n \frac{(4n1^2\pi^2+d^2kz[Eps,n1,n2]^2)Q2[n1,n2]Q4[n1,n2]}{kz[Eps,n1,n2]} \\ & = (Bx e^{ihqz} + Cx e^{-ihqz}) qz * \frac{a^2}{2} \end{aligned}$$

$$\begin{aligned} G1 &:= \sum_m \frac{(4m1^2\pi^2+d^2kz[1,m1,m2]^2)*Q2[m1,m2]*Q4[m1,m2]}{kz[1,m1,m2]} \\ G2 &:= \sum_m \frac{(4m1^2\pi^2+d^2kz[1,m1,m2]^2)*Q1[m1,m2]*Q4[m1,m2]}{kz[1,m1,m2]} \\ H &:= \sum_n \frac{(4n1^2\pi^2+d^2kz[Eps,n1,n2]^2)*Q2[n1,n2]*Q4[n1,n2]}{kz[Eps,n1,n2]} \end{aligned}$$

$$\begin{aligned} & -kz[1, 0, 0] \frac{2a^2}{\pi} + \frac{(Bx-Cx)}{d^4} G1 - \frac{1}{d^4} G2 = -(Bx + Cx)qz * \frac{a^2}{2} \\ & \frac{(Bx e^{ihqz} - Cx e^{-ihqz})}{d^4} H = (Bx e^{ihqz} + Cx e^{-ihqz}) qz * \frac{a^2}{2} \end{aligned}$$

$$\text{Simplify} \left[\text{Solve} \left[-kz[1, 0, 0] * \frac{2*a^2}{\pi} + \frac{(Bx-Cx)}{d^4} * G1 - \frac{1}{d^4} * G2 == -(Bx + Cx)qz * \frac{a^2}{2}, Bx \right] \right]$$

$$\text{Simplify} \left[\text{Solve} \left[\frac{(Bx e^{ihqz} - Cx e^{-ihqz})}{d^4} * H == (Bx e^{ihqz} + Cx e^{-ihqz}) qz * \frac{a^2}{2}, Bx \right] \right]$$

$$\left\{ \left\{ Bx \rightarrow \frac{2Cx G1\pi + 2G2\pi - a^2 Cx d^4 \pi qz + 4a^2 d^4 kz[1,0,0]}{2G1\pi + a^2 d^4 \pi qz} \right\} \right\}$$

$$\left\{ \left\{ Bx \rightarrow \frac{Cx e^{-2i h qz} (2H + a^2 d^4 qz)}{2H - a^2 d^4 qz} \right\} \right\}$$

$$\text{Simplify} \left[\text{Solve} \left[\frac{2Cx G1\pi + 2G2\pi - a^2 Cx d^4 \pi qz + 4a^2 d^4 kz[1,0,0]}{2G1\pi + a^2 d^4 \pi qz} == \frac{Cx e^{-2i h qz} (2H + a^2 d^4 qz)}{2H - a^2 d^4 qz}, Cx \right] \right]$$

$$\left\{ \left\{ Cx \rightarrow \frac{2e^{2i h qz} (2H - a^2 d^4 qz) (G2\pi + 2a^2 d^4 kz[1,0,0])}{\pi (-a^2 d^4 qz (-2(1 + e^{2i h qz}) H + a^2 d^4 (-1 + e^{2i h qz}) qz) + G1 (-4(-1 + e^{2i h qz}) H + 2a^2 d^4 (1 + e^{2i h qz}) qz))} \right\} \right\}$$

A.2.2 Mathematica Solution

*****Solution*****

$c := 3 * 10^8;$

$a := 6.0 * 10^3 - 3;$

$d := 10.0 * 10^3 - 3;$

$h := 18 * 10^3 - 6;$

$Epsv = 1;$

$Epsv = 1;$

$mmax = 4;$

$nmax = 4;$

$wmin = 10 * \pi * 10^9;$

$wmax = 61 * \pi * 10^9;$

$wpoints = 1000;$

$dw = N[(wmax - wmin)/(wpoints - 1), 5];$

$count = 1;$

$result = Array[0, wpoints];$

$For[w = wmin, w \leq (wmax + 0.3 * dw), w += dw,$

$Q1[m1_, m2_] := If[m1 == 0 \& \& m2 == 0, d^2, 0];$

$Q2[m1_, m2_] := If \left[m1 == 0, \frac{a^2 d^2 \left(1 + e^{-\frac{2ia m2 \pi}{d}} \right)}{(d^2 - 4a^2 m2^2) \pi}, \right.$
 $\left. - \frac{ia d^3 e^{-\frac{2ia(m1+m2)\pi}{d}} \left(-1 + e^{\frac{2ia m1 \pi}{d}} \right) \left(1 + e^{\frac{2ia m2 \pi}{d}} \right)}{2m1(d^2 - 4a^2 m2^2) \pi^2} \right];$

$Q4[m1_, m2_] := If \left[m1 == 0, \frac{a^2 d^2 \left(1 + e^{\frac{2ia m2 \pi}{d}} \right)}{(d^2 - 4a^2 m2^2) \pi}, - \frac{ia d^3 \left(-1 + e^{\frac{2ia m1 \pi}{d}} \right) \left(1 + e^{\frac{2ia m2 \pi}{d}} \right)}{2m1(d^2 - 4a^2 m2^2) \pi^2} \right];$

$kz[Epsv_, m1_, m2_] := \sqrt{Epsv(w/c)^2 - (2 * \pi * m1/d)^2 - (2 * \pi * m2/d)^2};$

$qz[Epsv_] := \sqrt{(Epsv(w/c)^2 - (\pi/a)^2)};$

A. Full Modal Matching Calculation

$$G1 = N \left[\sum_{m1=-mmax}^{+mmax} \sum_{m2=-mmax}^{+mmax} \frac{(4m1^2\pi^2+d^2kz[1,m1,m2]^2)*Q2[m1,m2]*Q4[m1,m2]}{kz[1,m1,m2]} \right];$$

$$G2 = N \left[\sum_{m1=-mmax}^{+mmax} \sum_{m2=-mmax}^{+mmax} \frac{(4m1^2\pi^2+d^2kz[1,m1,m2]^2)*Q1[m1,m2]*Q4[m1,m2]}{kz[1,m1,m2]} \right];$$

$$H = N \left[\sum_{n1=-nmax}^{+nmax} \sum_{n2=-nmax}^{+nmax} \frac{(4n1^2\pi^2+d^2kz[Epsv,n1,n2]^2)*Q2[n1,n2]*Q4[n1,n2]}{kz[Epsv,n1,n2]} \right];$$

$$Cx =$$

$$N \left[\left((2e^{2i h qz[Epsv]} (2H - a^2 d^4 qz[Epsv]) (G2\pi + 2a^2 d^4 kz[1, 0, 0])) / \right. \right. \\ \left. \left(\pi (-a^2 d^4 qz[Epsv]) (-2 (1 + e^{2i h qz[Epsv]}) H + a^2 d^4 (-1 + e^{2i h qz[Epsv]}) qz[Epsv]) + \right. \right. \\ \left. \left. G1 (-4 (-1 + e^{2i h qz[Epsv]}) H + 2a^2 d^4 (1 + e^{2i h qz[Epsv]}) qz[Epsv])) \right) \right];$$

$$Bx = N \left[\frac{Cx e^{-2i h qz[Epsv]} (2H + a^2 d^4 qz[Epsv])}{2H - a^2 d^4 qz[Epsv]} \right];$$

$$Dx[0, 0] = N \left[\frac{(Bx e^{i h qz[Epsv]} - Cx e^{-i h qz[Epsv]}) * Q2[0,0]}{e^{i h kz[Epsv,0,0]} d^2} \right];$$

$$trans = Abs[Dx[0, 0]]^2 * \sqrt{Epsv};$$

$$result = ReplacePart[result, trans, count];$$

$$count += 1;$$

]

$$ListPlot[result]$$

$$Export[$$

"C:\Users\Mel\My Documents\PhD\Square array square holes\Data\Finite thickness\d10\Td10a6h1000um.dat", result, "Lines";

References

- [1] SAUERMAN, T. Hilbert Cube (2008). [xix](#), [139](#)
- [2] EBBESEN, T.W., LEZEC, H.J., GHAEMI, H.F., THIO, T., AND WOLFF, P.A. Extraordinary optical transmission through sub-wavelength hole arrays. *Nature*, **391**(6668), 667 (1998). [1](#), [20](#), [57](#), [59](#), [84](#), [105](#)
- [3] WALSER, R.M. Electromagnetic metamaterials. *Complex Mediums Ii: Beyond Linear Isotropic Dielectrics*, **4467**, 1 (2001). [8](#)
- [4] SIHVOLA, A. Metamaterials in electromagnetics. *Metamaterials*, **1**(1), 2 (2007). [8](#)
- [5] METAMORPHOSE. Metamorphose: The Virtual Institute for Artificial Electromagnetic Materials and Metamaterials. [8](#)
- [6] SMITH, D.R., PADILLA, W.J., VIER, D.C., NEMAT-NASSER, S.C., AND SCHULTZ, S. Composite medium with simultaneously negative permeability and permittivity. *Physical Review Letters*, **84**(18), 4184 (2000). [8](#)
- [7] SHELBY, R.A., SMITH, D.R., AND SCHULTZ, S. Experimental verification of a negative index of refraction. *Science*, **292**(5514), 77 (2001). [8](#), [9](#)
- [8] WILTSHIRE, M.C. Optical materials. Bending light the wrong way. *Science*, **292**(5514), 60 (2001). [9](#)
- [9] VESELAGO, V.G. AND NARIMANOV, E.E. The left hand of brightness: past, present and future of negative index materials. *Nature Materials*, **5**(10), 759 (2006).
- [10] VESELAGO, V.G. Electrodynamics of Substances with Simultaneously Negative Values of Sigma and Mu. *Soviet Physics Uspekhi-Ussr*, **10**(4), 509 (1968). [9](#)

-
- [11] SMITH, D.R., PENDRY, J.B., AND WILTSHIRE, M.C.K. Metamaterials and negative refractive index. *Science*, **305**(5685), 788 (2004). [10](#)
- [12] SOUKOULIS, C.M. AND WEGENER, M. Past Achievements and Future Challenges in 3D Photonic Metamaterials. *Nature Photonics*, **5**(July), 1 (2011). [10](#)
- [13] SHIN, J., SHEN, J.T., AND FAN, P. Three-dimensional metamaterials with an ultra-high effective refractive index over broad bandwidth. [10](#)
- [14] PENDRY, J.B., SCHURIG, D., AND SMITH, D.R. Controlling electromagnetic fields. *Science*, **312**(5781), 1780 (2006). [10](#)
- [15] LEONHARDT, U. Optical conformal mapping. *Science*, **312**(5781), 1777 (2006). [10](#)
- [16] LEONHARDT, U. Optical Conformal Mapping and Dielectric Invisibility Devices. *Science Express* (2006). [10](#)
- [17] CUMMER, S.A., POPA, B.I., SCHURIG, D., SMITH, D.R., AND PENDRY, J. Full-wave simulations of electromagnetic cloaking structures. *Physical Review E*, **74**(3), (2006). [10](#)
- [18] ALU, A. AND ENGHETA, N. Plasmonic and metamaterial cloaking: physical mechanisms and potentials. *Journal of Optics A*, **10** (2008). [10](#)
- [19] ALU, A. AND ENGHETA, N. Achieving transparency with plasmonic and metamaterial coatings. *Physical Review E*, **72**(1), (2005). [10](#)
- [20] LAI, Y., CHEN, H., ZHANG, Z.Q., AND CHAN, C. Complementary Media Invisibility Cloak that Cloaks Objects at a Distance Outside the Cloaking Shell. *Physical Review Letters*, **102**(9), 1 (2009). [10](#)
- [21] MATUMURA, K., KAGAWA, Y., AND BABA, K. Light transmitting electromagnetic wave shielding composite materials using electromagnetic wave polarizing effect. *Journal of Applied Physics*, **101**(1), (2007). [10](#)
- [22] HAO, Y. AND MITTRA, R. *FDTD Modeling of Metamaterials: Theory and Applications*. Artech House, Inc. MA, Norwood, MA (2009). ISBN 978-1-59693-160-2. [11](#), [49](#)

-
- [23] GRIMALDI, F. *Physico mathesis de lumine, coloribus, et iride, aliisque annexis libri duo*. Vittorio Bonati, Italy (1665). [11](#), [35](#)
- [24] RIGAUD, S.J. *Correspondence of Scientific Men of the Seventeenth Century*, volume 2. Oxford University Press, Oxford, England (1841). [11](#)
- [25] YOUNG, T. The Bakerian Lecture: Experiments and calculations relative to physical optics. *Philosophical Transactions of the Royal Society of London Series a-Containing Papers of a Mathematical or Physical Character*, **94**, 1 (1804). [11](#)
- [26] FRESNEL, A. Memoire sur la diffraction de la lumiere. *Annales de la Chemie et de Physique*, **1**, 239 (1816). [11](#)
- [27] HUYGENS, C. *Traite de la lumiere*. Pieter van der Aa, Leiden, Netherlands (1690). [11](#)
- [28] HENKE, B.L., GULLIKSON, E.M., AND DAVIS, J.C. X-Ray Interactions - Photoabsorption, Scattering, Transmission, and Reflection at E=50-30,000 Ev, Z=1-92. *Atomic Data and Nuclear Data Tables*, **54**(2), 181 (1993). [11](#)
- [29] JOANNOPOULOS, J.D., VILLENEUVE, P.R., AND FAN, S.H. Photonic crystals: Putting a new twist on light (vol 386, pg 143, 1997). *Nature*, **387**(6635), 830 (1997). [11](#)
- [30] LANDAUER, R. Electrical Conductivity in Inhomogeneous Media. In *AIP Conference Proceedings*, pages 2–45. AIP (1978). [12](#)
- [31] ASPNES, D.E. Optical-Properties of Thin-Films. *Thin Solid Films*, **89**(3), 249 (1982). [12](#), [17](#)
- [32] GILLISPIE, C.C. *Dictionary of Scientific Biography*, volume IX. Scribner's, New York (1974). [12](#)
- [33] CLAUSIUS, R. *Die mechanische Behandlung der Electricitat*. Vieweg, Braunschweig (1879). [12](#)
- [34] LORENZ, L. Über die Refractionsconstante. *Wiedemannsche Annalen*, **11**(70-103) (1880). [12](#)
- [35] LORENTZ, H.A. *The Theory of Electrons*. B. G. Teubner, Leipzig (1909). [12](#)

-
- [36] GARNETT, J.C.M. Colours in metal glasses and in metallic films. *Philosophical Transactions of the Royal Society of London Series a-Containing Papers of a Mathematical or Physical Character*, **203**, 385 (1904). [12](#)
- [37] BRUGGEMAN, D.A.G. Calculation of different physical constants of heterogenous substances I Dielectric constants and conductivity of mixtures from isotropic substances. *Annalen Der Physik*, **24**(8), 665 (1935). [12](#)
- [38] BRUGGEMAN, D.A.G. Calculation of various physics constants in heterogeneous substances I Dielectricity constants and conductivity of mixed bodies from isotropic substances. *Annalen Der Physik*, **24**(7), 636 (1935).
- [39] BRUGGEMAN, D.A.G. Calculation of various physical constants of heterogeneous substances II. Dielectricity constants and conductivity of non regular multi crystal systems. *Annalen Der Physik*, **25**(7), 645 (1936). [12](#)
- [40] YOUNGS, I.J. *Electrical percolation and the design of functional electromagnetic materials*. Doctor of philosophy in electrical engineering, University of London, London (2001). [13](#), [16](#)
- [41] WU, L.Z., DING, J., JIANG, H.B., CHEN, L.F., AND ONG, C.K. Particle size influence to the microwave properties of iron based magnetic particulate composites. *Journal of Magnetism and Magnetic Materials*, **285**(1-2), 233 (2005). [13](#)
- [42] BREGAR, V.B. Effective-medium approach to the magnetics susceptibility of composites with ferromagnetic inclusions. *Physical Review B*, **71**(17), (2005).
- [43] LALANNE, P. Effective medium theory applied to photonic crystals composed of cubic or square cylinders. *Applied Optics*, **35**(27), 5369 (1996). [13](#), [17](#)
- [44] ASPNES, D.E. Local-Field Effects and Effective-Medium Theory - a Microscopic Perspective. *American Journal of Physics*, **50**(8), 704 (1982). [17](#), [18](#)
- [45] GAO, L., YU, K.W., LI, Z.Y., AND HU, B.B. Effective nonlinear optical properties of metal-dielectric composite media with shape distribution. *Physical Review E*, **6403**(3), (2001). [17](#)
- [46] GRANQVIST, C.G. AND HUNDERI, O. Conductivity of Inhomogeneous Materials - Effective-Medium Theory with Dipole-Dipole Interaction. *Physical Review B*, **18**(4), 1554 (1978). [17](#)

-
- [47] MILTON, G.W. Bounds on the Complex Dielectric-Constant of a Composite-Material. *Applied Physics Letters*, **37**(3), 300 (1980). 17
- [48] BERGMAN, D.J. Exactly Solvable Microscopic Geometries and Rigorous Bounds for the Complex Dielectric-Constant of a 2-Component Composite-Material. *Physical Review Letters*, **44**(19), 1285 (1980).
- [49] HASHIN, Z. AND SHTRIKMAN, S. A Variational Approach to Theory of Effective Magnetic Permeability of Multiphase Materials. *Journal of Applied Physics*, **33**(10), 3125 (1962). 17
- [50] DOYLE, W.T. AND JACOBS, I.S. The Influence of Particle-Shape on Dielectric Enhancement in Metal-Insulator Composites. *Journal of Applied Physics*, **71**(8), 3926 (1992). 18
- [51] CHANG, C.Y., KUO, L.C., AND HUI, P.M. Effects of Clustering in Binary Composites - Random Fractals. *Physical Review B*, **46**(22), 14505 (1992).
- [52] ZABEL, I.H.H. AND STROUD, D. Metal-Clusters and Model Rocks - Electromagnetic Properties of Conducting Fractal Aggregates. *Physical Review B*, **46**(13), 8132 (1992). 18
- [53] RAYLEIGH, L. On the influence of obstacles arranged in rectangular order on the properties of a medium. *Philosophical Magazine*, **34**, 481 (1892). 18
- [54] STROUD, D. AND PAN, F.P. Self-Consistent Approach to Electromagnetic-Wave Propagation in Composite Media - Application to Model Granular Metals. *Physical Review B*, **17**(4), 1602 (1978). 18
- [55] MCLACHLAN, D.S. An Equation for the Conductivity of Binary-Mixtures with Anisotropic Grain Structures. *Journal of Physics C-Solid State Physics*, **20**(7), 865 (1987). 18
- [56] MCLACHLAN, D.S. Equation for the Conductivity of Metal-Insulator Mixtures. *Journal of Physics C-Solid State Physics*, **18**(9), 1891 (1985).
- [57] MCLACHLAN, D.S. Equations for the Conductivity of Macroscopic Mixtures. *Journal of Physics C-Solid State Physics*, **19**(9), 1339 (1986).
- [58] MCLACHLAN, D.S. AND SAUTI, G. The AC and DC Conductivity (Dielectric Constant) of Composites. *Dielectrics Newsletter* (2008). 18

-
- [59] WOOD, R.W. On a remarkable case of uneven distribution of light in diffraction gratings problems. *Philosophical Magazine* (1902). [19](#)
- [60] GARCÍA DE ABAJO, F.J. AND GARCIA DE ABAJO, F.J. Colloquium: Light scattering by particle and hole arrays. *Reviews of Modern Physics*, **79**(4), 1267 (2007). [19](#), [38](#), [59](#), [61](#)
- [61] HIBBINS, A.P. *Grating Coupling of Surface Plasmon Polaritons at Visible and Microwave Frequencies*. Ph.D. thesis, University of Exeter (1999). [19](#), [25](#), [28](#)
- [62] RAYLEIGH, L. Note on the remarkable case of diffraction spectra described by Prof. Wood. *Philosophical Magazine*, **14**, 60 (1907). [19](#)
- [63] FANO, U. The Theory of anomalous diffraction gratings and of quasi-stationary waves on metallic surfaces (Sommerfeld's waves). *Journal of Optics*, **31**, 213 (1941). [20](#), [105](#)
- [64] BETHE, H.A. Theory of diffraction by small holes. *Physical Review*, **66**, 163 (1944). [20](#)
- [65] ULRICH, R. Far-Infrared properties of metallic mesh and its complementary structure. *Infrared Physics*, **7**(1), 37 (1967). [20](#), [38](#), [39](#), [41](#), [58](#), [94](#), [105](#)
- [66] ULRICH, R. Effective Low-Pass Filters for Far Infrared Frequencies. *Infrared Physics*, **7**(2), 65 (1967). [20](#), [58](#), [61](#)
- [67] CHEN, C.C. Diffraction of Electromagnetic Waves by a Conducting Screen Perforated Periodically with Circular Holes. *IEEE Transactions on Microwave Theory and Techniques*, **Mt19**(5), 475 (1971). [20](#), [59](#)
- [68] MCPHEDRAN, R.C., DERRICK, G.H., AND BOTTEN, L.C. *Electromagnetic Theory of Gratings*, volume 22. Springer-Verlag, Berlin (1980). [20](#), [38](#), [41](#)
- [69] SOMMERFELD, A. Over the production of the waves in the wireless telegraphy. *Annalen Der Physik*, **28**, 665 (1909). [20](#), [59](#)
- [70] ZENNECK, J. Over the reproduction of even electromagnetic waves of an even leader-flat and their relationship with the wireless telegraphy. *Annalen Der Physik*, **23**, 846 (1907). [20](#)

-
- [71] KRETSCHMANN, E. AND RAETHER, H. Radiative decay of non-radiative surface plasmons excited by light. *Z. Naturforsch*, **23A**, 2135 (1968). [20](#)
- [72] OTTO, A. Excitation of surface plasma waves in silver by the method of frustrated total reflection. *Z. Physik*, **216**, 398 (1968). [20](#)
- [73] TENG, Y.Y.Y. AND STERN, E.E.A. Plasma radiation from metal grating surfaces. *Physical Review Letters*, **19**(9), 511 (1967). [20](#)
- [74] HOOPER, I.R. *The Optical Response of Short-Pitch Surface-Relief Gratings*. Ph.D. thesis, Univeristy of Exeter (2002). [24](#)
- [75] BARLOW, H.M., CULLEN, A.L., MACFARLANE, G.G., STUART, B.I., LINHART, J.G., DYOTT, R.B., AND KARBOWIAK, A.E. Surface Waves. *Proceedings of the Institution of Electrical Engineers-London*, **100**(68), 329 (1953). [25](#), [59](#)
- [76] CUTLER, C.C. Genesis of the Corrugated Electromagnetic Surface (Corrugated Wave-Guide). *Ieee Antennas and Propagation Society International Symposium 1994, Vols I-Iii*, pages 1456–1459 2271 (1994). [25](#)
- [77] LOCKYEAR, M.J. *Electromagnetic surface wave mediated absorption and transmission of radiation at microwave frequencies*. Doctor of philosophy of physics, University of Exeter (2004). [27](#), [34](#), [36](#), [53](#)
- [78] POZAR, D.M. *Microwave Engineering*. John wiley & Sons, Inc., Hobokem, New Jersey, third edition (2005). [28](#), [32](#)
- [79] WHITBOURN, L.B. AND COMPTON, R.C. Equivalent-Circuit Formulas for Metal Grid Reflectors at a Dielectric Boundary. *Applied Optics*, **24**(2), 217 (1985). [38](#), [41](#)
- [80] COMPTON, R.C. Approximation Techniques for Planar Periodic Structures. *IEEE Transactions on Microwave Theory and Techniques*, **33**(10), 1083 (1985).
- [81] CHRISTOPOULOS, C., HERRING, J.C., AND SCARAMUZZA, R.A. Electromagnetic simulation using transmission-line modelling. In *IEE Colloquium on Transmission Line Matrix Modelling*. London (1991).

-
- [82] JOHNS, P.B. AND BEURLE, R.L. Numerical Solution of 2-Dimensional Scattering Problems using a Transmission-Line Matrix. *Proceedings of the Institution of Electrical Engineers-London*, **118**, 1203 (1971).
- [83] MUNK, B.A. *Frequency Selective Surfaces*. John Wiley & Sons, Inc., New York (2000). [58](#), [94](#)
- [84] MEDINA, F., MESA, F., AND SKIGIN, D.C. Extraordinary transmission through arrays of slits: a circuit theory model. *IEEE Transactions on Microwave Theory and Techniques* (2009). [38](#)
- [85] GARCIA-VIDAL, F.J., MARTIN-MORENO, L., AND PENDRY, J.B. Surfaces with holes in them: new plasmonic metamaterials. *Journal of Optics a-Pure and Applied Optics*, **7**(2), S97 (2005). [38](#), [41](#), [66](#)
- [86] PENDRY, J.B., MARTÍN-MORENO, L., GARCIA-VIDAL, F.J., AND MARTIN-MORENO, L. Mimicking surface plasmons with structured surfaces. *Science*, **305**(5685), 847 (2004). [41](#), [59](#), [105](#), [146](#)
- [87] SHEN, L.F., CHEN, X.D., AND YANG, T.J. Terahertz surface plasmon polaritons on periodically corrugated metal surfaces. *Optics Express*, **16**(5), 3326 (2008).
- [88] BRAVO-ABAD, J., MARTIN-MORENO, L., GARCIA-VIDAL, F.J., HENDRY, E., AND RIVAS, J.G. Transmission of light through periodic arrays of square holes: From a metallic wire mesh to an array of tiny holes. *Physical Review B*, **76**(24), 241102 (2007). [41](#), [66](#), [71](#), [78](#)
- [89] HENDRY, E., HIBBINS, A.P., AND SAMBLES, J.R. Importance of diffraction in determining the dispersion of designer surface plasmons. *Physical Review B*, **78**(23), 235426 (2008). [41](#), [66](#)
- [90] BRAVO-ABAD, J., GARCÍA-VIDAL, F., MARTÍN-MORENO, L., GARCIA-VIDAL, F.J., AND MARTIN-MORENO, L. Resonant transmission of light through finite chains of subwavelength holes in a metallic film. *Physical Review Letters*, **93**(22), 227401 (2004). [41](#), [75](#)
- [91] GARCIA DE ABAJO, F.J., GOMEZ-MEDINA, R., AND SAENZ, J.J. Full transmission through perfect-conductor subwavelength hole arrays. *Physical Review E*, **72**(1), 16608 (2005). [38](#), [41](#), [61](#), [76](#)

-
- [92] SAULEAU, R., COQUET, P., DANIEL, J.P., MATSUI, T., AND HIROSE, N. Study of Fabry-Perot cavities with metal mesh mirrors using equivalent circuit models, comparison with experimental results in the 60 GHz band. *International Journal of Infrared and Millimeter Waves*, **19**(12), 1693 (1998). [39](#), [40](#), [41](#), [146](#)
- [93] MARCUVITZ, N. *Waveguide Handbook*. McGraw Hill Book Company Inc., New York (1951). [40](#)
- [94] CHEN, C.C. Transmission of microwave through perforated flat plates of finite thickness. *IEEE Transactions on Microwave Theory and Techniques*, **21**(1), 1 (1973). [41](#)
- [95] MARY, A., RODRIGO, S.G., MARTIN-MORENO, L., AND GARCIA-VIDAL, F.J. Theory of light transmission through an array of rectangular holes. *Physical Review B*, **76**(19), 195414 (2007). [41](#), [84](#)
- [96] WOLFRAM RESEARCH, I. *Mathematica* (2008). [48](#), [168](#)
- [97] YEE, K.S. Numerical Solution of Initial Boundary Value Problems Involving Maxwells Equations in Isotropic Media. *Ieee Transactions on Antennas and Propagation*, **Ap14**(3), 302 (1966). [49](#)
- [98] TAFLOVE, A. Application of the finite-difference time-domain method to sinusoidal steady-state electromagnetic-penetration problems. *Ieee Transactions On Electromagnetic Compatibility*, **22**(3), 191 (1980). [49](#)
- [99] KAHNERT, F.M. Numerical methods in electromagnetic scattering theory. *Journal of Quantitative Spectroscopy & Radiative Transfer*, **79**, 775 (2003). [50](#)
- [100] SALOMON, L., GRILLOT, F., ZAYATS, A.V., AND DE FORNEL, F. Near-field distribution of optical transmission of periodic subwavelength holes in a metal film. *Physical Review Letters*, **86**(6), 1110 (2001). [50](#)
- [101] LAKHTAKIA, A. AND MULHOLLAND, G.W. On two numerical techniques for light scattering by dielectrci agglomerated structures. *J. Res. Natl. Inst. Stand. Technol.*, **98**, 699 (1993). [50](#)
- [102] DAVIES, R.W. *The Finite Element Method: A First Approach*. Oxford University Press, Oxford, England (1980). [50](#)

-
- [103] HRENNIKOFF, A. Solution of problems in elasticity by the framework method. *J. Appl. Mech.*, **A8**, 169 (1941). [50](#)
- [104] MCHENRY, D. A lattice analogy for the solution of plane stress problems. *J. Inst. Civ. Eng.*, **21**, 59 (1943). [50](#)
- [105] WILSON, E.L. AND NICKELL, R.E. Application of finite element method to heat conduction analysis. *Nucl. Engng. Des.*, **4**, 1 (1966). [50](#)
- [106] CONNOR, J.J. AND BREBBIA, C.A. *Finite element techniques for fluid flow*. Newnes-Butterworths, London (1976). [50](#)
- [107] GOULD, P.L., CATALOGLU, A., AND CLARK, R.E. Mathematical modelling of human aortic valve leaflets. *Applied Mathematical Modelling*, **1**, 33 (1976). [50](#)
- [108] ZIENKIEWICZ, O.C., TAYLOR, R.L., AND ZHU, J.Z. *The Finite Element Method*. Elsevier Butterworth-Heinemann, Oxford, England, 6th edition (2005). [50](#)
- [109] HFSSTM, A. AND ANSOFT CORPORATION. Ansoft HFSSTM. [51](#)
- [110] MARTIN-MORENO, L., GARCIA-VIDAL, F.J., LEZEC, H.J., PELLERIN, K.M., THIO, T., PENDRY, J.B., AND EBBESEN, T.W. Theory of extraordinary optical transmission through subwavelength hole arrays. *Physical Review Letters*, **86**(6), 1114 (2001). [57](#), [59](#), [153](#)
- [111] GENET, C. AND EBBESEN, T.W. Light in tiny holes. *Nature*, **445**, 39 (2007). [57](#)
- [112] ANTONETS, I.V., KOTOV, L.N., NEKIPELOV, S.V., AND GOLUBEV, Y.A. Nanostructure and conductivity of thin metal films. *Technical Physics*, **49**(3), 306 (2004). [57](#)
- [113] KELLY, R.J., LOCKYEAR, M.J., SUCKLING, J.R., SAMBLES, J.R., AND LAWRENCE, C.R. Enhanced microwave transmission through a patterned metal film. *Applied Physics Letters*, **90**(22), 223506 (2007).
- [114] LAGARKOV, A., ROZANOV, K., SARYCHEV, A., AND SIMONOV, N. Experimental and theoretical study of metal-dielectric percolating films at microwaves. *Physica A: Statistical and Theoretical Physics*, **241**(1-2), 199 (1997).

-
- [115] STONE, E. AND HENDRY, E. Dispersion of spoof surface plasmons in open-ended metallic hole arrays. *Physical Review B*, **84**(3) (2011). [57](#)
- [116] ANTONETS, I.V., KOTOV, L.N., NEKIPELOV, S.V., AND KARPUSHOV, E.N. Conducting and reflecting properties of thin metal films. *Technical Physics*, **49**(11), 1496 (2004). [57](#)
- [117] ULRICH, R. Interference filters for the Far Infrared. *Applied optics*, **7**(10), 1987 (1968). [58](#)
- [118] SHANAHAN, S.T. AND HECKENBERG, N.R. Transmission line model of substrate effects on capacitive mesh couplers. *Applied optics*, **20**(23) (1981). [58](#)
- [119] CHRIST, A., TIKHODEEV, S., GIPPIUS, N., KUHL, J., AND GIESSEN, H. Waveguide-Plasmon Polaritons: Strong Coupling of Photonic and Electronic Resonances in a Metallic Photonic Crystal Slab. *Physical Review Letters*, **91**(18), 1 (2003). [59](#)
- [120] EL-KADY, I., SIGALAS, M., BISWAS, R., AND HO, K. Metallic photonic crystals at optical wavelengths. *Physical Review B*, **62**(23), 299 (2000). [59](#)
- [121] O'BRIEN, S. Magnetic activity at infrared frequencies in structured metallic photonic crystals. *Journal of Physics: Condensed Matter*, **6383** (2002). [59](#)
- [122] FLEMING, J.G., LIN, S.Y., BISWAS, R., AND HO, K.M. photonic crystals with a large infrared bandgap. *Nature*, **417**(May), 1548 (2002). [59](#)
- [123] HIBBINS, A.P., EVANS, B.R., SAMBLES, J.R., AND SAMPLES, J.R. Experimental verification of designer surface plasmons. *Science*, **308**(5722), 670 (2005). [59](#)
- [124] ULRICH, R. AND TACKE, M. Submillimeter waveguiding on periodic metal structure. *Applied Physics Letters*, **22**(5), 251 (1972). [59](#), [105](#)
- [125] POPOV, E., NEVIERE, M., ENOCH, S., AND REINISCH, R. Theory of light transmission through subwavelength periodic hole arrays. *Physical Review B*, **62**(23), 16100 (2000).
- [126] BRAUN, J., GOMPF, B., KOBIELA, G., AND DRESSEL, M. How holes can obscure the view: Suppressed transmission through an ultrathin metal film by a subwavelength hole array. *Physical Review Letters*, **103**(20), 203901 (2009).

-
- [127] BARNES, W.L., MURRAY, W.A., DINTINGER, J., DEVAUX, E., AND EBBESEN, T.W. Surface plasmon polaritons and their role in the enhanced transmission of light through periodic arrays of subwavelength holes in a metal film. *Physical Review Letters*, **92**(10), (2004).
- [128] CHEN, C. Transmission through a conducting screen perforated periodically with apertures. *Microwave Theory and Techniques, IEEE Transactions on*, **18**(9), 627 (1970). [59](#)
- [129] EDMUNDS, J.D. *Microwave Transmissivity of Sub-Wavelength Metallic Structures*. Doctor of philosophy in physics, University of Exeter (2011). [60](#), [61](#), [63](#)
- [130] MURRAY, W.A. *Optical properties of nanoscale silver structures fabricated by nanosphere lithography*. Ph.D. thesis, University of Exeter, Exeter (2005). [62](#)
- [131] BABINET, M. Memoires d'optique meteorologique. *CR Acad. Sci.*, **4**, 638 (1837). [61](#)
- [132] COMPTON, R.C., MACFARLANE, J.C., WHITBOURN, L.B., BLANCO, M.M., AND MCPHEDRAN, R.C. Babinet Principle Applied to Ideal Beam-Splitters for Submillimeter Waves. *Optica Acta*, **31**(5), 515 (1984). [61](#)
- [133] FALCONE, F., LOPETEGI, T., LASO, M.A.G., BAENA, J.D., BONACHE, J., BERUETE, M., MARQUES, R., MARTIN, F., AND SOROLLA, M. Babinet principle applied to the design of metasurfaces and metamaterials. *Physical Review Letters*, **93**(19), 197401 (2004).
- [134] LUUKKONEN, O., SIMOVSKI, C., GRANET, G., GOUSSETIS, G., LI-OUBTCHENKO, D., RAISANEN, A.V., AND TRETAKOV, S.A. Simple and accurate analytical model of planar grids and high-impedance surfaces, comprising metal strips or patches. *Ieee Transactions on Antennas and Propagation*, **56**(6), 1624 (2008). [61](#)
- [135] BOOKER, H.G. Slot aerials and their relation to complementary wire aerials (Babinet's Principle). *J. Instn. Elect. Engrs.*, **93**(III A), 620 (1946). [61](#), [94](#)
- [136] BORN, M. AND WOLFF, E. *Principles of Optics*. Cambridge University Press, Cambridge (2002). [62](#), [130](#)

-
- [137] TAYLOR, M.C., EDMUNDS, J.D., HENDRY, E., HIBBINS, A.P., AND SAMBLES, J.R. Microwave response of hole and patch arrays. *Physical Review B*, **82**(15), (2010). [67](#), [68](#), [74](#), [80](#), [81](#), [105](#)
- [138] BRAVO-ABAD, J., FERNANDEZ-DOMINGUEZ, A.I., GARCIA-VIDAL, F.J., AND MARTIN-MORENO, L. Theory of extraordinary transmission of light through quasiperiodic arrays of subwavelength holes. *Physical Review Letters*, **99**(20), (2007). [66](#)
- [139] FANO, U. Effects of Configuration Interaction on Intensities and Phase Shifts. *Physical Review*, **1**(6), 1866 (1961). [69](#)
- [140] ROCKSTUHL, C., ZENTGRAF, T., MEYRATH, T.P., GIESSEN, H., AND LEDERER, F. Resonances in complementary metamaterials and nanoapertures. *Optics Express*, **16**(3), 2080 (2008). [71](#)
- [141] HUANG, X.R. AND PENG, R.W. General mechanism involved in subwavelength optics of conducting microstructures: charge-oscillation-induced light emission and interference. *Journal of the Optical Society of America a-Optics Image Science and Vision*, **27**(4), 718 (2010). [76](#)
- [142] EDMUNDS, J.D., HIBBINS, A.P., SAMBLES, J.R., AND YOUNGS, I.J. Resonantly inverted microwave transmissivity threshold of metal grids. *New Journal of Physics*, **12**, (2010). [82](#)
- [143] DEGIRON, A. AND EBBESEN, T.W. The role of localized surface plasmon modes in the enhanced transmission of periodic subwavelength apertures. *Journal of Optics A: Pure and Applied Optics*, **7**(2), S90 (2005). [84](#)
- [144] KOERKAMP, K., ENOCH, S., SEGERINK, F., VAN HULST, N., AND KUIPERS, L. Strong Influence of Hole Shape on Extraordinary Transmission through Periodic Arrays of Subwavelength Holes. *Physical Review Letters*, **92**(18) (2004).
- [145] GORDON, R., BROLO, A., MCKINNON, A., RAJORA, A., LEATHEM, B., AND KAVANAGH, K. Strong Polarization in the Optical Transmission through Elliptical Nanohole Arrays. *Physical Review Letters*, **92**(3) (2004).
- [146] CAO, H. AND NAHATA, A. Influence of aperture shape on the transmission properties of a periodic array of subwavelength apertures. *Optics Express*, **12**(16), 3664 (2004).

-
- [147] VAN DER MOLEN, K.L., KLEIN KOERKAMP, K.J., ENOCH, S., SEGERINK, F.B., VAN HULST, N.F., AND KUIPERS, L. Role of shape and localized resonances in extraordinary transmission through periodic arrays of subwavelength holes: Experiment and theory. *Physical Review B*, **72**(4), (2005). [84](#), [91](#)
- [148] JIA, W.L. AND LIU, X.H. Origin of superenhanced light transmission through two-dimensional subwavelength rectangular hole arrays. *European Physical Journal B*, **46**(3), 343 (2005).
- [149] DIMAIO, J.R. AND BALLATO, J. Polarization-dependent transmission through subwavelength anisotropic aperture arrays. *Optics Express*, **14**(6), 2380 (2006).
- [150] REN, X.F., ZHANG, P., GUO, G.P., HUANG, Y.F., WANG, Z.W., AND GUO, G.C. Polarization properties of subwavelength hole arrays consisting of rectangular holes. *Applied Physics B*, **91**(3-4), 601 (2008).
- [151] LEE, J., SEO, M., PARK, D., KIM, D., JEOUNG, S., LIENAU, C., PARK, Q.H., AND PLANKEN, P. Shape resonance omni-directional terahertz filters with near-unity transmittance. *Optics Express*, **14**(3), 1253 (2006).
- [152] LI, J.Y., HUA, Y.L., FU, J.X., AND LI, Z.Y. Influence of hole geometry and lattice constant on extraordinary optical transmission through subwavelength hole arrays in metal films. *Journal of Applied Physics*, **107**(7), (2010). [84](#)
- [153] ZHAO, Q., LI, C., ZHOU, Y., AND WANG, H. The mechanism of the polarization dependence of the optical transmission in subwavelength metal hole arrays. *Journal of Physics Condensed Matter*, **23**, 15005 (2011). [85](#)
- [154] SAUVAN, C., BILLAudeau, C., COLLIN, S., BARDOU, N., PARDO, F., PELOUARD, J.L., AND LALANNE, P. Surface plasmon coupling on metallic film perforated by two-dimensional rectangular hole array. *Applied Physics Letters*, **92**(1), (2008). [85](#)
- [155] MCPHEDRAN, R.C. AND MAYSTRE, D. Theory and Solar Application of Inductive Grids. *Applied Physics*, **14**(1), 1 (1977). [94](#)
- [156] YU, Z.N., DESHPANDE, P., WU, W., WANG, J., AND CHOU, S.Y. Reflective polarizer based on a stacked double-layer subwavelength metal grating structure fabricated using nanoimprint lithography. *Applied Physics Letters*, **77**(7), 927 (2000). [106](#)

-
- [157] ORTUNO, R., GARCIA-MECA, C., RODRIGUEZ-FORTUNO, F.J., MARTI, J., AND MARTINEZ, A. Role of surface plasmon polaritons on optical transmission through double layer metallic hole arrays. *Physical Review B*, **79**(7), (2009). [106](#)
- [158] CHENG, C., CHEN, J., WU, Q.Y., REN, F.F., XU, J., FAN, Y.X., AND WANG, H.T. Controllable electromagnetic transmission based on dual-metallic grating structures composed of subwavelength slits. *Applied Physics Letters*, **91**(11), (2007). [106](#)
- [159] HE, M.D., WANG, L.L., LIU, J.Q., ZHAI, X., WAN, Q., CHEN, X., AND ZOU, B.S. Controllable light transmission through cascaded metal films perforated with periodic hole arrays. *Applied Physics Letters*, **93**(22), (2008). [106](#), [163](#)
- [160] MIYAMARU, F. AND HANGYO, M. Anomalous terahertz transmission through double-layer metal hole arrays by coupling of surface plasmon polaritons. *Physical Review B*, **71**(16), (2005). [106](#)
- [161] MARCET, Z., HANG, Z.H., CHAN, C.T., KRAVCHENKO, I., BOWER, J.E., CIRELLI, R.A., KLEMENS, F., MANSFIELD, W.M., MINER, J.F., PAI, C.S., AND CHAN, H.B. Optical transmission through double-layer, laterally shifted metallic subwavelength hole arrays. *Optics Letters*, **35**(13), 2124 (2010). [106](#)
- [162] FABRY, C. AND PEROT, A. Theorie et applications d'une nouvelle methode de spectroscopie interferentielle. *Annales de la Chemie et de Physique*, **115** (1899). [106](#)
- [163] SCALORA, M., BLOEMER, M.J., AND BOWDEN, C.M. Laminated photonic band structures with high conductivity and high transparency: Metals under a new light. *Optics & Photonics News*, **10**(9), 23 (1999). [128](#)
- [164] SCALORA, M., BLOEMER, M.J., PETHEL, A.S., DOWLING, J.P., BOWDEN, C.M., AND MANKA, A.S. Transparent, metallo-dielectric, one-dimensional, photonic band-gap structures. *Journal of Applied Physics*, **83**(5), 2377 (1998).
- [165] LARCIPRETE, M.C., SIBILIA, C., PAOLONI, S., BERTOLOTTI, M., SARTO, F., AND SCALORA, M. Accessing the optical limiting properties of metallo-dielectric photonic band gap structures. *Journal of Applied Physics*, **93**(9), 5013 (2003). [128](#)

-
- [166] MACLEOD, H.A. *Thin Film Optical Filters*. Taylor & Francis, London, third edition (2001). [128](#), [137](#)
- [167] BERUETE, M., NAVARRO-CIA, M., AND SOROLLA, M. Strong lateral displacement in polarization anisotropic extraordinary transmission metamaterial. *New Journal of Physics*, **12**, (2010).
- [168] BERUETE, M., SOROLLA, M., AND CAMPILLO, I. Left-handed extraordinary optical transmission through a photonic crystal of subwavelength hole arrays. *Optics Express*, **14**(12), 5445 (2006).
- [169] SMITH, H.A., REBBERT, M., AND STERNBERG, O. Designer infrared filters using stacked metal lattices. *Applied Physics Letters*, **82**(21), 3605 (2003).
- [170] BERUETE, M., SOROLLA, M., NAVARRO-CIA, M., FALCONE, F., CAMPILLO, I., AND LOMAKIN, V. Extraordinary transmission and left-handed propagation in miniaturized stacks of doubly periodic subwavelength hole arrays. *Optics Express*, **15**(3), 1107 (2007). [128](#)
- [171] GEFFCKEN, W. Dispersion filters according to Christiansen in the formation of light monochromators. *Kolloid-Zeitschrift*, **86**(1), 55 (1939). [128](#), [137](#), [146](#)
- [172] PARSONS, J., HENDRY, E., AUGUIE, B., BARNES, W.L., AND SAMBLES, J.R. Localised modes of sub-wavelength hole arrays in thin metal films - art. no. 69880Y. *Nanophotonics Ii*, **6988**, Y9880 (2008). [128](#)
- [173] BUTLER, C.A.M., HOOPER, I.R., HIBBINS, A.P., SAMBLES, J.R., AND HOBSON, P.A. Metamaterial tunnel barrier gives broadband microwave transmission. *Journal of Applied Physics*, **109**(1) (2011). [128](#)
- [174] BUTLER, C.A.M., PARSONS, J., SAMBLES, J.R., HIBBINS, A.P., AND HOBSON, P.A. Microwave transmissivity of a metamaterial-dielectric stack. *Applied Physics Letters*, **95**(17) (2009). [137](#), [143](#), [144](#), [145](#), [146](#), [153](#)
- [175] KAIPA, C.S.R., YAKOVLEV, A.B., MEDINA, F., MESA, F., BUTLER, C.A.M., AND HIBBINS, A.P. Circuit modeling of the transmissivity of stacked two-dimensional metallic meshes. *Optics Express*, **18**(13), 13309 (2010). [128](#)
- [176] ATHERTON, T. AND MATHUR, H. A Photonics Analogy to Topological Insulators (2010). [129](#), [153](#), [154](#)

-
- [177] ATHERTON, T. AND MATHUR, H. Topological states in one dimensional solids and photonic crystals (2011). [129](#), [153](#), [154](#)
- [178] MOORE, J.E. AND BALENTS, L. Topological invariants of time-reversal-invariant band structures. *Physical Review B*, **75**(12), (2007). [129](#), [153](#)
- [179] FLEGG, H.G. *From Geometry to Topology*. The English Universities Press Ltd., London (1974). [129](#)
- [180] EULER, L. Solutio Problematis ad Geometriam Situs Pertinentis. *Commentarii Academiae Scientiarum Imperialis Petropolitanae*, pages 128–140 (1736). [129](#)
- [181] LISTING, J.B. *Vorstudien zur Topologie*. Vandenhoeck und Ruprecht, Gottingen (1848). [129](#)
- [182] TAIT, P.G. Johann Benedict Listing (obituary). *Nature*, **27**, 316 (1883). [129](#)
- [183] POINCARÉ, H. Analysis Situs. *Journal de l'Ecole Polytechnique*, **2**(1), 1 (1895). [129](#)
- [184] FITCH, W.M. Toward Defining the Course of Evolution: Minimum Change for a Specific Tree Topology. *Syst Biol*, **20**(4), 406 (1971). [129](#)
- [185] TOMALIA, D.A., NAYLOR, A.M., AND GODDARD, W.A. Starburst Dendrimers: Molecular-Level Control of Size, Shape, Surface Chemistry, Topology, and Flexibility from Atoms to Macroscopic Matter. *Angewandte Chemie International Edition in English*, **29**(2), 138 (1990). [129](#)
- [186] ALBERT, R. AND BARABÁSI, A.L. Topology of Evolving Networks: Local Events and Universality. *Physical Review Letters*, **85**(24), 5234 (2000). [129](#)
- [187] OLFATI-SABER, R. AND MURRAY, R. Consensus Problems in Networks of Agents With Switching Topology and Time-Delays. *IEEE Transactions on Automatic Control*, **49**(9), 1520 (2004). [129](#)
- [188] POLYAKOV, A. Quark confinement and topology of gauge theories. *Nuclear Physics B*, **120**(3), 429 (1977). [129](#)
- [189] KIBBLE, T.W.B. Topology of cosmic domains and strings. *Journal of Physics A: Mathematical and General*, **9**(8), 1387 (1976). [129](#)

-
- [190] PFUND, A.H. Highly Reflecting Films of Zinc Sulphide. *Journal of the Optical Society of America*, **24**(4) (1934). [137](#)
- [191] PENDRY, J. Negative refraction makes a perfect lens. *Physical review letters*, **85**(18), 3966 (2000). [137](#), [143](#)
- [192] RENTELN, P. AND DUNDES, A. Foolproof : A Sampling of Mathematical Folk Humor. *Notices of the AMS*, **52**(1), 24 (2005). [137](#), [139](#)
- [193] MOORE, J.E. Topological insulators. *IEEE Spectrum*, (july), 39 (2011). [137](#)
- [194] SMITH, D.R. AND SCHULTZ, S. Determination of effective permittivity and permeability of metamaterials from reflection and transmission coefficients. *Physical Review B*, **65**(19), 1 (2002). [140](#)
- [195] SCALORA, M., D'AGUANO, G., MATTIUCCI, N., BLOEMER, M.J., DE CEGLIA, D., CENTINI, M., MANDATORI, A., SIBILIA, C., AKOZBEK, N., CAPPEDDU, M.G., FOWLER, M., AND HAUS, J.W. Negative refraction and sub-wavelength focusing in the visible range using transparent metallo-dielectric stacks. *Optics Express*, **15**(2), 508 (2007). [143](#)
- [196] ZHANG, W., LEI, X., WANG, Z., ZHENG, D., TAM, W., CHAN, C., AND SHENG, P. Robust photonic band gap from tunable scatterers. *Physical review letters*, **84**(13), 2853 (2000). [143](#)
- [197] BAE, J., CHIAO, J.C., MIZUNO, K., AND RUTLEDGE, D.B. Metal mesh couplers using evanescent waves at millimeter and submillimeter wavelengths. *International Journal of Infrared and Millimeter Waves*, **16**(2), 377 (1995). [146](#)
- [198] WANG, Z., CHONG, Y., JOANNOPOULOS, J.D., AND SOLJACIĆ, M. Observation of unidirectional backscattering-immune topological electromagnetic states. *Nature*, **461**(7265), 772 (2009). [153](#)
- [199] ALEXEYEV, C.N., ALEXEYEV, A.N., FADEYEVA, T.A., LAPIN, B.P., AND YAVORSKY, M.A. Topological activity of layered chiral optical Bragg waveguides. *Journal of Optics*, **13**(9), 095701 (2011). [153](#)
- [200] HOOPER, I., PREIST, T., AND SAMBLES, J. Making Tunnel Barriers (Including Metals) Transparent. *Physical Review Letters*, **97**(5), 1 (2006). [153](#)

- [201] GADSDON, M.R., PARSONS, J., AND SAMBLES, J.R. Electromagnetic resonances of a multilayer metal-dielectric stack. *Journal of the Optical Society of America B*, **26**(4), 734 (2009). [153](#)
- [202] MARTIN, T. AND LANDAUER, R. Time delay of evanescent electromagnetic waves and the analogy to particle tunneling. *Physical Review A*, **45**(4), 2611 (1992). [153](#)
- [203] GARCÍA-VIDAL, F. AND MARTÍN-MORENO, L. Transmission and focusing of light in one-dimensional periodically nanostructured metals. *Physical Review B*, **66**(15), 1 (2002). [162](#)
- [204] DEPINE, R.A. AND SKIGIN, D.C. Scattering from metallic surfaces having a finite number of rectangular grooves. *Journal of the Optical Society of America A*, **11**(11), 2844 (1994).
- [205] DELGADO, V., MARQUES, R., AND JELINEK, L. Analytical theory of extraordinary optical transmission through realistic metallic screens. *Optics Express*, **18**(7), 6506 (2010). [162](#)
- [206] WANNEMACHER, R. Plasmon-supported transmission of light through nanometric holes in metallic thin films. *Optics Communications*, **195**(1-4), 107 (2001). [162](#)
- [207] TAKANO, K., MIYAMARU, F., SUMIKURA, H., NAGASHIMA, T., TANI, M., AND HANGYO, M. Enhanced THz Transmission and Polarization Conversion in Double-Layer Metal Hole Arrays. In *Joint 31st International Conference on Infrared Millimeter Waves and 14th International Conference on Terahertz Electronics, 2006. IRMMW-THz 2006*, volume 2742, pages 563–563. IEEE (2006). ISBN 1424404002. [163](#)